Aluminosilicate Borohydrides: NaBH$_4$ Embedded in Sodalite and Gel Structures

Von der Naturwissenschaftlichen Fakultät der

Gottfried Wilhelm Leibniz Universität Hannover

zur Erlangung des Grades

Doktor der Naturwissenschaften (Dr. rer. nat.)

genehmigte Dissertation

von

M. Sc. Lars Schomborg

geboren am 02.01.1984 in Osnabrück

2015

Referent: Prof. Dr. rer. nat. Claus Henning Rüscher

Korreferent: Prof. Dr. rer. nat. Josef-Christian Buhl

Korreferent: Prof. Dr. rer. nat. Thomas Bredow

Tag der Promotion: 24.07.2015

I Table of Contents

II Table of Figures

III Table Directory

IV List of Abbreviations

DTA   Differential thermal analysis
FTIR   Fourier transform infrared spectroscopy
TG   Thermogravimetry
XRD   x-ray diffraction
NMR   Nuclear magnetic resonance spectroscopy
σ   standard deviation
a.u.   area units

1.1. Zusammenfassung

Natriumborhydrid kann erfolgreich in eine aluminosilikatische Geopolymer-Matrix synthetisiert werden. Hierbei ist es möglich, bis zu 80 % einzubauen. Das erhaltene Material wird hinsichtlich seines $NaBH_4$ zu Matrix Verhältnisses und der Zusammensetzung der Matrix analysiert um daraus die Wasserstofffreisetzung zu optimieren. Mithilfe einer volumetrischen Gasbestimmung ist es möglich, die Kapazität der Wasserstoffspeicherung zu quantifizieren. Die Freisetzung des Gases erfolgt dabei mit einer säurekatalytischen Reaktion. Weitere Analysen erlauben zusätzlich neue Erkenntnisse über die Struktur der verwendeten Matrix, die als Zeolith-Precursor beschrieben werden kann. $NaBH_4$ wird außerdem in eine Sodalithmatrix eingebaut und analysiert. Hierzu werden drei Probenserien von verschiedenen Korngrößen und $NaBH_4$ zu Matrix Verhältnissen hergestellt und charakterisiert. Die Variation von Zusammensetzung und Morphologie führt zu deutlichen Veränderungen im Reaktionsverhalten des eingeschlossenen Salzes. Proben mit kleinerer Korngröße beinhalten größere Mengen von Wasser, das in den amorphen Bereichen der Matrix eingebaut ist. Diese Materialien weisen dann den größten Reaktionsgrad der thermischen Wasserstofffreisetzung auf, allerdings auf Kosten der Kapazität für $NaBH_4$. Zusammen mit der Änderung des $NaBH_4$ zu Matrix Verhältnisses ist es nunmehr möglich Proben herzustellen, die auf die gewünschte Fragestellung ausgerichtet sind: Höchstmöglicher Reaktionsgrad, höchstmögliche Menge an $NaBH_4$ oder eine Kombination daraus. Zudem werden die Einflüsse von Zusammensetzung und externen Parametern auf die thermische Wasserstofffreisetzung untersucht. Zu den externen Parametern gehören beispielsweise die Gasatmosphäre oder zusätzlich beigefügtes Wasser zur Reaktion. Zum Abschluss können Theorien widerlegt werden, die auftretende Spezies während der Reaktion fälschlich identifiziert haben. Dies gelang über die Anwendung neuer Methoden wie beispielsweise der ^{11}B MAS NMR hinsichtlich dieser Fragestellung. Die Untersuchungen des Mechanismus liefern neue Erkenntnisse über die Reaktion und werden hier vorgestellt.

Schlagwörter: Natriumborhydrid, Sodalith, Wasserstoff

1.2. Abstract

Sodium borohydride ($NaBH_4$) can be embedded successfully in an aluminosiliceous geopolymer type matrix with enclosing degrees of up to 80 wt%. The material is analyzed concerning the $NaBH_4$/matrix ratio, matrix composition and synthesis parameters to optimize the amount of hydrogen being released. Using a volume based method it is possible to quantify the hydrogen storage capabilities in the acid catalyzed reaction of $NaBH_4$. In addition further analyses exhibit new insights in the zeolite precursor matrix structure.

$NaBH_4$ is analyzed embedded in sodalite matrix, too. Three series of samples with different particle sizes and $NaBH_4$/matrix wt-ratios are synthesized and characterized. These variations in sample composition and sample morphology lead to significant changes in the reaction behavior of the enclosed $NaBH_4$. Material with smaller particle size shows a higher amount of water enclosed in amorphous areas of the sample. Those samples exhibit the highest reaction degree but at the expense of the lowest amount of $NaBH_4$ enclosed. Together with the variation of the $NaBH_4$/matrix wt-ratio it is possible to synthesize customized samples concerning the aims of analyzes: high reaction degrees, high enclathration degrees of $NaBH_4$ or a combination of both.

Using these samples the thermal hydrogen release reaction is analyzed concerning the influences of sample variations and external dependencies, like atmosphere and additionally added water. With new methods applied like ^{11}B MAS NMR, former theories on intermediate species formed are reviewed. A previously suggested identification of observed species could be corrected and new insights on the reaction mechanism can be presented.

2. Introduction

During the last years the necessity for new energy storage systems massively increased due to political decisions like the 'energy revolution' which promotes renewable energy sources. Especially solar- and wind energy are not available at constant level day and night. To make this energy constantly available it needs to be stored in an economic and safe way [1], [2].

Beside the massive efforts and progress in the research and development of secondary batteries also the classical chemical approach, storing energy as hydrogen-bearing compounds, is reasonable justified. In this research field, different ideas are under discussion, for example metal-organic framework compounds (MOFs), cryogenic and high pressure storages and several chemical alloys like metal hydrides, carbon nanotubes and clathrates [3]–[9]. The research of this thesis is based on sodium borohydride ($NaBH_4$) enclosed in two different types of matrixes.

Sodium borohydride was first synthesized in the 1940s [10]. Due to its high hydrogen capacity of 5.3 wt% molecular hydrogen (H_2) with the reaction with water, this material represents a promising research subject as hydrogen storage system [11]–[14]. Under dry conditions, sodium borohydride remains stable but hydrolyzes spontaneously in the presence of water, while generating hydrogen. Especially at temperatures above 40 °C this reaction takes place. The capacity equals 2.4 l H_2 per gram, which can be set free following the summarized reactions (1 and 2) given in [10]:

$$NaBH_4 + 4\ H_2O \rightarrow NaB(OH)_4 + 4\ H_2 \tag{1}$$

$$NaB(OH)_4 \rightarrow NaBO_2 + 2\ H_2O \tag{2}$$

$NaBH_4$ can furthermore be used as electrochemical energy carrier. In alkaline solutions and in presence of a catalyst the reaction follows equation 3. This reaction can be used in DBFC [15].

$$NaBH_4 + 8\ OH^- \rightarrow NaBO_2 + 6\ H_2O + 8\ e^- \tag{3}$$

During the last decades, the research in the field of $NaBH_4$ as energy carrier was discontinuous.

Why is $NaBH_4$ not already in use as energy carrier extensively? Here several reasons can be given. First of all, the synthesis is very expensive. In commercial use the synthesis route usually follows the *Brown-Schlesinger process* [10], [16]: The synthesis is a seven step process, if the production of raw hydrogen and sodium are also taken into account:

1. Steam reforming of methane to make hydrogen
2. Electrolysis of sodium chloride to make sodium metal
3. Refining of borax to make boric acid
4. Converting boric acid to trimethylborate with methanol
5. Reaction of sodium metal and hydrogen to make sodium hydride
6. Combining sodium hydride and trimethylborate to make sodium borohydride
7. Recycling sodium methoxide by product to methanol

The combination of these steps leads to the following summarized molecular formula:

$$4\ NaH + B(OCH_3)_3 \rightarrow NaBH_4 + 3\ NaOCH_3 \tag{4}$$
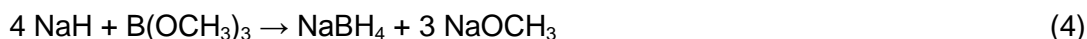
The second problem is the need of a catalyst to set free the whole amount of hydrogen. These catalysts are an additional economical factor as for example in [17]–[21].

Despite the massive efforts on research and development of the use of $NaBH_4$ as energy carrier the detailed reaction mechanism is still under discussion. The overall formula is mainly accepted as:

$$NaBH_4 + 2\ H_2O \rightarrow NaBO_2 + 4\ H_2 \tag{5}$$

The occurring intermediates are not yet identified. Without this information a direct reloading of the $NaBH_4$ or one of the intermediates is not possible yet. Up to now there are only recycling processes published like the reaction of $NaBO_2$ with magnesium under high hydrogen pressure following Kojima and Haga [22] or electrolysis reactions [23]. It is

probably possible to enable a direct back reaction from the intermediate reaction steps. Therefore it is of highest to improve the understanding of the reaction mechanism and the influence of different parameters.

Aims of the present study

The aim of the present work is the investigation of $NaBH_4$ bearing aluminosilicate materials. As first approach a new material is investigated which is based on the enclathration of $NaBH_4$ in a dried zeolite precursor solution. The properties of these geopolymer type materials are analyzed mainly focused on an optimized hydrogen amount.

The second material used is $NaBH_4$ enclosed in sodalite. The analyses of this material are focused on the influences of different synthesis variations on the product on the one hand and the reaction behavior on the other hand. In addition the reaction mechanism of the hydrogen release reaction is analyzed in detail concerning different internal and external parameters.

The analytical methods used in this thesis represent a broad variation of up to date analytics in the geosciences and materials sciences. All methods used are introduced briefly in the section '*Methods*' before the obtained results are presented and discussed.

Structure of the work

Chapter A is entitled '*Synthesis and Characterization of NaBH$_4$ Embedded in Geopolymer Type Gels*' and focuses on the enclathration of $NaBH_4$ in an aluminosilicate gel-matrix. Here the reaction mechanism is not in the foreground but the optimization of the material in order to obtain to an as high as possible hydrogen amount. In the first subdivision the synthesis variations are presented and the material is analyzed as a function of the different chemical compositions. The second part of Chapter A gives additional analyses, where not the whole series but selected samples were analyzed. In the third part the quantification of the hydrogen release is presented. The focus is on the volumetric determination of hydrogen released from the different series as characterized in the first

subchapter. From the amounts of hydrogen obtained experimentally the enclathration degree of $NaBH_4$ in the matrix is calculated in order to get information on the effectiveness of this new hydrogen storage system.

Chapter B is entitled '*Characterization of BH4-Sodalite: Synthesis Variations and Comparison*'. This Chapter focuses on the composition and the particle size of BH_4-Sodalite to gain deeper understanding of the material. Therefore three synthesis series are shown, which differ from each other by their synthesis temperature, the starting materials and the particle size of the products. In each series the $NaBH_4$/matrix wt-ratio is varied in the range from 0.03 to 1.5 in order to receive samples with different embedding degrees of $NaBH_4$. Thereby all obtained samples are supposed to have a constant molar Si/Al-ratio of 1. Kaolin is used as matrix reactant for the 120 °C and the 80 °C series, while for the 60 °C samples, a combination of sodium metasilicate and sodium aluminate is under investigation. The obtained samples were first characterized by X-ray diffraction and infrared spectroscopy. After that, the samples were analyzed by Differential Thermal Analysis and Thermogravimetry. Selected samples from these synthesis series are used for further characterizations and the study of the reaction mechanism of $NaBH_4$ in sodalite in Chapter C.

Chapter C is entitled '*Mechanism Study of the Hydrogen Release from BH4-Sodalite*' and focuses on the reaction of the BH_4^- enclosed in the sodalite structure. The mechanism is analyzed according to several parameters like atmosphere, temperature, availability of water and the chemical composition of the synthesis series, as presenteded in Chapter B. Additionally the intermediate species and the reaction products are described in more details.

3. Methods

3.1. Syntheses

3.1.1. Gel Precipitation

The gel syntheses took place under open conditions. The synthesis type is first described by Buhl et al. [24] and Rüscher et al. [25]. For the initial synthesis two solutions needed to be prepared. Solution I consisted of sodium aluminate ($NaAlO_2$, *Aldrich 307815*) solved at slightly increased temperatures in 1.5 ml water. Solution II consisted of sodium metasilicate (Na_2SiO_3, *Riedel-de Haën 13404*) also solved at slightly increased temperatures in 1.5 ml water. The same amount of sodium borohydride ($NaBH_4$, *Merck 806373*) was added to each of the solutions while stirring. After the reactants were completely dissolved, solution II was added to solution I drop by drop. With the first drop added, the gel precipitation was initiated. The obtained gels were stirred for the material to be homogenized. Afterwards, the $NaBH_4$-bearing gels were dried at elevated temperatures.

The syntheses were optimized with respect to several parameters. The $NaBH_4$/matrix wt-ratio was varied from 0.36 to 3.04. This ratio is defined as the mass of $NaBH_4$ used in both solutions divided by the sum of the mass of Na_2SiO_3 and $NaAlO_2$ used:

$$\frac{NaBH_4}{matrix} = \frac{m_{NaBH4}}{m_{Na2SiO3} + m_{NaAlO2}} \tag{6}$$

The molar Si/Al ratio of the matrix was varied from 0.22 to 2.69 and the synthesis temperature was varied from room temperature up to 110 °C.

3.1.2. Hydrothermal NaBH₄-Sodalite Syntheses

3.1.2. Hydrothermal NaBH₄-Sodalite Syntheses

Three synthesis-series were carried out, varying the $NaBH_4$/matrix wt-ratio from 0.03 to 1.5 as well as the synthesis temperature at 60, 80 and 120 °C. The $NaBH_4$/matrix wt-ratio is defined just as given in equation 6 for the 60 °C series. Equation 7 defines the $NaBH_4$/matrix wt-ratio for the 80 and 120 °C series:

$$\frac{NaBH_4}{matrix} = \frac{m_{NaBH4}}{m_{kaolin}} \qquad (7)$$

The syntheses were carried out, based on a procedure first described by Buhl et al. [26]. The required amount of $NaBH_4$-granulate, 1 g of the matrix reactant kaolin (*Fluka 60609*) and 10 ml of a freshly prepared 16 M sodium hydroxide (NaOH, *Merck 10646790*) solution were added into a Teflon liner. The Teflon liner was closed and set into a 50 ml Teflon coated *Berghof DAE-2* steel autoclave. These autoclaves were then heated for 24 h at 120 and 80 °C respectively. After the reaction the autoclaves with the inserted Teflon cups were opened and the excess of sodium hydroxide solution was decanted. The remaining greyish materials needs to be washed using a paper filter with distilled water to remove the base. Otherwise carbonate could form due to atmospherically absorbed CO_2 in the reaction with the high pH-value of the samples. Additionally remaining NaOH could crystallize during the following drying process. To remove the base about 500 ml of distilled water is needed till the pH-value of the fresh filtrate is at about 8. After the washing procedure, the samples were dried for 48 h at 80 °C in a drying chamber.

Special syntheses were carried out at 60 °C. At this reduced temperature the kaolin does not recrystallize to form a zeolite-type structure. Therefore sodium metasilicate and sodium aluminate were used as reactants to form the sodalites. For each synthesis 1.2 g of Na_2SiO_3 and 0.8 g $NaAlO_2$ were used to obtain a molar Si/Al ratio of 1. Those reactants were solved in 10 ml of a freshly prepared 5 M sodium hydroxide solution, each. The required mass of $NaBH_4$ was weighed into a Teflon liner and afterwards the silica and alumina solutions were added and the liners were closed. The liners were set into the same steel autoclaves, as described before. In this synthesis series, the reactants were heated for only

6 h at 60 °C. After the reaction, the autoclaves and the Teflon cups were opened and the slightly grey products were filled in centrifuge tubes, together with the excess of base and distilled water. After the centrifugation, the overlaying basic solution was decanted. To wash these samples, fresh distilled water was added and the samples were suspended and afterwards centrifuged, again. This washing procedure was repeated 8 times per sample. This washing effect corresponds to that of using about 500 ml water and paper filters. Paper filters could not be used for this synthesis series, because the small particles would immediately clog the filter pores. The samples were also dried for 48 h at 80 °C in a drying chamber.

3.1.3. Hydrothermal NaB(OH)$_4$-Sodalite Synthesis

The hydrothermal synthesis of NaB(OH)$_4$-Sodalite followed the above mentioned synthesis of NaBH$_4$-Sodalite at 120 and 80 °C respectively. As reactants for NaB(OH)$_4$-Sodalite 4 g of boric acid (H$_3$BO$_3$, *Riedel-de Haën 31146*), 1 g kaolin and 10 ml of 8 M sodium hydroxide solution were mixed together in the Teflon liners. The reaction time for this material is 48 h at 200 °C. Afterwards the product was also washed with distilled water using paper filters and dried for 48 h at 80 °C in a drying chamber [27].

3.2. Spectroscopic Methods

3.2.1. Fourier-Transformation-Infrared-Spectroscopy (FTIR)

The FTIR-measurements were carried out using the *Bruker Vertex 80v* spectrometer. The samples were mainly analyzed in the mid-infrared range between 370 and 5000 cm^{-1} with a resolution of 2 cm^{-1} and 32 scans. For the powder samples, the KBr-method was used. Typically about 1 mg of the sample was diluted in 199 mg of potassium bromide to form a solid pellet. For each sample three pellets were prepared to allow an error calculation. The data evaluation was carried out with *Bruker Opus 6.5* software. Using two different normalization methods, the possibly occurring errors due to sample preparation were reduced [28]. For the mass normalization the sample mass used for each pellet prepared

was normalized to 1 mg. The second method is based on the ν_{sym} T-O-T bands of the sodalite [27]. The measured integrated areas of occurring species is normalized to the area of this structure related wavenumber range. This method reduces preparation errors like inhomogeneity and different particle sizes in the pellet. All described effects were crosschecked with both normalization methods.

3.2.2. Temperature Dependent FTIR (T-FTIR)

The temperature-dependent FTIR measurements were carried out using the *Bruker IFS 66* spectrometer equipped with a special heating device, described by Rüscher [29]. Measurements were performed in the mid-infrared range between 370 and 5000 cm^{-1} with a resolution of 2 cm^{-1}. To avoid cation exchanges with the sample sodium chloride was used as pellet matrix in some cases instead of potassium bromide. The heating device effectively operates in the temperature range between 20 and 550 °C under vacuum conditions. It consists of an electric oven with a water cooling system and a special 99.99 % silver sample holder for an optimal heating flow into the pellet.

3.2.3. Nuclear Magnetic Resonance Spectroscopy (NMR)

All NMR measurements were carried out at the Institut für Geologie, Mineralogie und Geophysik of the Ruhr-Universität Bochum. The superconducting FT-NMR spectrometer is a *Bruker ASX 400 WB*, using a standard Dewar configuration. Spectra are given relative to $BF_3 \cdot Et_2O$. Measurements were used to analyze the occuring species in the thermal reaction starting from BH_4-Sod and $B(OH)_4$-Sod, respectively. Measuring parameters are given in Table 1. Selected spectra were evaluated using a peak-fit which was performed using the *dmfit* software [30].

Table 1: Measuring Parameters of ^{11}B MAS NMR and ^{11}B MQMAS NMR

Parameter	^{11}B MAS NMR	^{11}B MQMAS NMR
Rotor speed (ν_{rot})	12.5 kHz	12.5 kHz
No. of scans accumulated (NS)	6000	2400 - 4800
Recycle delay (D1)	1 sec	0.5 sec
Pulse duration (P1)	0.6 µsec	5.6 µsec
Probehead	4 mm MAS 1H	4 mm MAS 1H

3.3. X-Ray Diffraction

3.3.1. Powder Diffraction (XRD)

The samples were analyzed, using the *Bruker D8 Advantage* and the *Bruker D4 Endeavour* powder diffractometer. The diffractograms were measured between 5 and 80 °2θ. Step width and measuring time per step were varied for different samples. The used measuring parameters are given with the results. Both diffractometers use CuKα-radiation. The obtained data were evaluated using *STOE WinXPOW* and *Bruker TOPAS 4.2* software.

The gel samples were first analyzed as levigation-supplements due to their physical conditions. Additionally a specimen holder ring made of plastics for the *D8 Advantage* was realized, which allowed higher qualities of the measurements. For the sodalite samples a standard specimen holder ring was used.

The data were analyzed mainly for their lattice constants depending on the synthesis variations, the quality of the syntheses and for selected samples the average crystal size using the *Scherrer equation* [31].

3.4. Thermoanalytical Methods

3.4.1. Thermogravimetry / Differential Thermal Analysis (TG/DTA)

All measurements were carried out, using the *Setaram SetSys Evolution 1750* equipped with a combined measuring head *TGA-DTA 1600*. About 20 mg of the samples were heated in specified atmospheres, as synthetic air (80 % N_2/20 % O_2) or inert gas (here: He 99.9999). Different measurement programs were chosen with heating/cooling rates between 4 and 20 °C/min, temperatures up to 500 °C and holding times up to 48 h, typically under 20 ml/min gas flow.

Thermogravimetry (TG) shows even smallest changes in the sample mass during heating, while Differential Thermal Analysis (DTA) provides information about any energetical

changes in the sample caused by chemical reactions or phase transitions. Therefore a reference was measured at the same time as the sample. The temperature difference between sample and reference represents energetic changes during heating. For baseline correction reference measurements with two empty sample crucibles were carried out.

TG/DTA methods were used as stability tests for $NaBH_4$-gel samples. Furthermore the water content was determined. For the sodalite samples, this method was additionally used as a well defined reaction chamber for the study of the reaction mechanism of $NaBH_4$ in sodalite.

3.4.2. Karl-Fischer-Titration (KFT)

The used KFT device consists of a programmer controlled high frequency generator to allow heating temperatures up to 1300 °C and a *Mitsubishi CA100* titrator. The samples were heated in a platinum sample holder in an argon flow; the gas transported the released water to the titrator. Water enables the reaction of sulfurdioxide with iodide, which can be quantified:

$$2\ H_2O + SO_2 + I_2 \rightarrow SO_4^{2-} + 2\ I^- + 4\ H^+ \tag{8}$$

It is possible to measure sample masses of 5 to 50 mg with a detection limit of 5 µg H_2O. In mineralogy the main application is the determination of water contents of solid materials, such as minerals, rocks and glasses.

3.4.3. Carbon-Sulfur-Analysis (CS)

Carbon-Sulfur-analyses were carried out, using an *Eltra CS800*. Iron and tungsten chips were added to the sample material to provide entire oxidation and melting throughout the following heating process. The closed oven consists of an induction coil, which creates a strong magnetic field to heat up the material. While heating, oxygen is injected and the carbon and sulfur from the sample material are oxidized to CO_2 and SO_3, respectively. These gases were then measured, using an infrared detector. The detection limit of carbon is 6 µg and that of sulfur is 5 µg.

3.5. Volumetric Methods

3.5.1. Hydrogen Release

For the determination of hydrogen gas released a glass apparatus with a gas syringe as main element was constructed [32]. The measurements are based on a volumetric determination of the released gas from the samples which was set free by the addition of diluted acid. Figure 1 shows the schematic buildup.

Specific amounts of the dry, solid sample were disposed into the two-neck-bulb. With an injection needle a definite volume of a 3 % hydrochloric acid can be added trough a pierceable rubber plug to make sure the apparatus remains gastight. The gas syringe shows the amount of gas released. The added volumes of the acid were subtracted and the load of the glass piston was taken into account, following equation 9.

$$\left(\frac{m_{piston}}{g}\right) \Bigg/ \left(\frac{\pi \cdot (D_{piston})^2}{4}\right) = 1200 \text{ Pa} \qquad (9)$$

The mass of the piston (m_{piston}) is 92.83 g and its diameter (D_{piston}) is 3.108 cm, g is the acceleration of gravity 9.80665 m/s^2 [33]. The extra-load of the piston therefore increases the pressure in the system by 1200 Pa, which leads to a correction factor for the measured gas volumes of 1.0118 in relation to the normal pressure.
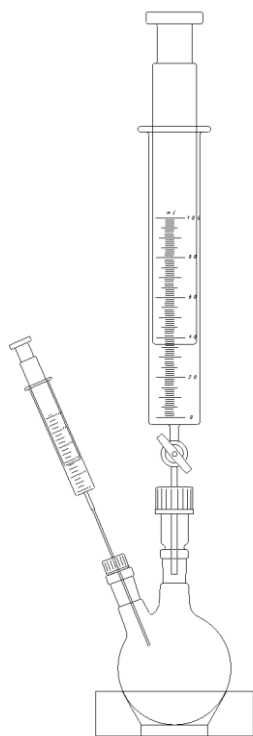
Figure 1: Scheme of the used glass apparatus for hydrogen release experiments

For every sample, at least three measurements with different sample weights were carried out. This way it is possible to determine the released hydrogen volume per 100 mg sample (NaBH$_4$ gel) and per 1 g sample (BH$_4$-sodalite), respectively, by linear regression and to calculate the errors of these analyses. To ensure that the released gas consists of hydrogen only or at least mainly of hydrogen, samples of the gas were analyzed with a gas detector with a detection limit of 1000 ppm for CO$_2$. Carbondioxide could be the only additional gas to be included in the samples. To confirm the release of hydrogen, the

oxyhydrogen-test was carried out for several samples. Afterwards, the obtained data were used to carry out back-calculations to connect the volume of released hydrogen with the amount of NaBH$_4$ definitely built in the gel-matrix. Additionally the amounts of hydrogen were connected to the integrated intensities of the BH$_4^-$ bands, obtained by infrared spectroscopy.

The errors of those measurements consisted of the reading error at the gas syringe (corrected with the piston load), which is expected to be 1 ml, which is the graduation of the scale. Another error was caused by the added volume of acid by the injection needle, which was experimentally determined against a graduated flask. The absolute error is ± 0.02 ml. As the volume of the added acid had to be taken into account twice, namely for adding the acid and afterwards for subtracting the volume from the gas volume, read at the gas syringe, it is multiplied by 2 in equation 10. Equation 11 gives the absolute error for a single hydrogen release experiment. As the actual result for a sample was calculated from several of those single measurements, using linear regression in *Microsoft Excel* with the integrated *RGP-function*, the overall error was calculated from a combination of the average error from the single measurements and the given error from the *RGP-gradient*, as shown in formula 11.

$$\Delta V_{gas, \text{ single measurement}} = \sqrt{\left[\left(\left(\frac{V_{acid}}{V_{gas}} \right)^2 \cdot 0.02^2 \right) \cdot 2 + \left(\frac{V_{gas}}{V_{gas}} \right)^2 \cdot 1^2 \right]} \tag{10}$$

$$\Delta V_{gas} / V_{gas} = \sqrt{\left[\left(\text{rel.error}_{RGP\text{-gradient}} \right)^2 + \left(\text{av.rel.error}_{gas, \text{ single measurement}} \right)^2 \right]} \tag{11}$$

The calculated, relative errors vary from 4 to 11 % for the NaBH$_4$-gels and from 5 to 12 % for the BH$_4$-sodalite samples.

3.5.2. Back Calculations

Using the obtained data from hydrogen release experiments it is possible to back-calculate an estimation of the amount of NaBH$_4$, which was built into the aluminosilicate matrix of the NaBH$_4$-gels and the sodalite structure, respectively (see equation 12). Those calculations

can be kept simple, the ideal gas law gives adequately precise results in the used temperature and pressure range, close to standard conditions [34]. For some data, a cross check using the *van-der-Waals* equation was performed; the results varied below 1/10 ‰ compared to the results obtained by the ideal gas law. For the calculations two assumptions were necessary: 1. The reaction takes place completely; 2. Four moles of hydrogen are released per mole of $NaBH_4$ by the reaction with the acid following reaction 1 & 2. Afterwards, the mass of $NaBH_4$ used during the synthesis can be compared to the mass of $NaBH_4$, which equals the obtained amount of released hydrogen. The errors of temperature and pressure variations due to weather are negligible, the relevant error consists of the measured volume of the released hydrogen only, as described above.

$$m_{NaBH4} = \frac{1}{4} \cdot M_{NaBH4} \cdot \left[\left(p_0 \cdot \frac{V_{H2,\,corr.}}{1000} \right) / (R \cdot T_0) \right] \tag{12}$$

with M_{NaBH4}=37.83 g/mole, p_0=1.013 bar, $V_{H2,\,corr.}$ in ml, R=0.08314472 l·bar·K^{-1}·mole^{-1} and T_0=293.15 K

3.6. Imaging Methods

3.6.1. Scanning Electron Microscope (SEM)

The samples were analyzed using a *Jeol JSM-6930A* SEM equipped with a *BRUKER XFlash Detektor 410-M-200*. The sample needs to be sputtered with a thin layer of gold to allow the electric charge, caused by the electron beam, to flow off. The electrons interact with the sample and secondary electrons are set free (back-scattered-electrons), which can be used to create image information. The investigations were performed at acceleration voltages of 10 and 20 kV and varied spot sizes.

With the obtained BSE-images a morphologic particle size distribution was done. The pictures were evaluated with the free, java-based Software *ImageJ* [35]. This program allows

to measure the length of drew lines in pixels; when this is also done for the scale of the BSE-

images, the particle size can be calculated.

Part A:

Synthesis and Characterization of NaBH$_4$ Embedded in Geopolymer Type Gels

4. NaBH$_4$-Gel

4.1. Sample Characterization of NaBH$_4$-Gel

The main characterization of the NaBH$_4$-gel samples consists of FTIR and, for some selected samples, XRD depending on their chemical compositions.

NaBH$_4$ is characterized via FTIR by a single sharp peak at 1123 cm^{-1} and a triplet peak at 2222, 2291 and 2383 cm^{-1}. These peak positions are in good agreement with literature results [36]–[39]. The peak at 1123 cm^{-1} is assigned to the B-H deformation signal v_4 of the BH$_4^-$ tetrahedral unit. The suggested ideal tetrahedral BH$_4^-$ unit should show two IR active modes (v_3 and v_4), only. However, the v_3 signal has approximately the same position as the overtone mode 2·v_4, which leads to a *Fermi Resonance* effect [40]. Therefore, two peaks become visible due to a splitting of the v_3 signal and shared intensities between the v_3 and 2·v_4 mode. Additionally the peak at 2389 cm^{-1} is a combination mode of $v_4 + v_2$; v_2 is Raman active only (peaked at 1274 cm^{-1}) [17], [41].

Especially the combination of the sodium containing samples with relatively high amounts of water together with the use of potassium bromide as FTIR pellet-material is problematic. In some cases the gel samples formed the stable compound NaBr·2H$_2$O during the pestling of the sample with the KBr. For a better comparison and later discussion a typical spectra of pure NaBH$_4$ and also NaBr·2H$_2$O obtained by the KBr method is shown in Figure 2.
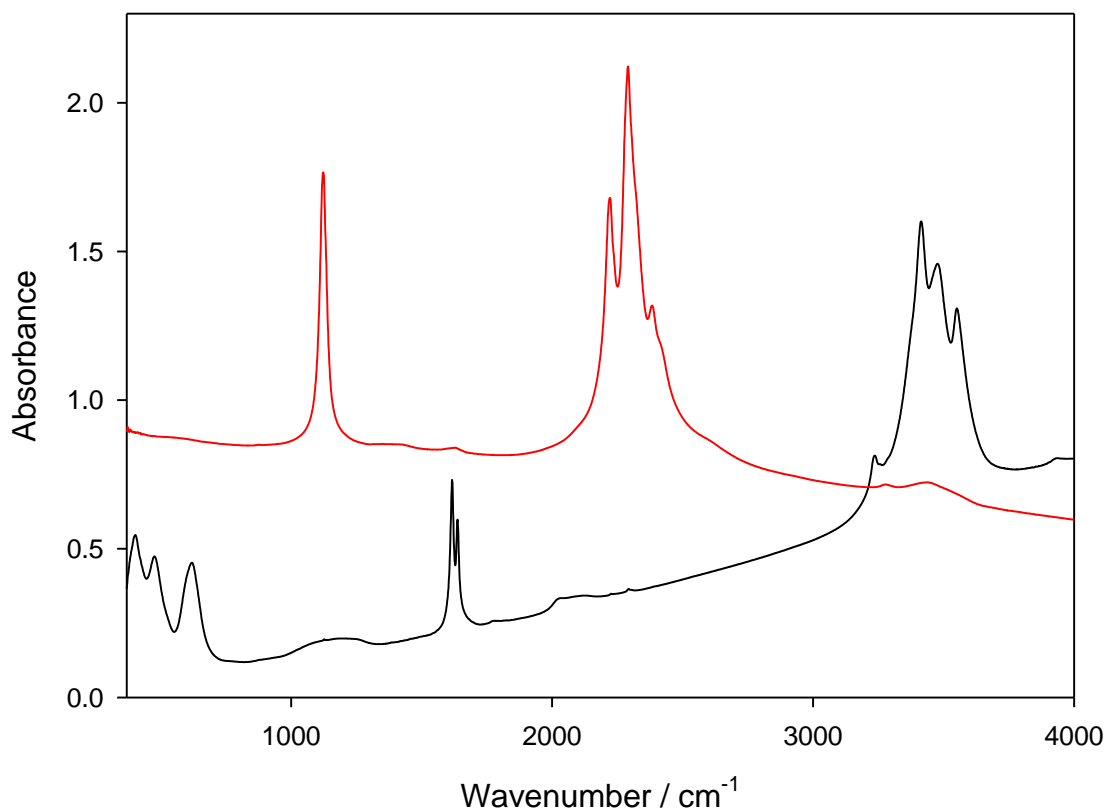
Figure 2: FTIR spectra of reactant NaBH$_4$ (red) and NaBr•2H$_2$O (black)

NaBr·2H$_2$O is characterized by four well-defined peaks of the OH-bonding at 3237, 3414, 3477 and 3551 cm^{-1}. The corresponding water signal shows two peaks at 1617 and 1638 cm^{-1}. Additionally, three more peaks are visible at 404, 476 and 619 cm^{-1} [36]. Exactly these peaks are positioned at almost the same wavenumbers as sample-related signals, which causes some problems while evaluation of the FTIR spectra.

4.1.1. Variation of the NaBH$_4$/matrix wt-ratio: Gel Series 1

The NaBH$_4$/matrix wt-ratio was varied as first parameter. The amounts of the aluminate and silicate matrix-reactants were kept constant to maintain a molar Si/Al ratio of 0.83. The amount of water used for both solutions and the drying process at 110 °C in a drying cabinet were also kept constant during this synthesis batch. Solubility experiments showed that a maximum of 850 mg of NaBH$_4$ could be solved in each of the pre-synthesis solutions I and II

(solubility of $NaBH_4$ in water 550 mg/ml, [42]). In Table 2, the used amounts of the reactants and the main sample parameters are summarized.

Table 2: Sample overview of the $NaBH_4$ gel Series 1: Variation of the $NaBH_4$/matrix ratio

$NaBH_4$/matrix wt-ratio	$NaBH_4$ / mg	$NaAlO_2$ / mg	Na_2SiO_3 / mg	molar Si/Al	Synthesis temperature / °C
0.36	200	250	310	0.83	110
0.89	500	250	310	0.83	110
1.43	800	250	310	0.83	110
2.14	1200	250	310	0.83	110
3.04	1700	250	310	0.83	110

The FTIR spectra of series 1 with varied $NaBH_4$/matrix wt-ratio between 0.36 and 3.04 are shown in Figure 3. The spectra were normalized on the integrated peak area of the peak at 987 cm^{-1}. These peaks indicate geopolymer matrix and include the sodalite contribution, too. All spectra exhibit the single, sharp peak and the triplet peak of the $NaBH_4$ at 1126 cm^{-1} and 2225, 2292 and 2387 cm^{-1}, respectively. The mentioned phase $NaBr \cdot 2H_2O$ is only visible in the spectrum of $NaBH_4$/matrix equals 0.89 (blue in Fig. 3) at peaks 404, 472, 618 cm^{-1} and the H_2O-peaks at 1618 and 1638 cm^{-1}. As an additional phase, sodium carbonate and sodium hydrogen carbonate can be identified via the peaks at 1447, 865 and 880 cm^{-1}, respectively [43]. The $NaCO_3$ and $NaHCO_3$ existence leads to the peak splitting at 865 and 880 cm^{-1}, respectively. This carbonate forms from the reaction of the high alkalinity of the sample with carbon dioxide from the atmosphere [34]. There are some additional minor peaks visible at 731, 695, 669 and 434 cm^{-1}. Together with the peak at 987 cm^{-1}, these indicate the presence of a sodalite related phase [26]. The composition of the matrix is discussed in detail in chapter 4.4.

The spectra of this synthesis-series show qualitatively the expected trend that the $NaBH_4$-related peaks increase in their intensities with increasing $NaBH_4$/matrix wt-ratio with the normalization on the matrix signal area at 987 cm^{-1}. The sodalite related peaks and the carbonate signals remain more or less constant with an increasing $NaBH_4$/matrix wt-ratio.
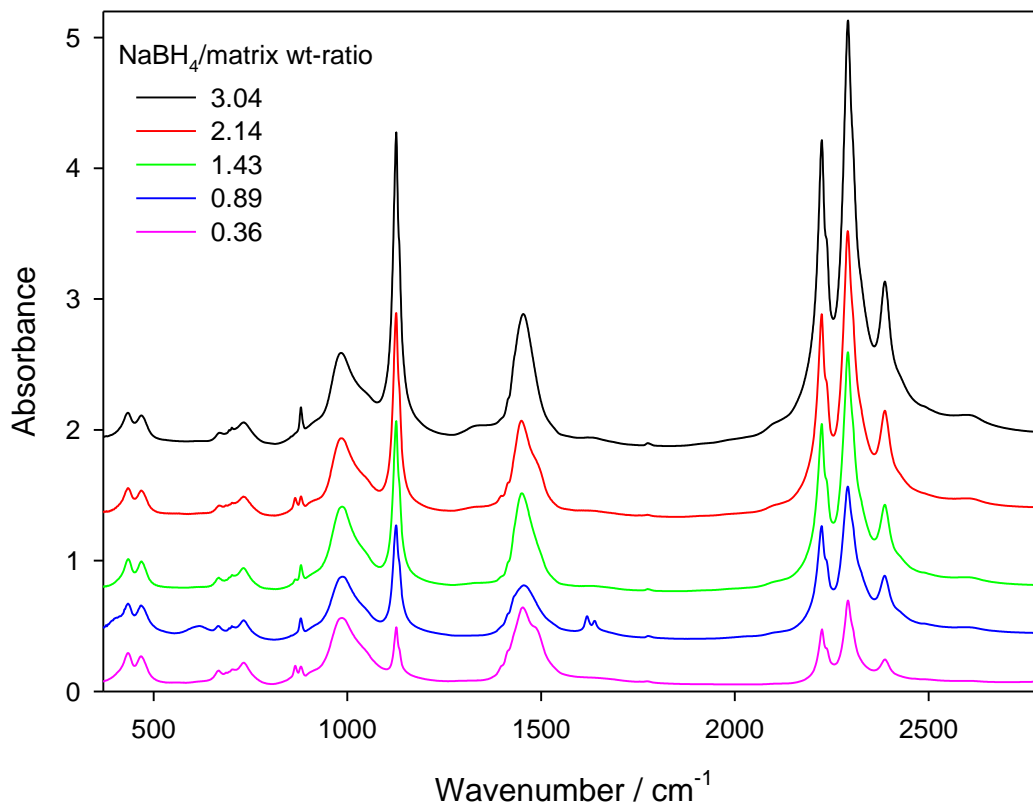
Figure 3: FTIR spectra of NaBH$_4$-bearing gels with different NaBH$_4$/matrix ratios, as given in the legend. All spectra are normalized on the peak area of the matrix peaks at 987 cm^{-1}.

Figure 4 shows the X-ray powder diffractograms of four samples of Series 1. The diffractograms are normalized on the reflex intensity of the 14.17 °2θ reflex of sodalite for better comparison. All samples show a broad diffraction peak range from 22 to about 50 - 60 °2θ with a maximum at 32 °2θ. Additionally, the reflexes of sodalite, NaBH$_4$ and carbonate are visible. In Table 3, the reflex positions and the corresponding phases are summarized. The reflex positions during the series may slightly vary. Only sample 0.34 shows an additional reflex at 10.55 °2θ, which could not be identified by reference materials.

Table 3: Reflex positions of x-ray diffraction data, NaBH$_4$-gels

Reflex position / °2θ	Corresponding species	Reflex position / °2θ	Corresponding species
10.55*	*unidentified signal*	39.94	Carbonate
14.17	Sod	41.10	Carbonate
16.96	*probably* Carbonate	41.32	NaBH$_4$
18.07	*sample holder*	41.61	NaBH$_4$
24.33	Sod	42.87	Sod
25.22	NaBH$_4$	46.64	Carbonate
29.16	NaBH$_4$	48.33	Carbonate
30.12	Carbonate	49.17	NaBH$_4$
31.58	Sod	51.49	NaBH$_4$
34.40	Carbonate	58.44	Sod
34.69	Carbonate	60.37	Sod
35.22	Carbonate	62.23	Sod
37.59	Sod	64.16	Sod
37.95	Carbonate		
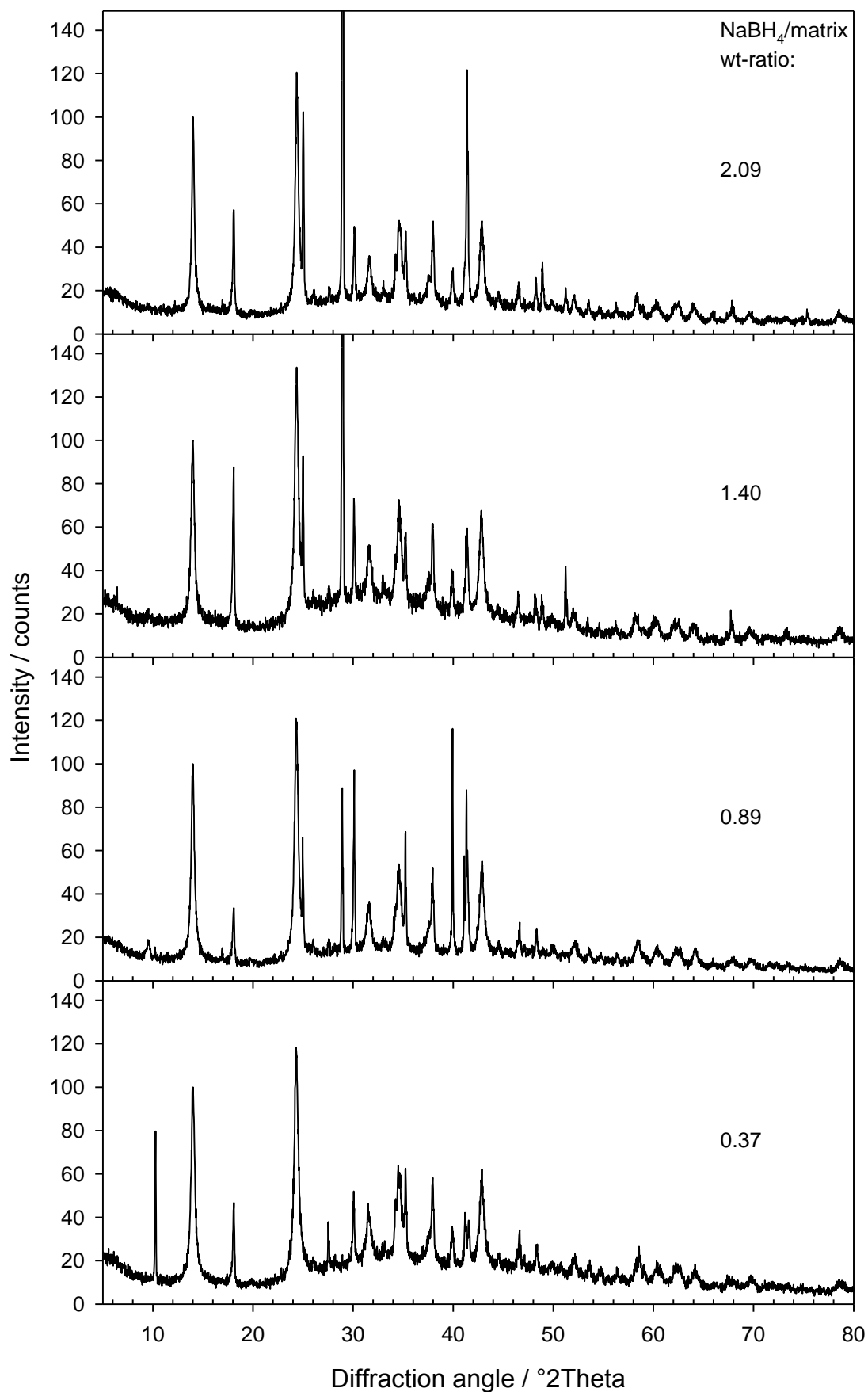
Figure 4: X-ray diffractograms of selected samples from gel Series 1

The diffractograms show the expected trend: with an increasing $NaBH_4$/matrix ratio the reflex intensities of the $NaBH_4$ reflexes also increase, for example at 29 °2θ. To be able to compare the amorphous phase of the samples, the diffractograms are only shown up to 150 counts in intensity. The mentioned $NaBH_4$ reflex at 29 °2θ has a normalized intensity for the 2.09 sample of 349 counts and for the 1.40 sample of 190 counts.

4.1.2. Variation of the matrix molar Si/Al ratio: Gel Series 2

To analyze the influence of the matrix molar Si/Al ratio, a synthesis batch with a constant $NaBH_4$/matrix ratio of 1, dried at 110 °C for two hours was prepared. The molar Si/Al ratio was varied from 0.22 to 2.69. The relatively low $NaBH_4$/matrix wt-ratio of 1 was chosen to prevent problems that may occur by dissolving the $NaBH_4$ in both the alumina-rich solution I and the silica-rich solution II, corresponding to the chosen Si/Al ratio. The used sample compositions are summarized in Table 4.

Table 4: Sample compositions of gel Series 2

molar Si/Al	total $NaBH_4$ / mg	$NaAlO_2$ / mg	Na_2SiO_3 / mg	$NaBH_4$/matrix wt-ratio
0.22	400	300	100	1
0.27	560	400	160	1
0.34	600	400	200	1
0.45	500	300	200	1
0.67	600	300	300	1
1.01	500	200	300	1
2.01	400	100	300	1
2.69	750	150	600	1

The sample with a molar Si/Al ratio of 0.22 did not form a stable gel in contrast to the other samples of this synthesis series. This sample remained wet after two hours at 110 °C and even extended drying time up to four hours.

Figure 5 shows the spectra of all samples of this synthesis batch (Series 2) with increasing molar Si/Al ratio of the matrix from top to bottom. The spectra are normalized on the integrated peak area of the $NaBH_4$-triplet signal for a better comparison of the matrices.

All samples exhibit the $NaBH_4$ related peaks as dominant signals. The positions of the triplet-structure are constant throughout the series at 2226, 2293 and 2389 cm^{-1}. Additionally, all samples show a shoulder peak at 2238 cm^{-1}. The single sharp band is located at 1127 cm^{-1} with a shoulder at slightly increased wavenumbers in all sample spectra.

The phase $NaBr \cdot 2H_2O$ is visible in all samples (only in small amounts in Si/Al = 2.01) apart from Si/Al = 1.01. These samples also show the OH-related signals of $NaBr \cdot 2H_2O$ at 3237, 3413, 3475 and 3549 cm^{-1}, the two H_2O signals at 1615 and 1637 cm^{-1} and the three peaks at 616, 402 and 476 cm^{-1}.

Carbonate can be identified in all samples. The two samples without or with only small amounts of $NaBr \cdot 2H_2O$ (Si/Al of 1.01 and 2.01) show a broad single peak at 1445 cm^{-1} for the carbonate species and signals at 864 and 879 cm^{-1}. The signal at 879 cm^{-1} is probably related to the formation of $NaHCO_3$. Samples with significant amounts of $NaBr \cdot 2H_2O$ show two peaks in the range of the carbonate at 1445 and 1494 cm^{-1}.
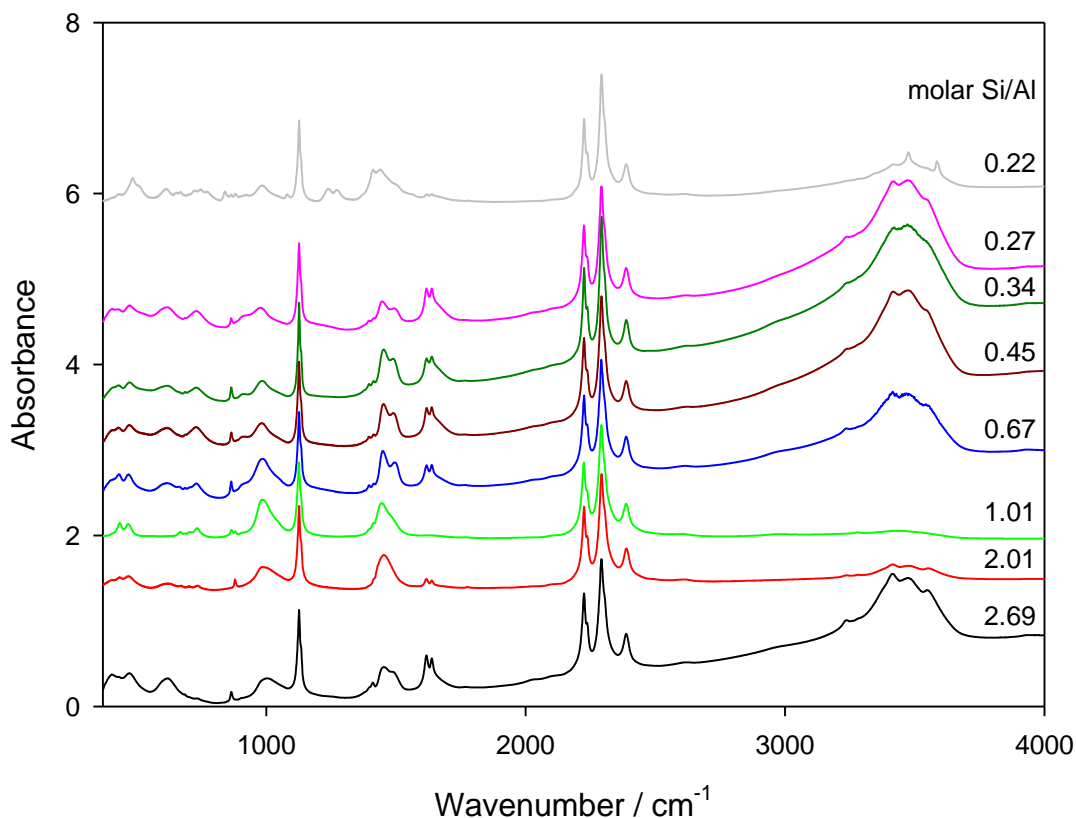
Figure 5: FTIR spectra of NaBH$_4$-bearing gels with constant NaBH$_4$/matrix ratio and varied molar Si/Al ratios of 0.22 to 2.69.

In Figure 6 selected samples of this synthesis batch are shown with a focus on the matrix vibrations in the wavenumber range from 370 to 1800 cm^{-1}. For the Si/Al ratio of 2.01 the peak at 984 cm^{-1} appears to be broader and not as high in intensity as the samples in the mid Si/Al ratios. The double peak at 431 and 471 cm^{-1} shows the same behavior. The already mentioned peaks at 617 and 398 cm^{-1} belong to NaBr·2H$_2$O. At 731, 703 and 668 cm^{-1} minor signals are visible, which might belong to formed sodalite species.

For the two selected samples of molar Si/Al ratios of 1.01 and 0.67, the spectra show the three characteristic sodalite related peaks at 731, 703 and 667 cm^{-1} as well as at 471 and 434 cm^{-1} with higher intensities. The peak at 984 cm^{-1} has also a higher intensity in comparison to the Si/Al ratio of 2.01. NaBr·2H$_2$O is visible in the spectrum of Si/Al = 0.67, which leads to the broad signal at 616 and 405 cm^{-1} covering the sodalite related peaks. This

spectrum shows the possible influence of the $NaBr \cdot 2H_2O$ or the water on the carbonate peak at 1450 cm^{-1} by the formation of a shoulder at 1496 cm^{-1}.

The FTIR spectrum of the sample with a Si/Al ratio of 0.22, which did not form a dry powder at all, shows only few similarities to the other spectra: $NaBr \cdot 2H_2O$ is indicated by the peaks at 1619 and 1638 cm^{-1} as well as at 435 and 614 cm^{-1}. The $NaBH_4$ peak in the wavenumber range shown is located at 1127 cm^{-1}. The matrix related peak at 984 cm^{-1} is only low distinct. Due to several new signals the sodalite related peaks around 700 cm^{-1} cannot be resolved properly. There are additional signals at 655, 667, 702, 725, 749 and 772 cm^{-1}. Probably carbonate and hydrogencarbonate related peaks are at 841, 865 and 881 cm^{-1}, while the main signal of the carbonate at 1441 also shows a shoulder at 1497 and a new signal at 1412 cm^{-1}. This sample shows decomposition products from the reaction of $NaBH_4$ at the positions 1239 and 1274 cm^{-1} [44].
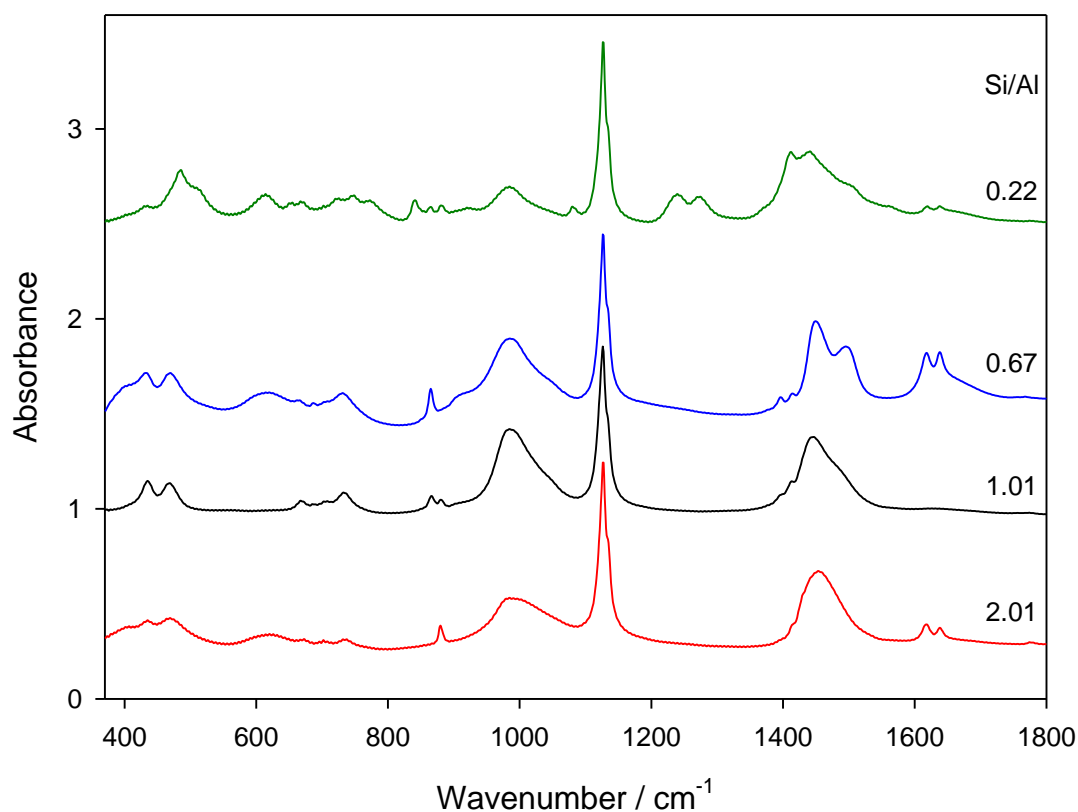
Figure 6: FTIR spectra of NaBH₄-bearing gels with constant NaBH₄/matrix ratio but varied molar Si/Al ratios. Only selected spectra are shown in the matrix related wavenumber range.

Figure 7 shows selected powder diffractograms of Series 2. Those samples show all effects occurring during the variation of the molar Si/Al ratio. The main reflexes occur just as described in the previous subchapter and summarized in Table 4. Here, the additional effects with variation of the molar Si/Al ratio will be described.

The first effect is visible at the reflex at 13.6 °2θ; in the diffractogram of the sample with Si/Al of 0.34, this reflex has the highest intensity. It is significantly reduced for increasing Si/Al ratios and completely disappears with an excess of silicon, as in the sample with Si/Al of 2.69 or already at Si/Al of 0.89, compare Figure 4, in series with varied $NaBH_4$/matrix. It is therefore very likely that this reflex is related to an alumina-species.

The second effect is related to the $NaBH_4$; the diffractogram of the Si/Al ratio shows only minor reflex intensities compared to the two other shown diffractograms. Especially the two samples with the low Si/Al ratios are well comparable, because they show almost the same reflex intensities for the sodalite related reflexes. The $NaBH_4$ reflexes are visible but show only about 15 % of the intensity, even though the FTIR spectra show comparable $NaBH_4$ amounts.
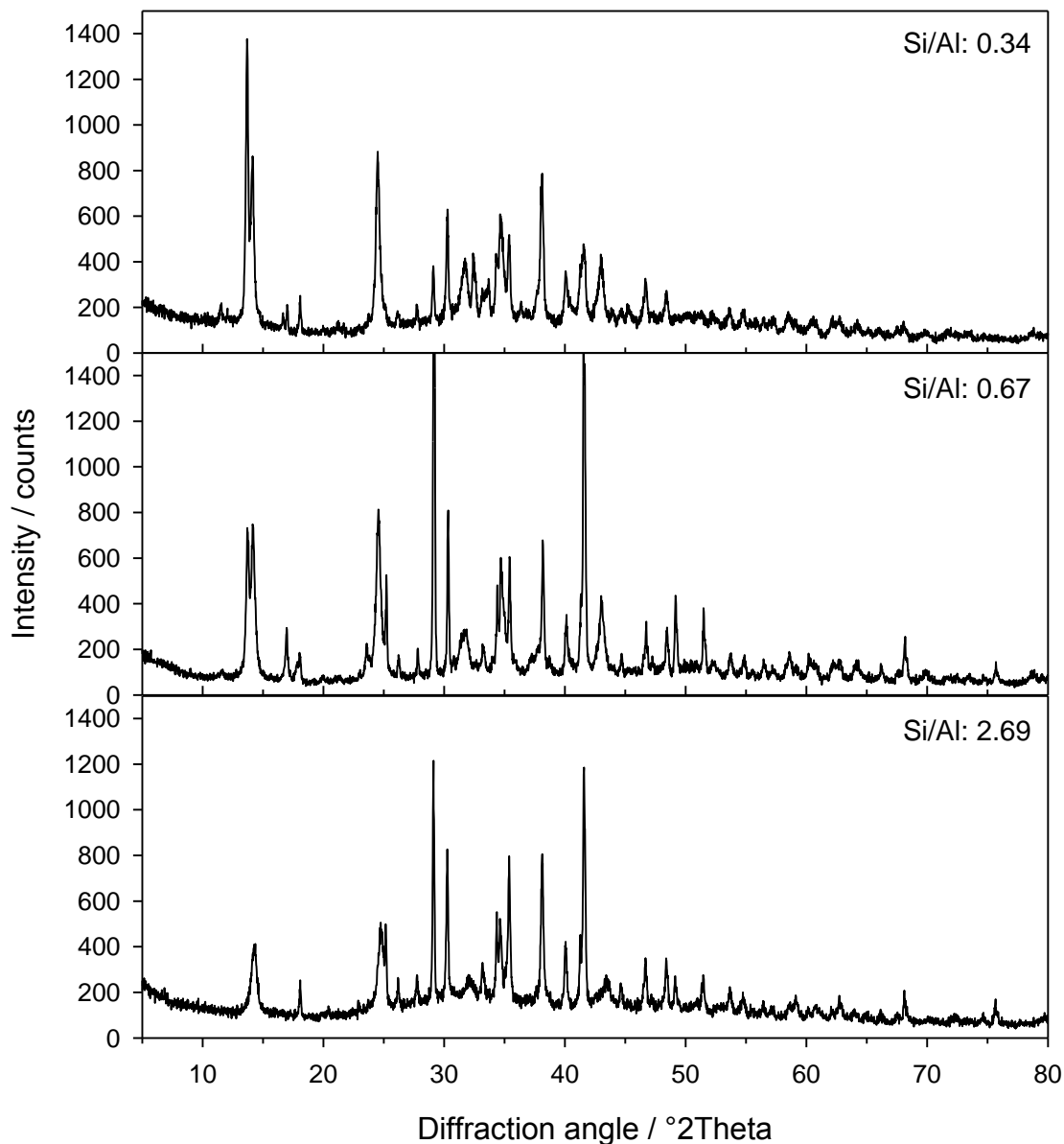
Figure 7: X-ray diffractograms of Gel Series 2. Only selected pattern are shown.

4.1.3. Variation of the synthesis temperature: Gel Series 3 A and B

Due to the possible reaction of the $NaBH_4$ with the remaining water after the gel precipitation at raised temperatures, the drying temperature was varied. Especially the amount of released hydrogen after the solidification of the gel stayed in the focus for this synthesis batch. Therefore two of the above mentioned gel syntheses were used, namely Series 3A and 3B with $NaBH_4$/matrix wt-ratio of 0.89 and 1.43, respectively. However the drying temperatures were varied from room-temperature to 110 °C. Directly after gel precipitation,

the gels gleamed. When they were completely dried, the gels turned into white. Due to the different drying temperatures, the drying time had to be varied, too, until the gels were completely dry. The drying process took 2 to 6 hours, whereas the gels at room temperature and at 40 °C remained wet even after 24 hours drying procedure. Therefore in the second synthesis batch, those temperatures were not used again. The results are summarized in Table 5 and 6.

Table 5: Sample compositions of Series 3A, temperature dependent with NaBH$_4$/matrix of 0.89

Synthesis temperature / °C	total NaBH$_4$ / mg	NaAlO$_2$ / mg	Na$_2$SiO$_3$ / mg	molar Si/Al	NaBH$_4$/matrix wt-ratio
20	500	250	310	0.83	0.89
40	500	250	310	0.83	0.89
60	500	250	310	0.83	0.89
80	500	250	310	0.83	0.89
95	500	250	310	0.83	0.89
110	500	250	310	0.83	0.89

Table 6: Sample compositions of Series 3B, temperature dependent with NaBH$_4$/matrix of 1.43

Synthesis temperature / °C	total NaBH$_4$ / mg	NaAlO$_2$ / mg	Na$_2$SiO$_3$ / mg	molar Si/Al	NaBH$_4$/matrix wt-ratio
60	800	250	310	0.83	1.43
80	800	250	310	0.83	1.43
95	800	250	310	0.83	1.43
110	800	250	310	0.83	1.43

FTIR analyses were only performed for selected samples of the first synthesis batch with a NaBH$_4$/matrix wt-ratio of 0.89 and only for three different synthesis temperatures. The 20 °C sample, which remained wet, shows high amounts of NaBr·2H$_2$O at 1619, 1638 and 402, 474 and 616 cm^{-1} (the additional OH-signals are not shown in Fig. 8). This sample shows only small amounts of carbonate at 1446, 864 and 701 cm^{-1}. The NaBH$_4$ is clearly present at 1126, 2224, 2292 and 2385 cm^{-1}. At 984 cm^{-1}, the matrix related signal is visible, it has in comparison only small intensity and occurs as a broad signal. The 80 °C sample

shows smaller intensities of the NaBr·2H$_2$O related signals but therefore far more intensive carbonate signals at 1455 and 880 cm^{-1}. At 1126, 2224, 2291 and 2386 cm^{-1} the NaBH$_4$ peaks are visible. This sample shows the matrix peak at 987 cm^{-1} and the peak has a higher intensity and a more specific form. Probably sodalite related signals are visible at 732, 666 and 694 cm^{-1}. The sample synthesized at 110 °C, shows the NaBH$_4$ signals at 1127, 2225, 2293 and 2388 cm^{-1}. The H$_2$O peak of the NaBr·2H$_2$O does not show the typical double peak but a strong peak at 1638 with a shoulder at 1630 cm^{-1}. The other signals of this species are only poorly resolved. At 1451 and 865 cm^{-1} the peaks of carbonate are visible, but there are several more signals around that peak at 1395, 1412 and a shoulder at 1448 cm^{-1}. The matrix related signals are visible at 433, 468, 732, 687, 666 and at 990 cm^{-1}.
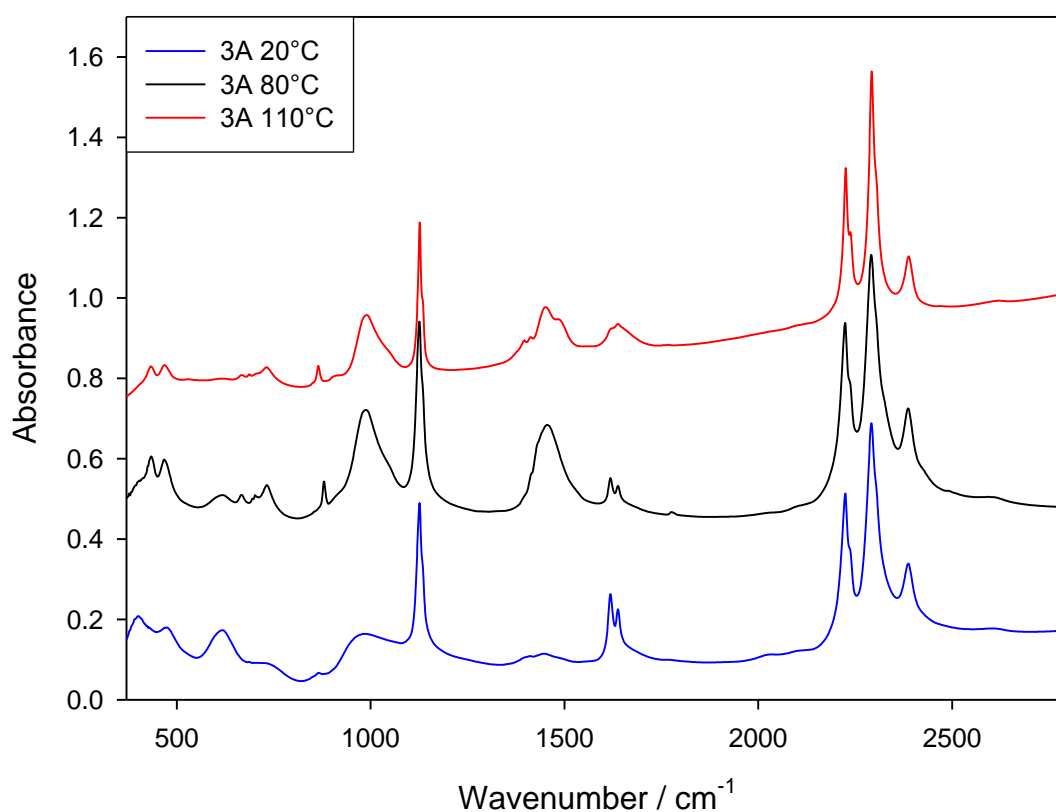
Figure 8: FTIR spectra of NaBH$_4$-bearing gels with NaBH$_4$/matrix ratio of 0.89, synthesized at 20 °C, 80 °C and 110 °C.

4.1.4. Combination of Parameters

To analyze how the varied parameters influence each other, a gel was synthesized with all parameters optimized for the highest possible hydrogen release. The gel has a $NaBH_4$/matrix wt-ratio of 3.04, a molar Si/Al ratio of 2.69 and was dried at 85 °C (Table 7).

Table 7: Sample composition of the optimized gel

Synthesis temperature / °C	total $NaBH_4$ / mg	$NaAlO_2$ / mg	Na_2SiO_3 / mg	molar Si/Al	$NaBH_4$/matrix wt-ratio
85	1700	110	450	2.69	3.04

Figure 9 shows the IR spectrum of this sample. It is dominated by the intensities of the BH_4^- related peaks at 1127, 2225, 2292 and 2388 cm^{-1}. This sample also shows the $NaBr \cdot 2H_2O$ signals at 1617 and 1638 and 3237, 3415, 3477 and 3552 cm^{-1}, as well as at 404, 473 and 619 cm^{-1}. Carbonate is visible at 880 and 1450 cm^{-1}. The matrix related peaks are only of little account visible at a broad signal at 1003 and a very fine peak at 732 cm^{-1}.
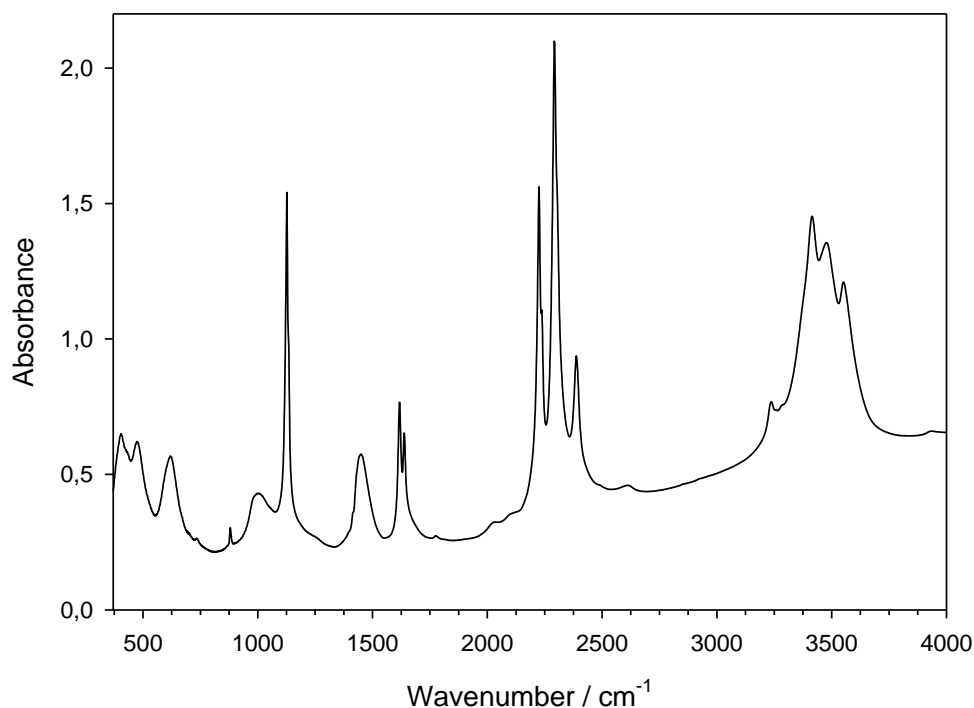
Figure 9: FTIR spectrum of the optimized gel

The powder diffraction shows also mainly reflexes of $NaBH_4$ (cf. Table 3 in chapter 4.1.1.), there are only small amounts of sodalite related signals visible.
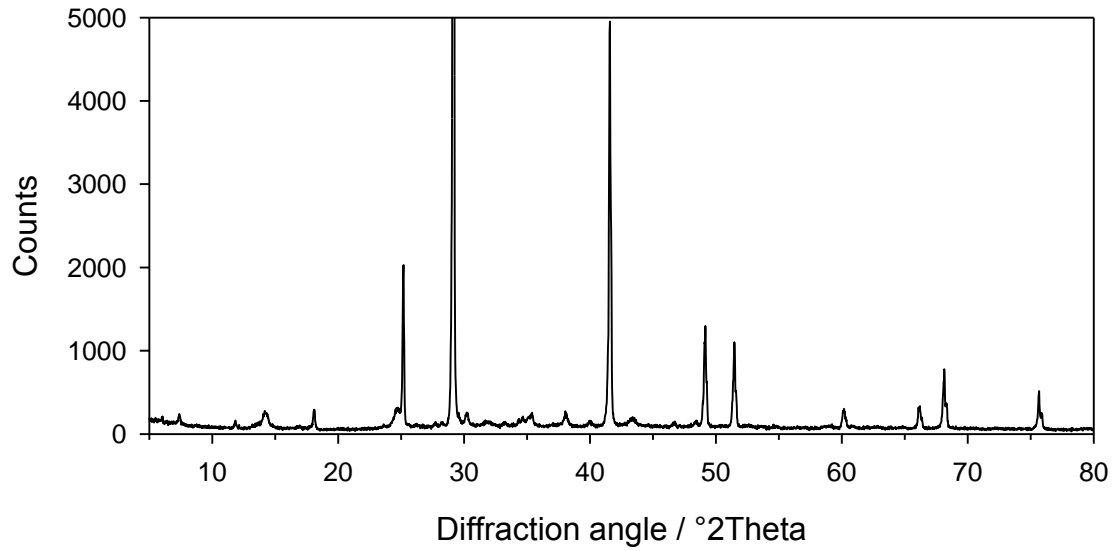
Figure 10: X-ray diffractogram of the optimized gel

4.2. Additional Analyses NaBH$_4$-Gel

In this chapter the results of additional analyses are presented. Those analyses were performed for selected samples only, in order to gain information on the general behavior of the system.

4.2.1. Crystallization Process T-IR

The crystallization process was analyzed by temperature dependent FTIR (described in Chapter 3.2.2.), using sample material from Series 1, with NaBH$_4$/matrix of 0.89. The sample was mixed with the KBr directly after gel precipitation. The initial spectrum (t=0, RT) is shown in Fig. 11 before drying. The spectrum shows the BH$_4^-$ peaks at 2226, 2292, 2388 and 1127 cm^{-1}. The OH-peak is represented by a broad signal around 3500 cm^{-1}, the peak shows high noise. At 1637 and 1617 cm^{-1} the stretch vibration of water is visible. Further peaks are located at 866, 1411 and 1448 cm^{-1}, which are related to carbonate. The matrix related peak at 996 cm^{-1} has a broad form and relatively low intensity. Further also very broad and therefore undefined signals are visible in the area from 400 to 800 cm^{-1}.

When starting the drying process at 110 °C, only few changes are visible. Already after five minutes at 110 °C, the peak at 866 cm^{-1} shifts to 881 cm^{-1} and remains there. With longer drying time, the two peaks around 1440 cm^{-1} converge to one at 1442 cm^{-1}. Another effect occurs in the wavenumber range from 500 to 800 cm^{-1}: The whole area shows a decrease in intensity with increasing drying time. The other changes are mainly drying effects; the intensity of the water stretching peak around 1630 cm^{-1} decreases with drying time, just as the OH-area. After complete cooling, the stretching mode of water is not visible anymore, while the OH-area still shows significant intensity (see Fig. 11). During the drying procedure, the BH$_4$-triplet peak remains stable, there is no sodalite forming visible.
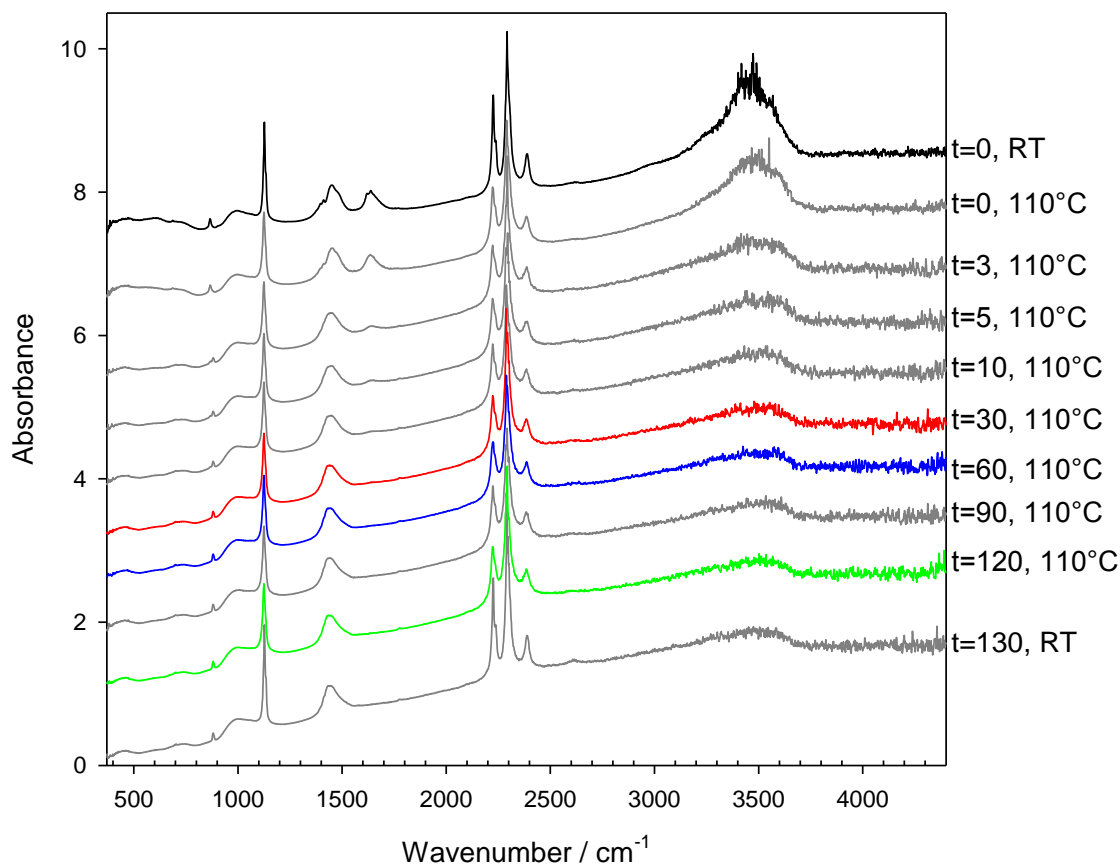
Figure 11: T-FTIR spectra of Series 1-0.89, measured at the given temperatures after time t in minutes. The chosen colors are analogue to the x-ray diffractograms in Figure 24 shown in the discussion (4.4.).

Figure 12 shows the integrated intensities of the water stretching vibrations around 1630 cm^{-1} (black dots) and of the OH-signals around 3600 cm^{-1} (red dots). The plots confirm the observations of the infrared spectra. Already after few minutes, the intensities of water and the OH-signals decrease exponentially. After about 25 minutes, both signals remain constant in their intensities, while the water signal reaches zero intensity and the OH-signal stays around 175 area units. The integrated intensity of the BH_4^- triplet peak scatters between 124 and 115 area units. Therefore it can be assumed that no significant decomposition or reaction of the $NaBH_4$ in the gel during the process took place.

Aluminosilicate Borohydrides: $NaBH_4$ Embedded in Sodalite and Gel Structures
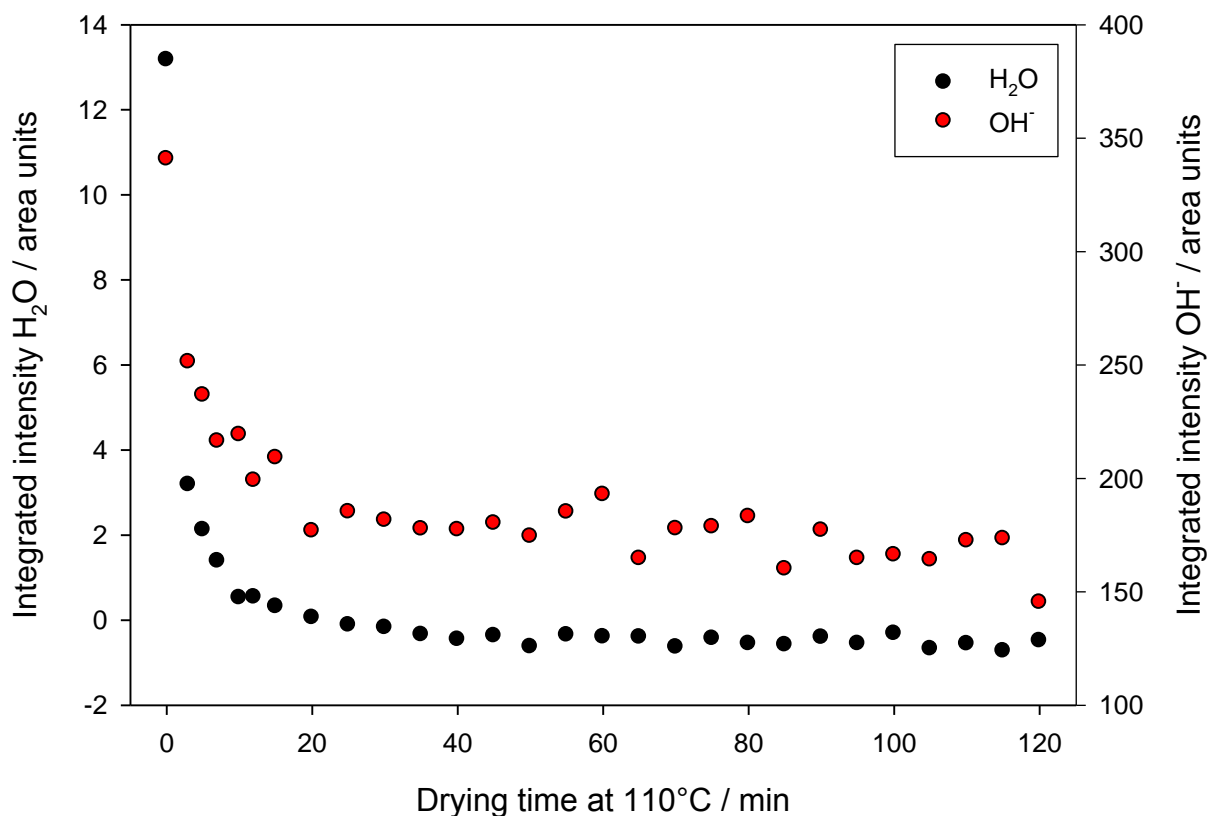
Figure 12: Plotted integrated intensities of molecular water bands (black) and OH bands (red) as function of drying time, obtained by T-FTIR.

4.2.2. SEM

Three different gel-samples were used as samples for the scanning electron microscope. Their synthesis parameters are given in Table 8.

Table 8: Synthesis compositions of the analyzed SEM samples

Sample	NaBH$_4$/matrix wt-ratio	molar Si/Al	Synthesis Temperature / °C
Gel_0.5_80	1.00	1.00	80
C_gel_0.75	3.04	2.69	85
A_Gel_120	0.89	0.83	120

The first sample (Gel_0.5_80) showed a porous structure in the SEM pictures (Fig. 13 a+b) at 500 x magnification. Even at 1500 x magnification, no separate particles were visible.

The whole material could be characterized as more or less spongy with several dikes. The borders of the material were quite sharp-edged.
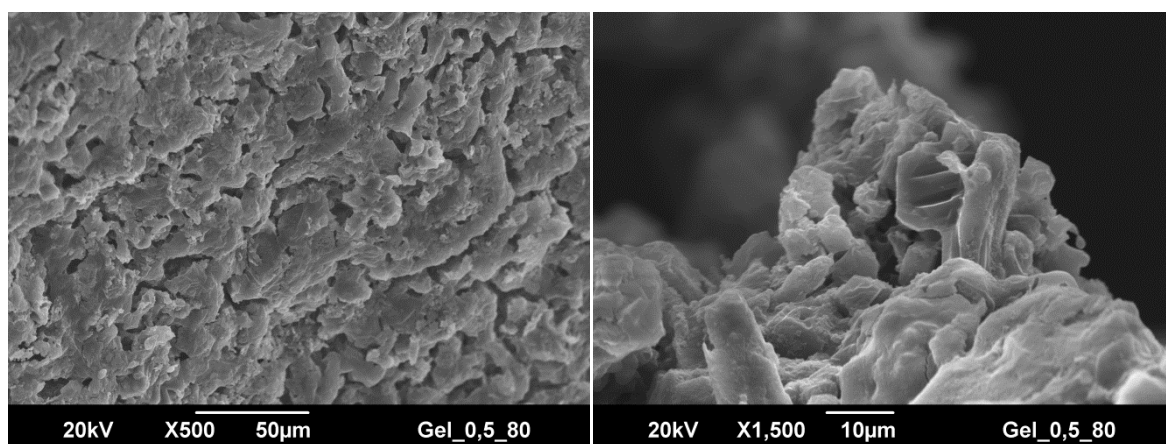
Figure 13 a+b: SEM pictures of gel_0.5_80 at different magnitudes

The second sample (C_gel_0.75) was very similar to the first sample, even when both samples were varied in almost all synthesis parameters. At 75 x magnification, the sample showed the spongy framework, just as the first sample. At 370 x magnification, a structure similar to a desiccation crack could be observed. At 5000 x magnification this sample did not show separate particles either (Fig. 14, a-c). The borders of this sample were more rounded compared to the first sample.
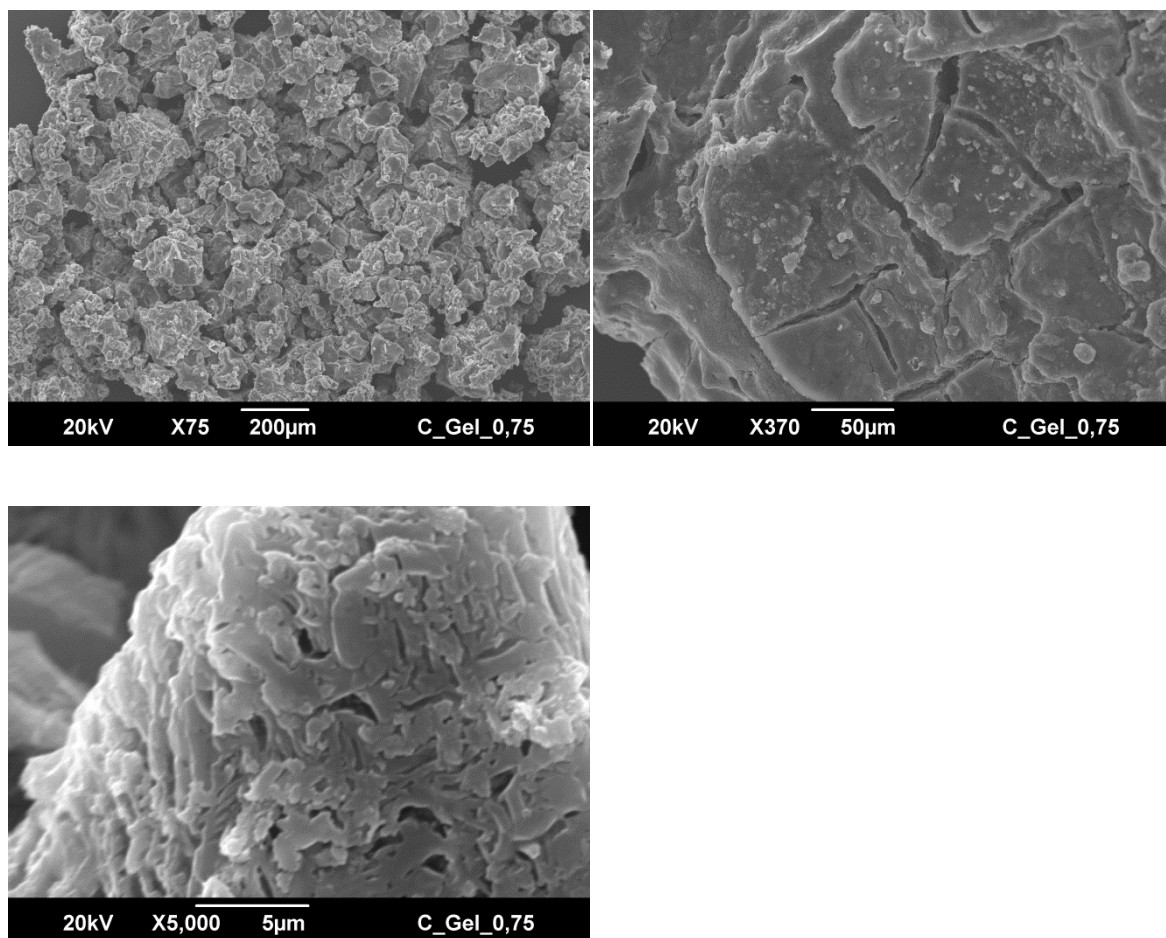
Figure 14 a-c: SEM pictures of C_gel_0.75 at different magnitudes

The third sample (Fig. 15 a-c) showed significant differences to the two other gel compositions: The material was less porous and it was obviously more sintered. At all magnification levels, the sample surface appeared to be glassy. There were only few borders visible, while the surface is more or less smooth.
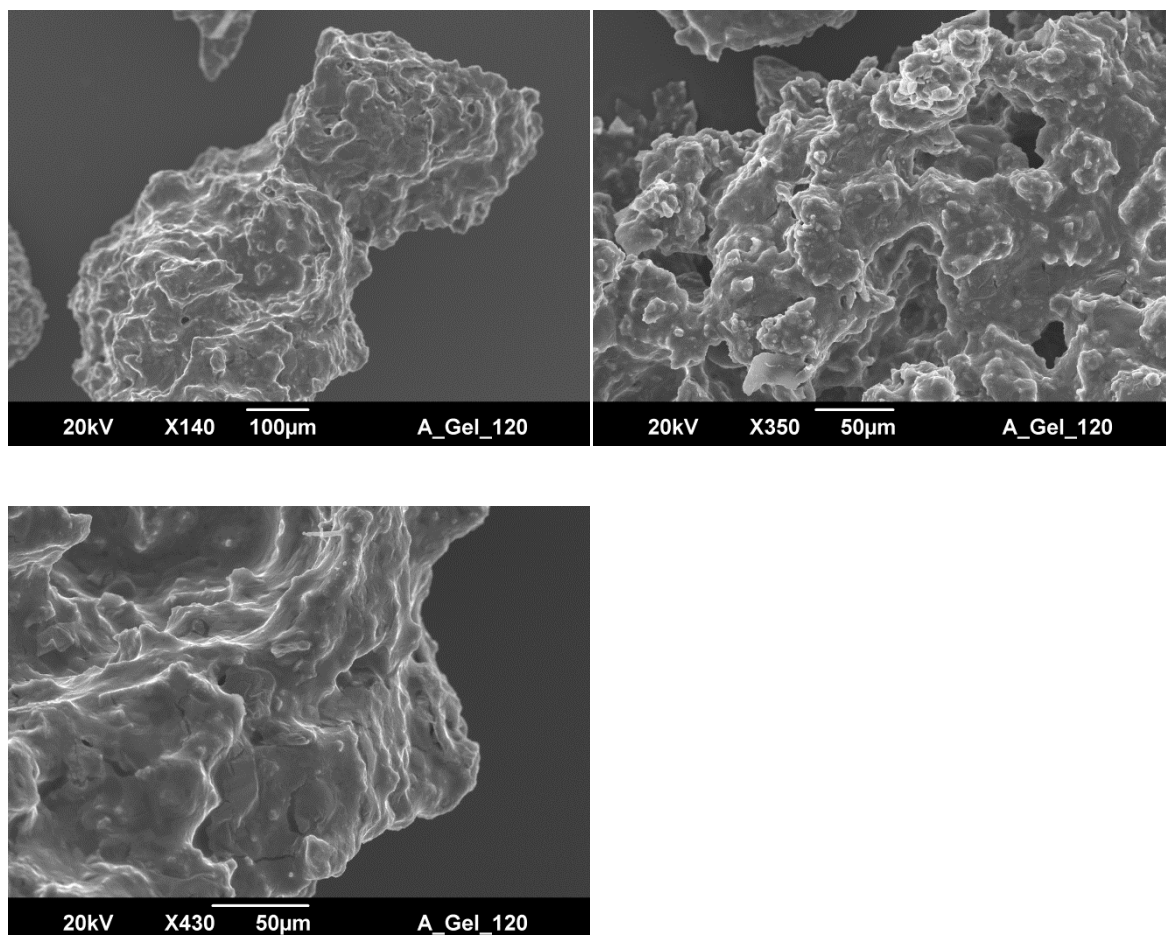
Figure 15 a-c: SEM pictures of A_gel_120 at different magnitudes

4.2.3. TG/DTA

The TG/DTA measurements were performed on two of the synthesis series. With these measurements, the water content was quantified and the temperature stability at raised temperatures was analyzed. The measuring parameters are given in Table 9. To avoid an entire decomposition of the containing $NaBH_4$, 375 °C was chosen as the maximal temperature.

Table 9: Summarized measuring parameters of TG/DTA

Maximal temperature / °C	Heating-/cooling rate / K/min	Carrier gas	Gas flow / ml/min	Holding time at T_{max} / min
375	5	Helium	20	15

In Table 10, the results of the analyses as function of $NaBH_4$/matrix with constant molar Si/Al ratio are summarized. The results clearly show, that the mass loss decreases with increasing $NaBH_4$/matrix ratio.

Table 10: Used sample materials, first batch.

Sample	$NaBH_4$/matrix wt-ratio	molar Si/Al	Mass loss / wt%
E_II	0.37	0.83	9.42
A_II	0.89	0.83	6.78
B_II	1.40	0.82	5.25
D_II	2.09	0.82	4.00

These results indicate that the water amount of the samples is mainly located and bound in the matrix and that it is not only adsorbed surface water.

A second synthesis batch was used with varied molar Si/Al ratios in the range of 0.5 to 2.0 at constant $NaBH_4$/matrix ratio of 1.0 and drying temperature of 80 °C as sample material.
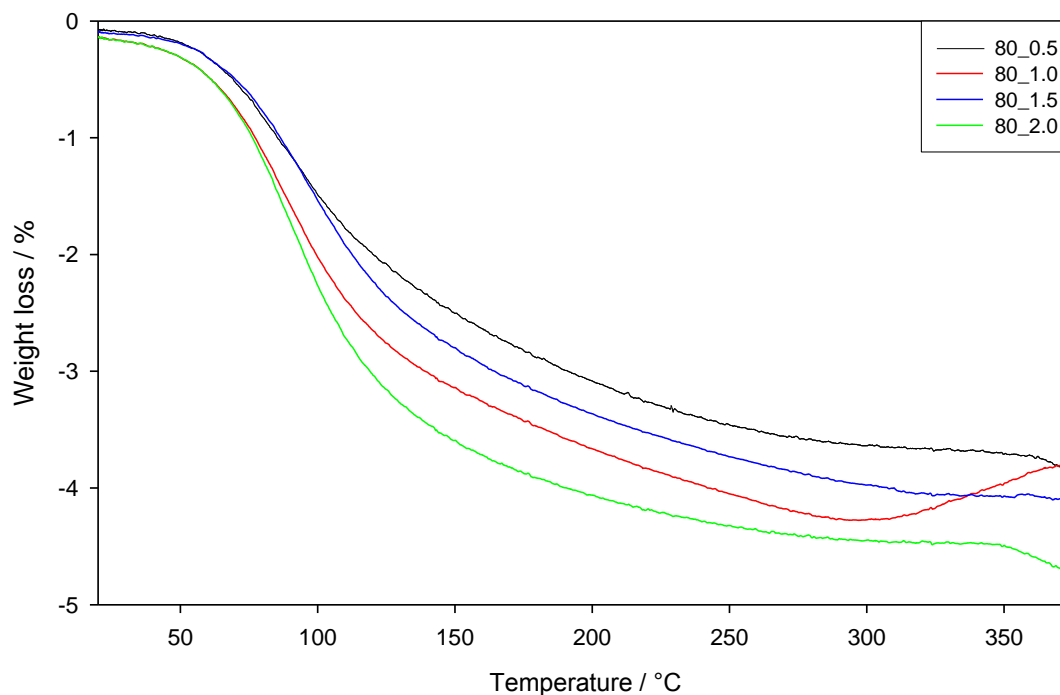
Figure 16: Plotted mass loss of samples with varied molar Si/Al ratio

Figure 16 shows the TG weight loss plot of the four samples as a function of the temperature. The overall behavior is quite similar with arising temperature up to 300 °C; the samples vary only slightly in their weight loss. Especially the sample with a molar Si/Al ratio of 1.0 shows an increase in weight above 300 °C, which is very uncommon. In Table 11, the overall weight loss is summarized together with the sample parameters.

Table 11: Summarized sample compositions and obtained mass losses

Sample	Molar Si/Al ratio	Synthesis temperature / °C	NaBH$_4$/matrix / wt%	Mass loss / wt%
80_0.5	0.5	80	1.0	4.11
80_1.0	1.0	80	1.0	4.14
80_1.5	1.5	80	1.0	4.06
80_2.0	2.0	80	1.0	4.84

Afterwards, the samples were analyzed using FTIR spectroscopy; the obtained spectra are shown in comparison with the initial spectra below. Figure 17 shows the spectra before the thermal treatment. The spectra show the peaks, already described in Chapter 4.1.2.; here also the effect of formed NaBr·2H$_2$O by sample preparation needs to be kept in mind.
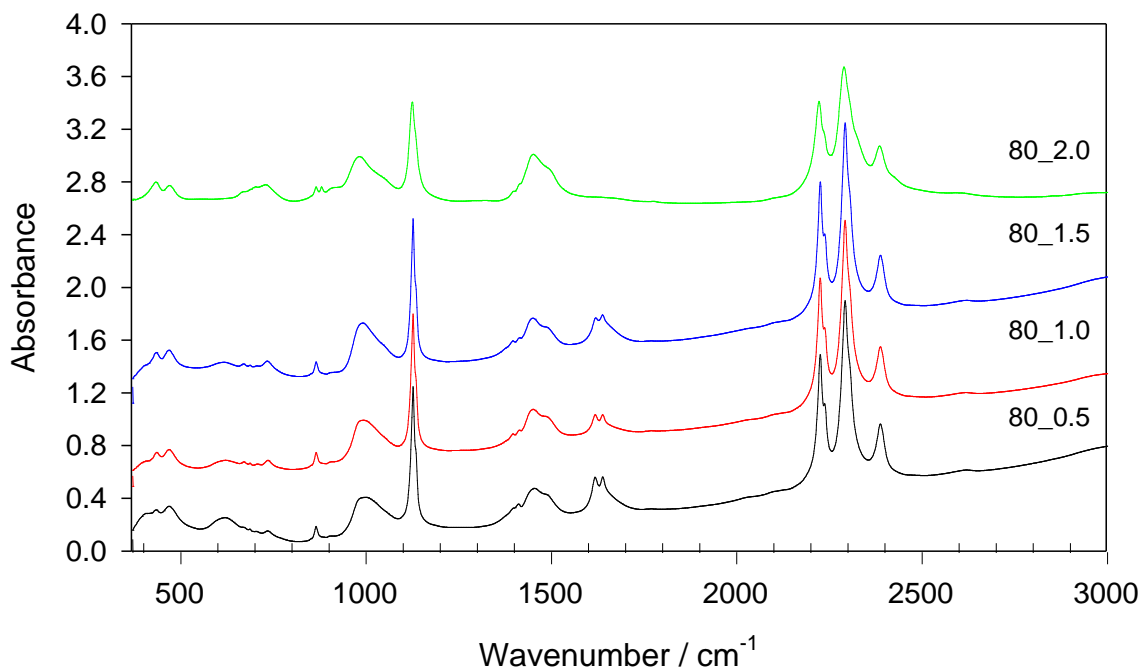
Figure 17: FTIR spectra of the samples with varied molar Si/Al ratios before TG/DTA treatment

Figure 18 shows the spectra of the samples after the TG/DTA measurements. $NaBH_4$ remains more or less constant and also the matrix shows no decomposition; the species remain the same as before the TG measurement. The formation of $NaBr \cdot 2H_2O$ by sample preparation occurs in the spectra with molar Si/Al 0.5, 1.5 and 2.0. The sample with a molar Si/Al ratio of 1.0 does not show this preparation effect. Due to this effect a decrease of water content cannot be clearly seen, using FTIR with the KBr method. Also the carbonate does not seem to be influenced in the given temperature range up to 375 °C.
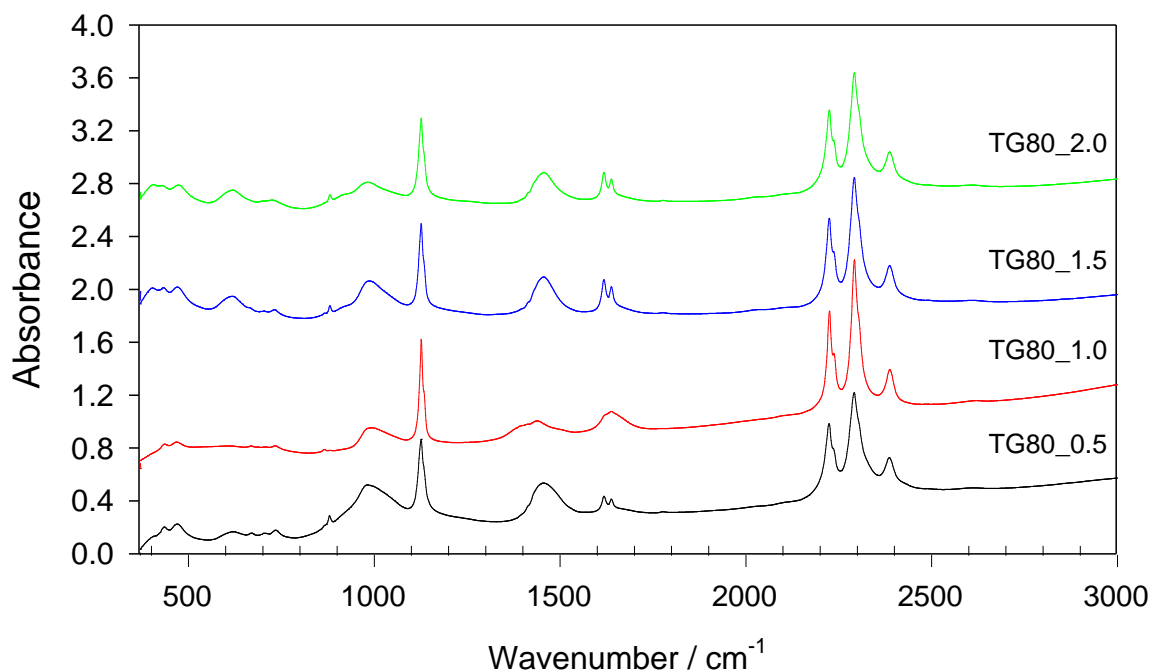
Figure 18: FTIR spectra of the samples with varied molar Si/Al ratios after TG/DTA treatment

4.2.4. Carbon-Sulfur Analyses

The aim of these analyses was mainly to confirm the existence of absorbed carbon in form of carbonate in the alkaline samples by the uptake of CO_2 from the atmosphere. Possibly carbonate related species are visible in FTIR spectra around 1450 cm^{-1} in almost all samples, especially after heating procedures. The sulfur content is not evaluated, because the amounts were below or only slightly above the detection limit of the CS-Analyzer, as expected.

In Table 12, the results of the CS-analyses for selected gel samples are summarized. The synthesis series with varied molar Si/Al ratios at 80 °C drying temperature and the gel with the optimized hydrogen content were chosen as sample material.

The results confirm the presence of carbonate in the samples. With 2.4 to 3.2 wt% the carbon amount is especially huge for samples with mid $NaBH_4$/matrix ratios. This series

shows a possible trend: the carbon amount is significantly lower for low molar Si/Al ratios (0.5 and 1.0), than in the samples with molar Si/Al ratios of 1.5 and 2.0.

The optimized gel (C_gel_0.75_1:4_85) shows a relatively low carbon content compared to the other gel samples. But the amount of 0.32 wt% is still significant.

Table 12: Summarized sample compositions and obtained carbon amount by CS analyses

Sample	NaBH$_4$/matrix / wt-ratio	Molar Si/Al	C / wt%
C_gel_0.75_1:4_85	3.04	2.69	0.316
Gel_80_0.5	1.0	0.5	2.489
Gel_80_1.0	1.0	1.0	2.379
Gel_80_1.5	1.0	1.5	3.182
Gel_80_2.0	1.0	2.0	3.116

4.3. Hydrogen Release NaBH$_4$-Gel

In this subchapter the results of the hydrogen release experiments are presented. The samples were varied within their NaBH$_4$/matrix wt ratio, the molar Si/Al ratio and the synthesis temperature. Additionally pure NaBH$_4$ was analyzed in the same way as reference and an optimized gel with the combination of all the mentioned parameters was analyzed.

4.3.1. Variation of the NaBH$_4$/matrix wt-ratio, Series 1

In the first synthesis-series, the NaBH$_4$/matrix wt-ratio was varied at constant molar Si/Al ratio of 0.83 and two hours drying at 110 °C. The dependence of the applied NaBH$_4$/matrix wt-ratio during synthesis shows an exponential trend when plotted against the amount of released hydrogen (see Fig. 19). For comparison, the pure NaBH$_4$ granulate without matrix was analyzed in the same way. It shows a release of 226.5 ml ± 16 ml, which is close to the theoretical value of 240 ml [45] calculated for 100 % pure NaBH$_4$ and an entire reaction with the added acid. The highest amount of released hydrogen from this NaBH$_4$ gel-series could be reached with a NaBH$_4$/matrix wt-ratio of 3.04. It was not possible to solve a higher mass of NaBH$_4$ in the synthesis solutions (cf. chapter 4.1.4., Table 2). This sample released 163 ml ± 6 ml of hydrogen, which equals 72 % of the released hydrogen amount of pure NaBH$_4$. The

exponential trend shown in Figure 19 also correlates to the performed back-calculations described in the following section. All data are summarized in Table 13.
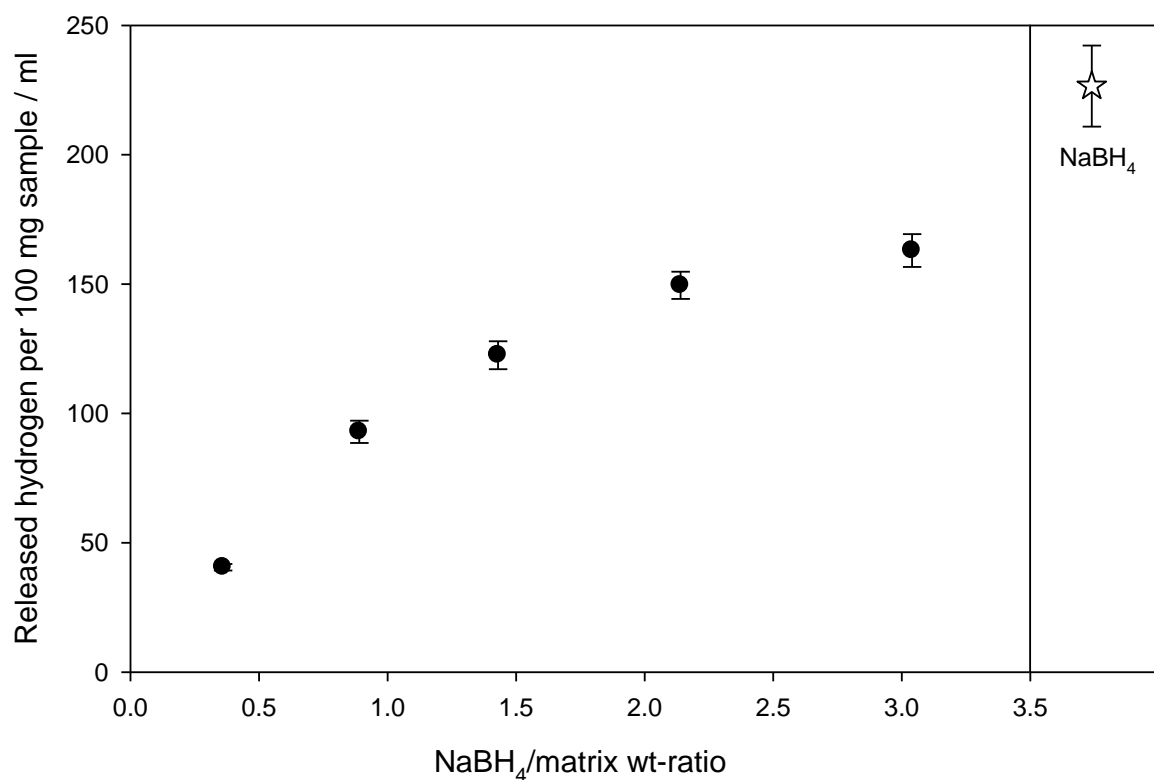
Figure 19: Released hydrogen per 100 mg sample of Series 1, samples have constant Si/Al ratio of 0.83 and were dried at 110 °C. For comparison the hydrogen release of pure NaBH$_4$ granulate is shown (white star). Errors calculated as described in 3.5.1.

Table 13: Summarized hydrogen release results for Series 1 and pure NaBH$_4$ as reference

NaBH$_4$/matrix	H$_2$ released per 100 mg sample / ml	Abs. Error / ml
0.36	40.5	± 1.3
0.89	92.9	± 4.3
1.43	122.5	± 5.4
2.14	149.5	± 5.3
3.04	162.9	± 6.3
NaBH$_4$	226.5	± 15.7

Back calculations: Variation of the NaBH$_4$/matrix wt-ratio, Series 1

The results of the performed back calculations as described in Chapter 3.5.2. are summarized in Table 14. With increasing NaBH$_4$/matrix wt-ratio, the effectively enclosed NaBH$_4$ in the gel also increases. Just as the direct measurements of the hydrogen release, the back calculations show an exponential behavior, converging to a limit value of 85 wt%.

Table 14: Results of back calculations for NaBH$_4$-gels in dependence of the NaBH$_4$/matrix ratio

NaBH$_4$/matrix	H$_2$ released per 100 mg sample / ml	Calculated mass NaBH$_4$ in gel per 100 mg / mg	Mass NaBH$_4$ used during synthesis per 100 mg / mg	Effectively enclosed NaBH$_4$ / wt%
0.36	40.5	15.9	26	61.3
0.89	92.9	36.5	47	77.7
1.43	122.5	48.2	59	81.6
2.14	149.5	58.8	68	86.4
3.04	162.9	64.1	75	85.4

4.3.2. Variation of the molar Si/Al ratio, Series 2

In this section, the results of the hydrogen release experiments for samples with different molar Si/Al ratios are shown. The samples have identical NaBH$_4$/matrix wt-ratios of 1 and were all dried at 110 °C for two hours. Figure 20 summarizes the results, which can be divided into three parts. For very low Si/Al ratios, such as 0.22, no stable gels can be formed. Samples with only slightly increased Si/Al ratios from 0.27 to 1.0 show an almost constant amount of released hydrogen around the expected values of 110 ml/100 mg sample, obtained through previously shown results. With further increasing Si/Al ratios above 2, the hydrogen release also slightly increases up to 120 ml/100 mg sample. These results are summarized in Table 15.
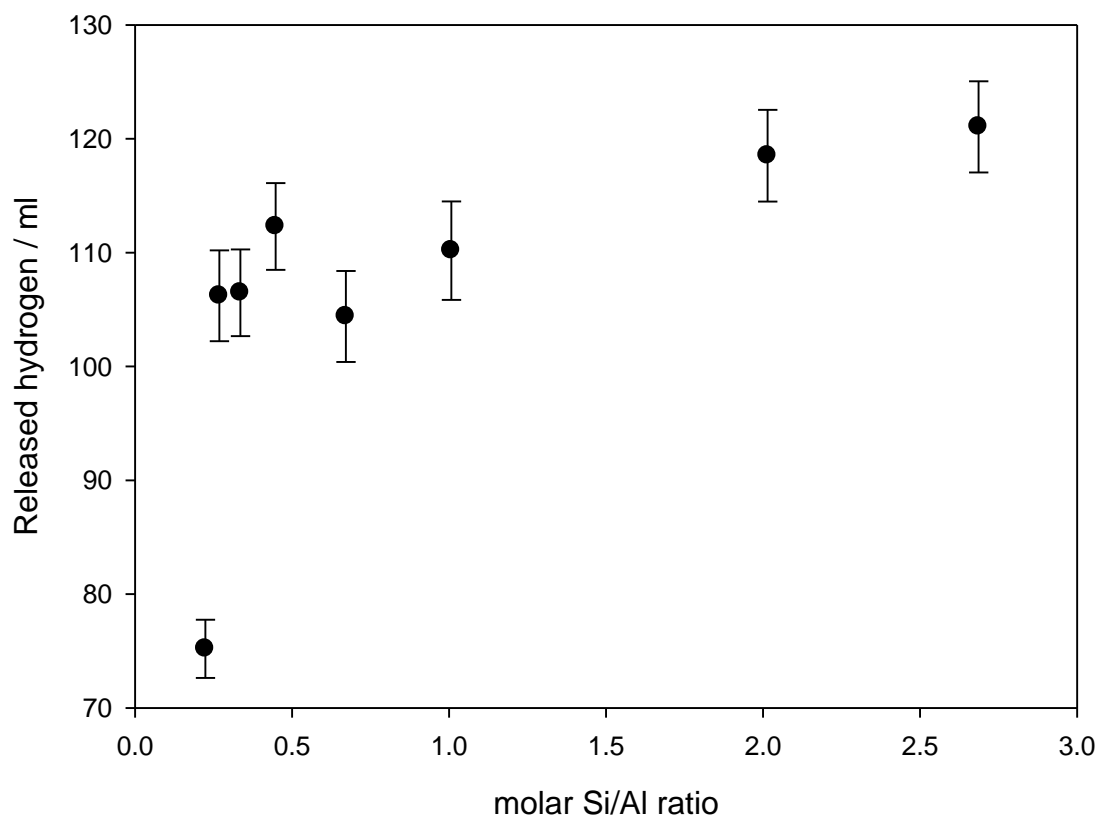
Figure 20: Released hydrogen per 100 mg sample as function of molar Si/Al ratio, samples have constant NaBH$_4$/matrix ratios of 0.5 and were dried at 110 °C. Errors calculated as described in 3.5.1.

Table 15: Summarized hydrogen release results for samples with varied molar Si/Al ratios

molar Si/Al	H$_2$ released per 100 mg sample / ml	Abs. Error / ml
0.22	75.2	± 2.6
0.27	106.2	± 4.0
0.34	106.5	± 3.8
0.45	112.3	± 3.9
0.67	111.1	± 3.8
1.01	110.2	± 4.3
2.01	118.5	± 4.0
2.69	121.0	± 4.0

Back calculations: Variation of the molar Si/Al ratio

The performed back calculations show an identical trend to the direct measurements (see Table 16). Effectively enclosed $NaBH_4$ in the gels show improved protection abilities with an increased molar Si/Al ratio of up to 95 wt% enclosing. In the molar Si/Al ratio range from 0.27 to 1.01 the enclosing is almost constant around 85 wt%. The two silica rich samples show an increased effectively enclosed amount of $NaBH_4$ of about 95 wt%. With a Si/Al ratio of 0.22 no stable gel could be formed. Hence the result of the back calculation does not allow a precise conclusion.

Table 16: Results of back calculations for $NaBH_4$-gels in dependency of the molar Si/Al ratio

molar Si/Al	H_2 released per 100 mg sample / ml	Calculated mass $NaBH_4$ in gel per 100 mg / mg	Mass $NaBH_4$ used during synthesis per 100 mg / mg	Effectively enclosed $NaBH_4$ / wt%
0.22	75.2	29.6	50	59.1
0.27	106.2	41.7	50	83.5
0.34	106.5	41.9	50	83.7
0.45	112.3	44.1	50	88.3
0.67	111.1	43.7	50	87.4
1.01	110.2	43.3	50	86.6
2.01	118.5	46.6	50	93.2
2.69	121.0	47.6	50	95.2

4.3.3. Variation of the synthesis temperature, Series 3A and 3B

Two synthesis series (3A and 3B) were chosen to analyze the influence of the synthesis temperature. Both series have an intermediate $NaBH_4$/matrix wt-ratio of 0.89 and 1.43 to provide the highest possible comparability. Two different ratios were chosen to analyze whether a possible trend works for different matrix amounts. For both synthesis batches, the results of the varied synthesis temperatures show similar results to those visualized in Figure 21. At room temperature the $NaBH_4$ gels do not dry without evacuating, so the obtained hydrogen release per 100 mg sample is relatively low. Samples dried at 40 and 60 °C show an intermediate amount of hydrogen released. The samples appeared to be dry but the drying process took up to 8 hours. For the samples dried at 110 °C approximately the same

hydrogen release could be measured. With drying temperatures of 80 and 95 °C, respectively, the highest amounts of released hydrogen can be obtained. Those samples were dried within only two hours.
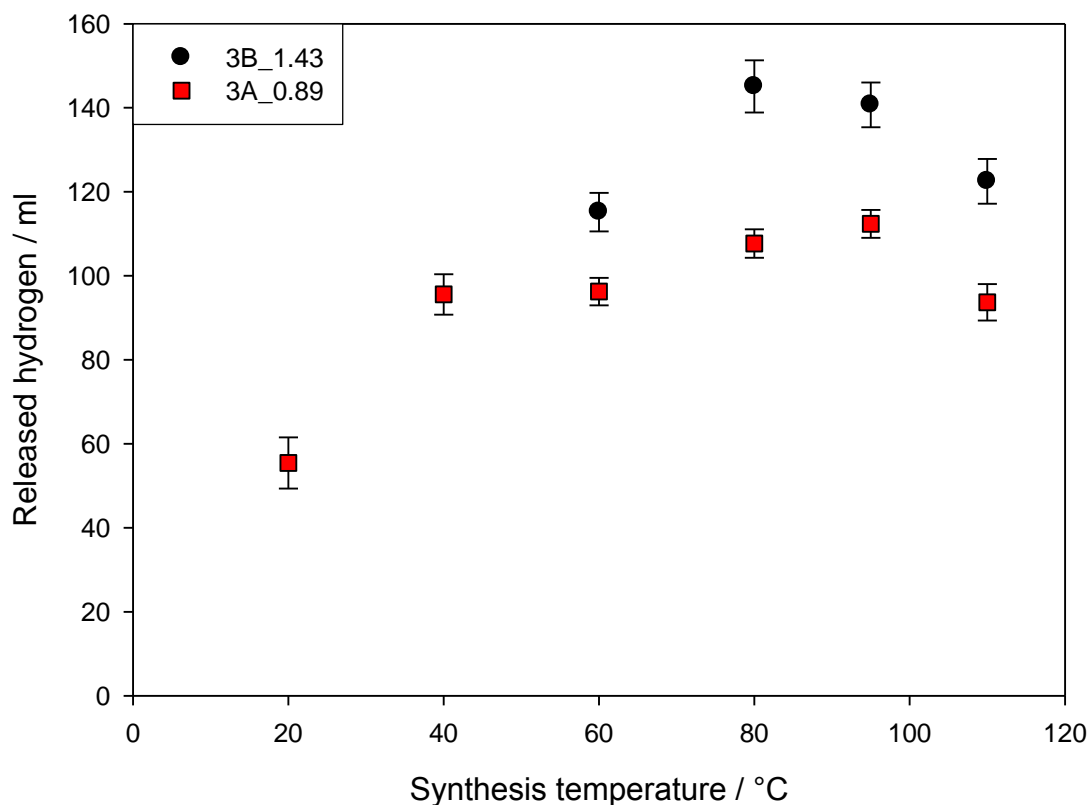
Figure 21: Released hydrogen per 100 mg sample as function of the synthesis temperature, samples have constant Si/Al ratio of 0.83. Two different syntheses with NaBH$_4$/matrix ratios of 0.89 (red squares) and 1.43 (black circles) are shown. Errors calculated as described in 3.5.1.

Table 17: Summarized hydrogen release results for samples with varied synthesis temperatures

T / °C	NaBH$_4$/matrix / wt-ratio	H$_2$ released per 100 mg sample / ml	Abs. Error / ml
20	0.89	55.4	± 6.1
40	0.89	95.6	± 4.8
60	0.89	96.2	± 3.3
80	0.89	107.7	± 3.4
95	0.89	112.4	± 3.3
110	0.89	93.7	± 4.4
60	1.43	115.2	± 4.6
80	1.43	145.1	± 6.2
95	1.43	140.7	± 5.3
110	1.43	122.5	± 5.3

Back calculations: Variation of the synthesis temperature

Back calculations show that at temperatures between 80 and 95 °C most $NaBH_4$ can be enclosed or is protected, respectively. Here, more than 90 wt% of $NaBH_4$ remained in the gel, compared to the mass used during the synthesis. At higher and lower temperatures, less $NaBH_4$ is enclosed after the synthesis. These trends and values are identical for both $NaBH_4$/matrix wt-ratios used. The results are summarized in Tables 18 and 19.

Table 18: Results of back calculations for NaBH₄-gels of Series 3A

T / °C	H_2 released per 100 mg sample / ml	Calculated mass $NaBH_4$ in gel per 100 mg / mg	Mass $NaBH_4$ used during synthesis per 100 mg / mg	Effectively enclosed $NaBH_4$ / wt%
20	55.4	21.8	47	46.3
40	95.6	37.6	47	79.9
60	96.2	37.8	47	80.5
80	107.7	42.3	47	90.1
95	112.4	44.2	47	93.9
110	93.7	36.8	47	78.4

Table 19: Results of back calculations for NaBH₄-gels of Series 3B

T / °C	H_2 released per 100 mg sample / ml	Calculated mass $NaBH_4$ in gel per 100 mg / mg	Mass $NaBH_4$ used during synthesis per 100 mg / mg	Effectively enclosed $NaBH_4$ / wt%
60	115.2	45.3	59	76.7
80	145.1	57.0	59	96.7
95	140.7	55.3	59	93.7
110	122.5	48.2	59	81.6

4.3.4. Combination of Parameters

The optimized gel ($NaBH_4$/matrix wt-ratio of 3.04, molar Si/Al ratio of 2.69, dried at 85 °C) released 181.6 ml hydrogen per 100 mg sample, which is an increased amount of hydrogen compared to the basic sample with the same $NaBH_4$/matrix ratio of 11.4 %. Concerning the back calculation, this means that 95.2 % $NaBH_4$ could effectively be enclosed in the optimized gel, compared to 85.4 % (C_gel, $NaBH_4$/matrix = 3.04, 110 °C drying temperature, molar Si/Al = 0.83).

4.4. Discussion NaBH$_4$-Gel

The results could verify our first principle investigations [17], [24], [32] as they could clearly show that it is possible to embed NaBH$_4$ in an aluminosilicate gel matrix. The influence of main experimental parameters like NaBH$_4$/matrix wt ratio, molar Si/Al ratio and drying temperature could be extensively discovered.

4.4.1. Structure

According to the obtained XRD-data, the matrix structure consists of amorphous and crystalline phases. The crystalline phases are NaBH$_4$ and sodalite, while the character of the amorphous phase was unclear up to now. An attempt to describe it as a geopolymer is given in the following lines. Following Davidovits, a geopolymer consists of polysialates, an abbreviation for silicon-oxo-aluminates. These networks are formed of SiO$_4$ and AlO$_4^-$ polyhedra units, linked by sharing all or a part of the oxygen atoms. Positive ions like Na$^+$, K$^+$ etc. balance the negative charge of Al^{3+} in IV-fold coordination in the network. Contrary to their corresponding crystalline zeolites, geopolymers are x-ray amorphous [46]. Their general chemical composition can be described by the empiric formula:

$$M_n(-(SiO_2)_x-AlO_2)_n, \; w \; H_2O \tag{13}$$

with x being 1, 2 or 3, depending on the type, M a monovalent cation, n the degree of polycondensation and w the water content enclosed in the pores. Table 20 shows some common geopolymer types [47], [48].

Table 20: Geopolymer types, overview

Name	Type	Abbrevation
Poly(sialate) (x=1)	M$_n$-(-Si-O-Al-O-)$_n$-	M-PS
Poly(sialate-siloxo) (x=2)	M$_n$-(-Si-O-Al-O-Si-O-)$_n$-	M-PSS
Poly(sialate-disiloxo) (x=3)	M$_n$-(-Si-O-Al-O-Si-O-Si-O-)$_n$-	M-PSDS

The aluminosilicate gels formed in the synthesis series with varied molar Si/Al ratio show a variation in the type of geopolymer network. This variation is depending on the

degree of polymerisation. The Si/Al ratio was varied from 0.22 to 2.69. Figure 22 shows the matrix relevant range of the obtained infrared spectra. The spectra are normalized on the peak intensity of the peak around 1000 cm^{-1} for better comparison.
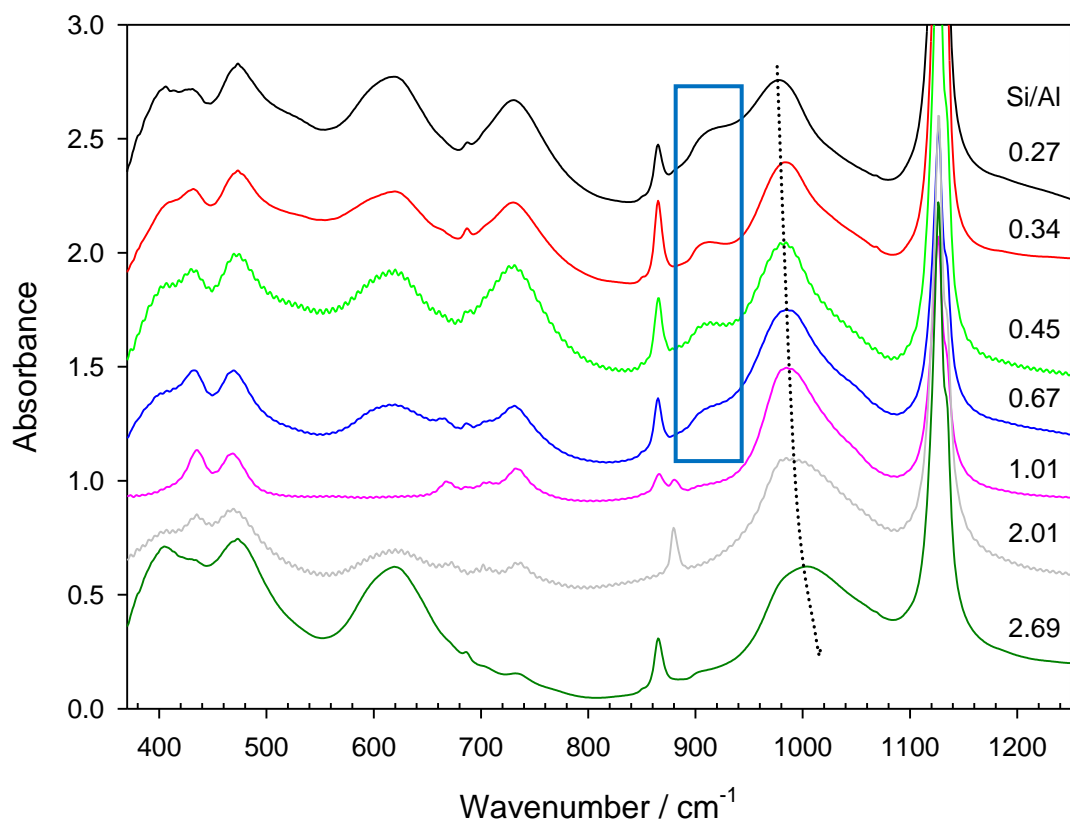
Figure 22: FTIR spectra of Si/Al series in the matrix range. Additional markings of Al-OH species (blue rectangle) and peak shift trend for orientation only.

Following Zhang et al. and Rüscher and Mielcarek [49], [50], the characteristic bands of the Si-O asymmetrical vibration shift towards higher wavenumbers with increasing Si amount in the geopolymer network. Thus the PSDS-type shows higher wavenumbers than the PSS- and PS-type. This effect can be observed in the given spectra, the band shifts from 975 cm^{-1} for Si/Al = 0.27 to 1004 cm^{-1} for Si/Al = 2.69 (the dotted line in Figure 22 shows the trend). The spectra also show a peak with decreasing area with increasing Si/Al ratio at 914 cm^{-1}, which is related to sixfold coordinated Al-OH swing vibrations (marked with blue rectangle in Fig. 22). The peak is not visible in the spectra with Si/Al above 1.01. Therefore, it can be concluded that an excess of aluminum cannot be embedded in the geopolymer

network, it is very likely that it forms $Al(OH)_3$ instead, due to the alkalinity of the system. An excess of silicon on the other hand, does not show the formation of Si-OH bands, which would be located at 840 cm^{-1} (bending vibration). The geopolymers obtained consist of short -Si-O-Al- units and a low degree of polymerisation, mainly. With increased molar Si/Al ratio the formation of longer chains increases. Examples for this effect are geopolymers built of waterglass and metakaolin. These materials show the Si-O peak at wavenumbers above 1010 cm^{-1} [49], [51].

It has to be kept in mind, though, that sodalite exists in crystalline form in the spectra shown, as well. The sodalite signals exhibit close similarities to the geopolymer phases, when analyzed by FTIR, due to their similar chemical bonds. An entire evaluation with FTIR only is therefore very complicated, especially due to the additional existence of the already mentioned phases like carbonate (686, 864 and 880 cm^{-1}) and sodiumbromide dihydrate (404 and 603 cm^{-1}).

The embedded NaBH$_4$ in contrast can be distinguished clearly by the B-H deformation signal at 1126 cm^{-1} [36] in the inset of the infrared spectra shown in Figure 23. In the complete spectra from 370 to 3800 cm^{-1} (cf. Figure 5) the B-H stretching bands are also visible at 2225, 2236 (sh), 2293 with a slight shoulder and 2388 cm^{-1}. The two shoulder peaks are related to the isotopic effect of ^{10}B and ^{11}B, which exist in nature in a ratio of 19.9 and 80.1 % [52]. The triplet-peak (ignoring the isotopic effect) is explained by *Fermi-resonance* effect. *Fermi-resonance* occurs, when a combination- or overtone-vibration has the same position (or energy) as a normal vibration, leading to a splitting of the peak positions and a share of intensity [40].

From the combination of x-ray diffraction data and peak form of the NaBH$_4$ triplet peak (see Figure 23), it can be concluded that the NaBH$_4$ is not formed inside the sodalite cages during gel precipitation. X-ray diffractograms show the reflex positions of the pure salt and secondly the peak positions of the FTIR spectra differ systematically (see Figure 23 and Table 21).

Table 21: FTIR peak position comparison between NaBH$_4$-gel, -salt and -sodalite

Material	Pos. v_4 / cm^{-1}	Pos. v_3 / cm^{-1}	Pos. 2 v_4/ cm^{-1}	Pos. v_2 + v_4/ cm^{-1}
NaBH$_4$-gel	1126	2225	2293	2388
NaBH$_4$ salt	1123	2222	2291	2383
BH$_4$-Sod	1133	2238	2287	2389
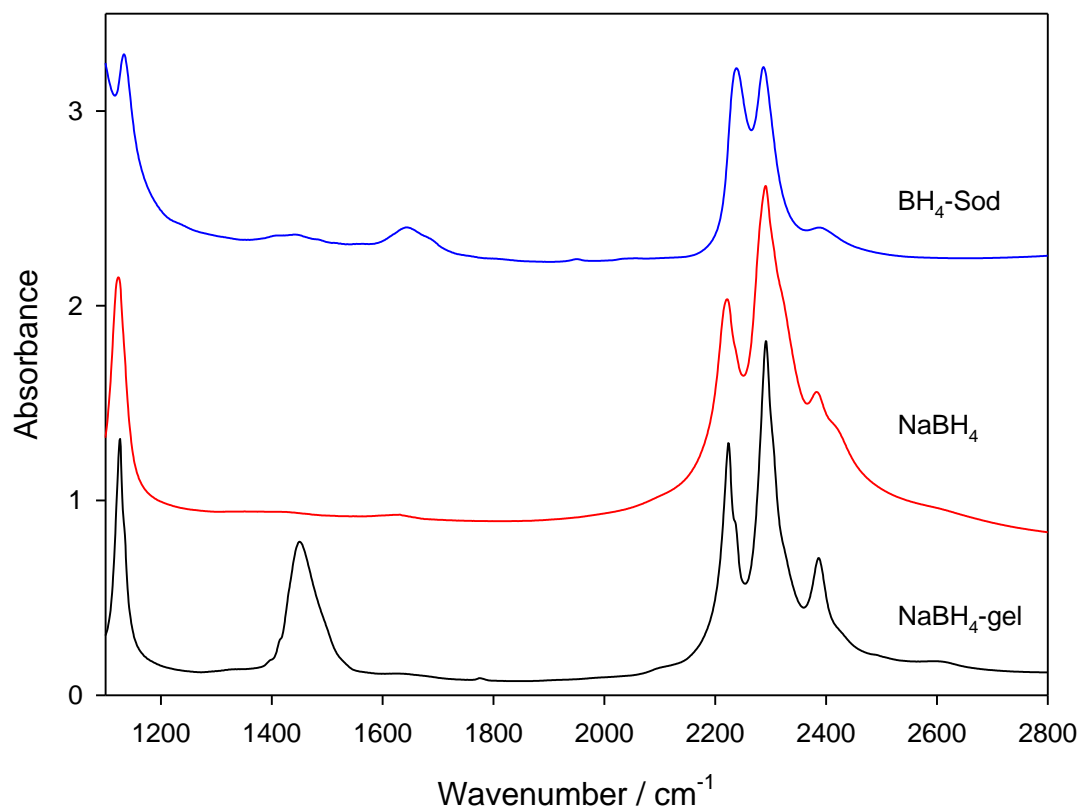
Figure 23: FTIR spectra for comparison of NaBH$_4$-gel, -salt and -sodalite

Additionally, as a function of drying time, the x-ray diffractograms obtained during the crystallization process (see below) show that the sodalite related reflexes occur before the crystallization of the NaBH$_4$. It is therefore more likely that the NaBH$_4$ crystallizes in the matrix of geopolymer type, amorphous areas. The crystallization process was analyzed in first principle studies [17]. A gel was prepared with the parameters: NaBH$_4$/matrix wt-ratio of 0.89 and a molar Si/Al ratio of 0.83. Four XRD measurements were performed, one before drying and three as function of time while drying under open conditions at 110 °C.
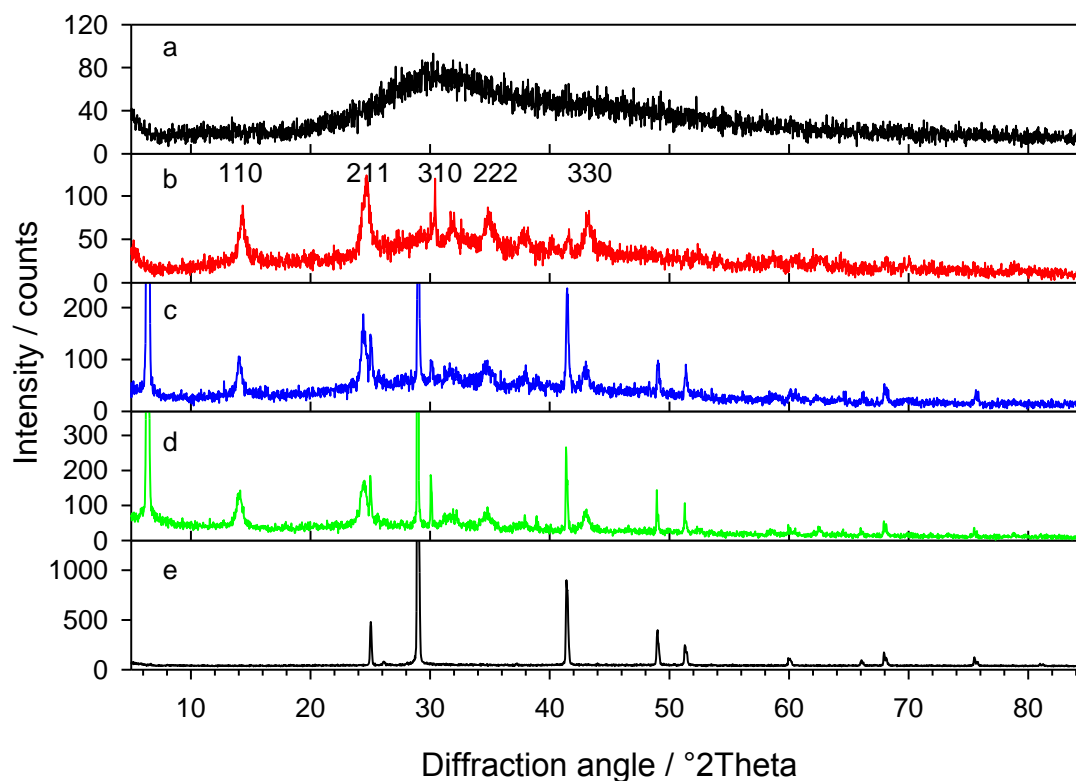
Figure 24: X-ray diffractograms of NaBH$_4$-gel A; a: directly after gel precipitation; b: after 30 min of drying at 110 °C; c: after 1 h drying at 110 °C; d: after 2 h drying at 110 °C; e: pure NaBH$_4$ salt for comparison [17]

Diffractogram *a* shows the gel directly after precipitation. It is completely amorphous with a broad signal around 30 °2θ. After 30 minutes drying at 110 °C the diffractogram shows broad but clear reflexes as shown in diffractogram *b*. Those signals can be assigned to sodalite related species. The reflexes are indicated with the hkl-tripel in diffractogram *b*. The broad background is also significantly present, so the material is partly amorphous. After one hour at 110 °C (see Fig. 24, c), sharp signals at the positions of NaBH$_4$ occur in addition to the sodalite reflexes. Beside these signals at 13.8 °2θ a strong reflex occurs, which can neither be assigned to sodalite nor to NaBH$_4$. After two hours (the 'normal' drying time at this temperature), the diffractogram shows only small further changes: The intensities of the NaBH$_4$-related reflexes increase while the amorphous content decreases. Diffractogram *e* shows sodium borohydride as pure phase for comparison.

Aluminosilicate Borohydrides: NaBH$_4$ Embedded in Sodalite and Gel Structures

4.4.2. Synthesis Variations

Another effect was observed for the molar Si/Al ratio of 0.34 in the x-ray-diffraction: The analyses of the hydrogen release experiments (see Chapter 4.3.2.) showed an only slightly smaller amount of embedded $NaBH_4$ of 106.5 ml/100 mg, compared to the other samples of this series. Furthermore, the FTIR spectrum showed high amounts of $NaBH_4$, but the x-ray diffractogram of this sample showed only small amounts of crystallized $NaBH_4$.

The existence of carbonate was confirmed by CS-analyzes, the amount of carbon is very high. It ranges from 0.3 wt% for highly enriched $NaBH_4$-gels to 3.2 wt% for intermediate amounts of $NaBH_4$. It can be concluded that the carbonate mainly forms in the alkaline matrix with water and the CO_2 from the surrounding atmosphere. With higher $NaBH_4$/matrix ratios the remaining water amounts after the drying process are lower because of the reduced amount of the matrix material, cf. Figure 25. Here, the obtained mass losses during the TG analyses are plotted against the $NaBH_4$/matrix ratio of the samples. The mass loss should be primarily due to water loss of the samples. These smaller amounts of water with higher $NaBH_4$/matrix ratio then lead to a reduced formation of carbonate.
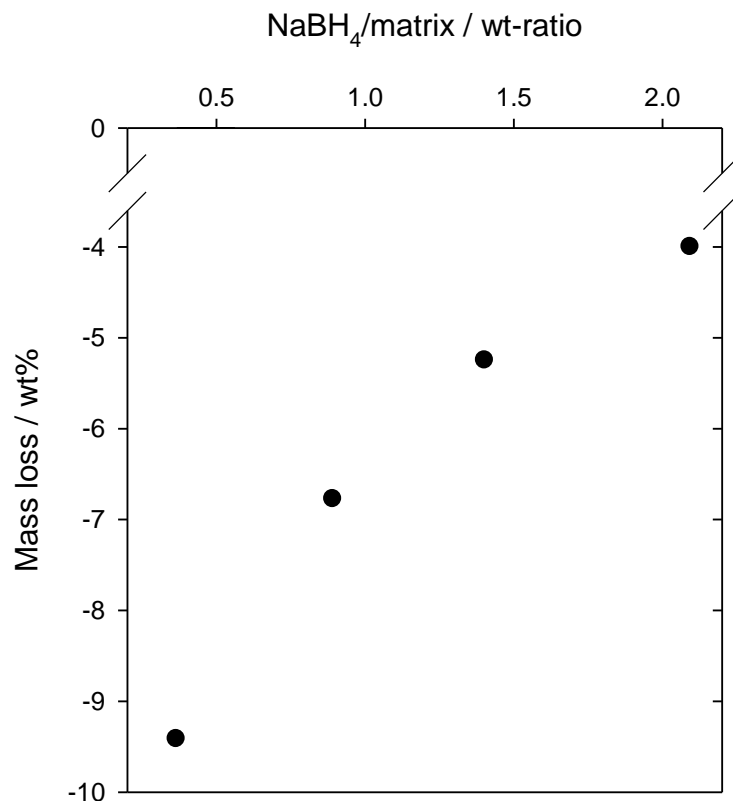
Figure 25: Plotted mass loss, obtained by TG up to 375 °C against the NaBH$_4$/matrix ratio.

It is possible to release up to 181.6 ml hydrogen per 100 mg sample, which is equivalent to 80 % of the pure NaBH$_4$ (226.5 ml/100 mg). To reach these high amounts, the gels were analyzed as a function of their NaBH$_4$/matrix ratio, the matrix molar Si/Al ratio and their drying temperature.

As a first parameter, the NaBH$_4$/matrix ratio was varied at a constant Si/Al ratio of 0.83 and a drying temperature of 110 °C. As expected, the amount of released hydrogen increases with higher amounts of NaBH$_4$ embedded in the matrix. The correlation can be quantified using a logarithmic equation:

$$y = 100.82 + 58.781 \cdot \ln(x) \tag{14}$$
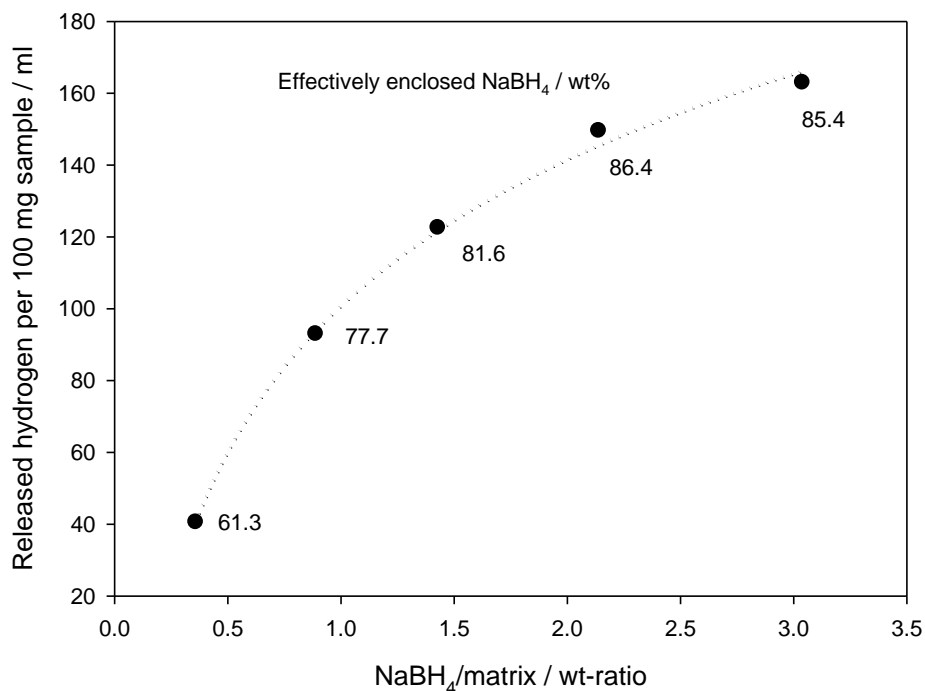
Figure 26: Plotted hydrogen release against the NaBH$_4$/matrix ratio. Additionally, for each data point the calculated effectively enclosed amount of NaBH$_4$ in percent is given

An unexpected effect becomes visible in the results of performed back calculations (see chapter 4.3.1. and results in Table 14). With low NaBH$_4$/matrix ratios, the calculated effectively enclosed amounts of NaBH$_4$ are lower than for higher NaBH$_4$/matrix ratios, although the protecting matrix amount is decreased. The highest effectively enclosed amount of NaBH$_4$ at drying temperatures of 110 °C is about 85 % in this series. A possible explanation could be the higher amount of water in the matrix. During the drying process, this water can react with the NaBH$_4$ and therefore reduces the later released amount of hydrogen. This effect takes place especially at raised temperatures; therefore the drying temperature was also varied.

The influence of the drying temperature was analyzed using two different NaBH$_4$/matrix ratios, both with a molar Si/Al ratio of 0.83. Both series showed the same behavior: the samples below 60 °C did not dry completely. Dried at 80 °C and 95 °C respectively, the gels released about 19 % more hydrogen compared to the initial synthesis dried at 110 °C. The back calculations show the corresponding values: At 110 °C dried

samples, effectively enclosed about 80 wt% of $NaBH_4$, calculated from the released hydrogen volume, while the analogous samples, dried at 80 °C and 95 °C, effectively enclosed more than 93 wt% of the used $NaBH_4$ (cf. Table 18 and 19). Following Filinchuk et al. [36], $NaBH_4$ forms a stable form $NaBH_4 \cdot 2H_2O$ with water in a temperature range of up to 40 °C. This decomposes again once the temperatures rises over 40 °C. The high pH value of the matrix stabilizes the $NaBH_4$ [53]–[55] explaining why temperatures far above 40 °C do not automatically lead to a decomposition of the $NaBH_4$ in the geopolymer. Due to the increased stability of this phase, there seems to be only a narrow temperature range from 75 to 100 °C with a good compromise between drying capability and a reaction degree of water with the $NaBH_4$ that is as low as possible.

The next varied parameter was the molar Si/Al ratio of the matrix. Concerning the amount of hydrogen released, it showed only minor effects. Several syntheses were carried out using molar Si/Al ratios between 0.22 and 2.69. The ratio of 0.22 did not form a stable gel at all. Thus the released amounts of hydrogen per 100 mg sample range from 106.2 to 121.0 ml, see Table 15 in Chapter 4.3.2. The hydrogen release data as function of the Si/Al ratio can be divided into three parts: Si/Al 0.27 and 0.34 show a release of 106 ml, Si/Al from 0.45 to 1.01 show a release around 111 ml and the ratios above 2.0 show an increased release of hydrogen of 118.5 or 121.0 ml, respectively. Hence, an increased Si/Al ratio from a balanced Si/Al ratio only leads to a maximum of 9.3 % more hydrogen released.

Even though the combination of the parameters show the highest hydrogen amounts of 181.6 ml per 100 mg sample, the hydrogen amount is not as high as would be expectable with an additional behavior of the optimized parameters. The increase between the basic sample, dried at 110 °C, $NaBH_4$/matrix of 3.04 and a molar Si/Al ratio of 0.83, and the optimized sample is only 11.4 %. It can therefore be concluded that the parameters cannot easily be combined. The highest effect can be reached by an increased $NaBH_4$/matrix ratio and by decreasing the drying temperature.

The gel samples show an impressive long-term stability. Figure 27 shows two exemplarily samples, which were stored for 9 months. The FTIR spectra show only minor changes, mainly due to the sample preparation for FTIR measurements.
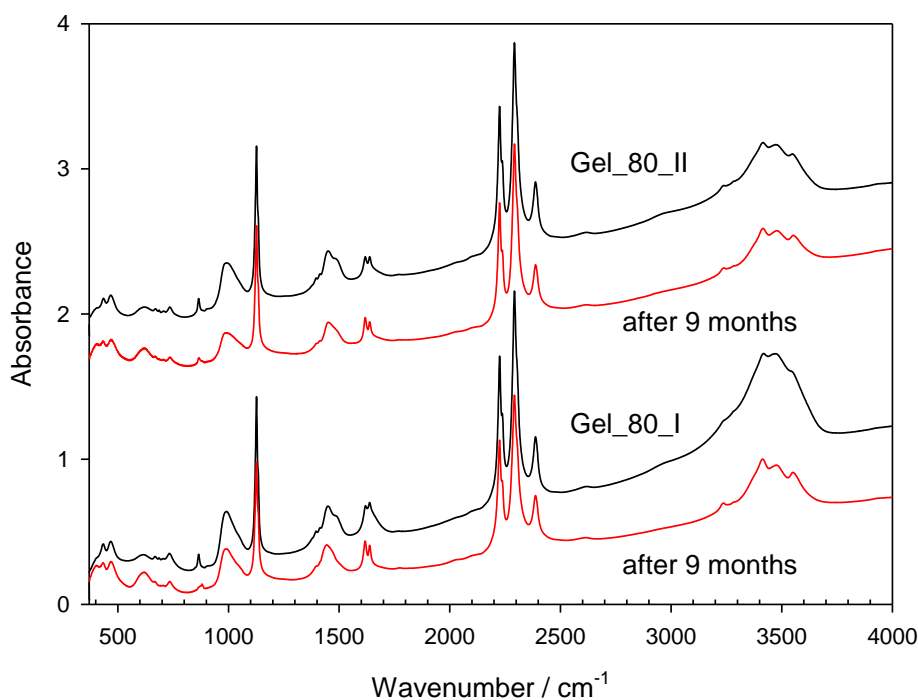
Figure 27: Exemplarily BH₄-gels stored for nine months. FTIR spectra before and after the long-term stability analysis.

Further optimizations require far more synthesis series with more combinations of the different parameters to analyze the interactions between those. As a further required step, the matrix system itself should be varied concerning its chemical composition, for example by reducing the alkalinity to inhibit the formation of carbonate or the use of potassium bearing reactants to reduce the amount of formed sodalite.

Part B:

Characterization of BH_4-Sodalite:

Synthesis Variations and Comparison

5. NaBH$_4$-Sodalite: Sample Characterization

5.1. NaBH$_4$-Sodalite 120 °C

The synthesis batch was prepared, as described in Chapter 3.1.2.. In Table 22 the sample names and the weights of reactants used are summarized. For some compositions more than one synthesis was carried out to verify the samples obtained. Those samples are marked as 'a to d' in the first column of Table 22. All samples exist as white powders, after the drying procedure.

Table 22: Sample overview of the 120 °C synthesis batches: Variation of the NaBH$_4$/matrix ratio

Sample 120 °C	NaBH$_4$ / g	Kaolin / g	NaBH$_4$/matrix wt-ratio
0_120	0	1.0	- (0)
0.03_120	0.03	1.0	0.03
0.05_120	0.05	1.0	0.05
0.07_120	0.07	1.0	0.07
0.1_120	0.1	1.0	0.1
0.2_120_a	0.2	1.0	0.2
0.2_120_b	0.2	1.0	0.2
0.3_120	0.3	1.0	0.3
0.4_120	0.4	1.0	0.4
0.6_120_a	0.6	1.0	0.6
0.6_120_b	0.6	1.0	0.6
0.6_120_c	0.6	1.0	0.6
0.6_120_d	0.6	1.0	0.6
0.8_120	0.8	1.0	0.8
1.0_120_a	1.0	1.0	1.0
1.0_120_b	1.0	1.0	1.0
1.3_120	1.3	1.0	1.3
1.5_120	1.5	1.0	1.5

5.1.1. XRD

As first, the synthesis series was characterized by X-ray diffraction using the *Bruker D4* diffractometer with the parameters, summed up in Table 23. The mentioned secondary Ni-filter was installed during the experimental work and is therefore marked with a star. In the following diffractograms the samples measured with the secondary Ni-filter are also marked

with a star at their given $NaBH_4$/matrix wt-ratio. The effect of the filter is visible especially at low diffraction angles, without the filter, the diffractograms show a significant rise towards the y-axis.

Table 23: Used measuring parameters for XRD analyses on Bruker D4

Measuring parameters Bruker D4	
Geometry	Bragg-Brentano
Detector	Scintillation Counter
Scan Type	Locked Couple
Scan Mode	Continuous scan
Measuring range / °2θ	5.0 – 80.0
Step size / °2θ	0.02
Time/step / sec	5
Filter	Secondary Ni-filter*
Gen. voltage / kV	40
Gen. current / mA	40
Sample rotation	None
Sample holder	Specimen holder ring

The obtained powder diffraction patterns are summarized in Figures 28 to 30. All patterns show the characteristic sodalite reflexes and are in good agreement with literature [26] and ICSD database data (ICSD 153255) [56].

Figure 28: X-ray diffractograms of the 120 °C series with NaBH4/matrix wt-ratios from 0.0 to 0.1 from bottom to top

Figure 29: X-ray diffractograms of the 120 °C series with NaBH$_4$/matrix wt-ratios from 0.2 to 0.6 from bottom to top

Figure 30: X-ray diffractograms of the 120 °C series with NaBH$_4$/matrix wt-ratios from 0.8 to 1.5 from bottom to top

From the data obtained, the lattice parameter for the samples were calculated after the sodalite reference (ICSD 153255), symmetry *P-43n* [57] using the software *STOE*

WinXPOW. The lattice parameters are shown in Table 24, according to the NaBH$_4$/matrix wt-ratio.

Table 24: Calculated lattice parameters of BH$_4$-sodalite 120 °C synthesis batch, using STOE WinXPow

NaBH$_4$/matrix wt-ratio	Lattice parameter / Å	Cellvolume / Å^3
- (0)	8.9514(13)	717.25(18)
0.03	8.9567(8)	718.54(11)
0.05	8.9305(7)	712.24(9)
0.07	8.9254(6)	711.03(8)
0.1	8.9205(8)	709.84(11)
0.2	8.9239(9)	710.67(13)
0.2	8.9230(11)	710.45(15)
0.3	8.9235(4)	710.57(5)
0.4	8.9260(8)	711.18(12)
0.6	8.9271(8)	711.43(11)
0.6	8.9242(7)	710.72(9)
0.6	8.9253(5)	711.01(8)
0.6	8.9263(9)	711.24(13)
0.8	8.9249(7)	710.90(9)
1.0	8.9284(8)	711.73(11)
1.3	8.9214(4)	710.07(6)
1.5	8.9280(3)	711.63(4)

The sample without NaBH$_4$ and the NaBH$_4$/matrix ratios of 0.03 show significant increase in the lattice parameter and the cellvolume. All other lattice parameter and cell volume remain almost constant around 8.925(3) Å and 710.8(9) Å^3, respectively with increasing NaBH$_4$/matrix ratios.

5.1.2. FTIR

Furthermore all samples are also analyzed, using FTIR with the KBr-method. Three pellets per sample were prepared and measured, to obtain error values for the following evaluations. To be able to compare the integrated intensities of the different species in different samples,

the TOT normalization method was used, described in 3.2.1.. Additionally a sample mass normalization was performed on the pellet preparation to cross-check the effects observed.

The samples of this synthesis batch show the bands of the aluminosilicate sodalite framework in the area from 400 to 1000 cm^{-1} in the IR-spectra, regardless of their $NaBH_4$/matrix wt-ratio. The asymmetric stretching TOT-bands v_{as} occur at about 990 cm^{-1}, the three symmetric TOT-bands v_{sym} between 630 and 750 cm^{-1} and the two δ-TOT-bands δ at 430 and 470 cm^{-1} [26], [58], respectively. Only the two samples without any $NaBH_4$ and with only 0.03 $NaBH_4$/matrix show differences in the framework bands. Here, the signals at 460 cm^{-1} exhibit higher absorbance values than the signal at 430 cm^{-1}, compared to all other $NaBH_4$/matrix ratios, where the 430 cm^{-1} signal shows the higher absorbance. The symmetric TOT-bands show similar differences; here also the two mentioned samples, exhibit different relative absorbance values, compared to the samples with higher $NaBH_4$/matrix ratios. Around 600 cm^{-1} an underground signal is visible for the samples with $NaBH_4$/matrix below 0.07, which is probably related to residual reactants or small amounts of zeolite A [59], [60].

All samples contain molecular water, indicated by the δ-H_2O around 1650 cm^{-1}, the intensity of these bands decreases with increasing $NaBH_4$/matrix ratio. The broad signal between 2800 and 3750 cm^{-1} belongs to OH-vibrations, caused by water, too [61].

The imbedded BH_4^- is visible by the v_4 vibration in from of a 'shoulder' at 1134 cm^{-1} and the *Fermi-resonance* intensified triplet-peak at 2238 (*2·v$_4$*), 2287 (*v$_3$*) and 2390 cm^{-1} (*v$_2$+v$_4$*) [36]. Those signals increase with increasing $NaBH_4$/matrix ratio as expected.

The samples with $NaBH_4$/matrix ratios below 0.07 show broad signals between 1380 and 1500 cm^{-1}, probably related to carbonate species [61], [62].

Figure 31: Spectra of representative samples from the 120 °C synthesis batch, shown are increasing NaBH₄/matrix ratios from bottom to top.

Figure 32 displays the average integrated intensities of BH_4^- and water, in dependence of the NaBH₄/matrix wt-ratio, after TOT-normalization. The absolute values of the integrated intensities of the water corresponding signals is critically. It is possible to increase the amount of water by sample preparation, due to prolonged pestilisation. Due to the decrease of the particle size of the KBr and the sample while pestling, the hygroscopicity increases. This trend was also cross-checked by a normalization, using the sample mass, as described in 3.2.1.. The integrated peak areas of the BH_4^--corresponding signals are plotted in the same graph to show the correlation with the water content. With increasing NaBH₄/matrix ratio, the integrated intensities of the BH_4^--correlated peaks also increase, as expected. But at a ratio of 0.6 the integrated intensities reach a limit value. At higher NaBH₄/matrix ratios, the NaBH₄ related bands remain constant. The values converge a limit of about 30 area units exponentially. For the water-related bands, an almost inverse trend

can be observed. With increasing NaBH$_4$/matrix ratio, the integrated intensities of the water peaks decrease. Above a ratio of 0.4 the decrement slows down.

Figure 32: Shown are the average integrated intensities (filled) of BH$_4^-$ (black circles) and water (cyan triangles) of the 120 °C series as function of the NaBH$_4$/matrix ratio. White symbols show additional measurements, the error bars represent 2·σ

5.1.3. TG/DTA

All samples of the synthesis batch are analyzed on their water content and reaction behavior, using Thermogravimetry and Differential Thermo Analysis (TG/DTA). The measuring parameters remain constant and are summarized in Table 25. For evaluation of the data, only the heating curves of the measurements are used.

Table 25: Measuring parameters for TG/DTA analyses

Maximal temperature / °C	Heating-/cooling rate / K/min	Carrier gas	Gas flow / ml/min	Holding time at max. temperature / min
500	4	Helium	20	60

Thermogravimetric results confirm the exponential decrement, shown by the integrated intensities of the water-correlated bands (Fig. 32). In Figure 33, the raw data of selected TG-curves are shown for the heating period, only. The plotted mass loss in dependency of the $NaBH_4$/matrix wt-ratio shows the highest mass loss with the lowest $NaBH_4$/matrix ratio. Above 0.6 $NaBH_4$/matrix, the mass loss remains almost constant around 1.2 wt%. The highest mass loss was observed for the sample without $NaBH_4$, this sample shows a mass loss of 10.34 wt%. Detailed mass losses are given in Table 26, the values for samples, marked with a star represent an average value for several measurements of this chemical composition.

Table 26: Detailed mass losses of the 120 °C series obtained by TG up to 500 °C

NaBH$_4$/matrix wt-ratio	Mass loss / wt%
- (0)	10.336
0.03	6.730
0.05	4.827
0.07	5.377
0.1	3.552
0.2*	2.875
0.3	1.844
0.4	2.402
0.6*	1.227
0.8	1.242
1.0*	1.593
1.3	0.466
1.5	1.031
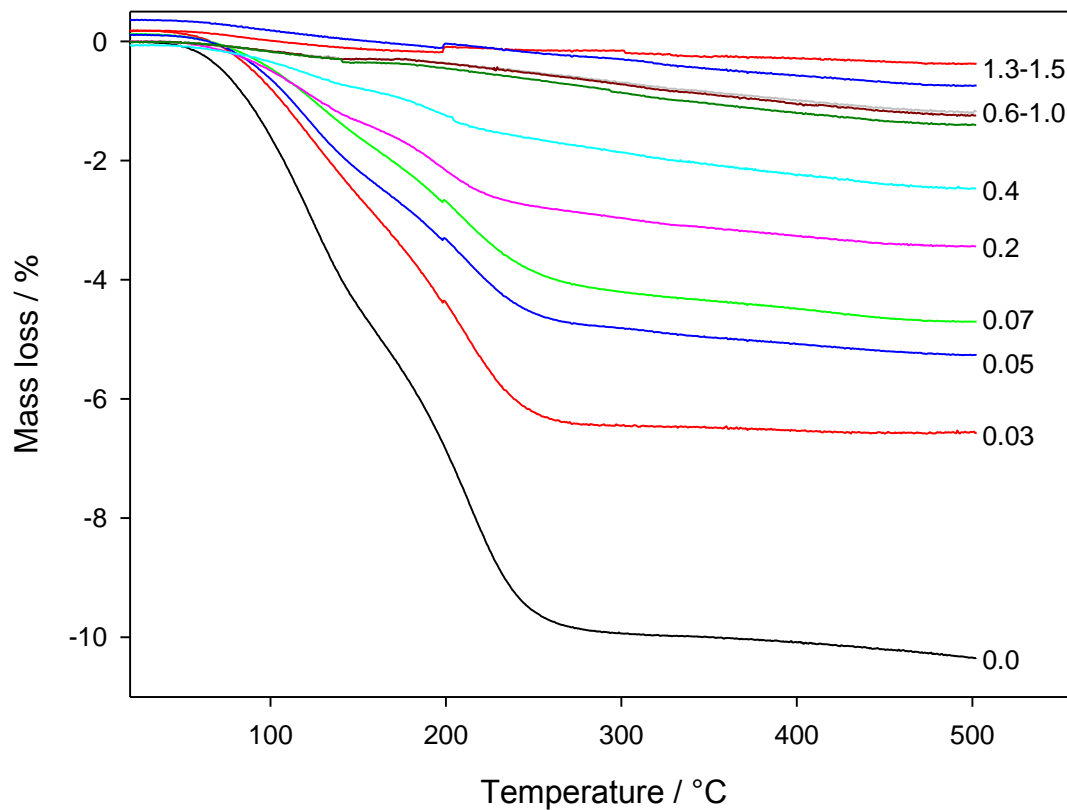
Figure 33: Thermogravimetric curves for the heating period of the varied NaBH$_4$/matrix wt-ratios as given in the Figure of the 120 °C series.

Figure 34 shows the results of the TG as function of the NaBH$_4$/matrix wt-ratio. The data show an exponential decrease of the mass loss with increasing NaBH$_4$/matrix wt-ratio up to 0.6. With further increase the mass loss remains constant.

Figure 34: Shown is the mass loss of the synthesis batch 120 °C during TG/DTA measurements up to 500 °C as function of the NaBH₄/matrix ratio. For repeated analyses (white circles show the single measurements, black circles the average values) the error bars are given as 2·σ.

The results of the DTA measurements are divided into three Figures (35 to 37) for the sake of clarity. The sample without $NaBH_4$ (0.0 - hydro-sod) shows three remarkable effects: At about 50 °C an endothermic peak is visible, which merges into the second, more pronounced signal with a maximum at 120 °C. The third signal has its maximum at 210 °C and is also an endothermic effect. At further increased temperatures no more effects can be observed, which are sample related. With small $NaBH_4$/matrix ratios, the DTA curves vary only slightly. The three measurements, shown in Figure 35 ($NaBH_4$/matrix 0.03 to 0.07) exhibit the same endothermic signals as the hydro-sod sample. Those effects are reduced in their intensities but are located at the same temperatures. The sharp step at 100 °C is related to a measuring inaccuracy of the reference. This step does not influence the evaluation of the data.

Figure 35: DTA curves of the 120 °C series, samples with NaBH$_4$/matrix wt-ratio from 0.0 to 0.07. The signals are shown for the heating procedure, only.

With further increasing NaBH$_4$/matrix ratio, the two mentioned effects at 120 and 210 °C, respectively, show a further decrease in their intensity. Figure 36 shows the DTA curves of the samples with a NaBH$_4$/matrix ratio from 0.1 to 0.4. Up to the ratio of 0.4 the endothermic effects are still visible at the mentioned temperatures. The signal around 50 °C is present in small amounts for NaBH$_4$/matrix ratios of 0.1 and 0.2 only, with further increase this signal becomes more pronounced again. Above 350 °C the DTA curves decrease smoothly. This effect is probably related to an apparatus effect and therefore not necessarily a sample effect.

Figure 36: DTA curves of the 120 °C series, samples with NaBH$_4$/matrix wt-ratio from 0.1 to 0.4. The signals are shown for the heating procedure, only.

The samples with NaBH$_4$/matrix ratios of 0.6 and above show a very similar developing. Only the 50 °C signal is clearly visible throughout these samples. With increasing NaBH$_4$/matrix ratio, the effect seems to me more pronounced. The endothermic effects at 120 and 210 °C, respectively, cannot be observed clearly. For the two samples with NaBH$_4$/matrix of 1.3 and 1.5 the step in the DTA curve at 100 °C is related to an inaccuracy of the reference, again.

Figure 37: DTA curves of the 120 °C series, samples with NaBH$_4$/matrix wt-ratio from 0.6 to 1.5. The signals are shown for the heating procedure, only.

5.2. NaBH$_4$-Sodalite 80 °C

The synthesis batch was prepared, as described in chapter 3.1.2.. In Table 27 the sample names and the weights of reactants used are summed up. After the drying procedure, all samples occurred as white powders, there were no differences visible.

Table 27: Sample overview of the 80 °C syntheses batches: Variation of the NaBH$_4$/matrix ratio

Sample 80 °C	NaBH$_4$ / g	Kaolin / g	NaBH$_4$/matrix wt-ratio
M_0_80	0	1.0	- (0)
L_0.03_80	0.03	1.0	0.03
L_0.05_80	0.05	1.0	0.05
L_0.07_80	0.07	1.0	0.07
LD_0.1_80	0.1	1.0	0.1
M_0.2_80	0.2	1.0	0.2
LD_0.2_80	0.2	1.0	0.2
LD_0.3_80	0.3	1.0	0.3
M_0.4_80	0.4	1.0	0.4
M_0.6_80	0.6	1.0	0.6
M_0.8_80	0.8	1.0	0.8
M_1.0_80	1.0	1.0	1.0
L_1.3_80	1.3	1.0	1.3
L_1.5_80	1.5	1.0	1.5

5.2.1. XRD

This synthesis series was also analyzed by x-ray diffraction; the used measuring parameters were identical as for the 120 °C synthesis-series (see Table 23, chapter 5.1.1.).
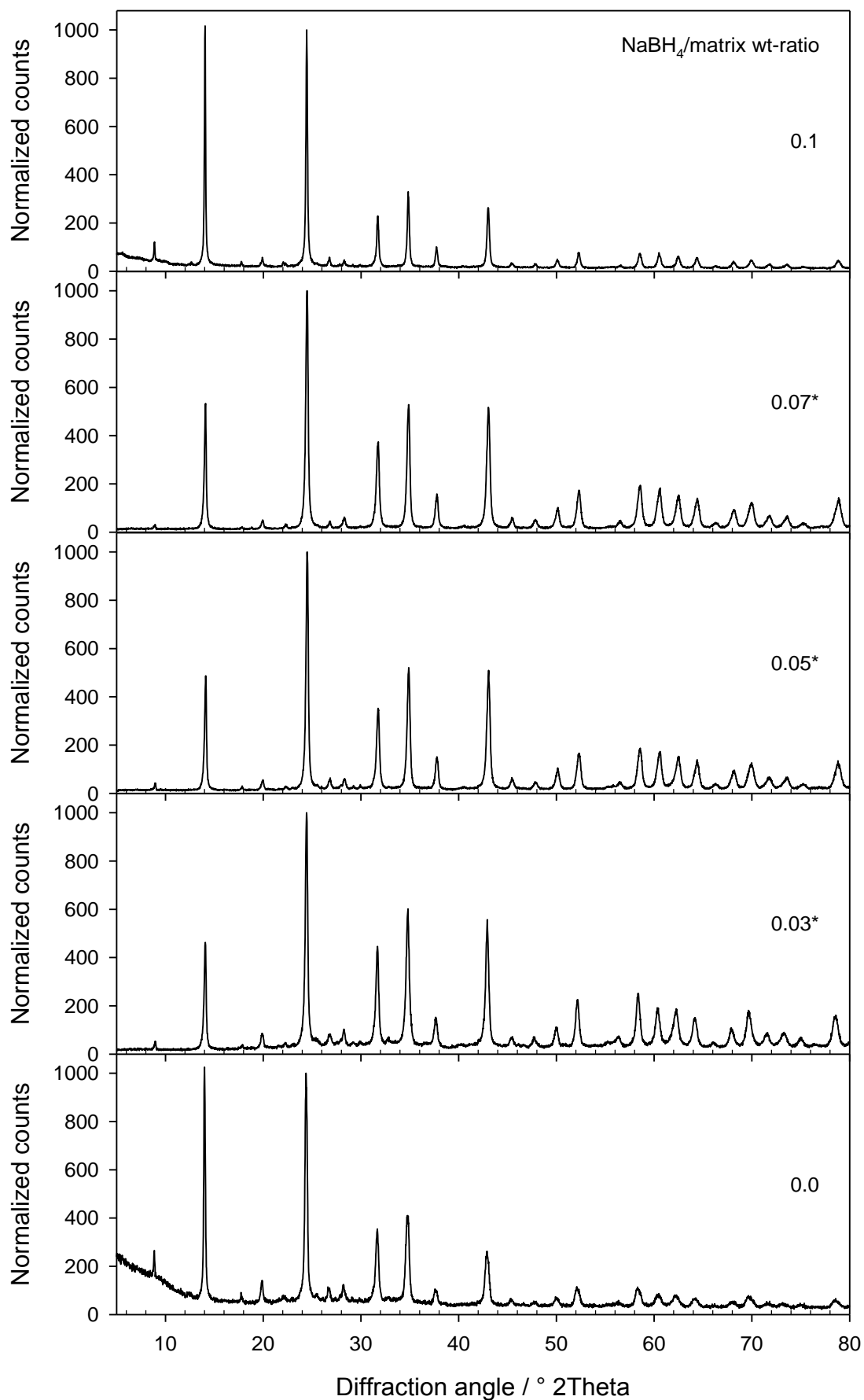
Figure 38: X-ray diffractograms of the 80 °C series with NaBH$_4$/matrix wt-ratios from 0.0 to 0.1 from bottom to top
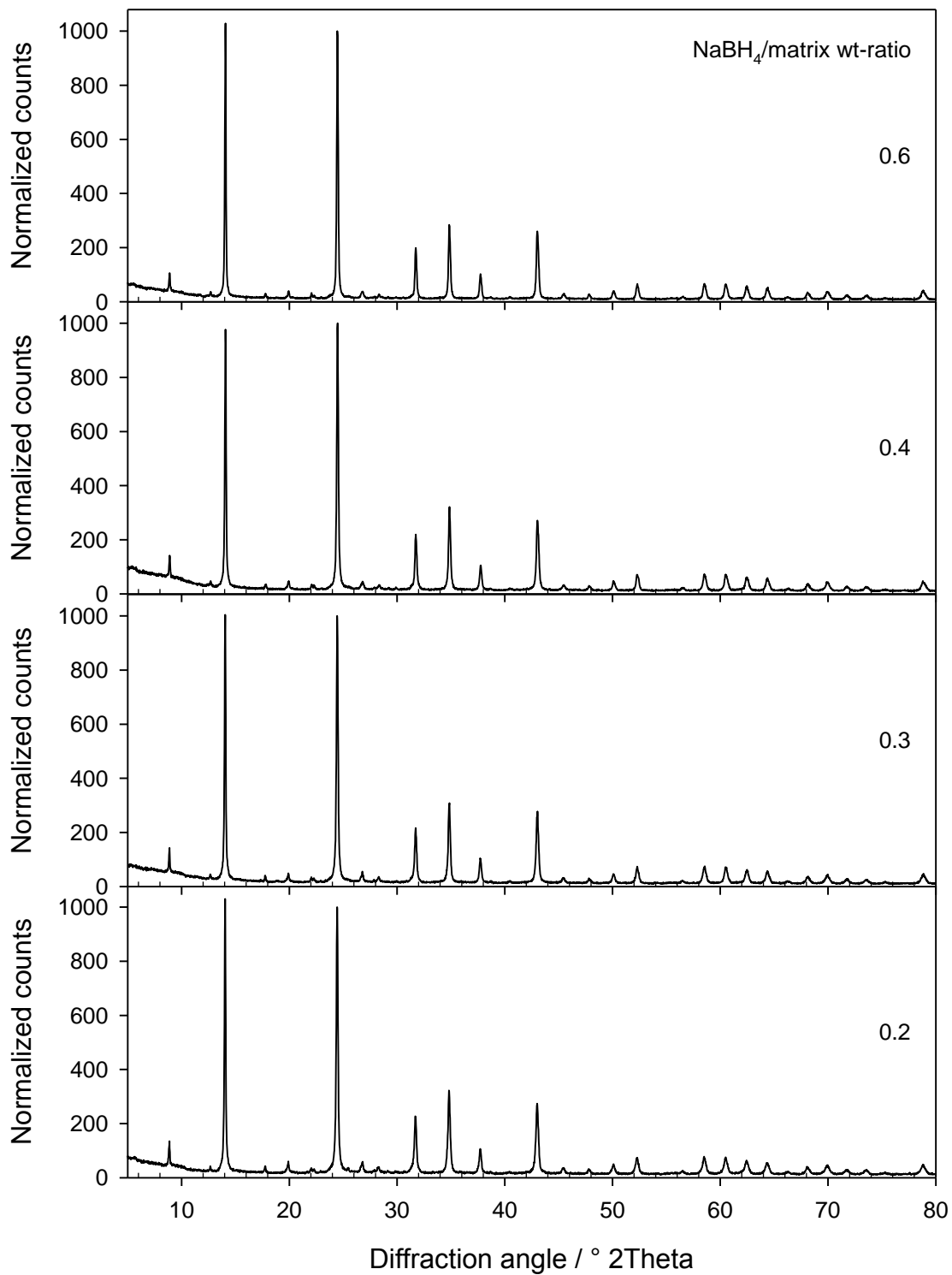
Figure 39: X-ray diffractograms of the 80 °C series with NaBH$_4$/matrix wt-ratios from 0.2 to 0.6 from bottom to top
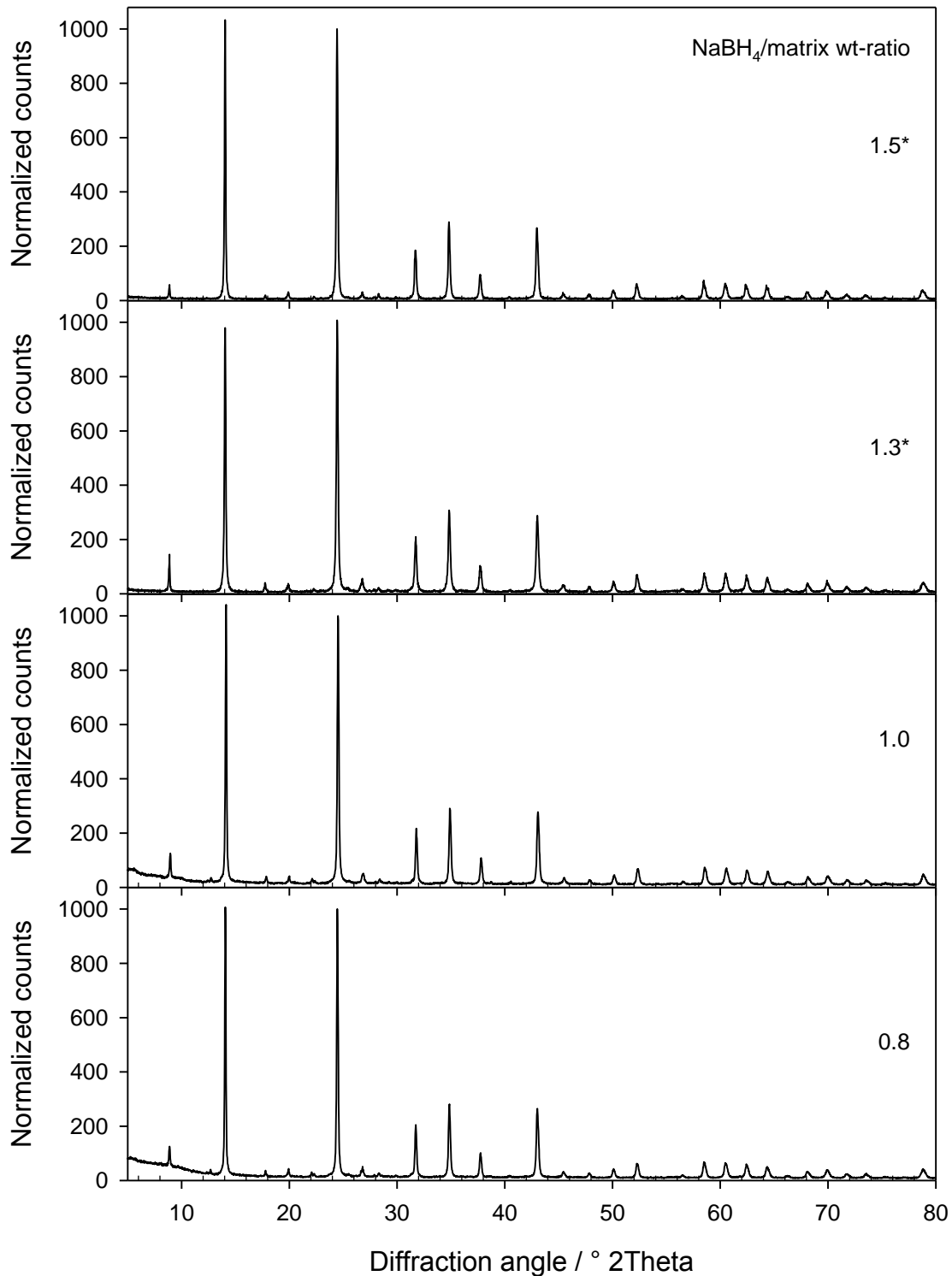
Figure 40: X-ray diffractograms of the 80 °C series with NaBH$_4$/matrix wt-ratios from 0.8 to 1.5 from bottom to top

Analogous calculations of the lattice parameters of the 80 °C samples, summed up in Table 28, show similar results to the 120 °C samples. The blank sample without $NaBH_4$ has the highest lattice parameter and cell volume, already at and above a $NaBH_4$/matrix ratio of 0.1 the lattice parameters remain constant around 8.9308(20) Å. The highest $NaBH_4$/matrix ratios of 1.3 and 1.5 show further increasing lattice parameters.

Table 28: Calculated lattice parameters of BH$_4$-sodalite 80 °C synthesis batch, using STOE WinXPow

Sample	Lattice parameter / Å	Cellvolume / Å^3	NaBH$_4$/matrix wt-ratio
0.0_80	8.9421(17)	715.02(23)	-
0.03_80	8.9399(12)	714.49(17)	0.03
0.05_80	8.9337(14)	713.02(19)	0.05
0.07_80	8.9326(10)	712.75(13)	0.07
0.1_80	8.9229(8)	712.10(12)	0.1
0.2_80_a	8.9297(4)	712.05(6)	0.2
0.2_80_b	8.9311(3)	712.40(4)	0.2
0.3_80	8.9297(6)	712.05(9)	0.3
0.4_80	8.9308(3)	712.30(4)	0.4
0.6_80	8.9306(3)	712.25(4)	0.6
0.8_80	8.9315(4)	712.49(5)	0.8
1.0_80	8.9316(6)	712.51(8)	1.0
1.3_80	8.9375(3)	713.93(4)	1.3
1.5_80	8.9369(4)	713.77(5)	1.5

5.2.2. FTIR

FTIR analyses show, that the synthesis products, obtained by the synthesis temperature of 80 °C are very similar to the samples, synthesized at 120 °C. All samples show the already mentioned sodalite framework bands. The asymmetric stretching TOT-signals v_{as} are located around 990 cm^{-1}, while the three symmetric TOT-bands v_{sym} can be found between 630 and 750 cm^{-1}. The two δ-TOT-bands are located at 430 and 470 cm^{-1}. Similar to the 120 °C samples, the spectra of the samples with a $NaBH_4$/matrix ratio below 0.07 show differences in the relative signal intensities. The bands at 460 cm^{-1} show higher absorbance than the bands at 430 cm^{-1}, this effect does not occur anymore for samples with $NaBH_4$/matrix ratios

of 0.07 and above. For the symmetric TOT-bands, only the sample without any $NaBH_4$ shows different relative absorbance between the three bands, compared to the other samples.

Just as the samples prepared at 120 °C, all spectra here show the δ-H_2O band at 1650 cm^{-1}, indicating molecular water. The samples show the same trend, regarding the increase of the $NaBH_4$/matrix absorbance going along with decrease of the water band. All samples show the broad signal of the OH-vibrations in the range from 2800 to 3750 cm^{-1}.

The BH_4^--bands are also visible at the same positions as in the 120 °C samples. At 1134 cm^{-1} the v_4 band is visible in form of a shoulder on the framework signal in all spectra, which contain $NaBH_4$. The triplet peak, consisting of the $2 \cdot v_4$, v_3 and v_2+v_4 bands is located at 2239, 2289 and 2390 cm^{-1}. The peak intensities also increase with increasing $NaBH_4$/matrix ratio. The spectra of $NaBH_4$/matrix 1.3 and 1.5 show a double peak at 1290 and 1310 cm^{-1} with small intensity, respectively. Carbonate related bands in the range from 1380 to 1500 cm^{-1} are visible in samples with $NaBH_4$/matrix ratios below 0.1.
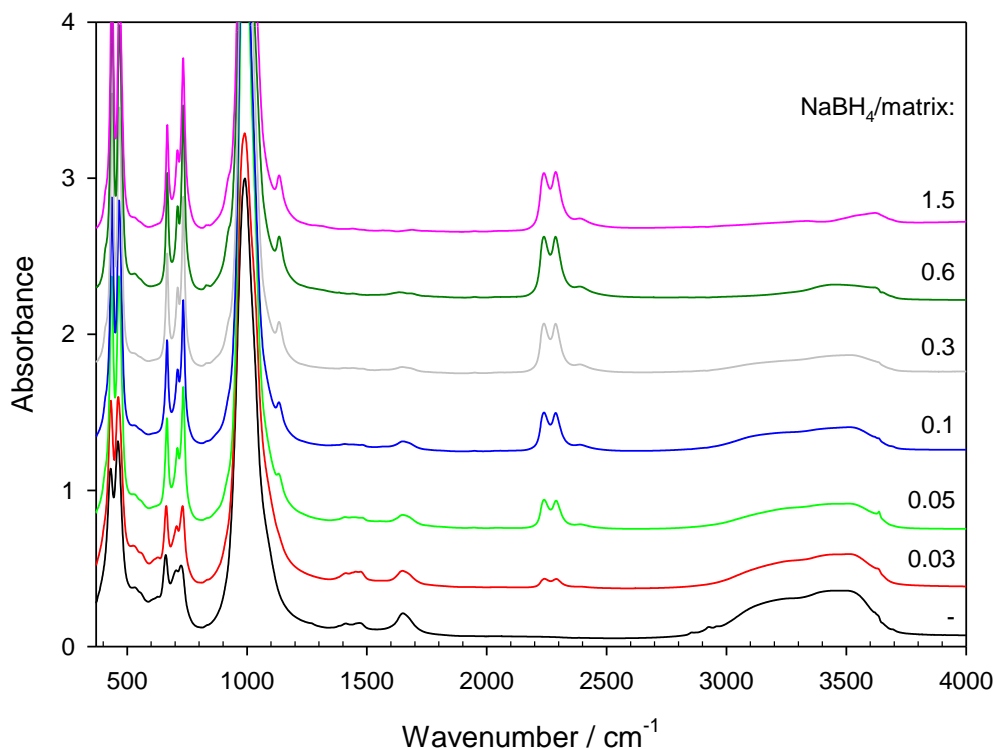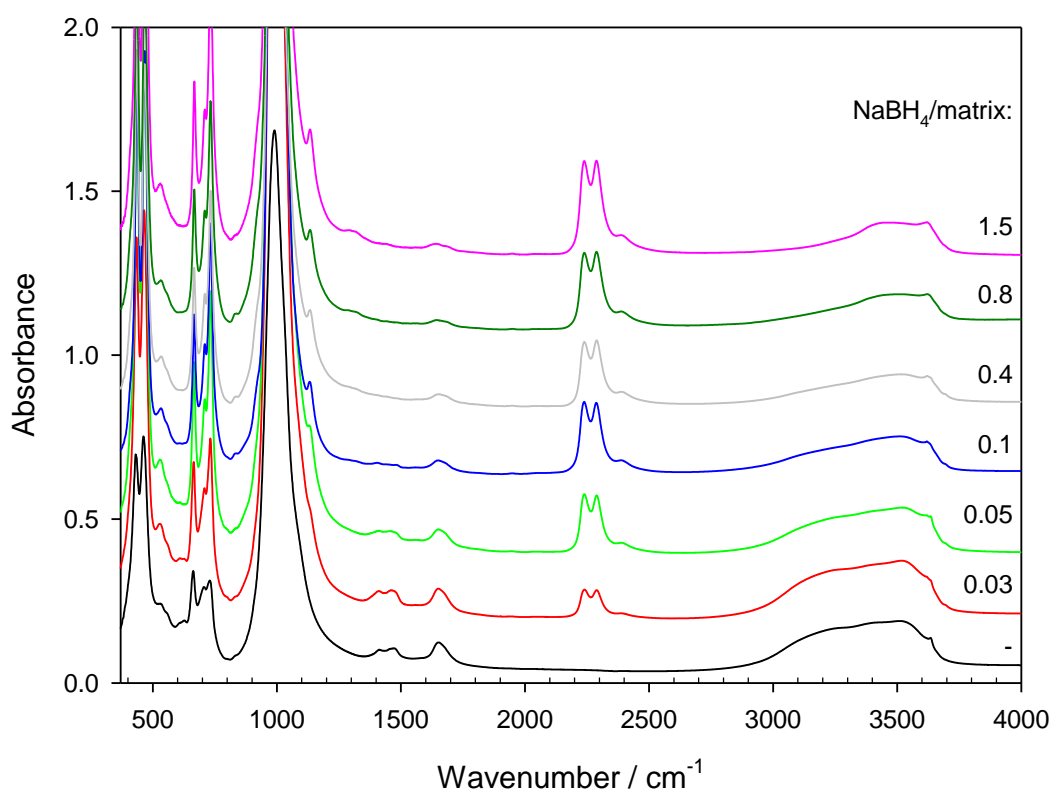

Figure 41: Spectra of representative samples from the 80 °C synthesis batch, shown are increasing NaBH₄/matrix ratios from bottom to top.

Integrated intensities of the obtained, TOT-normalized IR-spectra for the water and BH$_4^-$ bands show a similar behavior to the 120 °C samples. The blank sample without NaBH$_4$ shows the highest amount of molecular water and no BH$_4^-$ bands. Whereas the addition of tiny amounts of NaBH$_4$ during synthesis (NaBH$_4$/matrix = 0.03) already lead to significantly decreasing amounts of water and clearly detectable signals of imbedded BH$_4^-$. With increasing NaBH$_4$/matrix ratios up to 0.2, the integrated intensities of the BH$_4^-$ related bands increase, while the water bands decrease. Above NaBH$_4$/matrix = 0.2 the integrated intensities of both species remain almost constant, even though both trends show an exponential behavior. The maximum intensities of the water bands is 1.8, while the BH$_4^-$ related intensities reach a limit value of about 30 relative absorbance area units, see Figure 42.
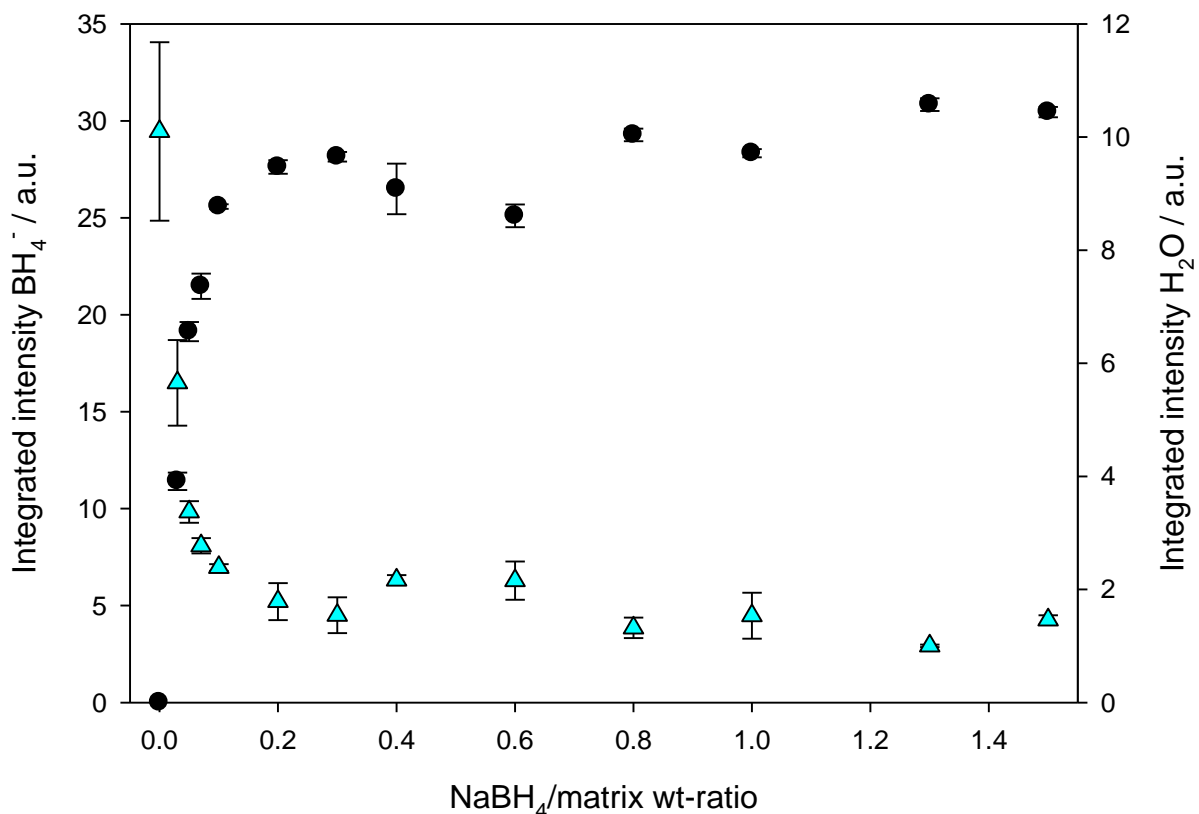
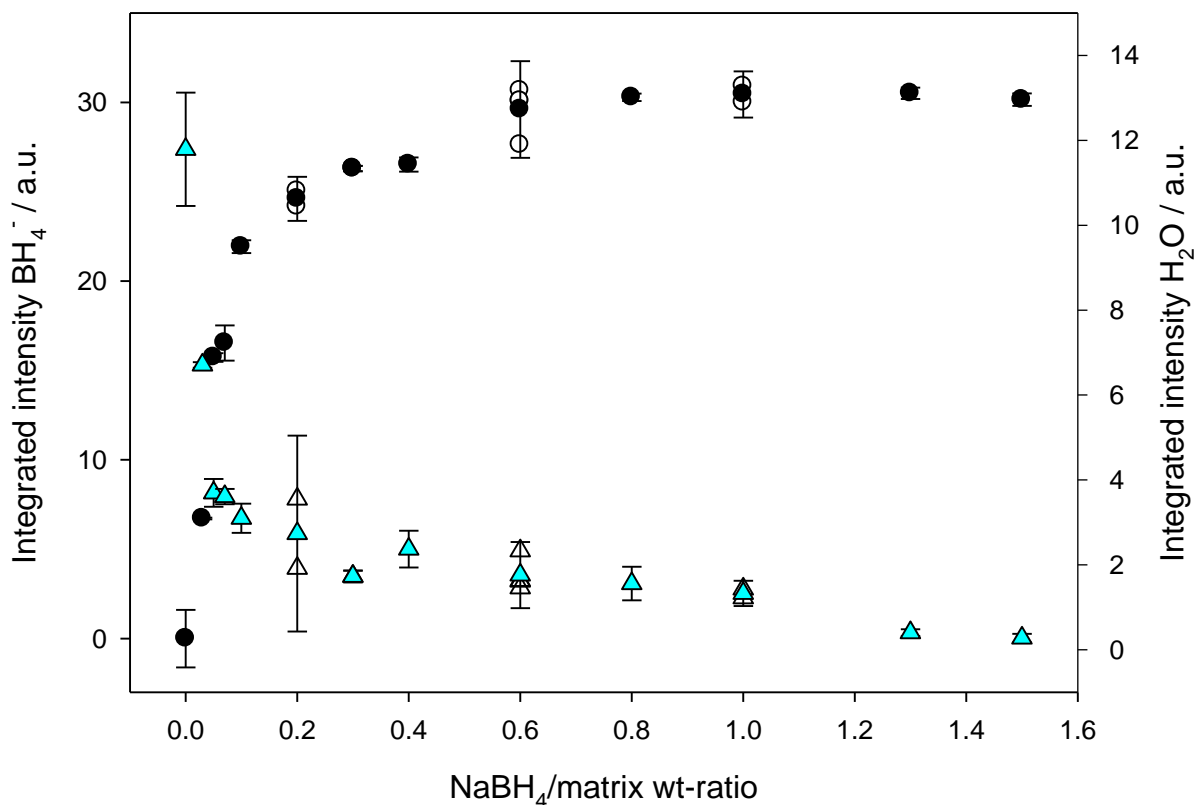**Figure 42: Shown are the average integrated intensities of BH$_4^-$ (black circles) and water (cyan triangles) as function of the NaBH$_4$/matrix ratio for the 80 °C synthesis batch, the error bars represent 2·σ**

5.2.3. TG/DTA

The samples were analyzed by TG/DTA, analogous to the 120 °C series (measuring parameters, see Table 25 in chapter 5.1.1.). The mass loss of the 80 °C samples, obtained by TG/DTA measuring up to 500°C, is shown in Figure 43. Again, the 80 °C samples exhibit the same exponential trend as the 120 °C samples. The blank sample shows the highest mass loss of 8.9 wt%, with increasing $NaBH_4$/matrix ratio the mass loss decreases until it reaches the limit value of about 2.5 wt% above $NaBH_4$/matrix of 0.2. This observation is in good agreement with the trend given by the integrated intensities of molecular water, obtained by IR (see Fig. 42). Detailed results are summarized in Table 29.
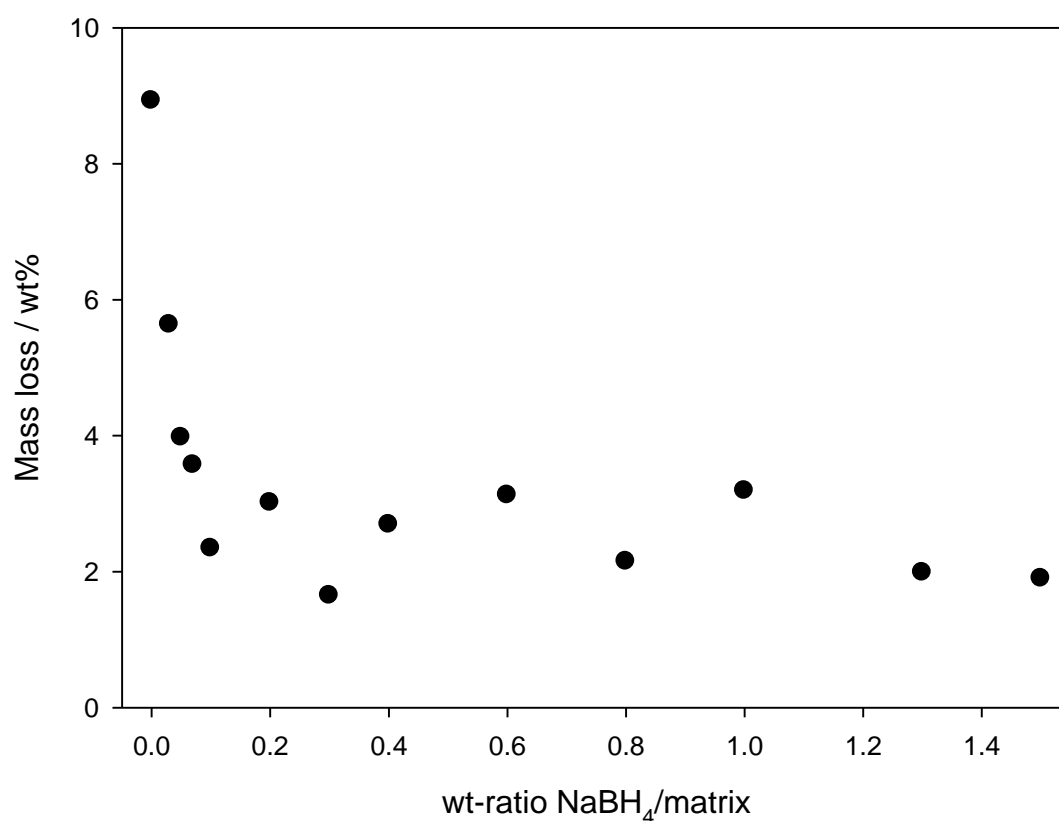
Figure 43: Shown is the mass loss of the synthesis batch 80 °C during TG/DTA measurements up to 500 °C as function of the $NaBH_4$/matrix ratio.

Table 29: Detailed mass losses of the 80 °C series obtained by TG up to 500 °C

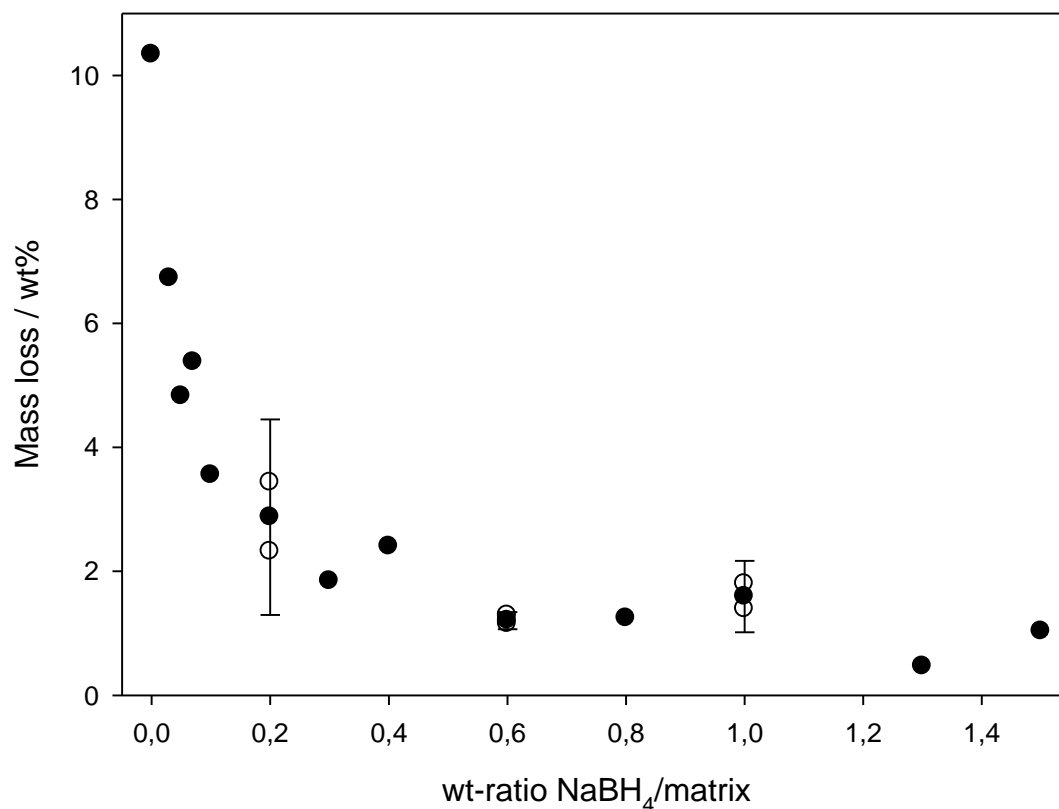| NaBH$_4$/matrix wt-ratio	Mass loss / wt%
- (0)	8.927
0.03	5.632
0.05	3.973
0.07	3.568
0.1	2.340
0.2*	3.012
0.3	1.646
0.4	2.691
0.6	3.122
0.8	2.150
1.0	3.664
1.3	1.985
1.5	1.897

The DTA curves of the 80 °C series show a very similar developing compared to the 120 °C series. In the following Figures (44 to 46) the DTA curves are shown for the heating phase, only. Starting with the hydro-sod (NaBH$_4$/matrix 0.0); the endothermic signals are visible at the same temperatures like in the 120 °C series. They occur at about 50 °C, 120 °C and 210 °C. The signal at 120 °C occurs more broad in the 80 °C series. With only small amounts of NaBH$_4$ used, the signals become less distinct. From a NaBH$_4$/matrix wt-ratio of 0.03 to 0.1, as shown in Figure 44, the three signals seem to decrease in their intensities and become harder to be resolved properly.

Figure 44: DTA curves of the 80 °C series, samples with NaBH$_4$/matrix wt-ratio from 0.0 to 0.1. The signals are shown for the heating procedure, only.

With further increased NaBH$_4$/matrix wt-ratio this trend proceeds. At ratios of 0.2 and 0.3 the signal at 120 °C is still visible while the 210 °C signal becomes more indifferent. At ratios of 0.4 and 0.6 the signal at 120 °C shows a further reduced intensity. At the same ratios the effect at 50 °C shows an increase in intensity. The signal at 210 °C is only minor visible.
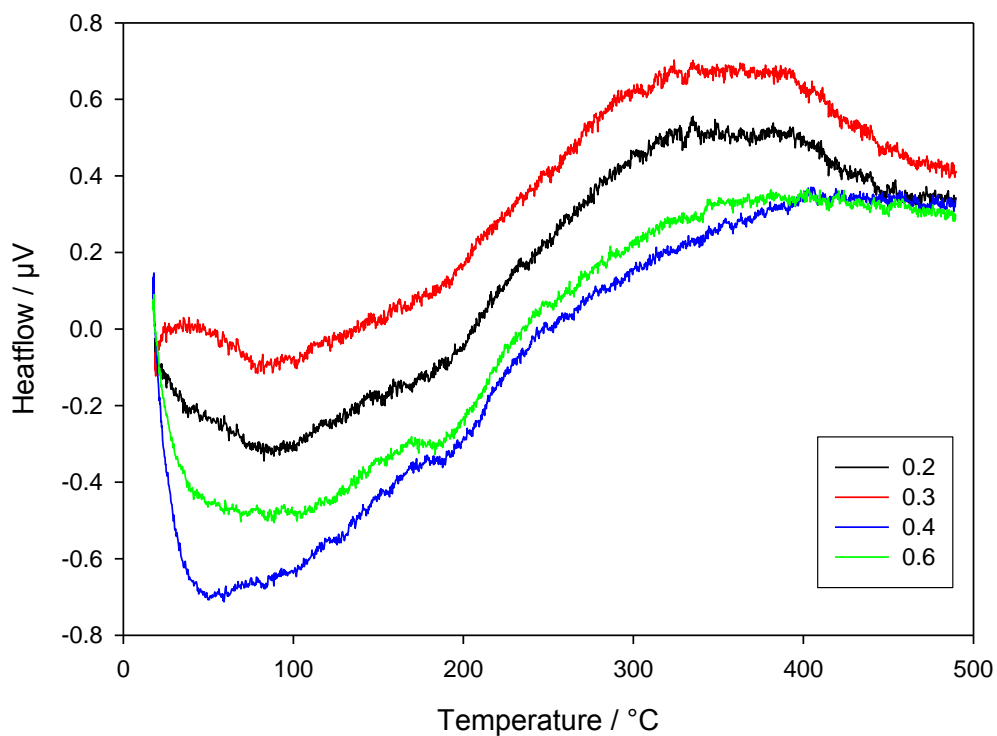
Figure 45: DTA curves of the 80 °C series, samples with NaBH$_4$/matrix wt-ratio from 0.2 to 0.6. The signals are shown for the heating procedure, only.

The DTA curves of the NaBH$_4$/matrix ratios from 0.8 to 1.5 of the 80 °C series are shown in Figure 46. They exhibit the same developing as the 120°C series; the signals at 120 and 210 °C are not visible anymore. The effect at 50 °C clearly exists and becomes more pronounced with increasing NaBH$_4$/matrix wt-ratio.
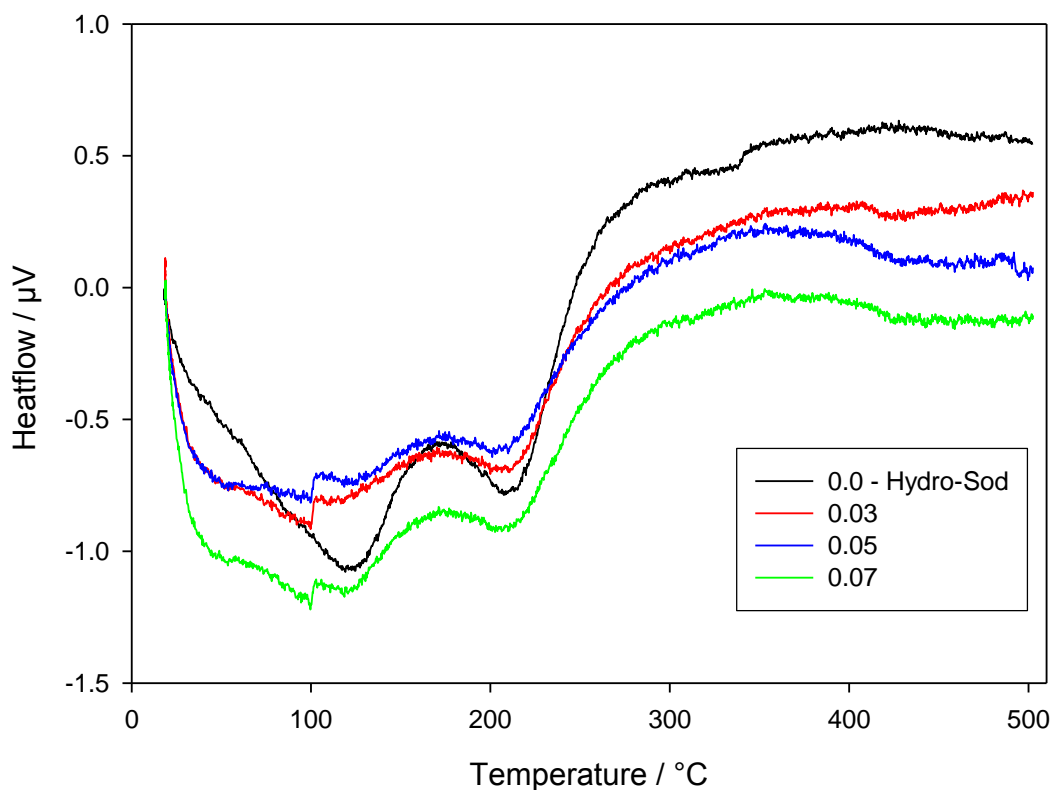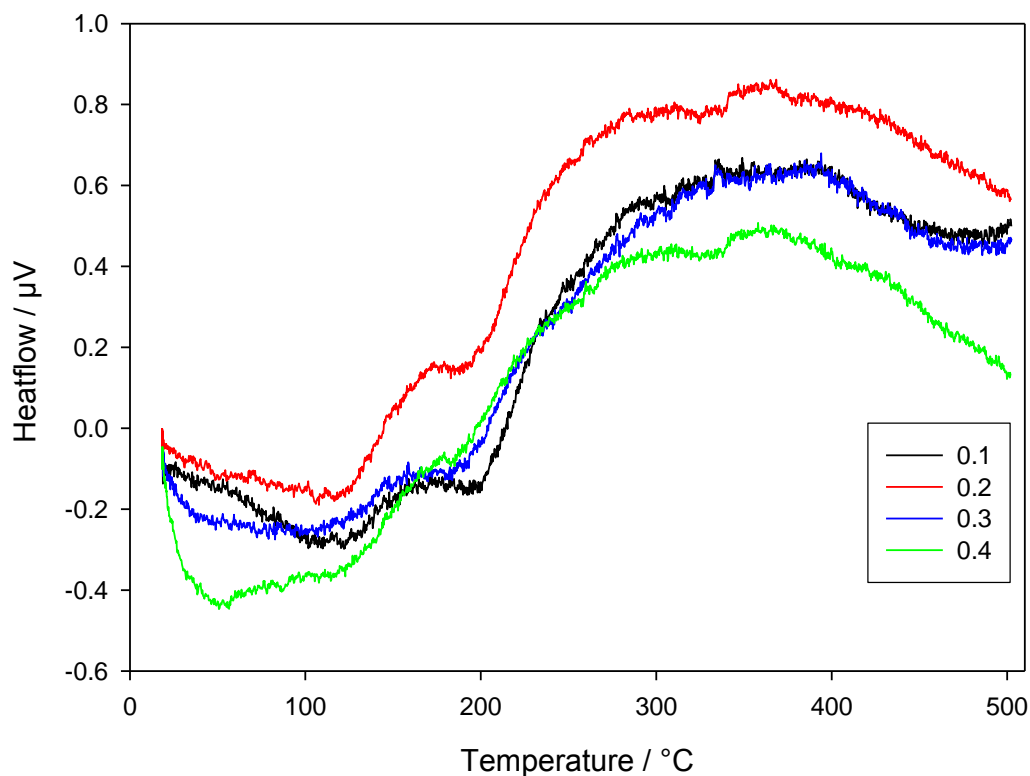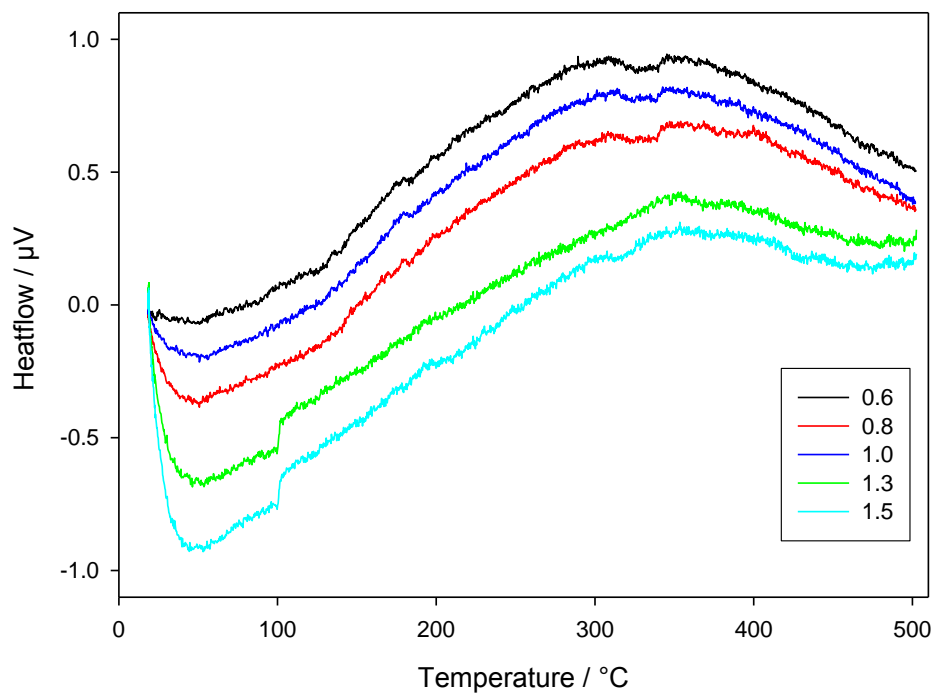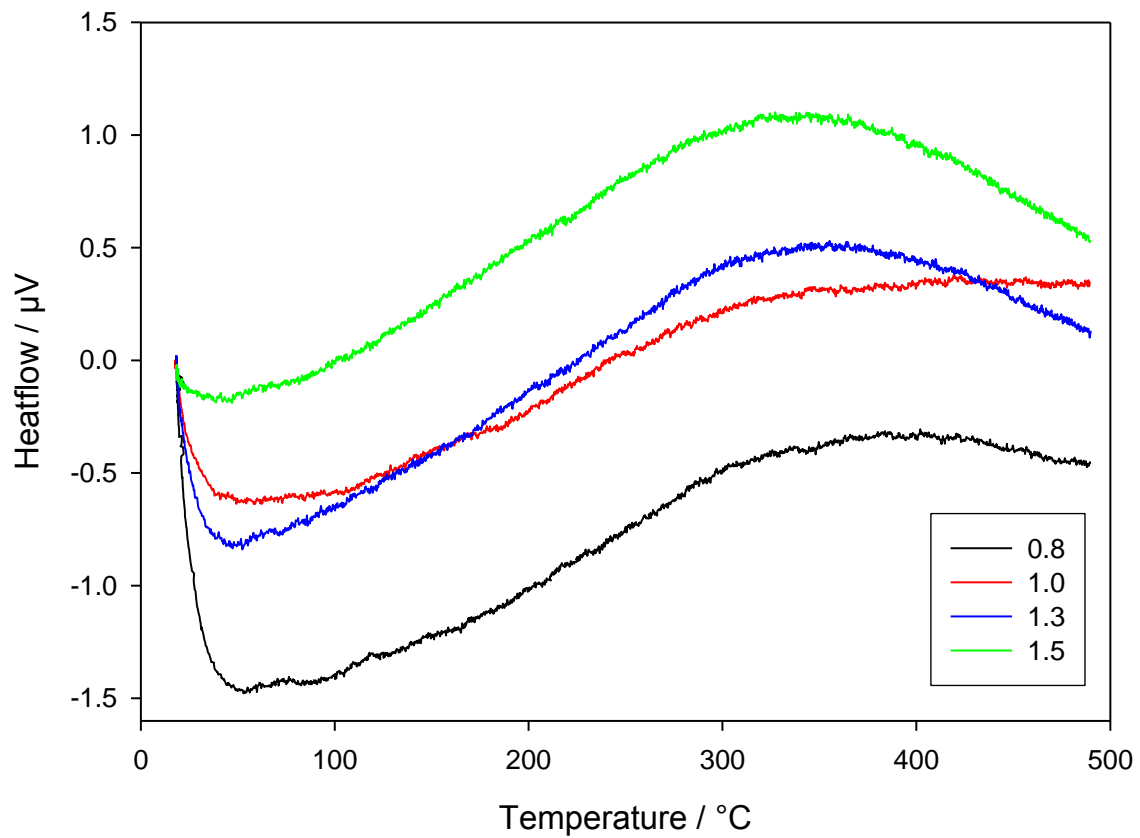
Figure 46: DTA curves of the 80 °C series, samples with NaBH$_4$/matrix wt-ratio from 0.8 to 1.5. The signals are shown for the heating procedure, only.

5.3. NaBH$_4$-Sodalite 60 °C 'nano'

This synthesis batch was synthesized, as described in Chapter 3.1.2., following the changed synthesis way without kaolin. The reactants were chosen to receive a molar Si/Al ratio of 1.0 just as by the use of kaolin. In Table 30, the sample names, their NaBH$_4$/matrix ratios and the reactants used are summarized.

Table 30: Sample overview of the 60 °C sodalite synthesis batch: Variation of the NaBH$_4$/matrix ratio

Sample 60 °C	NaBH$_4$ / g	Na$_2$SiO$_3$ / g	NaAlO$_2$ / g	NaBH$_4$/matrix wt-ratio
L_0.0_nano	0	1.2	0.8	- (0)
L_0.05_nano	0.1	1.2	0.8	0.05
L_0.1_nano	0.2	1.2	0.8	0.1
L_0.2_nano	0.4	1.2	0.8	0.2
L_0.3_nano	0.6	1.2	0.8	0.3
L_0.4_nano	0.8	1.2	0.8	0.4
L_0.8_nano	1.6	1.2	0.8	0.8
L_1.3_nano	2.6	1.2	0.8	1.3

5.3.1. XRD

The synthesis series was analyzed by x-ray diffraction, using the *Bruker D4* diffractometer and with measuring parameters, given in Table 23. The obtained diffractograms are shown in Figures 47 to 49. In this series, it becomes obvious, that with increasing NaBH$_4$/matrix wt-ratio different zeolite species crystallize. For low NaBH$_4$/matrix ratios, the diffractograms show mainly zeolite A and an amorphous phase, indicated by the broad intensity below the reflexes. Only small amounts of the aimed for sodalite can be seen. With increasing NaBH$_4$/matrix wt-ratio, the amount of sodalite increases, relative to the zeolite A, while the amount of amorphous material seems to remain constant. Above a NaBH$_4$/matrix ratio of 0.8, there is no significant amount of zeolite A remaining. This effect is best visible at the reflexes of LTA (Linde Typ A, zeolite A) at 7.2, 10.2, 12.4 and 16.1 and the SOD-reflex at 14.1 °2θ (see Fig. 47 to 49).
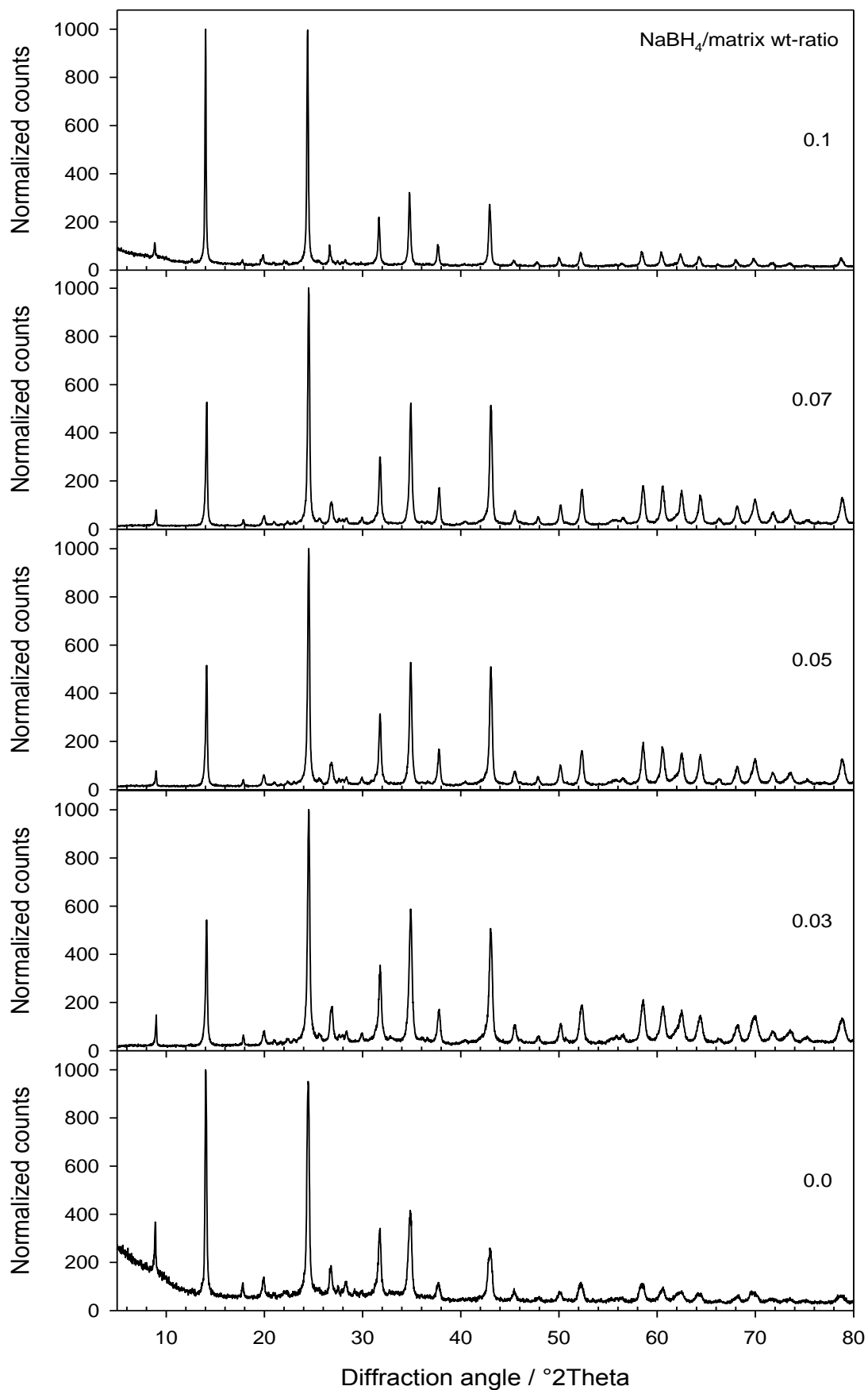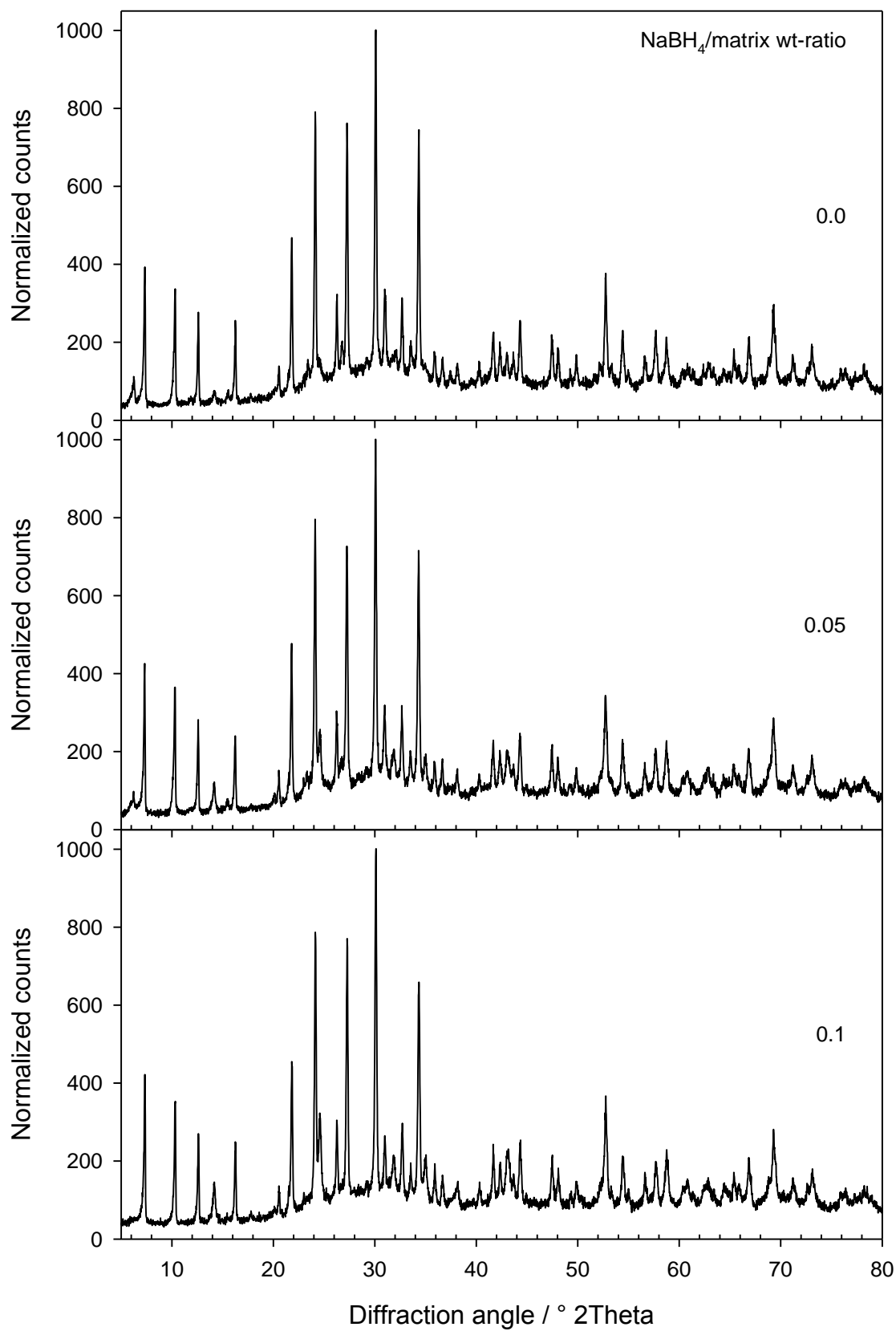
Figure 47: X-ray diffractograms of the 60 °C series with NaBH$_4$/matrix wt-ratios from 0.0 to 0.1 from top to bottom
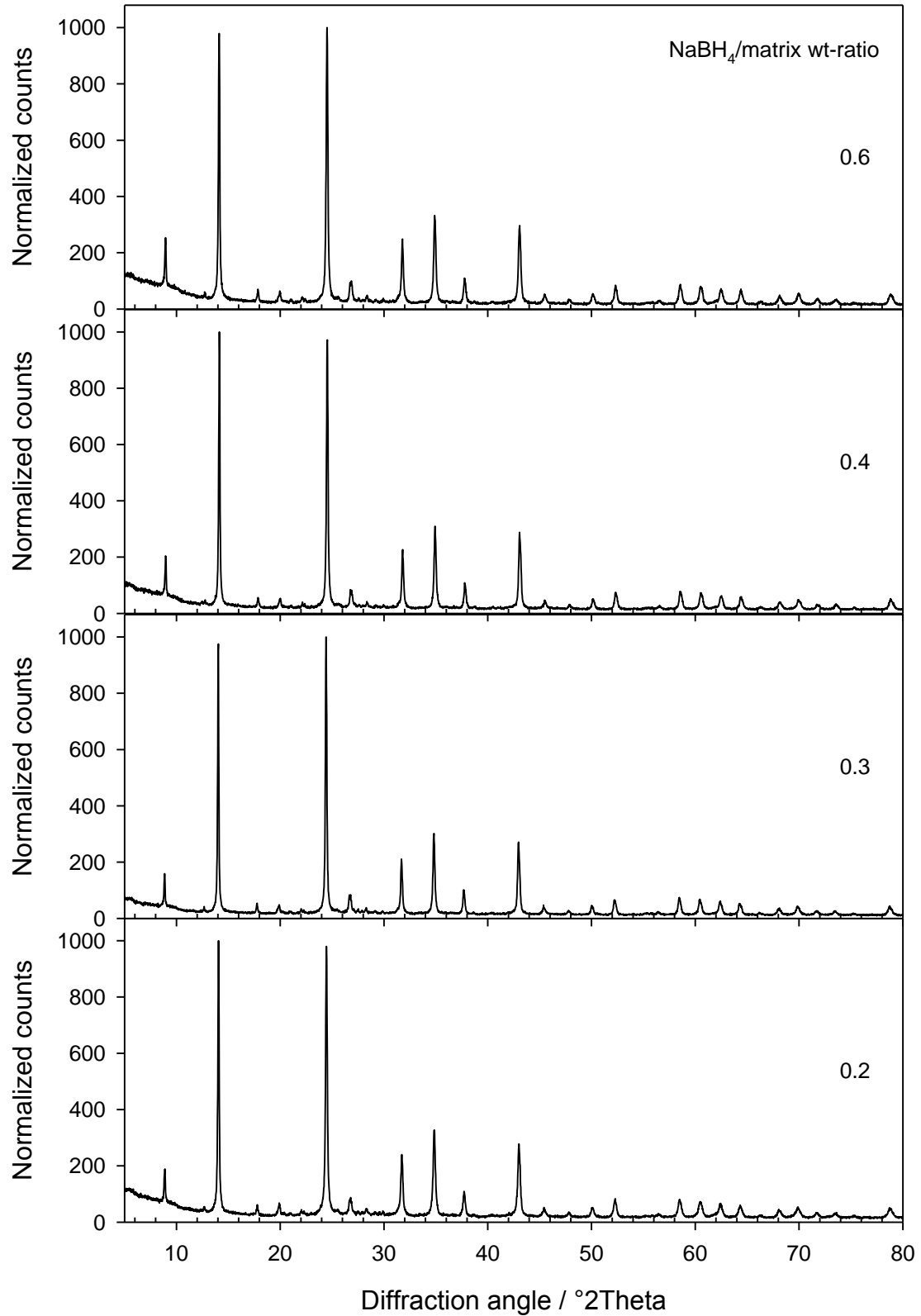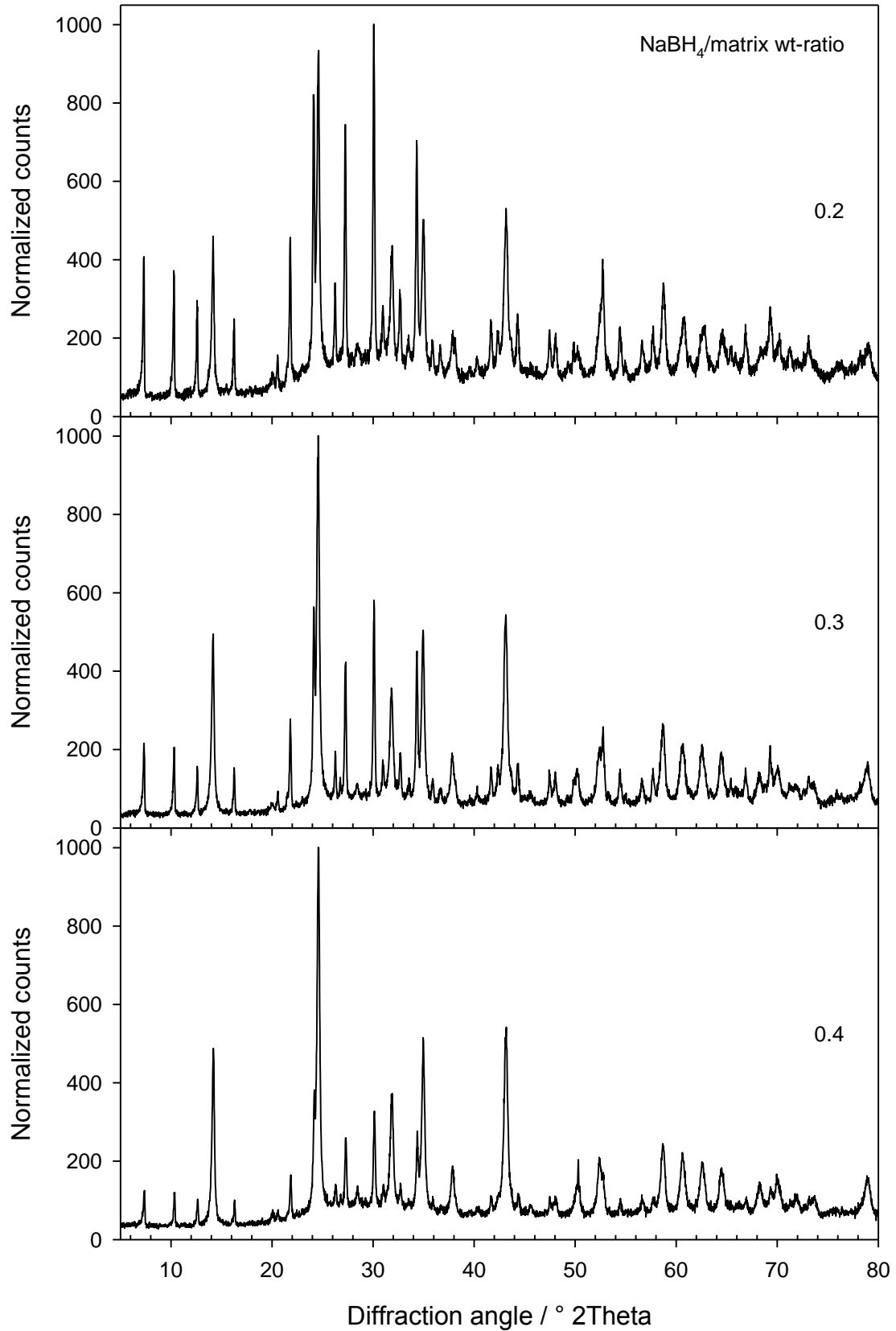
Figure 48: X-ray diffractograms of the 60 °C series with NaBH$_4$/matrix wt-ratios from 0.2 to 0.4 from top to bottom
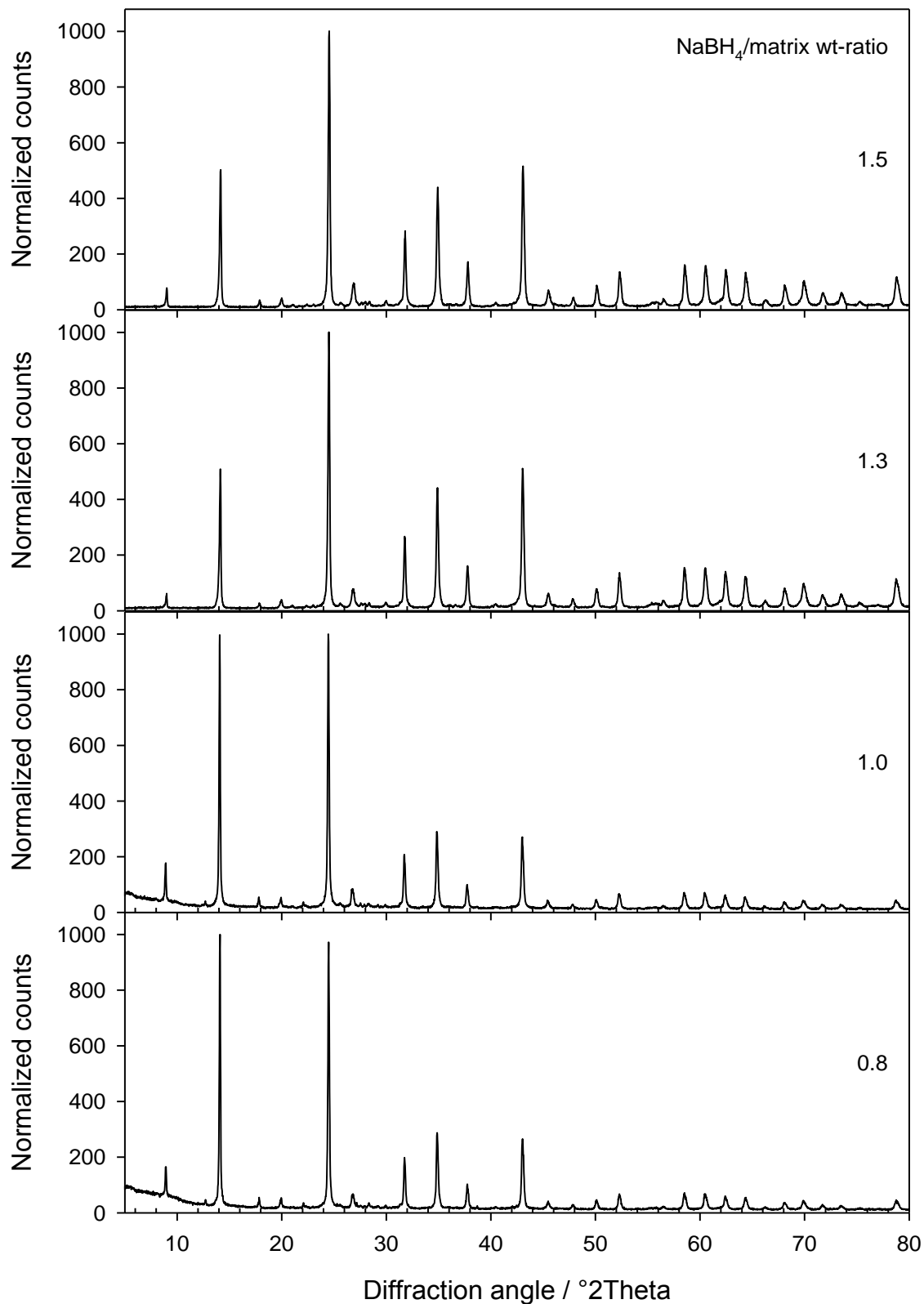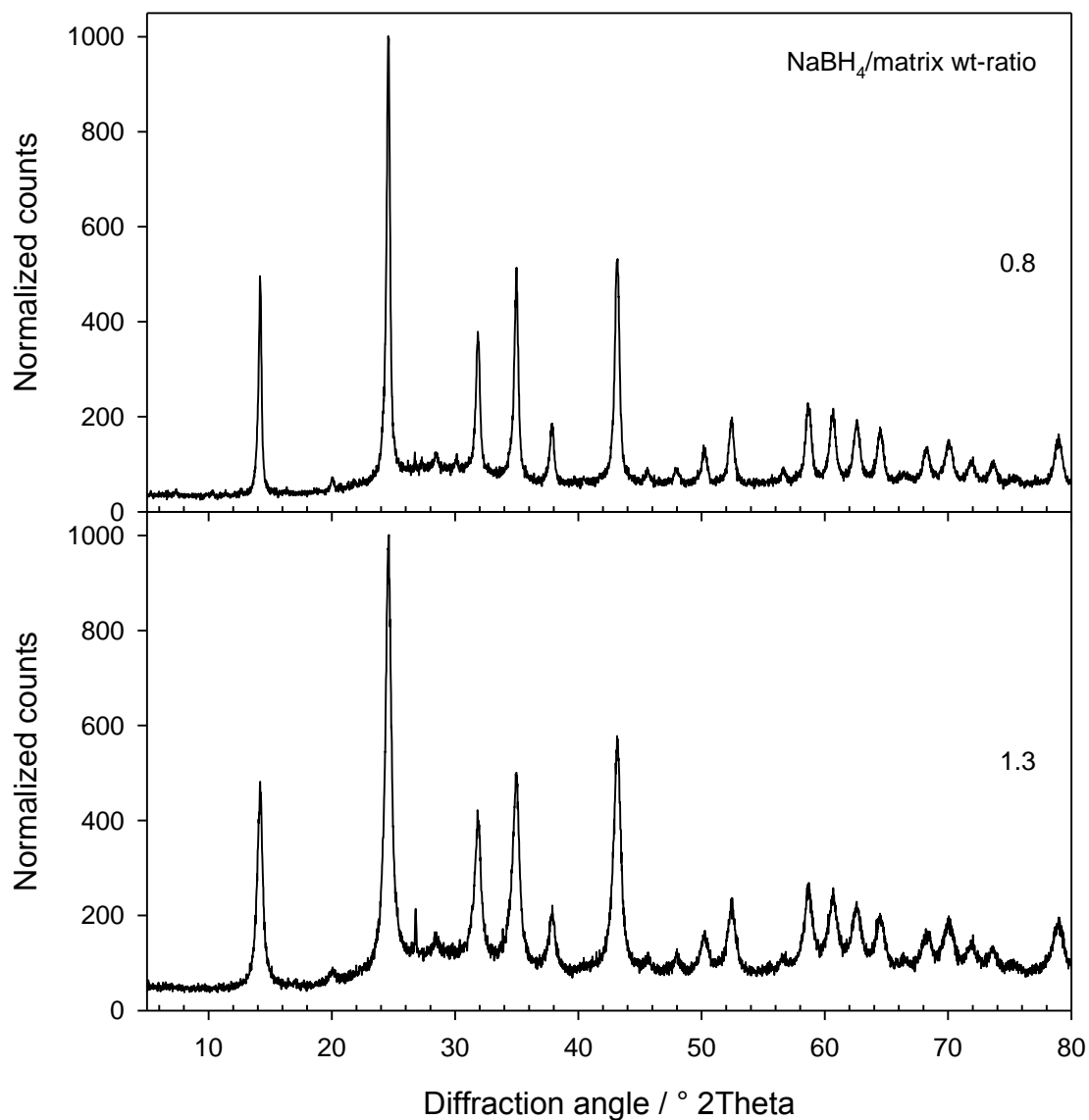
Figure 49: X-ray diffractograms of the 60 °C series with NaBH$_4$/matrix wt-ratios of 0.8 (top) and 1.3 (bottom)

In Figure 50, as reference the normalized diffractograms of LTA (black) and sodalite (red) are shown together.
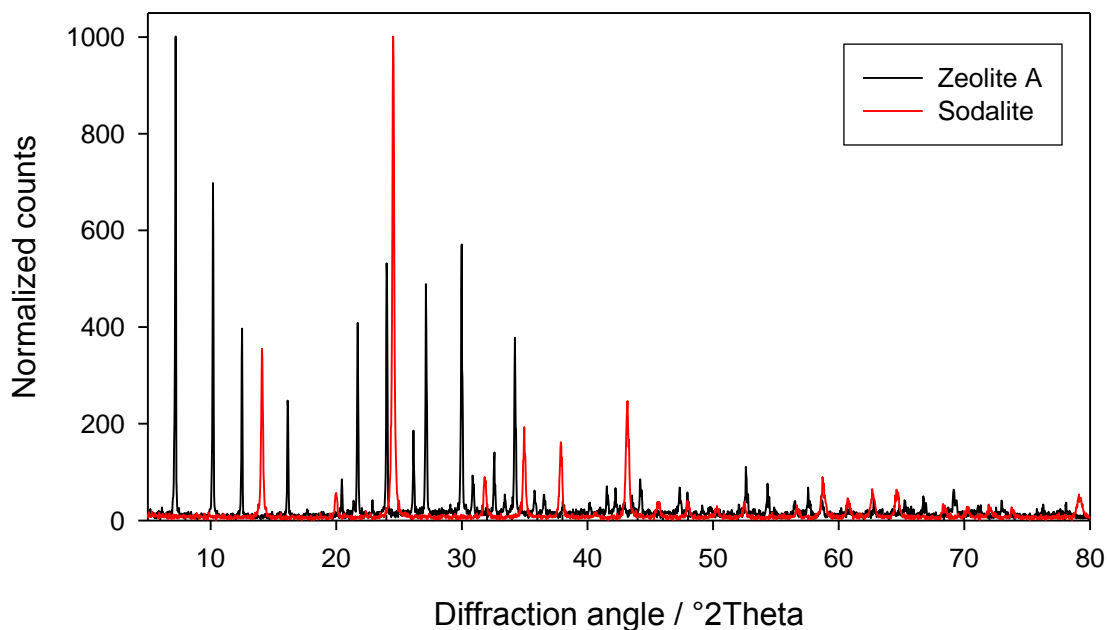
Figure 50: Comparison of zeolite A(black) and sodalite(red) x-ray diffraction pattern

5.3.2. FTIR

FTIR spectroscopy shows that the 60 °C samples are very different compared to the two other synthesis batches (Fig. 51). The blank sample, without any $NaBH_4$ shows aluminosilicate framework bands at 380, 460, 555 and 990 cm^{-1} and a broad area between 630 and 810 cm^{-1} with only small peaks. The two peaks at 380 and 555 cm^{-1} are related to zeolite A. Furthermore this sample shows a large signal assigned to molecular water at 1630 cm^{-1} and an huge broad OH-related signal between 2800 and 3700 cm^{-1}. The $NaBH_4$ bearing samples can be divided in three parts: $NaBH_4$/matrix of 0.05 and 0.1 do not show clear framework signals of sodalite but still the zeolite A related bands. Those samples resemble the blank. They show the same framework bands with only a slightly visible, additional shoulder signal at 434 cm^{-1}. Even though the BH_4^--triplet peak at 2242, 2293 and 2387 cm^{-1} is only minor distinctive. For $NaBH_4$/matrix ratios between 0.2 and 0.4 the zeolite A related peaks decrease with increasing $NaBH_4$/matrix. These samples show the known framework bands of sodalite between 630 and 750 cm^{-1} and the double-peak of the δ-TOT-bands δ at 435 and 468 cm^{-1}. These three samples reveal an increase in the BH_4^- related

signals and a new double peak at 1290 and 1315 cm^{-1}, respectively. Only the two samples with the highest NaBH$_4$/matrix ratios of 0.8 and 1.3 show sodalite framework bands without residuals of zeolite A. Those samples exhibit the highest signal intensities of the BH$_4^-$ related bands. They do also show the double peak at 1290 and 1315 cm^{-1}, respectively.
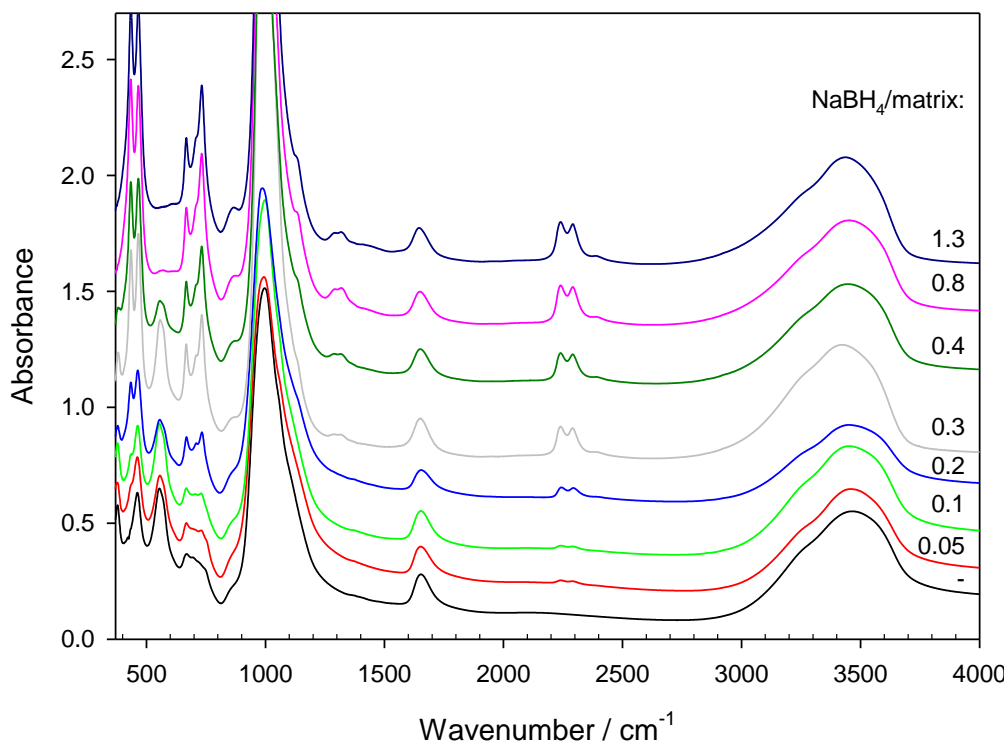
Figure 51: Spectra of representative samples from the 60 °C synthesis batch, shown are increasing NaBH$_4$/matrix ratios from bottom to top.

Due to the additional bands of the zeolite A, the spectra of the 60 °C synthesis-batch cannot be evaluated with the TOT-normalization method, otherwise the integrated intensities of water and BH$_4^-$ would be over-interpreted for NaBH$_4$/matrix ratios below 0.4. Therefore the integrated intensities of water and BH$_4^-$ are normalized by the used sample mass in the pellets, normalized on 1 mg. The data obtained are displayed in Figure 52, due to the mass-normalization the error bars are increased, especially for the molecular water signals. For the BH$_4^-$ intensities the NaBH$_4$/matrix ratios can be divided in the same three areas as before: The blank sample and the NaBH$_4$/matrix ratios of 0.05 and 0.1 show almost no imbedded NaBH$_4$. For the samples with zeolite A and sodalite framework structures (NaBH$_4$/matrix 0.2

to 0.4) show increasing intensities correlated to the $NaBH_4$/matrix ratios. While the samples with sodalite framework structures only ($NaBH_4$/matrix = 0.8 and 1.3) show the highest BH_4^- intensities but no further increase with increasing $NaBH_4$/matrix ratio.

Evaluation of the water band intensities shows a more or less constant amount of water in the samples, independent of the $NaBH_4$/matrix ratio.
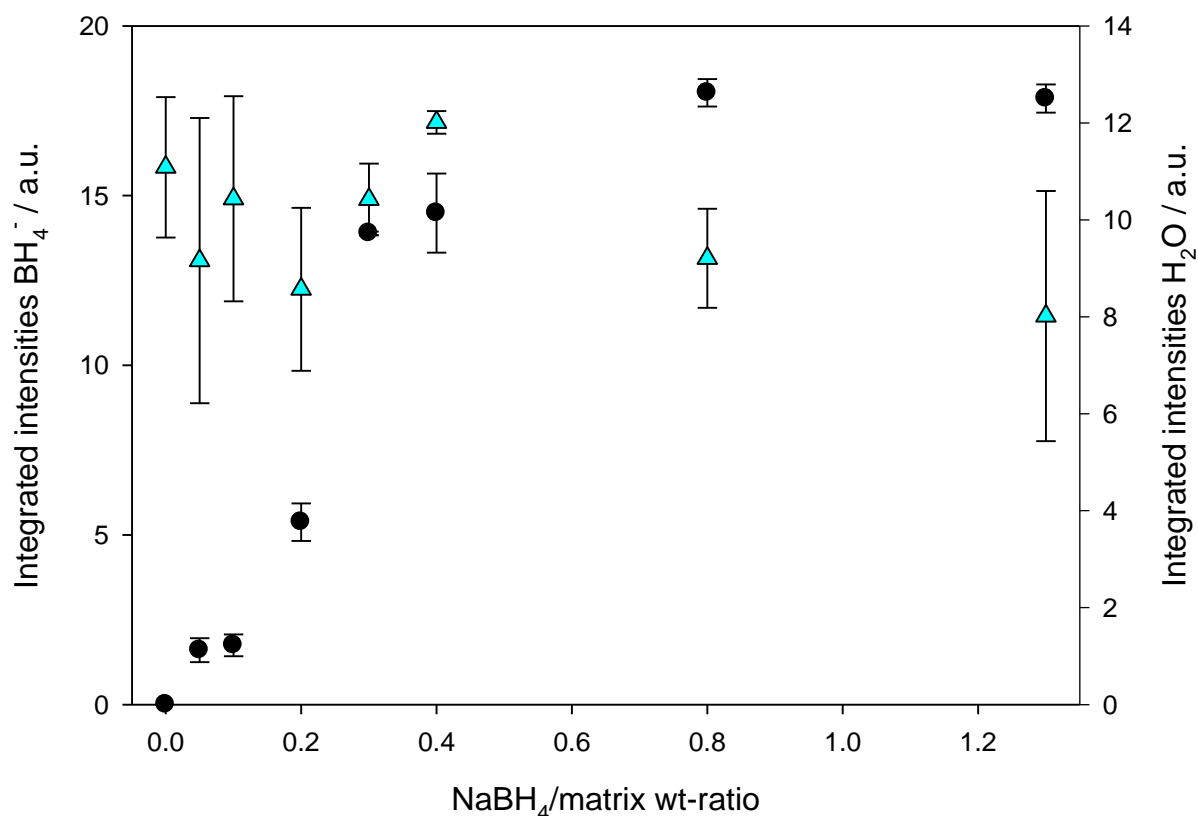
Figure 52: Shown are the average integrated intensities (filled) of BH_4^- (black circles) and water (cyan triangles) as function of the $NaBH_4$/matrix ratio for the 60 °C synthesis batch, the error bars represent 2·σ. These intensities are normalized on the sample mass.

5.3.3. TG/DTA

Thermogravimetric data up to 500 °C reveal a decreasing mass loss with increasing $NaBH_4$/matrix ratio, see Figure 53 and Table 31. The blank sample without $NaBH_4$ loses 14.5 wt%, the further samples show a linear function of the mass loss till a $NaBH_4$/matrix ratio of 0.4. The three samples with the $NaBH_4$/matrix ratio of 0.4, 0.8 and 1.3 show an almost constant mass loss of about 8 wt%.
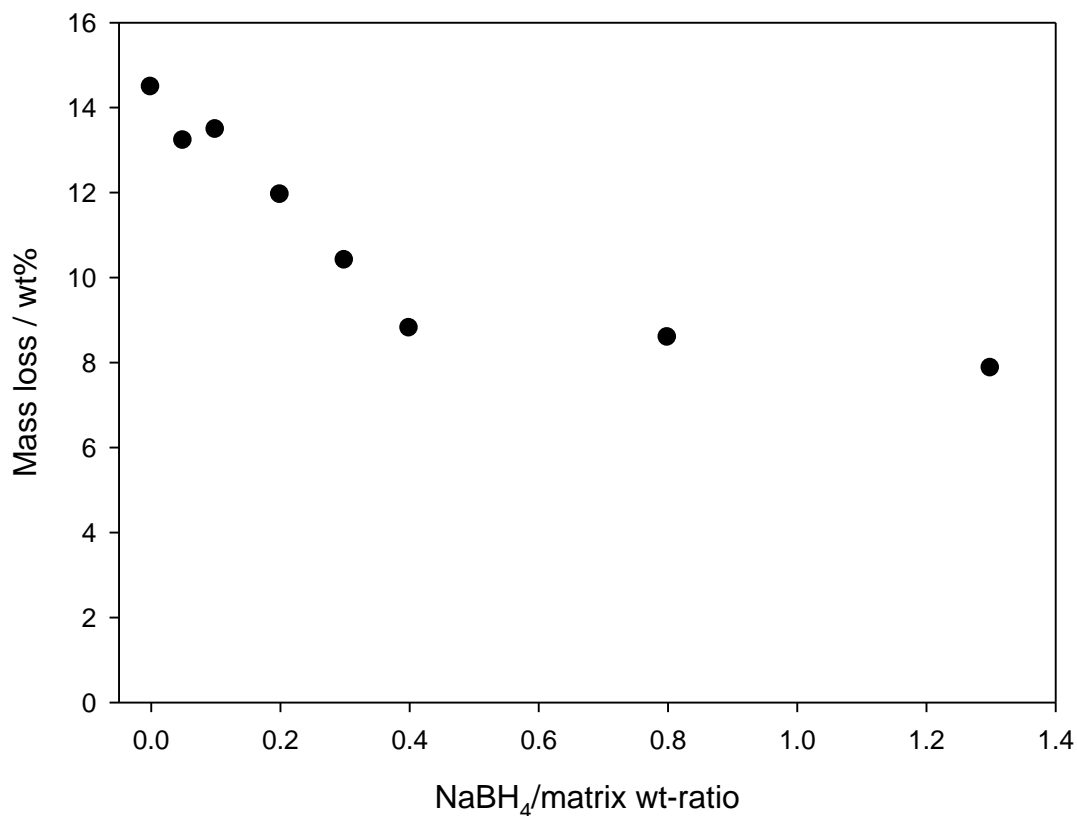
Figure 53: Shown is the mass loss of the synthesis batch 60 °C during TG/DTA measurements up to 500 °C as function of the NaBH₄/matrix ratio.

Table 31: Summarized mass losses of the 60 °C series up to 500 °C obtained by TG

NaBH$_4$/matrix wt-ratio	Mass loss / wt%
- (0)	14.478
0.05	13.217
0.1	13.479
0.2	11.944
0.3	10.397
0.4	8.799
0.8	8.582
1.3	7.862

The DTA curves of this series are divided in the NaBH$_4$/matrix from 0.0 to 0.4 in Figure 54 and 0.8 and 1.3 in Figure 55 to concern the different reaction products; zeolite A, sodalite and a coexistence of both, as described before. The data of this series are

significantly different to the two other series. Samples with $NaBH_4$/matrix ratio from 0.0 to 0.2 show two endothermic signals. The first effect is visible as plateau around 50 °C the second and stronger signal is located at 125 °C. With further increased $NaBH_4$/matrix ratio, the second signal seems to become broader and its position is slightly shifted to lower temperatures below 120 °C. The two samples with $NaBH_4$/matrix ratios of 0.3 and 0.4 possibly show an additional effect; the curves decrease above temperatures of 380 °C.
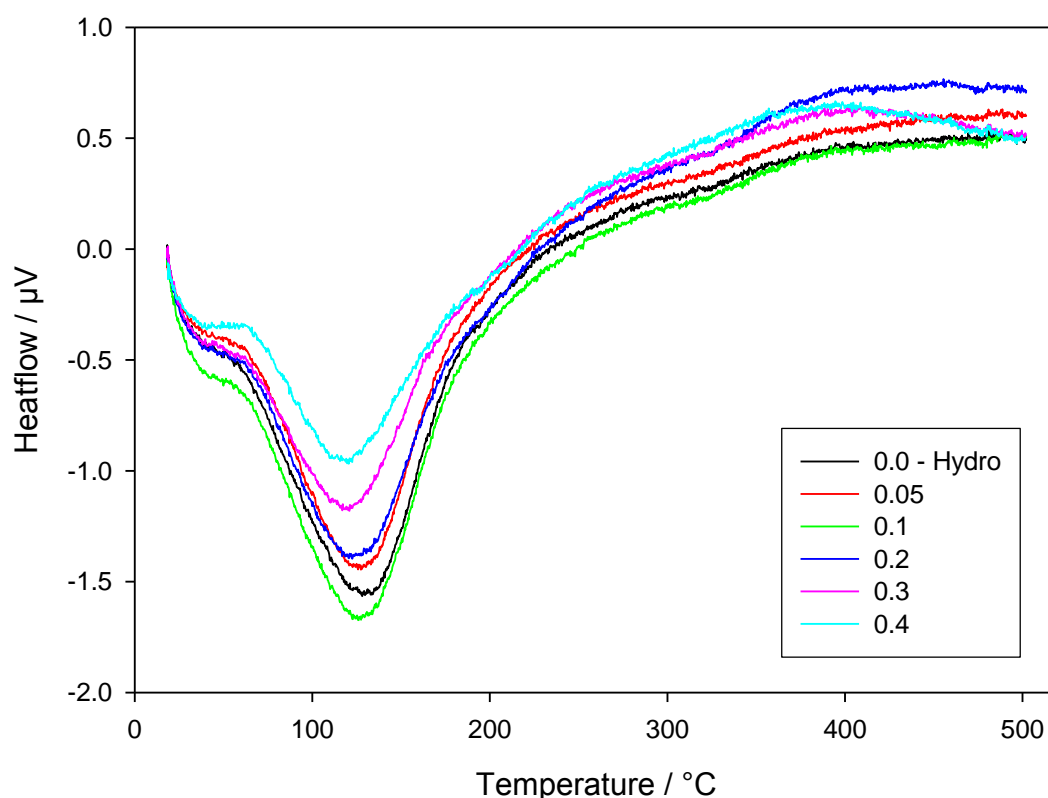
Figure 54: DTA curves of the 60 °C series, samples with NaBH₄/matrix wt-ratio from 0.0 to 0.4. The signals are shown for the heating procedure, only.

Figure 55 shows the DTA signals of the sodalite samples of this series. The curves are similar to the 0.3 and 0.4 ratio samples but the effects are more pronounced with the higher $NaBH_4$/matrix ratios. The broadening effect of the second endothermic signal increases to a small plateau at its minimum, starting below 100 °C. Both samples also show the decrease of the curve above 380 °C.
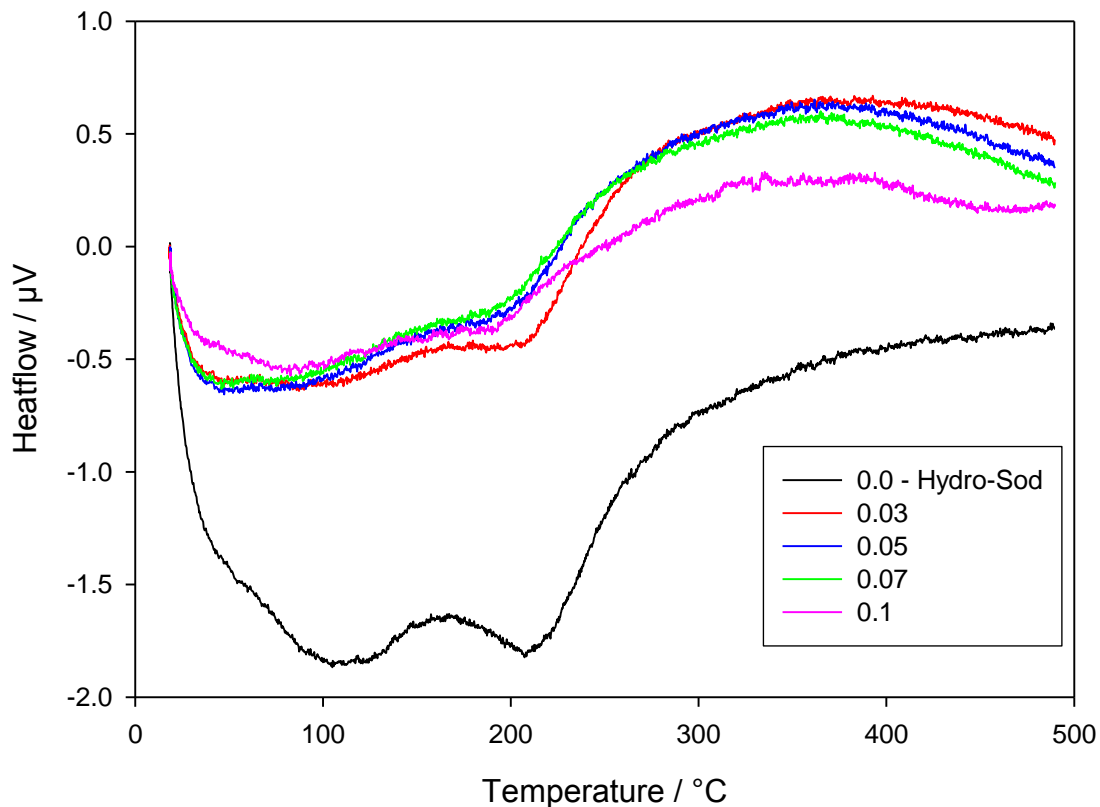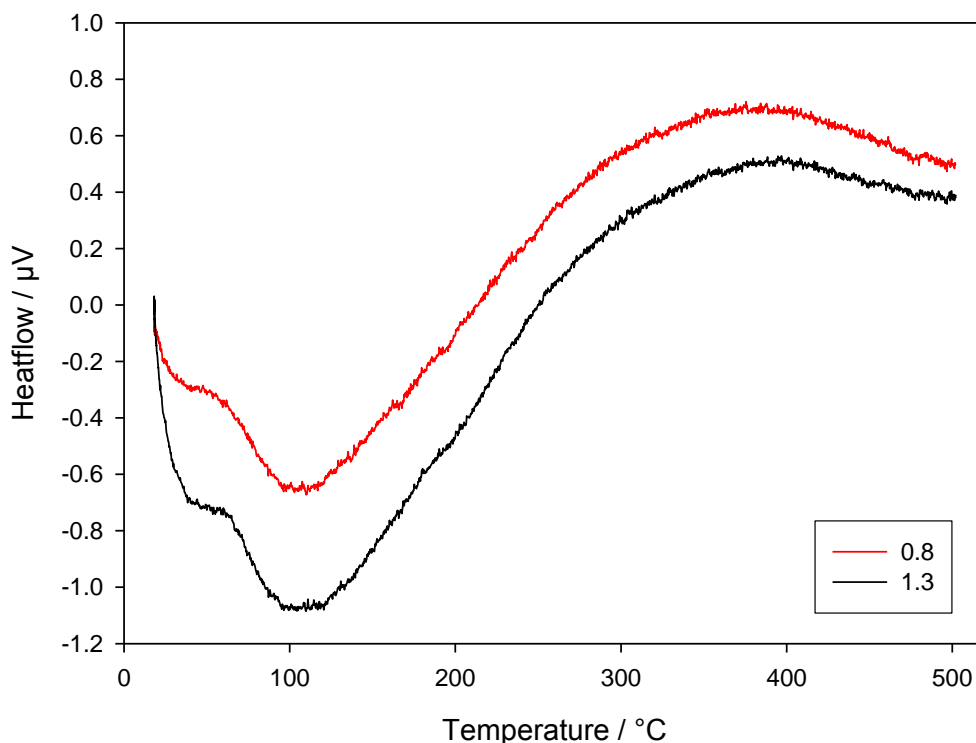
Figure 55: DTA curves of the 60 °C series, samples with NaBH$_4$/matrix wt-ratios of 0.8 and 1.3. The signals are shown for the heating procedure, only.

5.4. Additional Analyses NaBH$_4$-Sodalite

In this chapter the results of additional analyses are presented. Those analyses were performed for selected samples only, in order to gain information on the general behavior of the system.

5.4.1. Particle Size Analysis Sodalite

The morphological particle size analysis was carried out, using BSE images of the synthesis batches, obtained by a *JEOL JSM-6390 A* SEM. The images were evaluated with the freeware *ImageJ* [35]. This program is able to measure lines or areas, which are plotted in an image. The absolute values are calculated using the given scale of the BSE-image. Two lines (diameter) were plotted per particle for an estimate of an average size of the morphological particles. A valid statistical distribution could be obtained using six images for each sample and evaluating 224 to 428 particles. In Figure 56, the particle size distribution is

shown and Table 32 summarizes the median and average values of the particle sizes for the three synthesis batches.
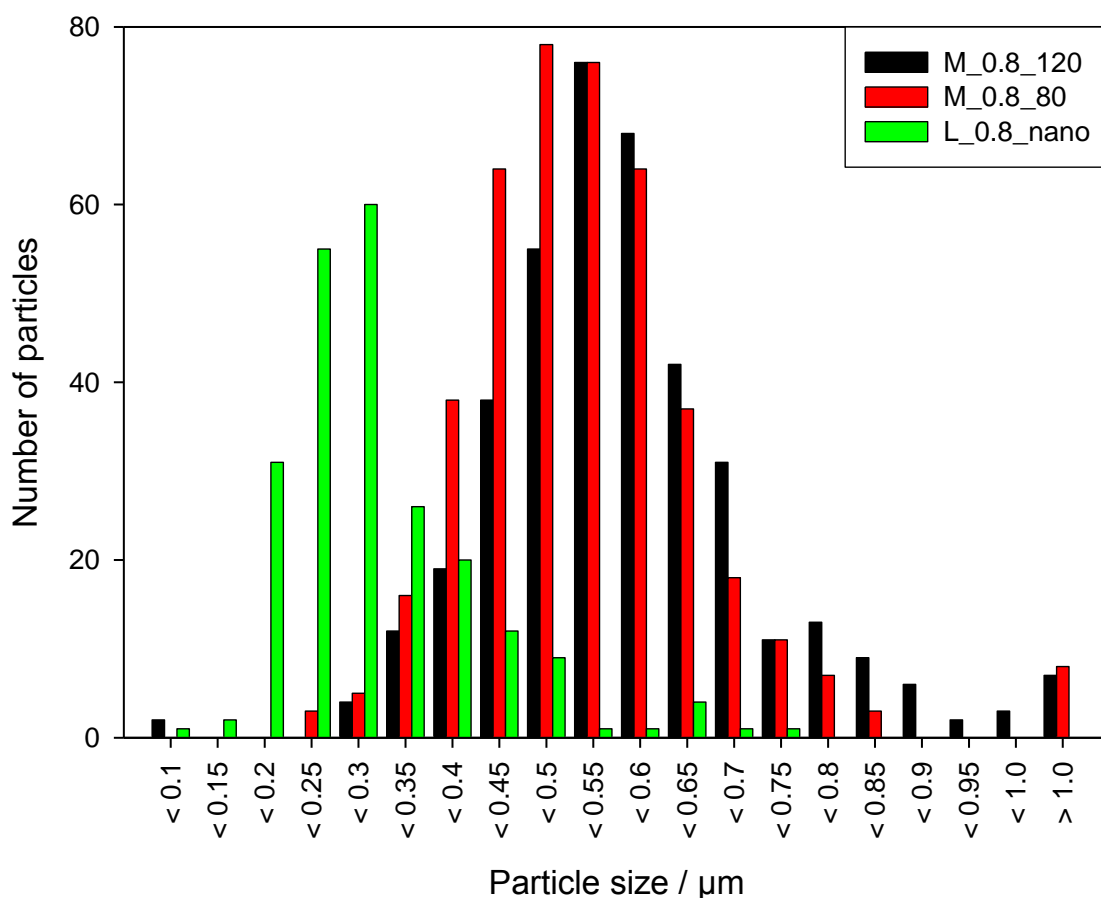
Figure 56: Graphical distribution of the quantity of particles as function of their size for one NaBH$_4$/matrix ratio of each of the three synthesis batches.

Table 32: Summarized results of particle sizes, obtained from BSE-pictures evaluated using _ImageJ_ for three samples with identical NaBH$_4$/matrix ratios but different synthesis temperatures

Synthesis	Median particle size	Average particle size	Number of analyzed particles
M_0.8_120	0.548 µm	0.564 µm	398
M_0.8_80	0.509 µm	0.525 µm	428
L_0.8_nano	0.268 µm	0.289 µm	224

In Figure 57 a-c exemplarily BSE pictures of the three synthesis series are shown. It is obvious that the 60 °C synthesized particles are of smaller size compared to the two other

series. The 120 °C particles occur more homogenous in their particle size, while the 60°C and 80 °C series show several very big particles. The particle shape is throughout the series very similar; the particles occur mainly round, sometimes with corners up to a flattened octagon shape.
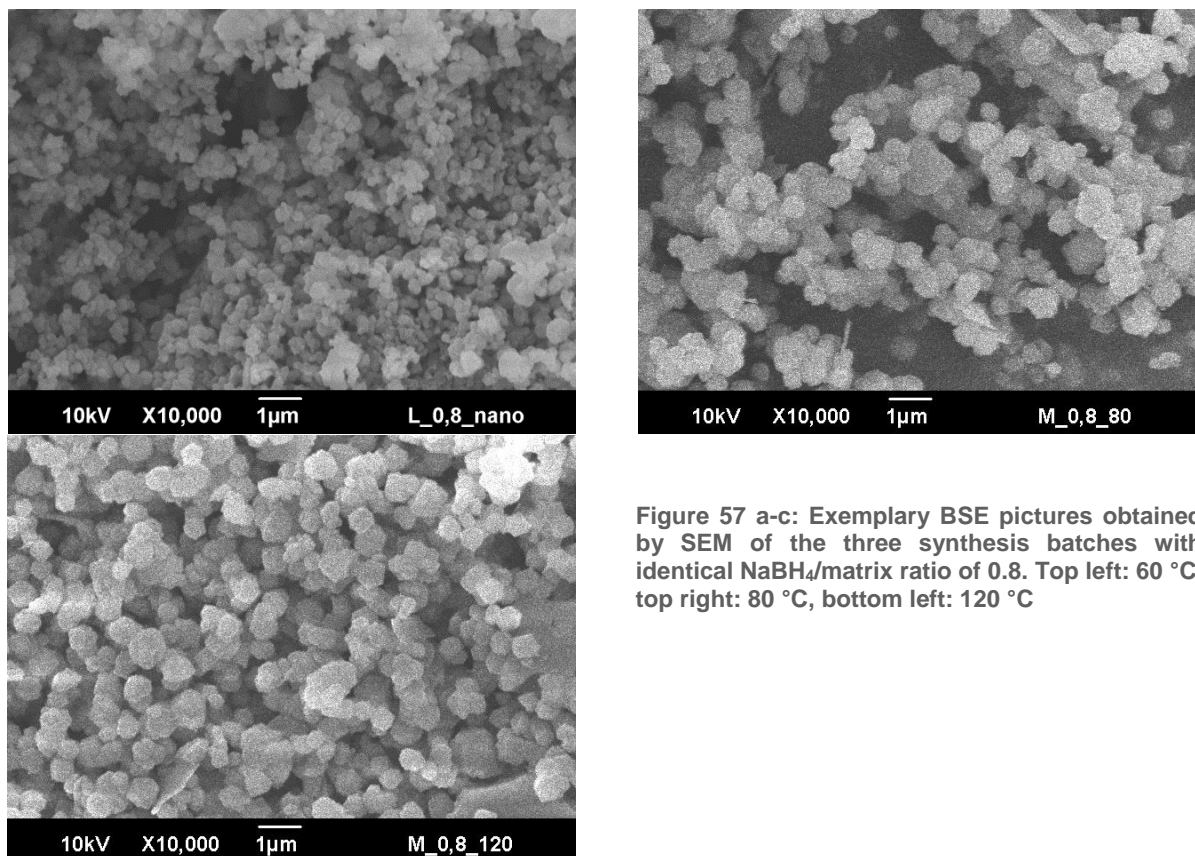
Figure 57 a-c: Exemplary BSE pictures obtained by SEM of the three synthesis batches with identical NaBH$_4$/matrix ratio of 0.8. Top left: 60 °C, top right: 80 °C, bottom left: 120 °C

5.4.2. Hydrogen Release BH$_4$-Sod

The dependency of the volume of released hydrogen as a function of NaBH$_4$/matrix wt-ratio for samples of the 120 °C synthesis batch are shown. The values show an exponential trend (Figure 58): the volume of the released hydrogen increases with increasing NaBH$_4$/matrix ratio, reaching a limit value at NaBH$_4$/matrix ratio above 0.6 of about 180 ml hydrogen per gram sample. The samples with NaBH$_4$/matrix ratios of 0.03 and 0.05 did not show measurable amounts of hydrogen.
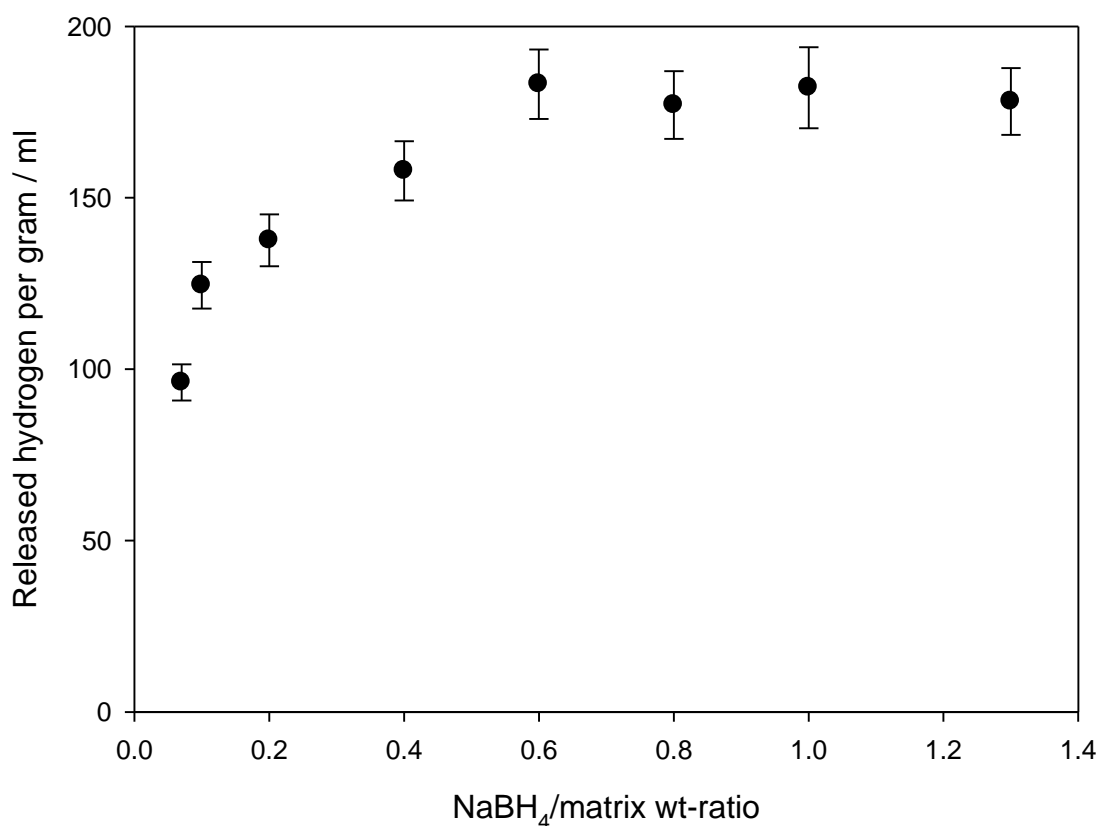
Figure 58: Released hydrogen per gram sample as function of the NaBH$_4$/matrix ratio for the synthesis batch 120 °C. Error bars calculated as described in 3.5.1.

Back-calculations

The results of the back-calculations (summarized in Table 33) show that not more than about 70 mg of NaBH$_4$ can be incorporated per gram sample. The effectively enclosed amount of NaBH$_4$ decreases with increasing NaBH$_4$/matrix wt-ratio.

Table 33: Results of back-calculations of 120 °C-samples from hydrogen release experiments

Sample	H_2 released per gram sample / ml	Mass $NaBH_4$ in sodalite per gram / mg	Mass $NaBH_4$ used during synthesis per gram / mg	Effectively enclosed $NaBH_4$ / wt%
L_0.07_120	96.1	37.78	65	58.13
SE_0.1_120	124.5	48.92	91	53.76
M_0.2_120	137.6	54.09	167	32.39
M_0.4_120	157.8	62.04	286	21.69
M_0.6_120	183.1	71.98	375	19.20
M_0.8_120	177.1	69.60	444	15.68
M_1.0_120	182.1	71.59	500	14.32
L_1.3_120	178.1	70.00	565	12.39

The smallest amount of $NaBH_4$ used during the syntheses, which can be measured by the hydrogen release apparatus (see Fig. 1 in Chapter 3.5.), show an effectively enclosed amount of $NaBH_4$ below 60 %. A compromise between the highest possible amount of stored $NaBH_4$ and efficiency needs to be done depending on the use of the material.

Three samples of identical $NaBH_4$/matrix wt-ratios of 1.3 from the different synthesis batches (Chapter 5.1.; 5.2.; 5.3.) are compared regarding the hydrogen release volume as function of particle size. This ratio was chosen, to make sure, that even the 60 °C sample consists of sodalite particles, only. The results are shown below in Figure 59. The 120 °C sample released 178 ± 9.7 ml of hydrogen per gram, the 80 °C sample 165 ± 9.0 ml per gram and the 60 °C sample released 84 ± 4.6 ml hydrogen per gram sample.
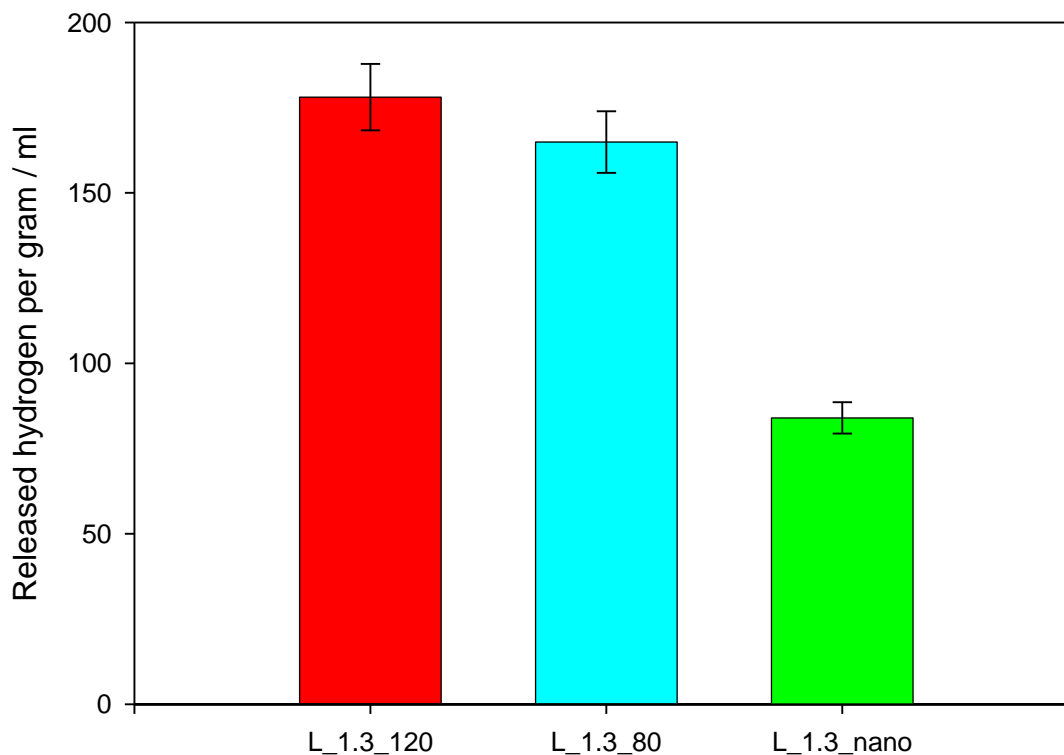
Figure 59: Summarized hydrogen release per gram sample for the three synthesis batches with a constant NaBH$_4$/matrix ratio of 1.3. Errors calculated as described in 3.5.1.

5.4.3. CS-Analyses

Selected samples of the three synthesis series were analyzed. Table 34 summarizes the results of the CS-analyses. The synthesis-series at 120 °C and 80 °C show that the carbon content decreases with increasing NaBH$_4$/matrix wt-ratio. The two hydro-sodalites (NaBH$_4$/matrix = 0.0) have carbon amounts of 0.28 and 0.4 wt%. Samples with the highest NaBH$_4$/matrix ratio show the smallest carbon results with amounts of 0.04 to 0.07 wt%.

The samples of the 60 °C series show throughout the NaBH$_4$/matrix range from 0 to 0.8 a more or less constant amount of Carbon at low values between 0.05 and 0.08 wt%.

Table 34: Summarized results of the CS analyses for the three synthesis series and varied NaBH$_4$/matrix wt-ratios.

Sample	NaBH$_4$/matrix / wt-ratio	Carbon content / wt%	Error / wt%
M_0.0_120	- (0)	0.403	0.0092
L_0.05_120	0.05	0.212	0.0102
L_1.5_120	1.5	0.041	0.0101
M_0.0_80	- (0)	0.284	0.0089
L_0.05_80	0.05	0.171	0.0097
L_1.5_80	1.5	0.073	0.0098
0.0_nano	- (0)	0.078	n. a.
0.4_nano	0.4	0.048	n. a.
0.6_nano	0.6	0.062	n. a.
0.8_nano	0.8	0.066	n. a.

5.4.4. Water Content from KFT

KFT analyses were carried out for selected samples of the 120 °C sodalite series. Samples were analyzed with KFT with an as possible analogous TG-program (20 ml/min He, 20 °C/min heating-cooling rate). The KFT heating device provides some problems; it is not designed to perform constant and relatively low heating rates, especially in the needed temperature range up to 500 °C. The results may have an error due to very high heating rates below 200 °C. The temperature reached 100 °C below one minute and the wanted heating rate of 20 °C/min was realized about above 200 °C.

In Table 35, the obtained mass losses of the TG measurements and the KFT analyses are summarized, together with the given errors of the two methods. The values for the total mass losses range from 6.2 to 1.9 wt% and for the water amount from 5.9 to 1.2 wt%.

Table 35: Summarized results of KFT water amounts and analogous TG mass losses for different NaBH$_4$/matrix ratios

NaBH$_4$/matrix	Mass loss TG / wt%	abs error / wt%	KFT H$_2$O / wt%	abs error / wt%
0.05	6.235	0.002	5.93	0.23
0.1	4.747	0.002	4.77	0.22
0.2	3.737	0.002	3.59	0.22
0.4	2.646	0.002	2.45	0.23
0.6	1.877	0.002	1.20	0.24
1.5	2.008	0.002	1.18	0.21

After each measurement, TG and KFT, the sample material was also analyzed by FTIR to compare the reaction degree, which might explain the differences in the obtained values between the two methods. In Figure 60 and 61, the FTIR spectra are shown for the different NaBH$_4$/matrix ratios before the treatment and after TG and KFT, respectively.
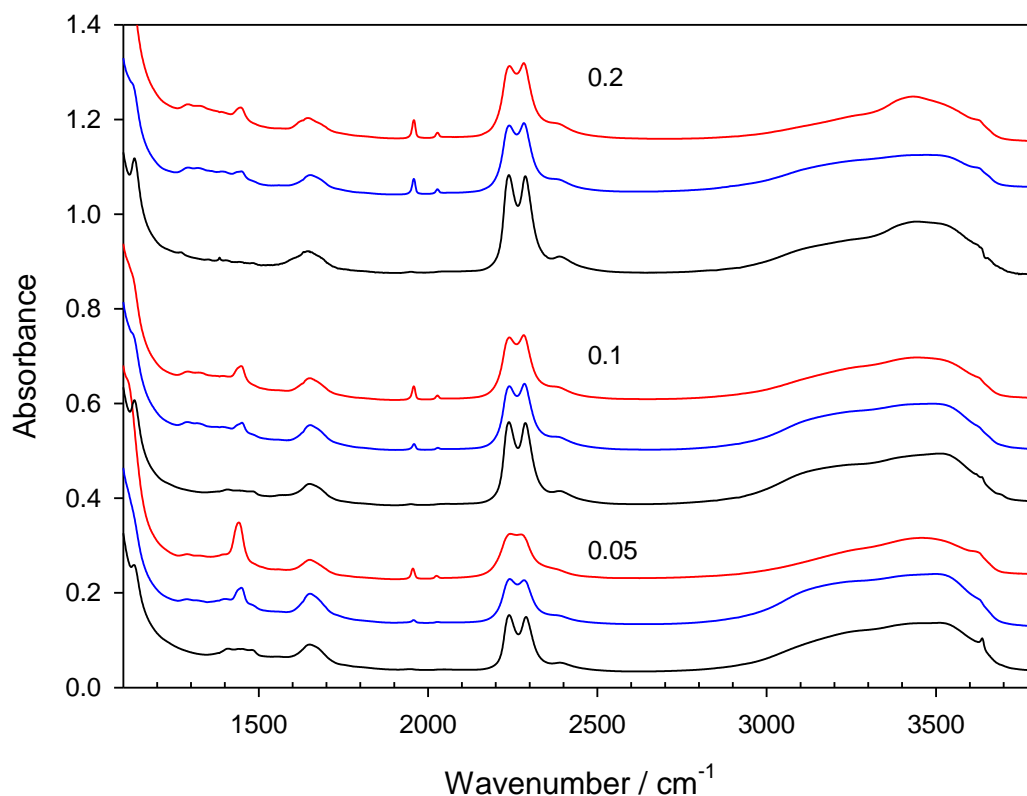
Figure 60: FTIR spectra of the samples with given NaBH$_4$/matrix ratios from 0.05 to 0.2 after TG analyses (red), KFT (blue) and before treatment (black)
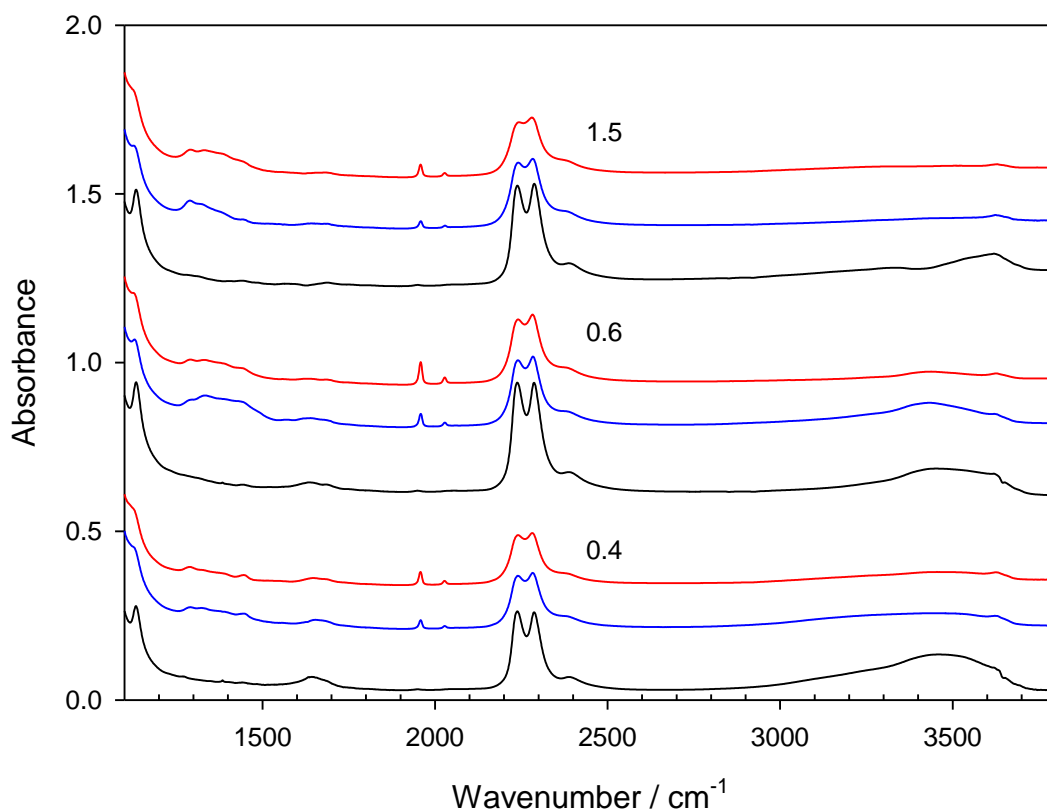
Figure 61: FTIR spectra of the samples with given NaBH$_4$/matrix ratios from 0.4 to 1.5 after TG analyses (red), KFT (blue) and before treatment (black)

The spectra show the already described species, see Chapter 5.1. It is obvious that the spectra after the TG analyses show a higher amount of formed BO_2^-, visible at the higher intensities of the double peak at 1952 and 2023 cm^{-1}. In average, the TG measurements show the double amount of formed BO_2^-, obtained by integrated intensities of the FTIR spectra. The BH_4^- decrease is also higher for the TG measurements but only in average for about 2 %. The spectra of the low NaBH$_4$/matrix wt-ratios show higher amounts of the carbonate related peak at 1450 cm^{-1}, especially visible in the spectra after TG measurements. This effect is probably related to the longer overall reaction time (TG cools down with 20 °C/min, KFT at ambient conditions).

5.5. Discussion BH$_4$-Sodalite

The sodalite matrix itself is well understood and is under research since its discovery by Jaeger in 1929 [63], [64]. In principal the formation of the sodalite structure takes place under mild hydrothermal parameters and a silicate and aluminate source is needed but also a wide variety of different metal cations can substitute aluminum and silicon in the structure [65]–[67]. In the presence of suitable template ions or molecule, the sodalite structure forms from solutions during the hydrothermal reaction around these templates. Various molecules or ions can work as templates, such as H_2O, NO_3^-, CN^- or BH_4^- and several more [68]–[71]. These cage fillings have a strong influence on the structure of the sodalite. The sodalite cages expand, due to the different sizes of the templates, which is possible because of the flexible structure of sodalite. The structural bond lengths and angles can vary in wide range [72], [73]. A direct enclosing of molecular hydrogen in zeolites is also under research but did not show high storage capacities, so far, for example [74].

NaBH$_4$ embedded in sodalite was first described in 2005 by Buhl et al. [26], [75]. Here the principle synthesis was analyzed and improved by the parameters alkalinity, temperature and duration to obtain a pure phase of microcrystalline BH$_4$-sod. In 2010 the next step was done by reducing the particle size of BH$_4$-sod to the so called nano-BH$_4$-sod [76], [77].

During this work, both approaches of the BH$_4$-sod synthesis were combined and complemented by the variation of the NaBH$_4$/matrix wt-ratio. The influences of the variations were analyzed quantitatively for the sodalite samples obtained.

Three synthesis series were carried out with varied NaBH$_4$/matrix wt-ratio at temperatures of 120, 80 and 60 °C. The 120 and 80 °C series were quite similar while the 60 °C series showed a changed behavior in several analyses.

The hydrothermal synthesis always leads to amounts of other enclathrated species like (OH•H$_2$O)$^-$, CO_3^{2-} and H_2O [26], [78], [79] and as shown here by CS analyses, IR and

TG/DTA. It is very likely that these species are enriched in samples with low $NaBH_4$/matrix wt-ratios.

5.5.1. Structure and Synthesis

Figure 62 shows the calculated lattice parameters for sodalite for both synthesis series (80 and 120 °C). Lattice parameters were calculated following symmetry P-43n and are in good agreement with former publications [17], [26]. The lattice parameters show the inverse trend compared to the TOT-positions (see Figure 63); the blank samples ($NaBH_4$/matrix = 0.0) show the highest lattice parameters. With increasing $NaBH_4$/matrix wt-ratio the lattice parameters decrease for both series. Between 0.1 and 0.3 the lattice parameters run through a minimum, with further increased $NaBH_4$/matrix wt-ratio the lattice parameters slightly increase. The 1.3 sample of the 120 °C series shows an unexpected low value for the calculated lattice parameter probably due to impurities during the synthesis.
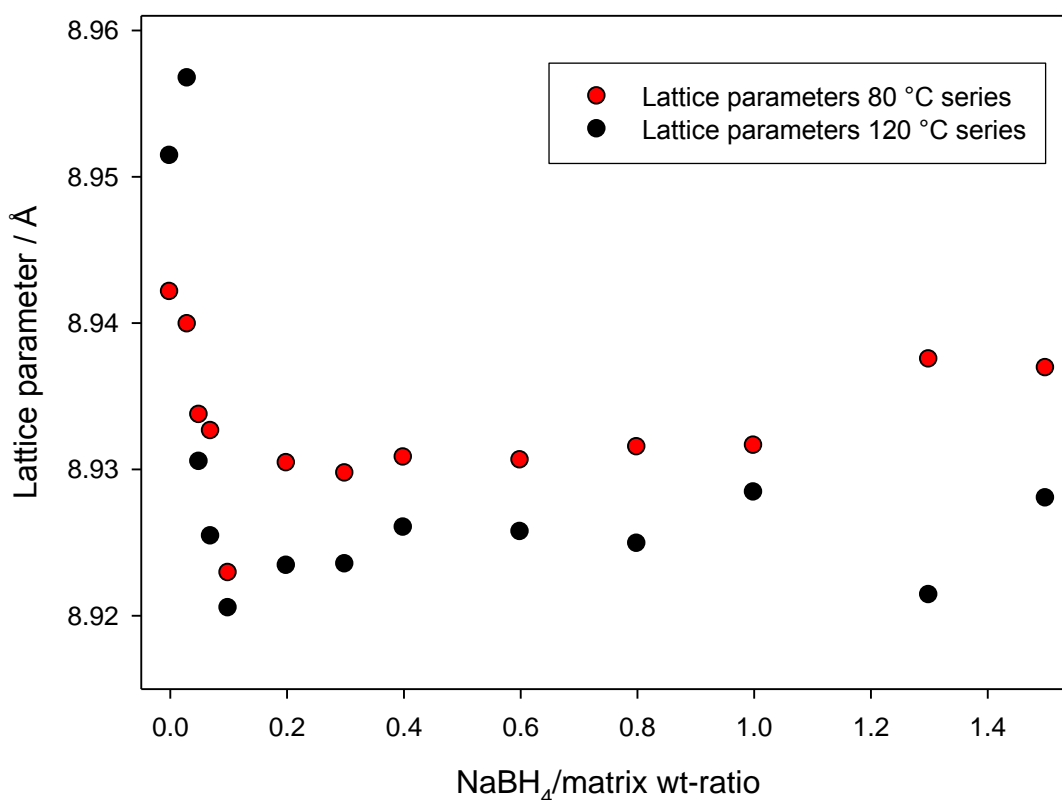
Figure 62: Calculated lattice parameters of the 120 °C (black) and the 80 °C (red) series for varied NaBH4/matrix wt-ratios. Data points represent values obtained as described in Chapter 5.1.1. and 5.1.2.

Following Henderson and Taylor, the positions of the infrared absorption bands of aluminosilicate sodalites depend mainly on the framework structure. In more detail, their position is determined by the T-O bond length and the T-O-T angles, which are correlated to the size of the cage-filling cation or molecule and therefore also directly connected to the lattice parameter [80]. Henderson and Taylor described trends for the v_{as} T-O-T, v_s T-O-T and δ O-T-O. In this work the sum of the three mainly existing v_s T-O-T positions are used for evaluation. These three peaks show identical behavior and therefore the sum of their positions can be used for evaluation of effects correlated to the cage-fillings.

The evaluation of the infrared-spectra of the 120 °C synthesis series shows for the sum of v_s TOT-positions an interesting behavior (see Fig. 63). Above a wt-ratio of only 0.05 $NaBH_4$/matrix there is no significant change in the TOT-positions visible, the value remains constant at about 2111 cm^{-1}. For the ratios of 0.03, 0.05 and the comparison specimen without $NaBH_4$, the values vary from 2089 cm^{-1} to 2109 cm^{-1}. This variation indicates that only small amounts of $NaBH_4$ suffice to work as templates for the creation of BH_4-sodalites. The large error for the blank sample (0.0 $NaBH_4$/matrix) results from the inhomogeneity of the sample; the spectrum shows large amounts of water and significant intensities of carbonate-related bands. The high amounts of carbonate are confirmed by CS (see Chapter 5.4.3.) especially for low $NaBH_4$/matrix wt-ratios. Those different cage fillings lead to variations in the structure of the three TOT-peaks and their ratios to each other.

The same evaluation for the 80 °C series is also shown in Figure 63. Data show a similar behavior compared to the 120 °C series; only the samples with the lowest $NaBH_4$/matrix ratio differ from further samples. The blank sample ($NaBH_4$/matrix = 0.0) shows the smallest sum but also the biggest error. As described for the 120 °C samples, the error probably occurs due to high water and carbonate amounts and therefore inhomogeneous crystallization and/or cage-fillings of the sodalite. The sum of the peak positions increases till an $NaBH_4$/matrix ratio of 0.1 and remains constant even for higher

ratios at about 2109 cm^{-1} and is therefore slightly smaller than for the samples, synthesized at 120 °C.
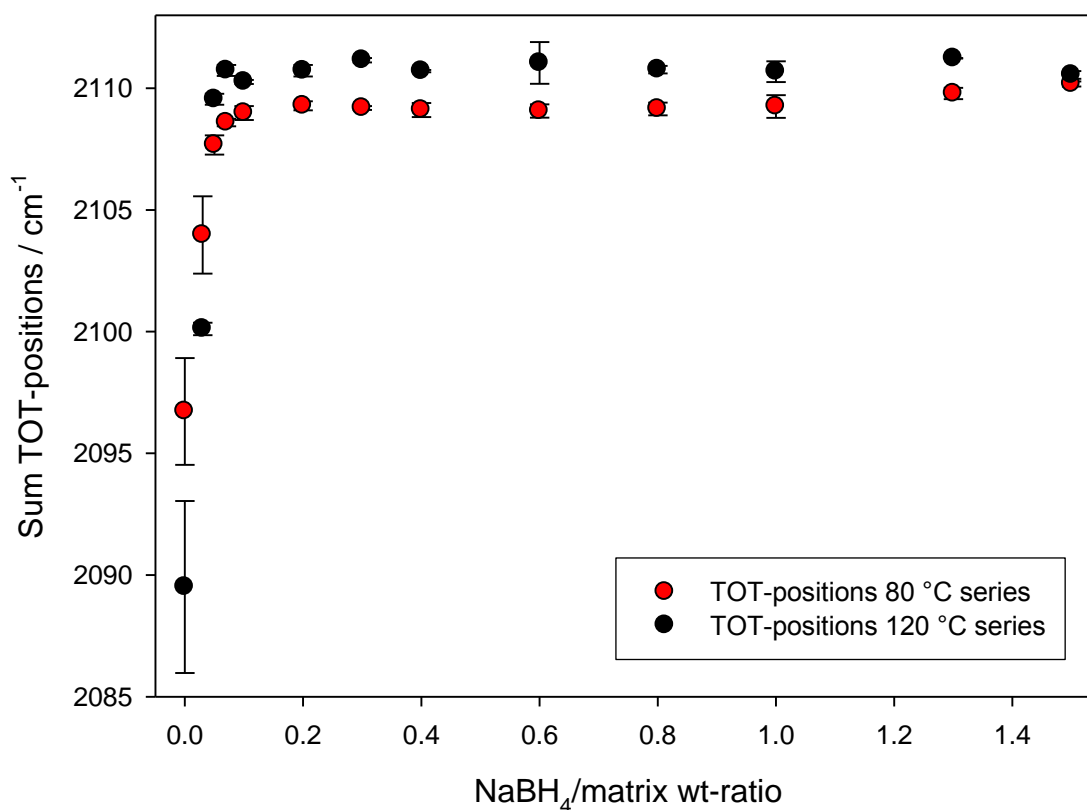
It can be concluded that the BH$_4$-Sod together with its Na$^+$ for charge balance has an higher influence on the long-range order compared to the neutral hydro-sod amounts. These local charges seem to affect the structure even if their concentration is very low. At NaBH$_4$/matrix ratios above 0.2 the hydro-sod shows no more effect on the TOT-position and the lattice parameter, despite that the amount of BH$_4^-$ can be increased up to an NaBH$_4$/matrix wt-ratio of 0.6 according to FTIR in the three synthesis series (see Fig. 32, 42 and 52). A further increased NaBH$_4$/matrix wt-ratio does not lead to a significant increase of purity or a higher degree of embedding of NaBH$_4$ in the sodalite.

The 60 °C series formed zeolite A mainly for $NaBH_4$/matrix wt-ratios below 0.3. The ratios 0.3 and 0.4 lead to co-crystallization of zeolite A and sodalite, only above a ratio of 0.8 pure BH_4-sodalite could be formed (see x-ray diffractograms Fig. 48 and 49). This effect results of the low synthesis temperature of 60 °C and the changed starting materials as source of aluminate and silicate. Following Barrer the sort of zeolite being formed depends on various parameters like the reactants, their pre-treatment and chemical composition, homogeneity and pH of the reactant mixture, seeding, temperature, pressure and addition of additives [79].

5.5.2. Water

How is the water bound in the system of BH_4-Sodalite? Two possible sources of internal water need to be considered: Water bound in the sodalite cages as hydro-sod [68], [81] and water bound in the amorphous areas of the matrix.

The overall water amount was determined, using the mass loss via TG. With a comparison by KFT it could be shown that the mass loss data are related to the internal water of the sodalite type samples. This method leads to good results for the sample materials used: For comparison of the two methods samples of the 120 °C series were used. The results are plotted as function of the $NaBH_4$/matrix ratio in Figure 64. Here, it becomes obvious that both methods show the same trends and more or less same amounts. The mass loss and the water content decrease with increasing $NaBH_4$/matrix ratios up to a ratio of 0.6. Above that ratio, both values remain constant. KFT shows up to a $NaBH_4$/matrix wt-ratio of 0.4 identical or slightly lower water amounts, compared to the mass losses obtained. This difference is increased for the two samples with the highest $NaBH_4$/matrix wt-ratios of 0.6 and 1.5. This effect occurs due to the different heating and cooling rates in the KFT.
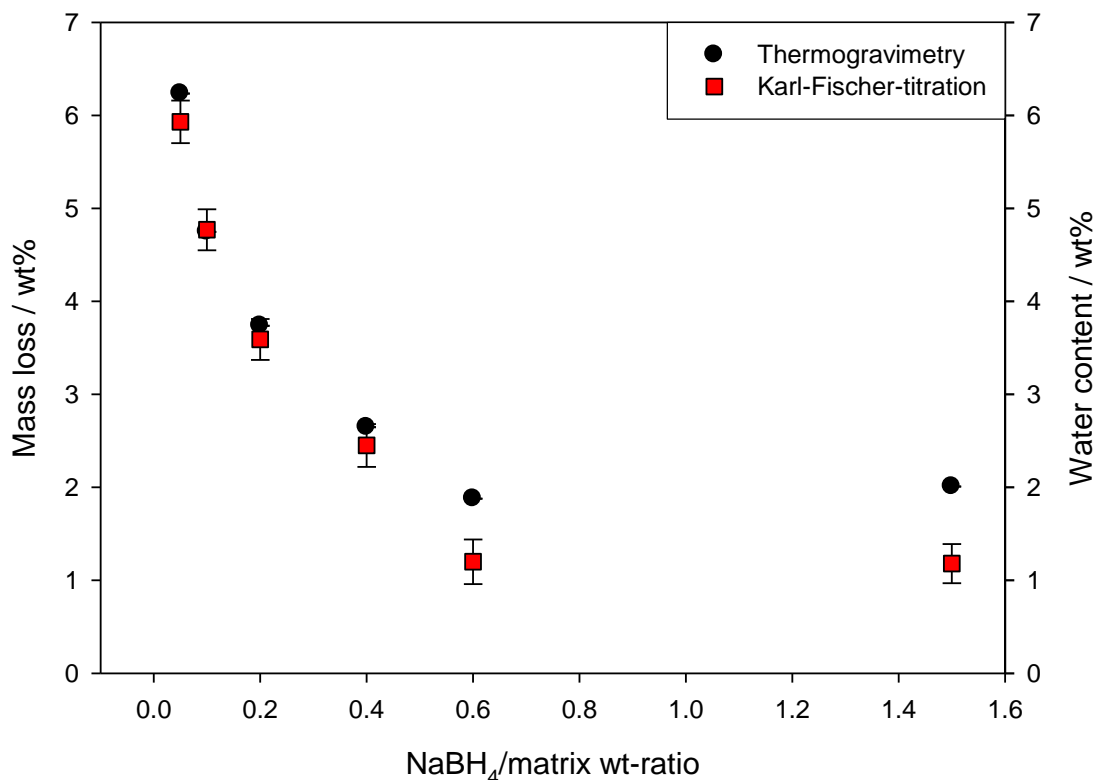
Figure 64: Plotted mass losses (black circles) and water amounts (red squares) as function of the NaBH$_4$/matrix ratio

How to differentiate between the hydro-sod and the amorphous bound water?

Following Felsche and Luger [68] the DTA signals of pure non-basic hydro sodalite (Na$_6$[AlSiO$_4$]$_6\cdot$8H$_2$O) show two endothermic effects at 130 and 230 °C, respectively. These characteristic signals are also visible in the 80 °C and 120 °C series at low NaBH$_4$/matrix wt-ratios. Comparing pure hydro-sodalite with the NaBH$_4$/matrix wt-ratio sample of 1.0 (Fig. 65), both synthesized at 120 °C concerning their TG and DTA results, it becomes obvious that only small amounts of water are bound in the hydro-sodalite form in the BH$_4$-Sod samples with NaBH$_4$/matrix above 0.6. The hydro-sodalite shows the characteristic DTA curve with two strong endothermic effects at 120 °C and 220 °C, respectively. These signals are not visible in samples with high amounts of NaBH$_4$. The slightly shifted temperatures can be explained by different measuring parameters (Felsche and Luger: Heating rate 10 °C/min; atmosphere N$_2$) and the sample compositions.
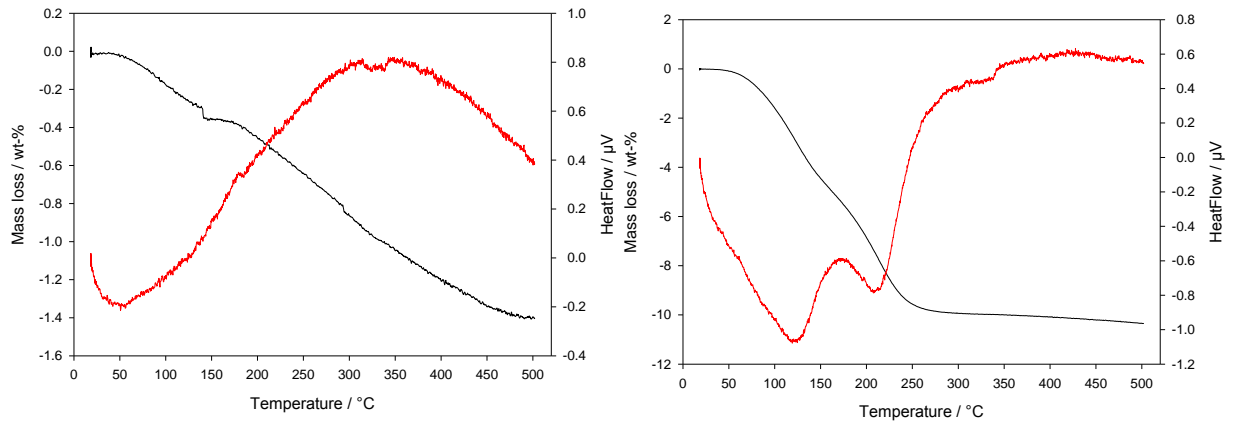
Figure 65: TG/DTA results of NaBH₄/matrix ratios 1.0 (left) and 0.0 (right) of the 120 °C synthesis series.

Figure 66 shows the integrated intensities of the endothermic DTA-signal at around 210 °C obtained for the 80 and 120 °C series. The data show the same exponential decrease with increasing NaBH₄/matrix wt-ratio as obtained for molecular water using IR (cf. Fig 32 and 42).
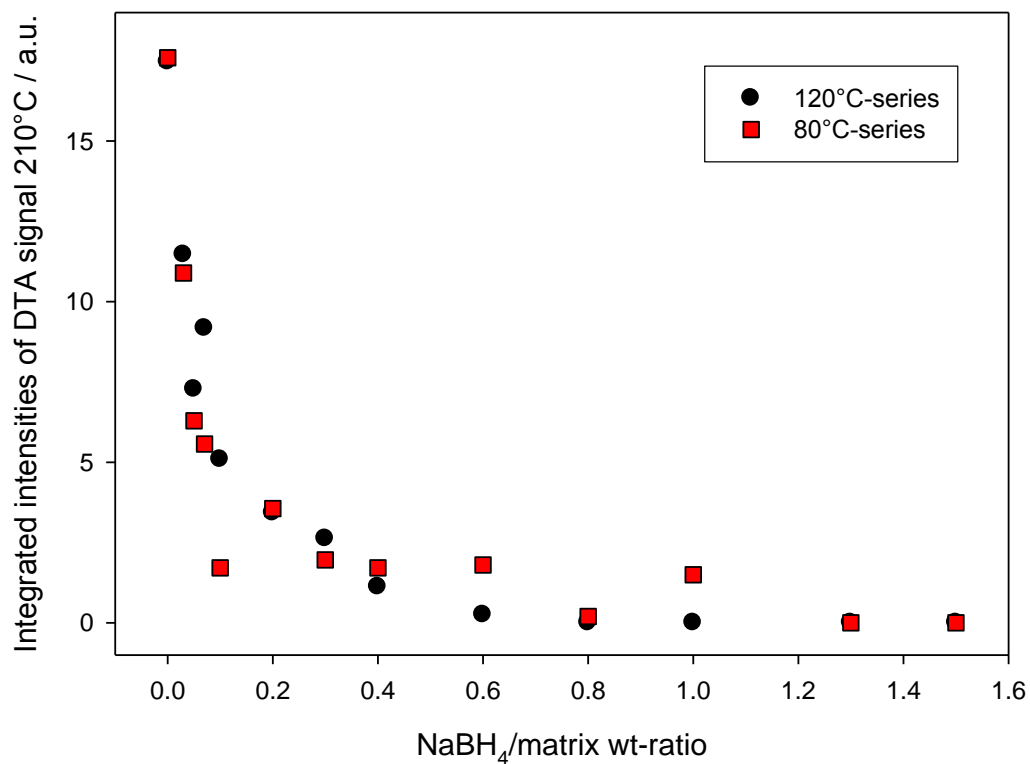
Figure 66: Integrated intensities of DTA-signals, obtained for the 80 and 120 °C series.

These results show that the amount of hydro-sod can be varied within a synthesis series by using different $NaBH_4$/matrix wt-ratios. With increased $NaBH_4$/matrix wt-ratio the amount of hydro-sodalite decreases.

The amount of water bound in the amorphous areas can be estimated by the combination of the mass loss obtained and the absence of the characteristic DTA signals of the hydro-sodalite: For the three series the mass loss as function of the $NaBH_4$/matrix wt-ratio is determined. The plots obtained (Figures 34, 43 and 53) show that the mass loss decreases with increasing $NaBH_4$/matrix wt-ratio and reaches a limit value. This limit value depends on the morphological particle size and is used for the estimation, as shown in Figure 67 using the example of the 120 °C series. The dark blue area represents the water amounts, bound in the β-cages of the sodalite, forming the hydro-sodalite. The light blue areas show the water, which is bound in the amorphous parts of the matrix. Minor amounts of hydro-sodalite cannot be excluded even for $NaBH_4$/matrix wt-ratios above 0.6 and are therefore added.
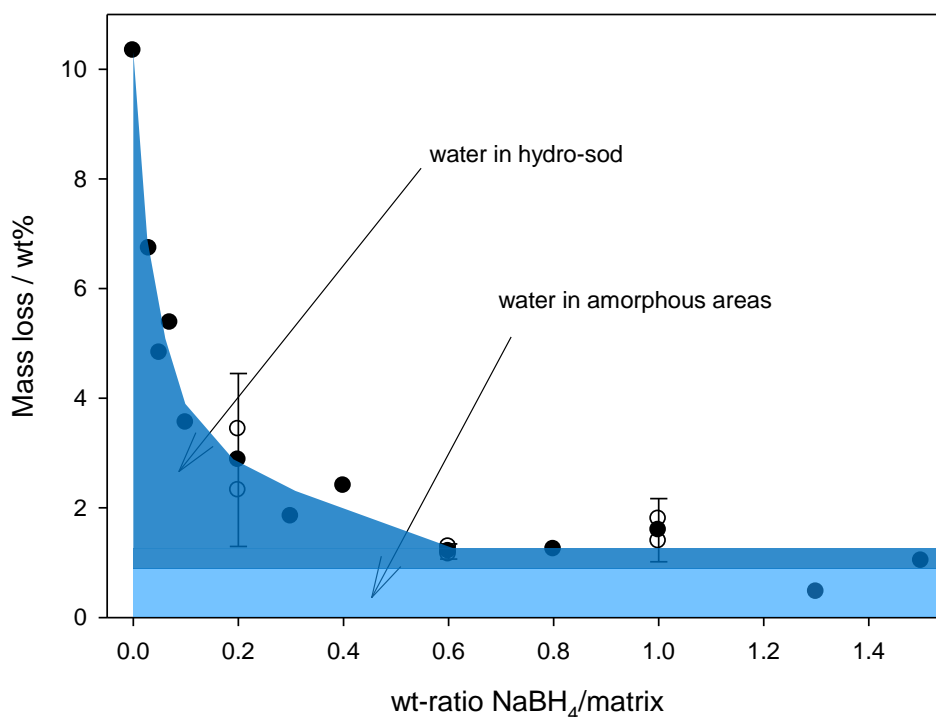
Figure 67: Graphical estimation of the two different water containing areas, shown exemplarily for the TG results of 120 °C series.

This estimation gives values of about 1 wt% water, bound in the amorphous areas for the 120 °C series, about 2 wt% for the 80 °C series and about 8 wt% for the 60 °C series. The 60 °C series is different to the two other series, even the $NaBH_4$-free sample does not show DTA signals of a hydro-sodalite, because at low temperatures zeolite A is formed, as described in the previous section. Samples of this series with $NaBH_4$/matrix wt-ratios above 0.6 consist of BH_4-sod mainly and can therefore be treated in the same way.

These samples can be compared throughout the synthesis. The $NaBH_4$/matrix wt-ratio of 0.8 was chosen for a comparison of the particle size obtained for the three different synthesis temperatures of 60 °C, 80 °C and 120 °C. The average morphological particle size was analyzed as 0.564 µm, 0.525 µm and 0.289 µm for the 120, 80 and 60°C series. Figure 68 shows the correlation of the particle size and the mass loss obtained by TG in the temperature range up to 500 °C. The mass loss follows a linear decrease with increased average particle size. This mass loss is caused by higher amounts of water in the amorphous areas of the matrix. In the next section, the reaction mechanism will be discussed in detail; the smaller particle size also shows a higher reaction degree but the mass loss is mainly caused by the water amount.
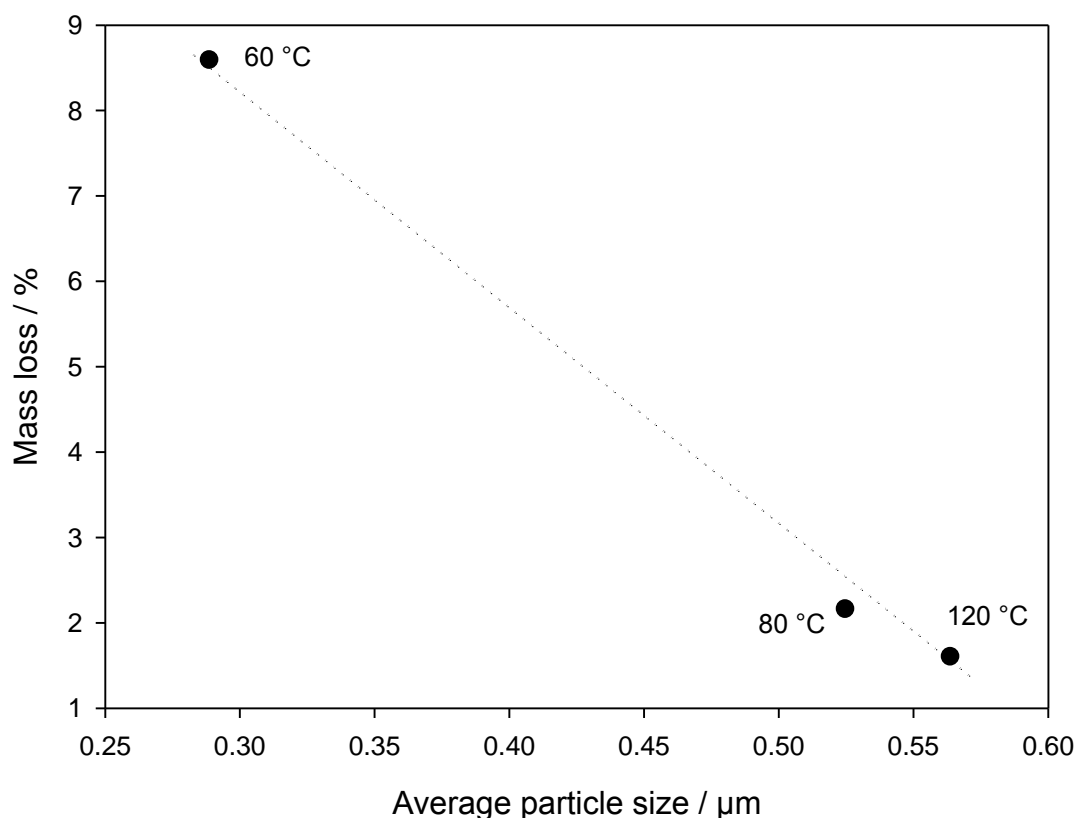
As shown it is not possible to increase the amount of BH$_4^-$ in the sodalite above a NaBH$_4$/matrix wt-ratio of 0.6 throughout the three synthesis series. These samples represent the highest possible degree of BH$_4^-$ enclathration. The mass loss as function of the NaBH$_4$/matrix wt-ratio confirms this thesis; with the lowest amount of NaBH$_4$ used as template the highest mass losses were obtained in the TG measurements (see Tables 26 and 29). From the mass loss differences between the hydro-form (0.0 NaBH$_4$/matrix) and the high NaBH$_4$/matrix ratios (> 0.6) for the three series, the enclathration degree can be estimated; the mass loss consists of water loss mainly, the amount of hydrogen released has only minor effects on the mass differences. Hence the percentage reduced mass loss of these samples within a series, should give a suitable approximation of the enclathration degree with NaBH$_4$. Calculated for the 120 °C series the mass loss decreased from 10.336 to

1.112 wt%, which means that about 90 % of the sample consists of BH_4-sodalite. The 80 °C series shows a lower degree of enclathration of about 71 % only. The calculation was also performed for the 60 °C series, even though the hydro form consists of zeolite A, only. Table 36 summarizes the calculations. This calculated enclathration degree of about half the amount of $NaBH_4$ in the 60 °C series compared to the 80 °C and 120 °C series, respectively, fits to the relative amounts of released hydrogen, discussed in the fourth section of this discussion.

Table 36: Calculations of the enclathration degree of NaBH$_4$ in the three sodalite series with NaBH$_4$/matrix wt-ratio > 0.6

	120 °C	80 °C	60 °C
Mass loss 0.0 / wt%	10.336	8.927	14.50
Average mass loss > 0.6 / wt%	1.112	2.560	8.414
Approximated enclathration degree NaBH$_4$ / %	≈ 90	≈ 71	≈ 42*

5.5.3. Further Enclathrated Species

Carbon should be embedded as carbonate entirely. The evaluation has to be divided into the 120 °C and 80 °C series on one hand and the 60 °C series on the other hand.

In the 120 °C and 80 °C series, already small amounts of formed BH_4-sod decrease the uptake of CO_2 by about 50 %, comparing the Carbon values of the $NaBH_4$/matrix ratios of 0.0 to 0.05. The lowest amounts were detected in samples with highest $NaBH_4$/matrix ratios. On the other hand, the amount of Carbon is more or less constant in the 60 °C series, independently from the $NaBH_4$/matrix ratio. It can therefore be concluded that the Carbonate is formed mainly in the hydro-sodalite parts of the samples. The amount of amorphous water within the series seems to be constant, but the hydro-sodalite amount decreases in the 120 °C and 80 °C series with increasing $NaBH_4$/matrix wt-ratio. The 60 °C series shows no evidence concerning DTA (see chapter 5.3.3.) on hydro-sodalite formed, at all, but is supposed to have the highest amounts of water bound in the amorphous areas. The

carbonate formed is visible in the FTIR spectra by the characteristic peak at 1440 cm^{-1} [61]. Before a heating procedure this peak is broad, it tends to become more pronounced and sharp with higher intensities after thermal treatment.

5.5.4. Hydrogen Release

The hydrogen release experiments provide revealing insights in the BH$_4$-sodalite system. For the 120 °C series the hydrogen release was analyzed as function of the NaBH$_4$/matrix wt-ratio during synthesis. The results show an exponential increase of the hydrogen released with increasing NaBH$_4$ used up to a limit value of 180 ml/g reached at a NaBH$_4$/matrix wt-ratio of 0.6 (see Fig. 58, Chapter 5.4.2.). The same trend could be observed for the integrated intensities of the BH$_4^-$ related signals obtained by FTIR (see. Fig. 32). The maximal value of hydrogen released equals 8 % of the pure NaBH$_4$ (exp. 2265 ml H$_2$/g). An ideal BH$_4$-sodalite with the formula Na$_8$[AlSiO$_4$]$_6$(BH$_4$)$_2$ should release 207.4 ml H$_2$/g calculated with the ideal gas law. The difference between this theoretical value and the data obtained can mainly be explained by the co-crystallization of hydro-sodalite and amorphous areas and measurement uncertainties; as described above, the amount of these side products can reach up to 10 wt%. This amount would explain the difference on its own. Additionally the experimental determined amount of hydrogen released for pure NaBH$_4$ was also about 5 % below the theoretical value (theo. 2400 ml H$_2$/g), so the values obtained were all a bit underestimated probably.

Figure 69 shows the correlation of effectively enclosed NaBH$_4$ from back calculations (see Table 33) and hydrogen released for the 120 °C series. The already mentioned maximum of hydrogen capacity can be observed for NaBH$_4$/matrix ratios of 0.6 and above. At the same time, the efficiency shows a further decrease. Efficiency is calculated by the difference between amount of NaBH$_4$ used in the synthesis and the amount of NaBH$_4$ calculated backwards from the amount of hydrogen released. It can be concluded that the highest efficiency can only be reached by low degrees of enclathration of NaBH$_4$. On the

other hand, high amounts of hydrogen can only be realized by a lack of efficiency: The NaBH$_4$ needs to be added in a surplus during the synthesis. A higher NaBH$_4$/matrix wt-ratio than 0.6 shows no advantages.
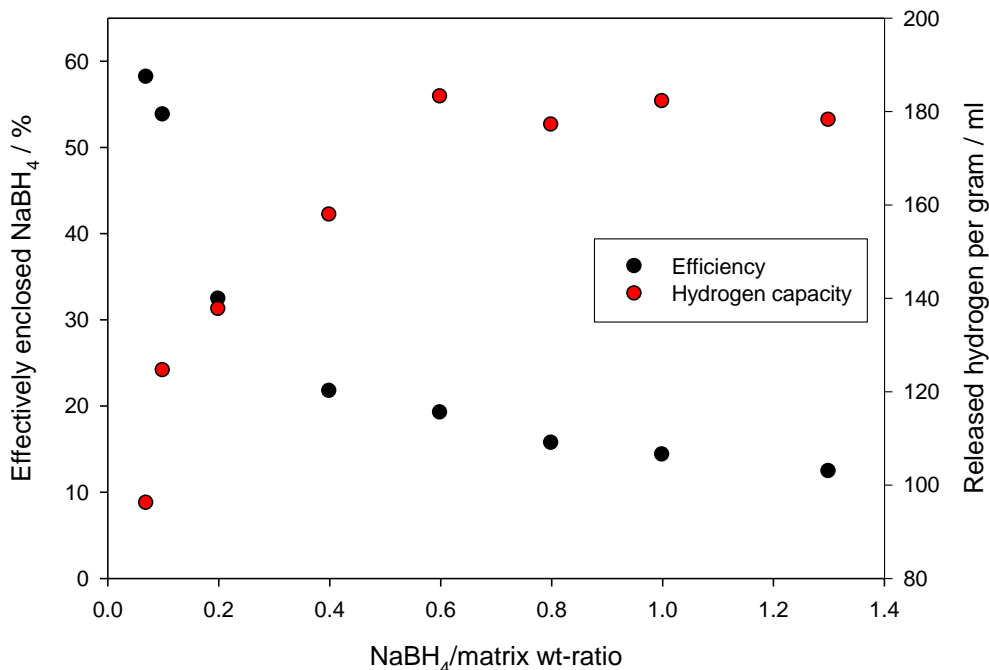
Figure 69: Correlation between effectively enclosed NaBH$_4$ and hydrogen amounts released. Data shown for the 120 °C series.

Figure 70 shows the correlation between the hydrogen released and the integrated intensities of the BH$_4^-$ related peaks obtained by FTIR for the 120 °C series. The data points show a linear behavior for NaBH$_4$/matrix wt-ratios up to 0.4. Further increased ratios neither lead to a further increase in integrated intensity nor to an increased hydrogen release. This effect confirms the observation that no further NaBH$_4$ can be embedded in the sodalite matrix above a NaBH$_4$/matrix wt-ratio of 0.6. Temperature depending decrease of the BH$_4^-$ related species and the afterwards measured release of hydrogen do also plot along the given trendline. This Figure confirms also that the NaBH$_4$ is the source of the gas volume released.
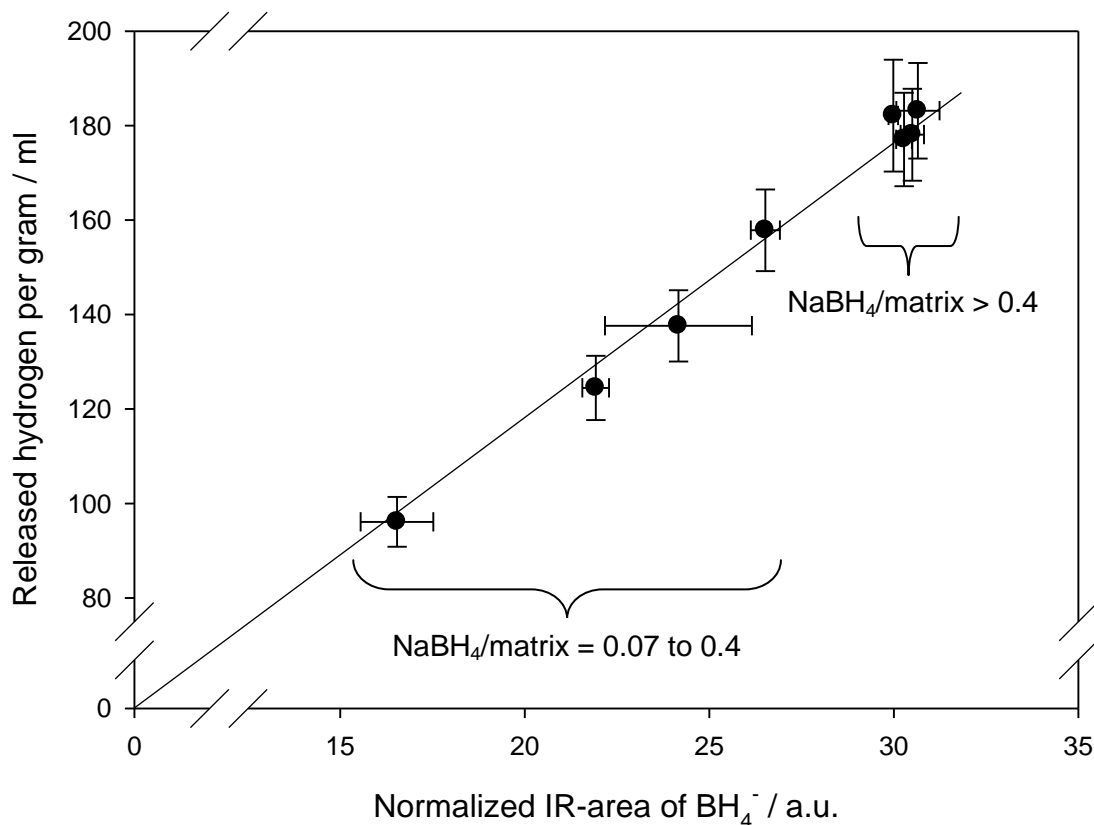
Figure 70: Correlation of the TOT-normalized area of BH$_4^-$ obtained by FTIR and the hydrogen amount released.

Figure 71 shows the hydrogen released plotted versus the average particle size for the three synthesis series (60 °C, 80 °C and 120 °C). The average particle size was determined for the samples with a NaBH$_4$/matrix wt-ratio of 0.8, while the hydrogen amount released was measured for a NaBH$_4$/matrix wt-ratio of 1.3. These differences are negligible since all data like FTIR and XRD show no significant changes at NaBH$_4$/matrix wt-ratios above 0.6 throughout the three series. The plot shows a linear increase of the amount of hydrogen released and with increasing average particle size.
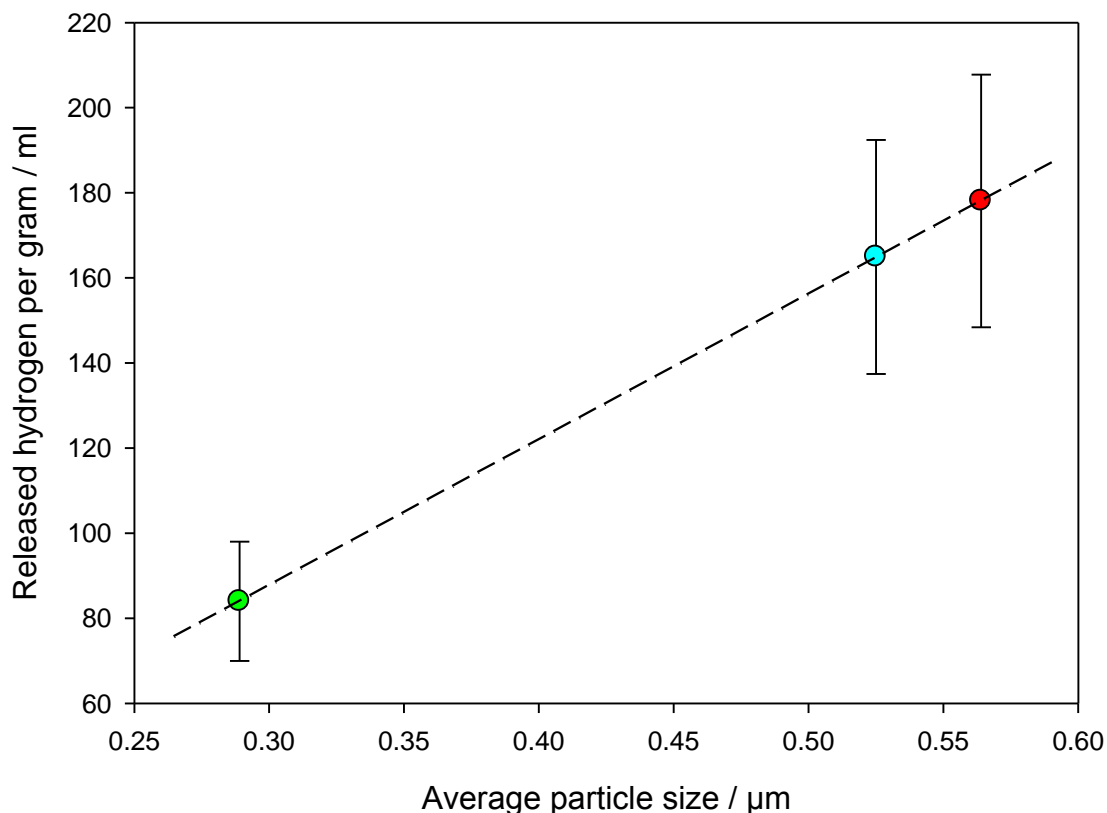
Figure 71: Hydrogen release as function of the average particle size (green 60 °C, blue 80 °C, red 120 °C) all samples have an identical NaBH$_4$/matrix wt-ratio of > 0.6

The decrease of the hydrogen amount released can be explained by the lower BH$_4$-sodalite to water ratio (degree of enclathration) for the 60 °C and the 80 °C series compared to the 120 °C series. Additionally, the bigger particle size should lead to an increased protection of the embedded NaBH$_4$ due to the reduced particle surface. These two effects also have high influence on the reaction of the embedded NaBH$_4$, which will be discussed in the next chapter.

Part C:

Mechanism Study of the Hydrogen

Release from BH$_4$-Sodalite

6. Mechanism Study: Hydrogen Release from BH$_4$-Sodalite

In this chapter the hydrogen release of BH$_4$-sodalite is analyzed. First of all the starting position will be briefly summarized. As theoretical reaction mechanism a stepwise substitution reaction was published in 2012, based on FTIR results mainly [17] according to previously results [37]:

$$BH_4^- + H_2O \qquad \rightarrow H_3BOH^- + H_2 \tag{15a}$$

$$H_3BOH^- + H_2O \qquad \rightarrow H_2B(OH)_2^- + H_2 \tag{15b}$$

$$H_2B(OH)_2^- + H_2O \qquad \rightarrow HB(OH)_3^- + H_2 \tag{15c}$$

$$HB(OH)_3^- + H_2O \qquad \rightarrow B(OH)_4^- + H_2 \tag{15d}$$

Furthermore it was further postulated, that at least two intermediate species (marked as A and B) occur during the reaction to B(OH)$_4^-$, which afterwards dehydrates in a two-step-reaction over BO(OH)$_2^-$ to BO$_2^-$. Hydrogen is only released until the formation of B(OH)$_4^-$ in the mechanism. In Figure 72, the visible species, starting from BH$_4$-Sod are shown in form of infrared spectra. Figure 73 shows the spectra of the dehydration steps, starting from directly synthesized B(OH)$_4$-Sod.
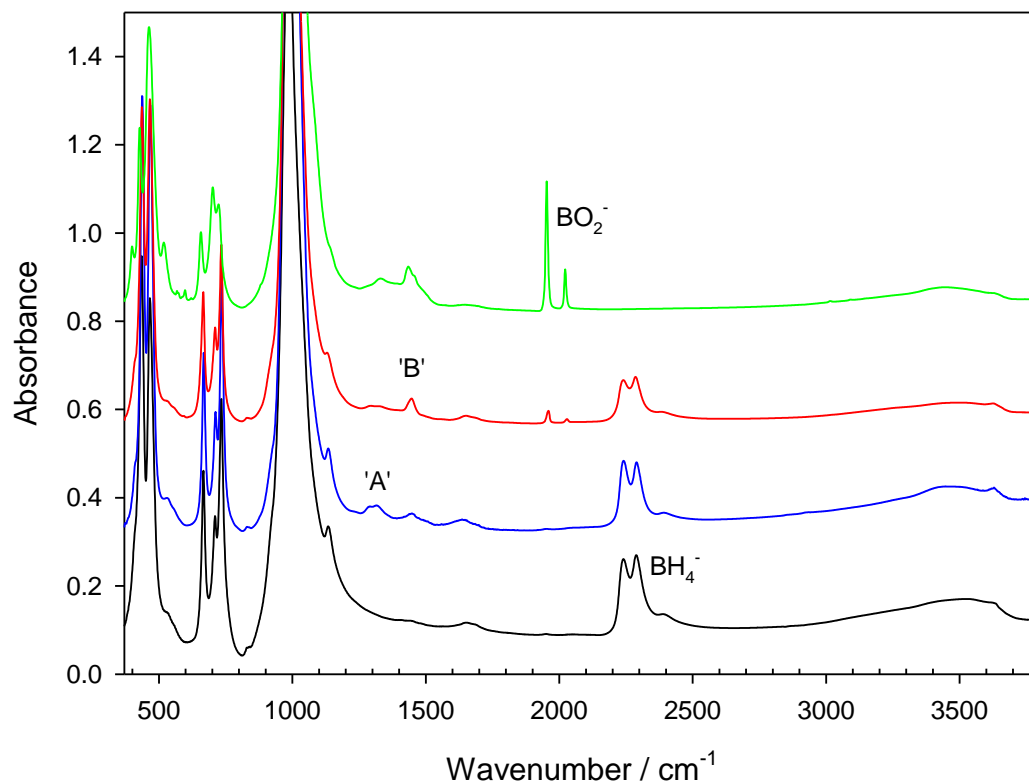
Figure 72: FTIR spectra of BH$_4$-Sod and three tempered steps
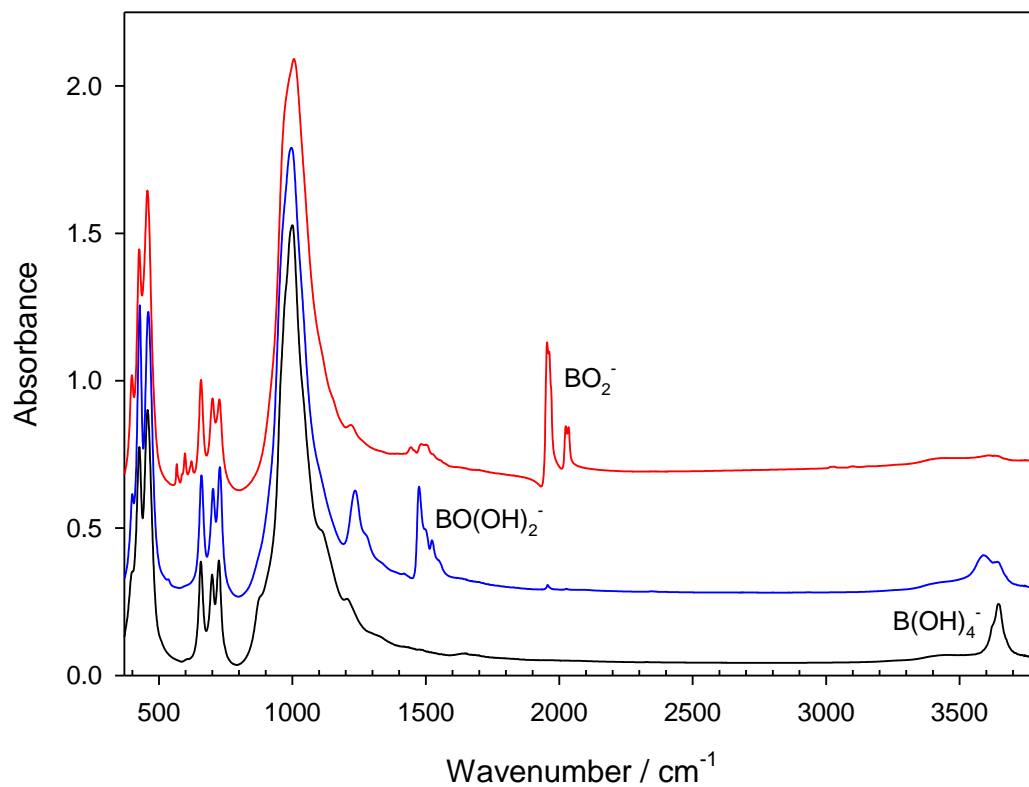
Figure 73: FTIR spectra of B(OH)$_4$-Sod and two tempered steps

6.1. Experimental Analyses on Species 'A'

During the last years the species 'A' was interpreted as an intermediate in the theoretical reaction mechanism, given in the introduction of this chapter. This species occurs in all infrared spectra of BH_4-Sod as first signal during thermal treatment in form of a double peak at 1290 and 1310 cm^{-1} at temperatures above 200 °C. Species 'A' was therefore supposed to be one of the postulated intermediates as H_3BOH^-, $H_2B(OH)_2^-$ or $HB(OH)_3^-$. Several publications discussed the existence of H_3BOH^-, too, like [37], [82], [83].

To identify which of the species 'A' might be or at least to be able to exclude some of the possible species, the hydrogen release apparatus was used. A sample was synthesized, following the description, given in chapter 3.1.2. with a $NaBH_4$/matrix wt-ratio of 0.6 and a synthesis temperature of 120 °C. From half of the material, the hydrogen content of this sample (E4) was determined, as given in Chapter 3.5.1.. The second half of the sample (E4_T3) was thermally treated to obtain a reaction degree above 12 %, the heating procedure included 48 h at 200 °C, followed by 18 h at 225 °C and 18 h at 250 °C. This thermal reaction was performed in a tube furnace under water loaded air flow. Figure 74 shows the infrared spectra of the primary material (E4) and the material after the partial reaction (E4_T3). It shows only signals of species 'A' beside the BH_4^- and sodalite signals.
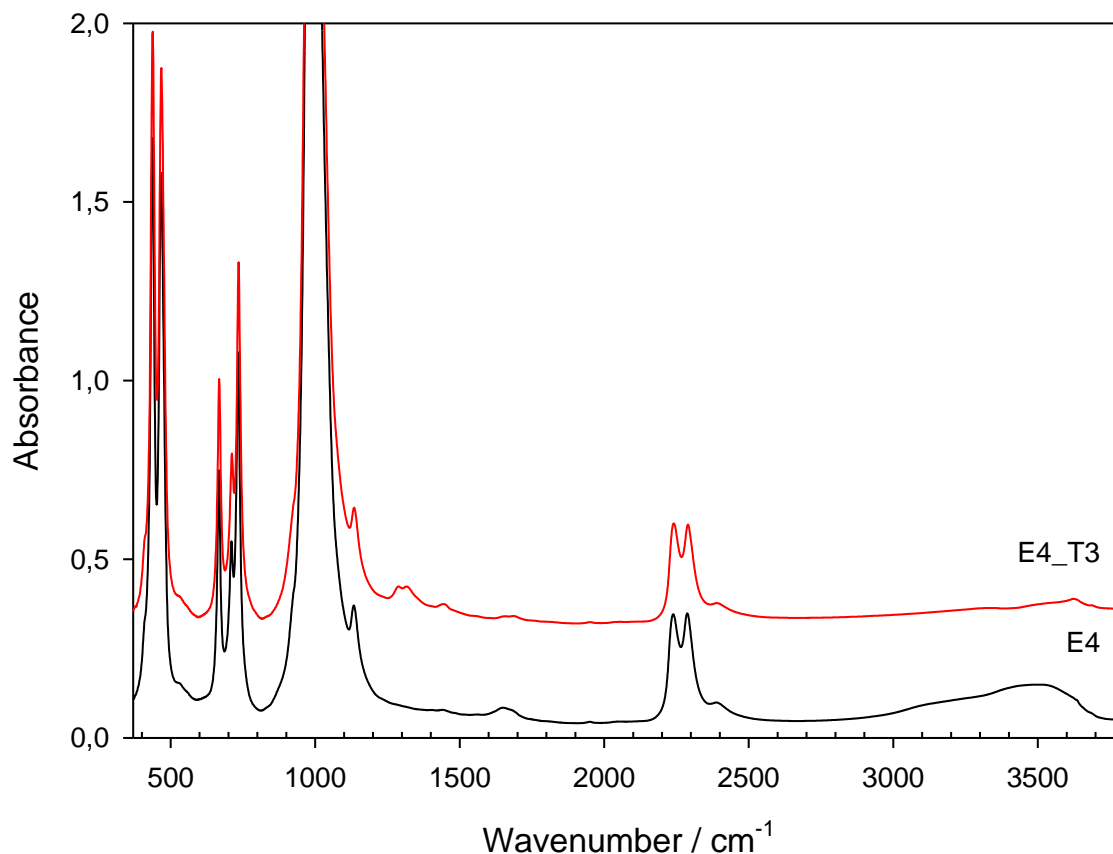
Figure 74: FTIR spectra of sample E4 and before and after the thermal treatment.

In Table 37, the relevant results of the hydrogen release experiments and the IR intensities are summarized. Additionally a mass normalization was performed, leading to an only minor lower reaction degree.

Table 37: Comparison of tempered and as synthesized sample for identification of species 'A'.

	E4	E4_T3
TOT-normalized, integrated intensity BH_4^- triplet / area units	27.813 ± 0.581	24.255 ± 0.153
RD: TOT-normalized reaction degree / %	-	12.78
Released Hydrogen per g / ml	163.8 ± 8.76	144.0 ± 7.71

Hydrogen can only be released out off the B-H bonds in the BH_4-molecule and the possible intermediates $H_{4-x}B(OH)_x$. Thus the remaining hydrogen in the sample E4_T3 can be calculated for the possible species following equation 16:

$$H_2(E4\_T3) = H_2(E4) - RD \cdot H_2(E4) + \left[\frac{4-x}{4} \cdot RD \cdot H_2(E4)\right] \qquad (16)$$

With $H_2(E4)$ as released hydrogen in ml per g of sample E4 and RD as reaction degree or decrease of integrated BH_4^- intensity of E4. Due to this with every 5.24, respectively 4.91 ml less released hydrogen from E4_T3, than the released hydrogen from E4, the next suggested intermediate species becomes more likely (Tab. 38).

Table 38: Calculated amount of hydrogen release for intermediate species assumed.

Species	TOT-normalized: Calculated H_2 release per g / ml	Mass-normalized: Calculated H_2 release per g / ml
H_3BOH^-	158.57	158.89
$H_2B(OH)_2^-$	153.32	153.99
$HB(OH)_3^-$	148.09	149.08
Species without B-H bond	142.85	144.18

From this calculation and the experimental obtained hydrogen release of E4_T3 of 144.0 ± 7.71 ml/g it is indicated that species 'A' does not contain any B-H bonds and therefore cannot be one of the so far postulated intermediates $H_{4-x}B(OH)_x$. The calculated errors need to be taken into account, so this method on its own does not have the capability to disprove the old interpretations.

As second approach, a peak fit, using *dmfit* [30], of the B-H area in the infrared spectra, was performed (see Fig. 75 and 76). The idea is to fit the spectrum of sample E4 in the range of the B-H stretching modes from 2100 to 2650 cm^{-1} [84], [85]. Afterwards, the spectrum of the thermal treated sample E4_T3 was fitted with analogous peaks. If species 'A' contains B-H bonds, the fitting of this spectrum should not provide a matching result, because an additional B-H containing species would inevitably lead to additional peaks in

this wavenumber range. Therefore, if the peak fitting leads to good results without adding new peaks, it is a good hint, that species 'A' contains no B-H bonds.

The following Figures show the fitted spectra of the samples E4 and E4_T3. The fitting quality with six peaks for E4 is very good, the *adj. R-Square* value is 0.9998, for the spectrum of E4_T3 also six peaks were used for the fit, leading to *adj. R-Square* of 0.9996. Fitting parameters are given in Table 39.
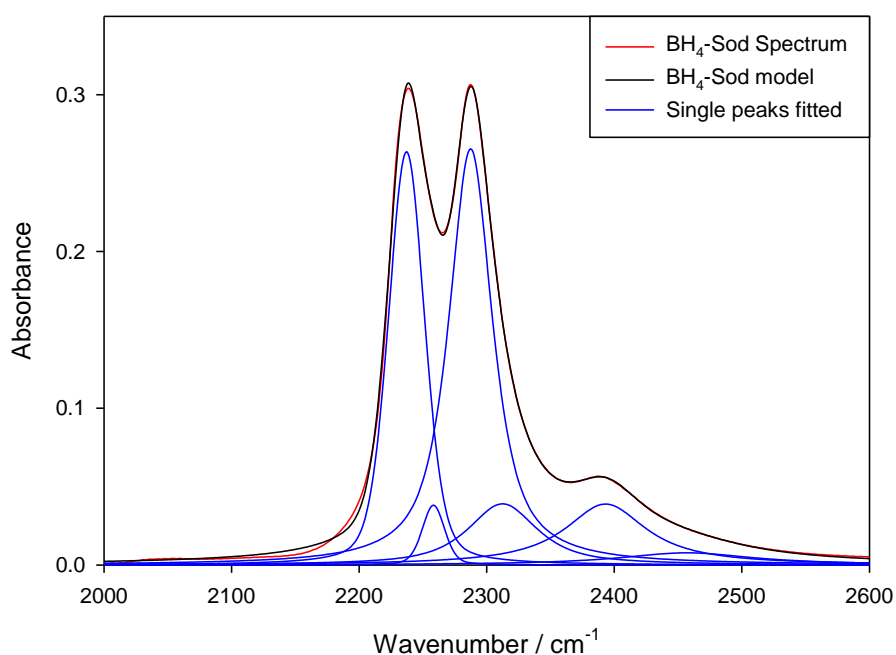
Figure 75: FTIR spectrum (red) and model (black) of the BH₄-Sod sample in the B-H wavenumber range from 2000 to 2600 cm⁻¹ before tempering.
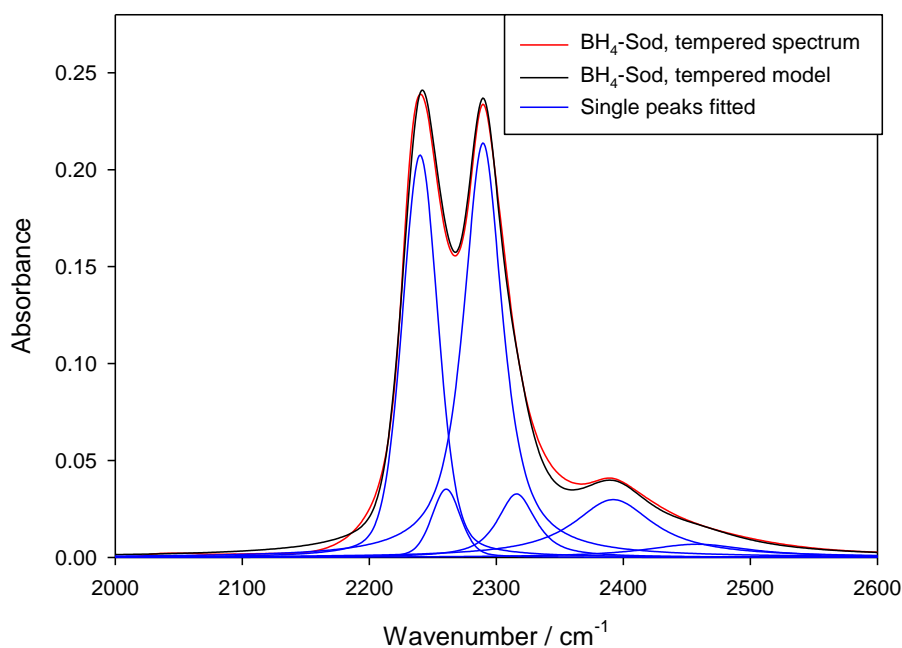
Figure 76: FTIR spectrum (black) and model (red) of the BH$_4$-Sod sample in the B-H wavenumber range from 2000 to 2600 cm^{-1} after tempering.

Table 39: Fitting parameters of the BH$_4^-$ areas before and after tempering

	Position / cm^{-1}	Amplitude	Width / cm^{-1}	Gauß/Lorentz	Area / %
E4	2237.16	0.26	33.35	0.7	29.74
	2258.28	0.04	20.69	0.7	2.69
	2287.43	0.27	40.83	0.2	43.00
	2312.46	0.04	64.57	0.2	9.71
	2393.19	0.04	77.53	0.0	11.71
	2456.82	0.01	128.39	0.0	3.15
E4_T3	2240.01	0.21	33.01	0.7	32.40
	2260.52	0.04	26.67	0.7	4.50
	2289.52	0.21	36.34	0.2	42.95
	2315.98	0.03	35.73	0.2	6.49
	2392.04	0.03	76.87	0.0	11.52
	2458.00	0.01	100.64	0.0	2.13

Those results strongly indicate that species 'A' is not one of the formerly published intermediates and that it is not a borohydride species, at all.

6.2. NMR

The ^{11}B MAS NMR results are summarized in Figure 77 and the magnified area of the further products on the right hand side. Three temper steps of 250, 300 and 400 °C are shown in addition to the starting material. The starting material is a BH_4-sod with a $NaBH_4$/matrix wt-ratio of 0.6 synthesized at 120 °C.
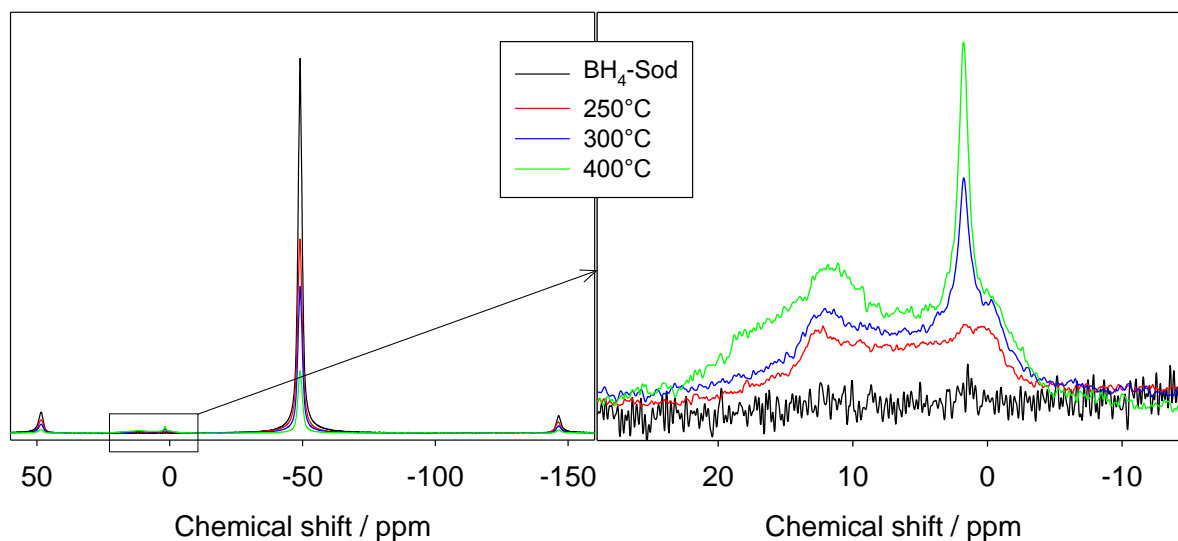
Figure 77: [11]**B MAS NMR spectra, overview (left) and magnified area of products (right). The intensities are shown as measured.**

The main peak is located at -49.09 ppm and is correlated with the BH_4^-, the two side bands are positioned at 48.54 ppm and -146.50 ppm, respectively. Qualitatively the signals of the BH_4^- decrease with higher heating temperatures. The magnified area of the spectra from 29 ppm to -15 ppm shows the new formed signals due to the heating processes. With higher temperatures the areas of these new signals increase. The starting material (black) shows no significant signals in the mentioned range. After heating up to 250 °C (red) new signals become visible. At this temperature the quadrupole signal is dominating, while the signal at 1.78 ppm which is correlated to $B(OH)_4^-$ is only minor distinguishable. At 300 °C (blue) the $B(OH)_4^-$ signal is more pronounced. With further heating up to 400 °C (green) a

new signal at 10.99 ppm can be detected. The single peaks fitted are shown below in Figure 78 and are evaluated in Table 40.
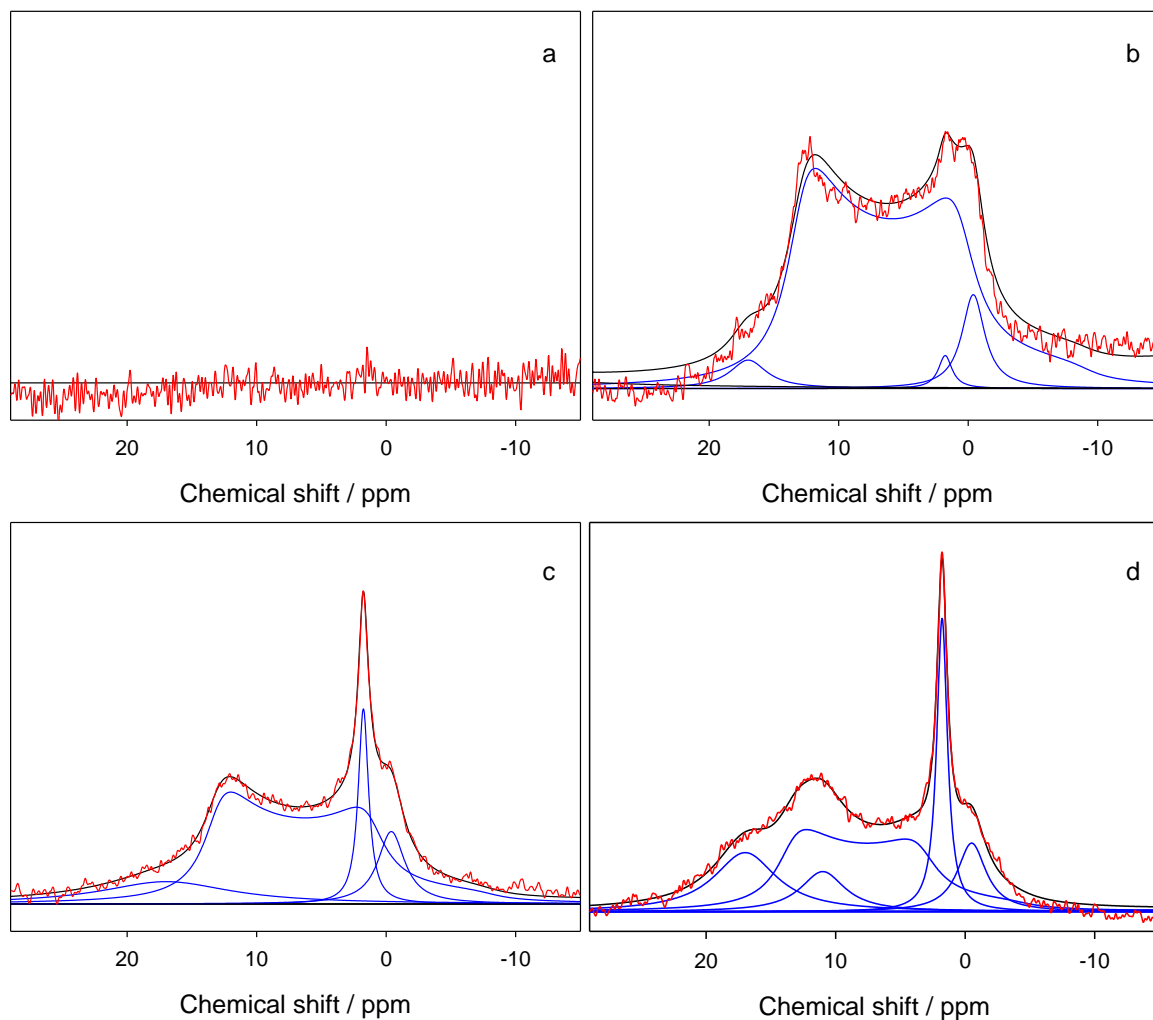
Figure 78: ¹¹**B MAS NMR spectra; as measured (red), overall fit (black) and single peaks fitted (blue). BH₄-sod (a), after 2 h at 250 °C (b), after 2 h at 300 °C (c) and after 2 h at 400 °C (d), all heated under waterloaded flowing N₂. Y-axis is enlarged for best overview each.**

Figure 78 (*a* - *d*) shows the four spectra obtained by ^{11}B MAS NMR and the fitted peaks in the chemical shift range from 29 to -15 ppm. The y-axes of the four spectra do not use the same scale. In Table 40 the relative areas of the integrated intensities of the fitted peaks are summarized for comparison, while the spectra are used for description of the peaks fitted.

As already mentioned in spectrum *a* there are no signals in the shown range visible. After the heating process up to 250 °C (spectrum *b*) four peaks (in addition to the BH_4^- signals) need to be fit to give an adequate result. At -0.51 and 16.98 ppm two gaussian/lorentzian peaks (GL) are used. Together with a quadrupole signal at 16.51 ppm and a minor GL signal of $B(OH)_4^-$ at 1.78 ppm the fit reproduces very well the measured spectrum.

To fit the spectrum of the 300 °C sample (spectrum *c*) there are no further peaks necessary. The relative areas of all peaks in the given range increase, while the BH_4^- signals decrease (cf. Tab. 40). Especially the signal of $B(OH)_4^-$ at 1.78 ppm increases.

After heating to 400 °C (spectrum *d*) an additional GL peak needs to be fit at 10.99 ppm. The intensities show the same trend as before: With increasing temperature the BH_4^- related signals decrease while the signals in the given range increase.

Table 40 summarizes the results of the peak fit, it includes the fits of the BH_4^- signals. The integrated intensities are given as relative areas (area-%) where 100 % is the sum of the signals between 60 and -160 ppm. In the last row the areas of the signals in the range from 29 to -15 ppm are summarized.

Table 40: Summarized results of the ^{11}B NMR spectra with peak fits for temperatures up to 400 °C starting from BH$_4$-Sod.

		20 °C	250 °C	300 °C	400 °C
GL1	Position / ppm	-49.09	-49.02	-49.09	-49.11
	Amplitude	52571.72	55127.23	20643.17	8782.37
	Width / ppm	1.71	2.06	1.94	1.97
	Area / %	88.99	85.06	82.57	71.81
GL2	Position / ppm	-146.50	-146.31	-146.52	-146.51
	Amplitude	2450.06	3166.10	996.69	396.12
	Width / ppm	2.09	2.29	2.35	2.26
	Area / %	5.07	5.41	4.56	3.36
GL3	Position / ppm	48.54	48.50	48.55	48.64
	Amplitude	2989.50	3765.25	1256.60	475.69
	Width / ppm	2.01	2.21	2.19	2.24
	Area / %	5.94	6.22	5.99	3.83
Quad 1	Position / ppm		16.59	16.61	16.42
	Amplitude		977.36	566.39	650.92
	em_au		333.89	339.37	417.99
	Lb / ppm		3.43	3.36	3.51
	nuQ / KHz		1301.86	1276.49	1176.27
	Em / Lorentz Hz		440.89	430.83	450.58
	Area / %		2.88	4.49	9.16
GL4	Position / ppm		16.98	17.00	16.98
	Amplitude		45.41	38.59	151.97
	Width / ppm		3.44	10.95	5.87
	Area / %		0.12	0.93	4.14
GL5	Position / ppm		1.77	1.75	1.78
	Amplitude		52.62	351.73	753.72
	Width / ppm		1.28	1.01	1.00
	Area / %		0.05	0.79	3.50
GL6	Position / ppm		-0.40	-0.39	-0.51
	Amplitude		149.37	132.40	176.44
	Width / ppm		2.13	2.30	2.68
	Area / %		0.25	0.68	2.20
GL7	Position / ppm				10.99
	Amplitude				103.28
	Width / ppm				4.16
	Area / %				2.00
Area without BH$_4^-$ / %		0.00	3.30	6.76	21.00

Figure 79 displays the FTIR spectra of the same samples for comparison. The spectrum of the sample heated to 250 °C (red) shows slightly decreased amounts of the BH_4^- signals, visible at the triplet-peak around 2250 cm^{-1} and the peak at 1130 cm^{-1} (shoulder). The signals of species 'A' can be observed at 1290 and 1310 cm^{-1}, respectively. Furthermore the water amount decreased during heating, visible at the lower intensities around 1630 and 3600 cm^{-1}. In the O-H range a maximum can be observed, which is related to the formation of small amounts of $B(OH)_4^-$. Further heating to 300 °C exhibits an ongoing decrease of the BH_4^- related signals and a further increase of species 'A'. In addition the signal at 1440 cm^{-1} and the $B(OH)_4^-$ signal increase compared to the previous spectrum. The spectrum of the 400 °C sample shows further decreased BH_4^- signals, while the intensities of the $B(OH)_4^-$ peak and species 'A' remain constant. At 1959 and 2028 cm^{-1} two signals are observed, they are related to the formation of BO_2^-. Additional to the signal at 1440 cm^{-1} a further signal occurs at 1450 cm^{-1} and 1500 cm^{-1}.
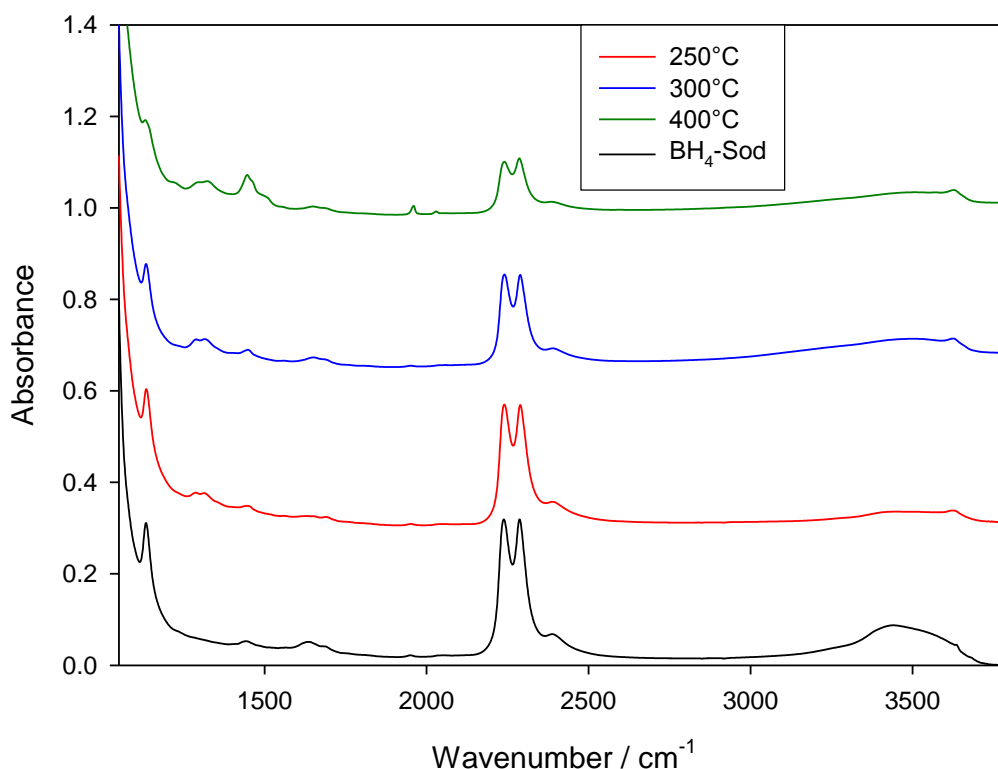
Figure 79: FTIR spectra of the same samples for comparison.

6.3. TG Series

In this subchapter, the thermal reaction of BH_4-sod is analyzed in dependence of reaction temperature, reaction time and atmosphere. The experiments were carried out in the *Setaram SetSys Evolution 1750* TG/DTA, thus it is possible to control the reaction parameters very precisely. As sample material, the microcrystalline BH_4-Sod with a $NaBH_4$/matrix wt-ratio of 0.6, synthesized at 120 °C (name: E), was chosen. The temperatures ranged from 200 to 500 °C and the reaction time was varied from 15 min to 48 h. The measurements were carried out in a synthetic air flow (80 % N_2/20 % O_2) in order to analyze a possible influence of the atmosphere on the reaction, selected analyses were repeated under flowing helium. In Table 41, the TG/DTA parameters are summarized. Data were evaluated for the relevant signals, obtained by FTIR.

Table 41: Measuring parameter used for TG-series

Parameter	Value
Carrier gas	syn. air / He
Carrier Flow / ml/min	20
Temperature / °C	150 - 500
Holding time / h	0.25 - 48
Heating- cooling rate / K/min	5

6.3.1. TG Series - Temperature

Reaction degree and the occurring species are closely related to the temperature, the samples were exposed to. The influence is shown in the following by samples, heated up to 400 °C, with a holding time of 12 h under flowing synthetic air. Figure 80 shows the FTIR spectrum of the base sample (E) and the spectra after the thermal treatment.
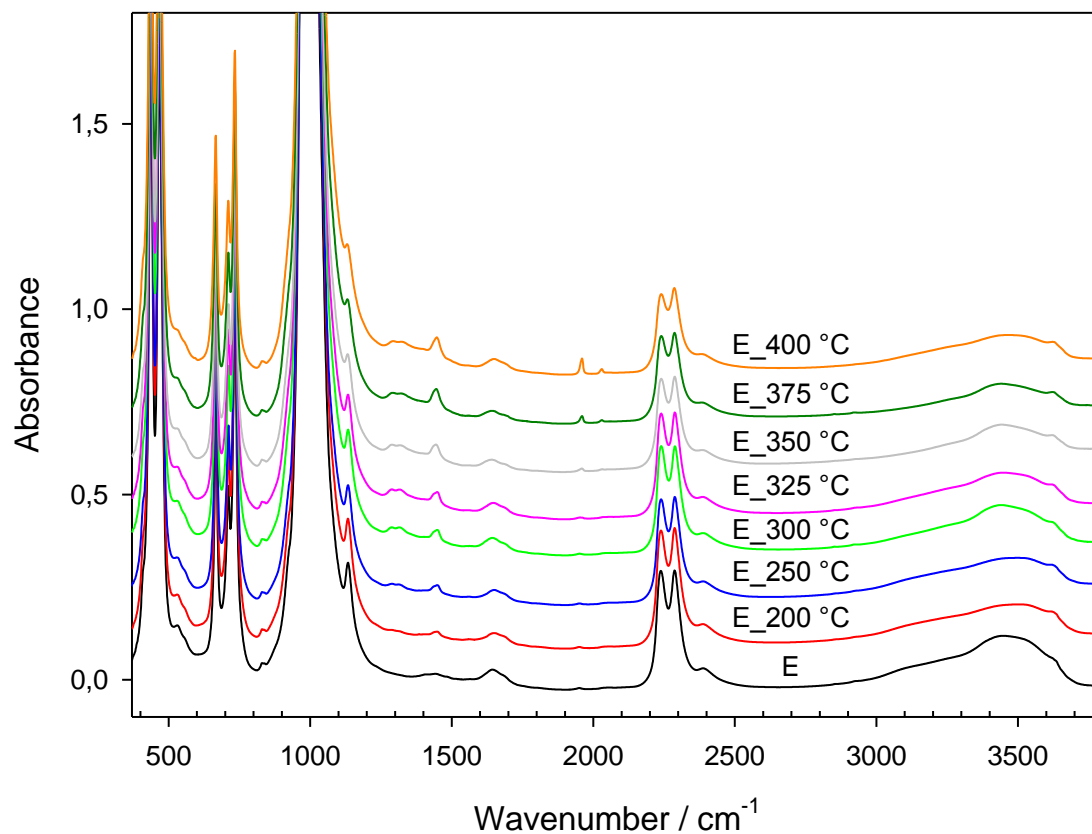
Figure 80: FTIR spectra of synthesis batch E, tempered at different temperatures. Spectra are normalized on the mass used for pellet preparation.

Figure 81 shows the mass normalized integrated intensities of the spectra from Figure 80 for the species BH_4^- and BO_2^-, plotted against temperature. The values were normalized on the sample mass used. BH_4^- intensities remained constant up to 150 °C, above that temperature, the intensities decrease slightly till 275 °C. With further increased temperature, the intensities show a linear decrease in the range from 325 to 400 °C. BO_2^- can be detected at temperatures above 275 °C. Above 325 °C the intensities increase exponentially.
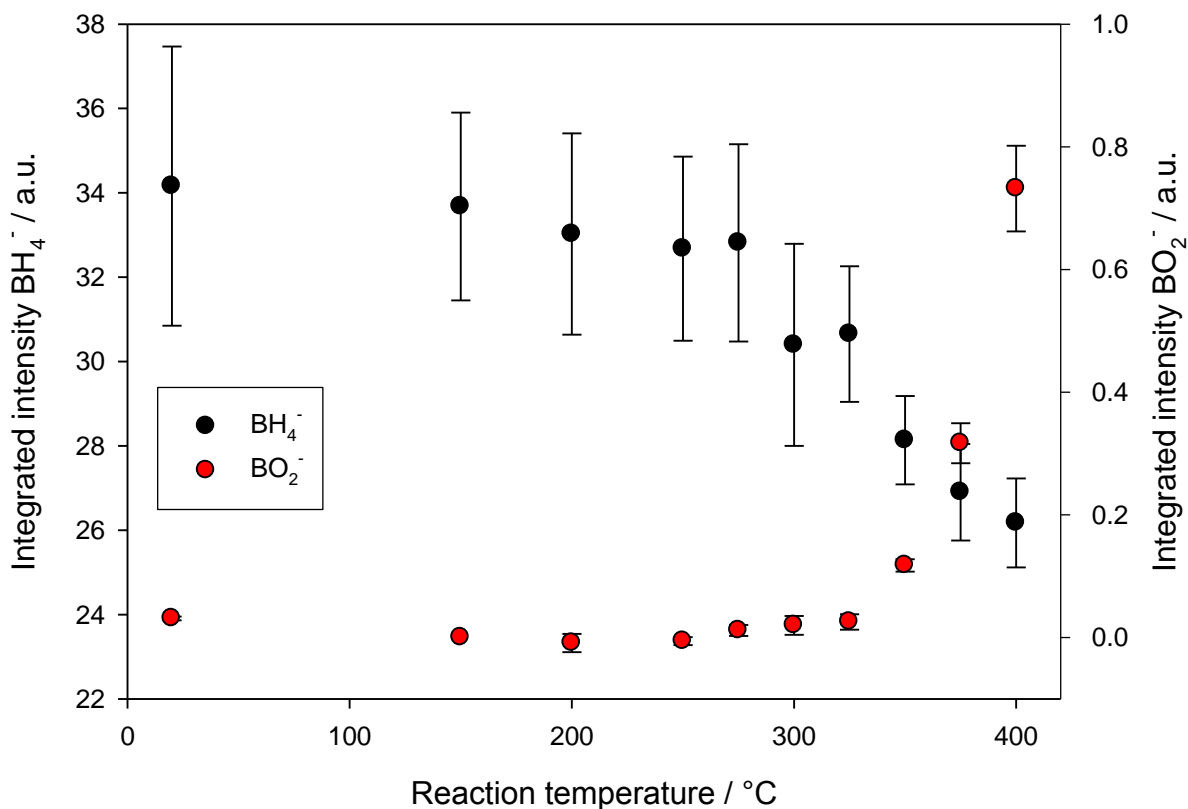
Figure 81: Integrated intensities of BH₄⁻ (black) and BO2- (red) obtained from FTIR spectra shown in Figure 80. Error bars represent 2·σ.

The integrated intensities of species 'A' are displayed in Figure 82. Below 200 °C this species shows no intensity. From 200 °C to 350 °C the integrated intensities increase, run through a maximum and decrease above 350 °C.
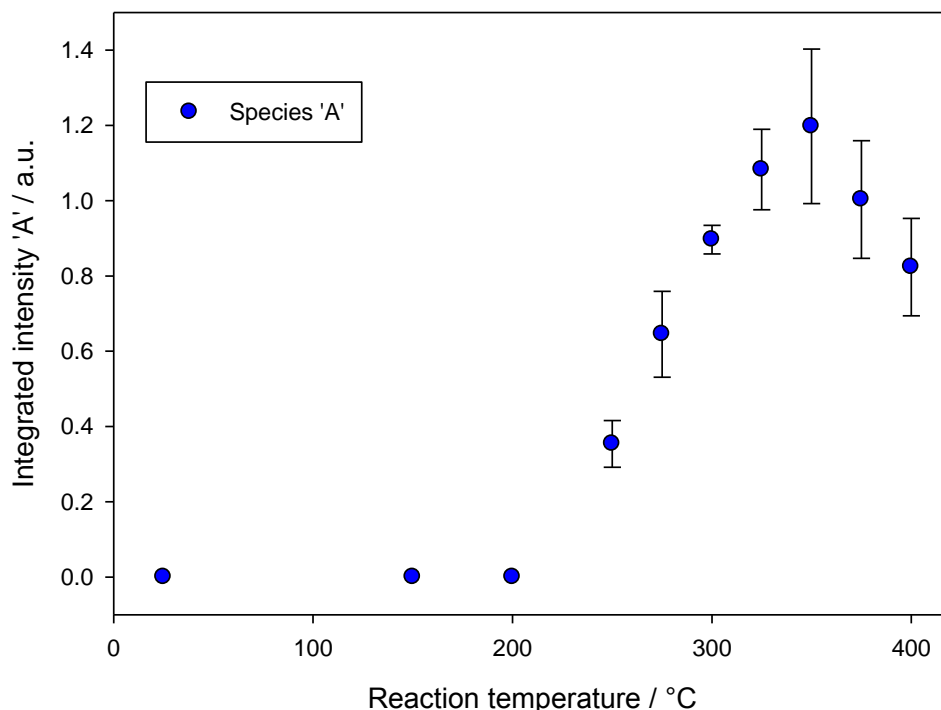
Figure 82: Integrated intensities of species 'A' obtained from FTIR spectra shown in Figure 80. Error bars represent 2·σ.

6.3.2. TG Series - Time

The starting material *E* was analyzed in the TG/DTA with varied holding times from 15 minutes to 12 hours with different maximal temperatures. The heating and cooling rate was kept constant for all analyses at 5 °C/min. All measurements were carried out under a synthetic air flow (20 ml/min).

Figure 83 shows the mass normalized integrated intensities of BH_4^- of the samples obtained after the thermal treatment in comparison with the starting value. After 15 minutes of holding time, all samples showed a decrease in their BH_4^- intensities corresponding to the maximum temperature; the higher the maximum temperature the higher the intensity decrease. After one hour holding time the integrated intensities decreased further, independently of the maximum temperatures. The sample behavior changed with longer holding times; the intensities remained constant in the temperature range from 250 to 350 °C at a holding time of 6 hours, while the samples tempered at 375 and 400 °C showed a further

decrease in their BH_4^- intensities. After 12 hours hold at the different maximum temperatures, the intensities of BH_4^- showed no further decrease at 250 and 400 °C within the given errors. The intermediate temperatures lead to a further decrease of the BH_4^- intensities after 12 hours holding time.
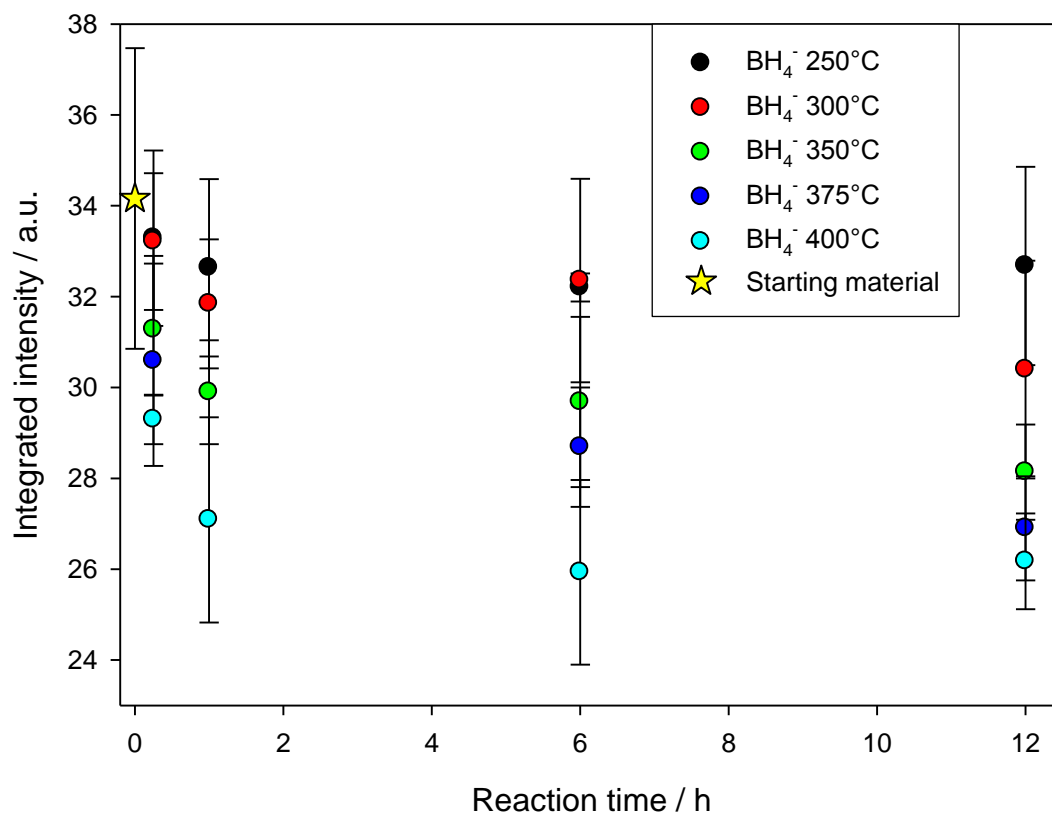
Figure 83: Integrated intensities of BH_4^- after TG/DTA measurements. Temperature ranges from 250 to 400 °C and reaction time ranges from 15 minutes to 12 hours. Error bars represent 2·σ. Integrated intensity before the thermal treatment is given as reference (yellow star).

Figure 84 shows the mass normalized integrated intensities of BO_2^- in the same way. The temperatures 250 and 300 °C showed no measureable intensities of BO_2^- within the reaction times applied. BO_2^- showed first significant intensities at temperatures above 350 °C under flowing synthetic air. The temperatures 350, 375 and 400 °C showed identical trends; with increased temperature the intensities increased and with longer holding times the intensities increased, too.
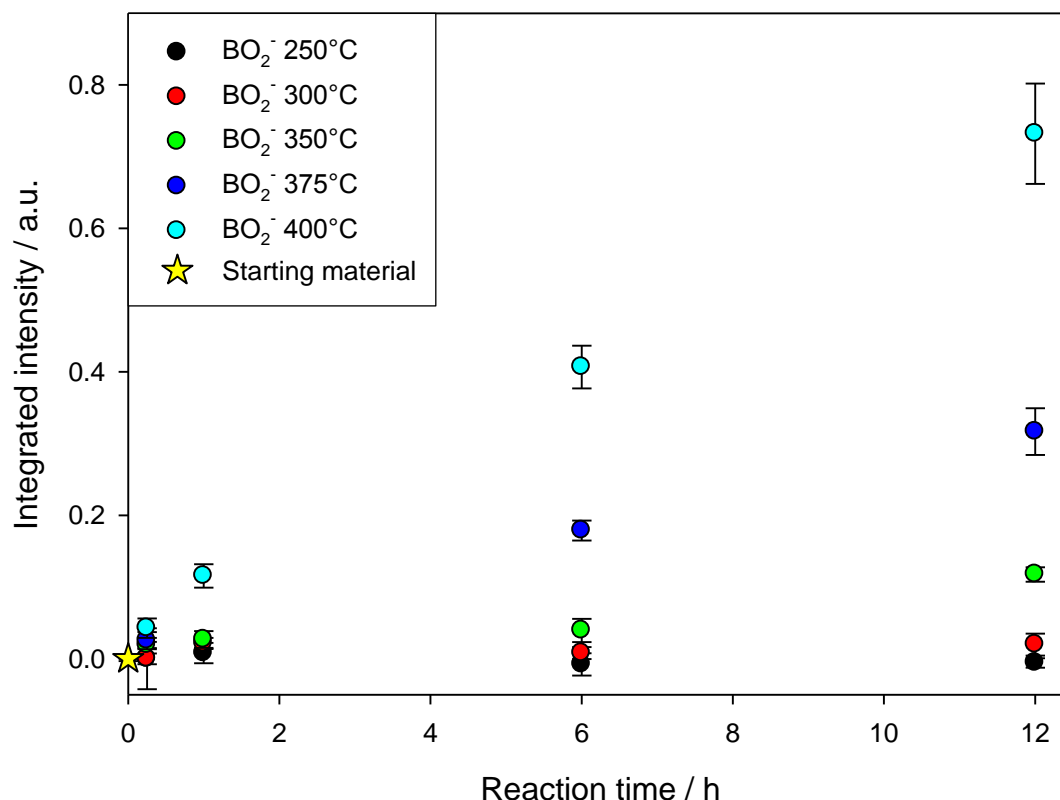
Figure 84: Integrated intensities of BO$_2^-$ after TG/DTA measurements. Temperature ranges from 250 to 400 °C and reaction time ranges from 15 minutes to 12 hours. Error bars represent 2·σ. Integrated intensity before the thermal treatment is given as reference (yellow star).

The integrated intensities of species 'A' are displayed in Figure 85. At temperatures of 250 and 300 °C the integrated intensities show an exponential increase with longer reaction time but with higher intensities at 300 °C. With higher temperatures the intensities increase rapidly, too, but with longer reaction times the intensities remain more or less constant. The intensities of the 400 °C series show a decrease after 6 hours reaction and a slightly increase with further reaction time. The integrated intensities of species 'A' after 12 hours are identical within the errors for all temperatures above 300 °C.
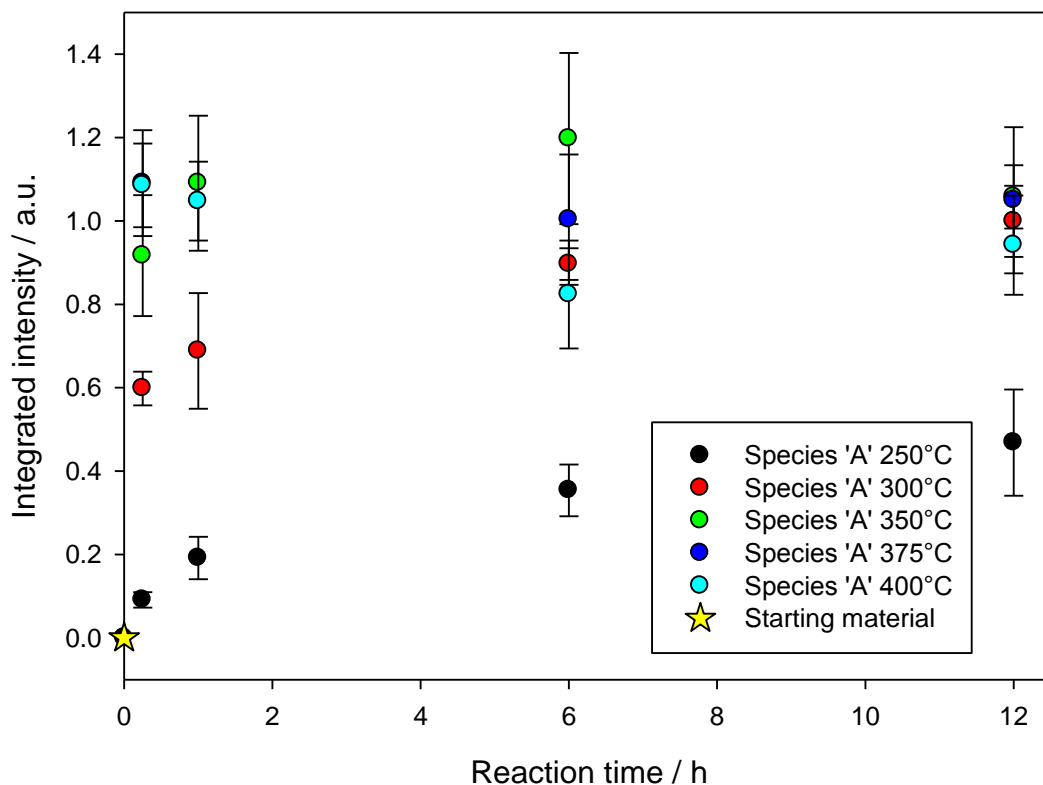
Figure 85: Integrated intensities of species 'A'¨ after TG/DTA measurements. Temperature ranges from 250 to 400 °C and reaction time ranges from 15 minutes to 12 hours. Error bars represent 2·σ. Integrated intensity before the thermal treatment is given as reference (yellow star).

The Figures below (86 to 88) display the FTIR spectra of the samples tempered at 250, 350 and 400 °C for the reaction times from 0.25 hours to 12 hours. Colours of the spectra are chosen analogous to the data points used in the previous Figures. The spectra of the 250 °C series show increasing amounts of the signals at 1290 and 1310 cm^{-1} with increasing reaction time. Furthermore the carbonate related signal changes from broad in the starting material to a well defined peak at 1440 cm^{-1}.
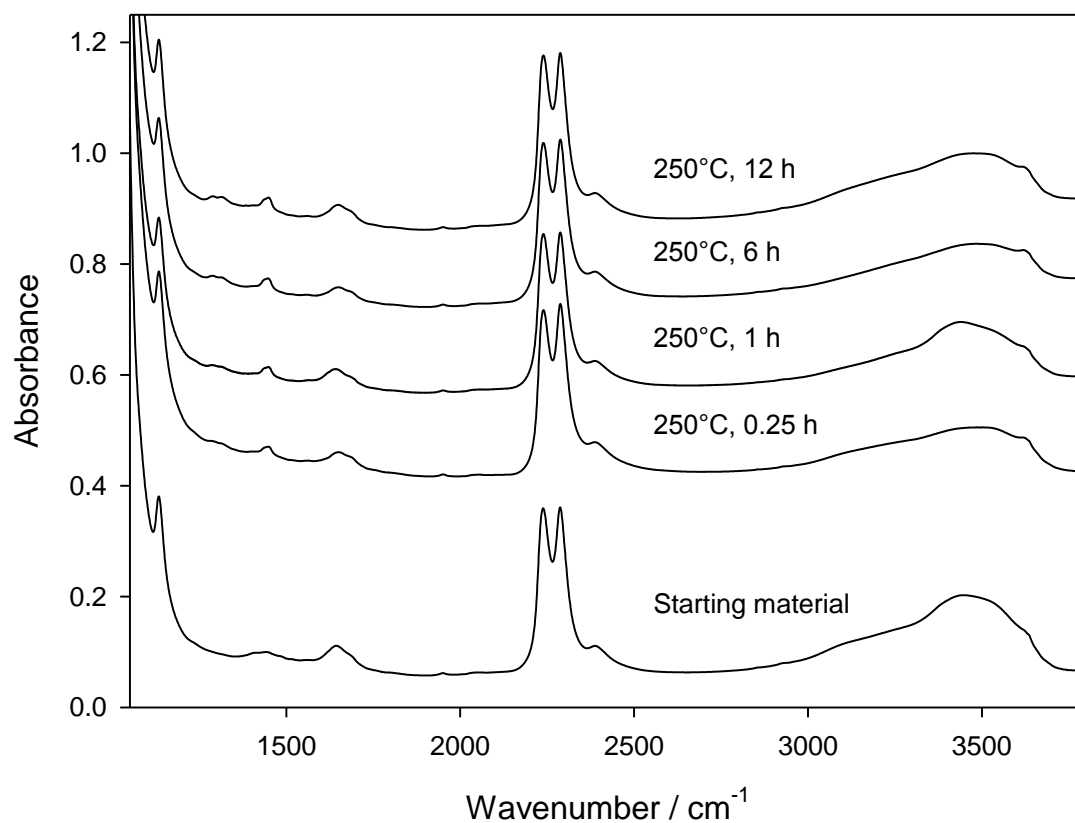
Figure 86: FTIR spectra of the 250 °C series with reaction times from 15 minutes to 12 hours, the spectrum of the starting material is given for comparison (bottom).

Spectra of the 350 °C series exhibit intensities of the signals at 1290 and 1310 cm^{-1}, which show no change with further reaction time. The carbonate signal becomes even more pronounced. After 6 hours first signals of formed BO_2^- can be observed at 1958 and 2029 cm^{-1}. The intensities of BO_2^- increase with longer reaction time.
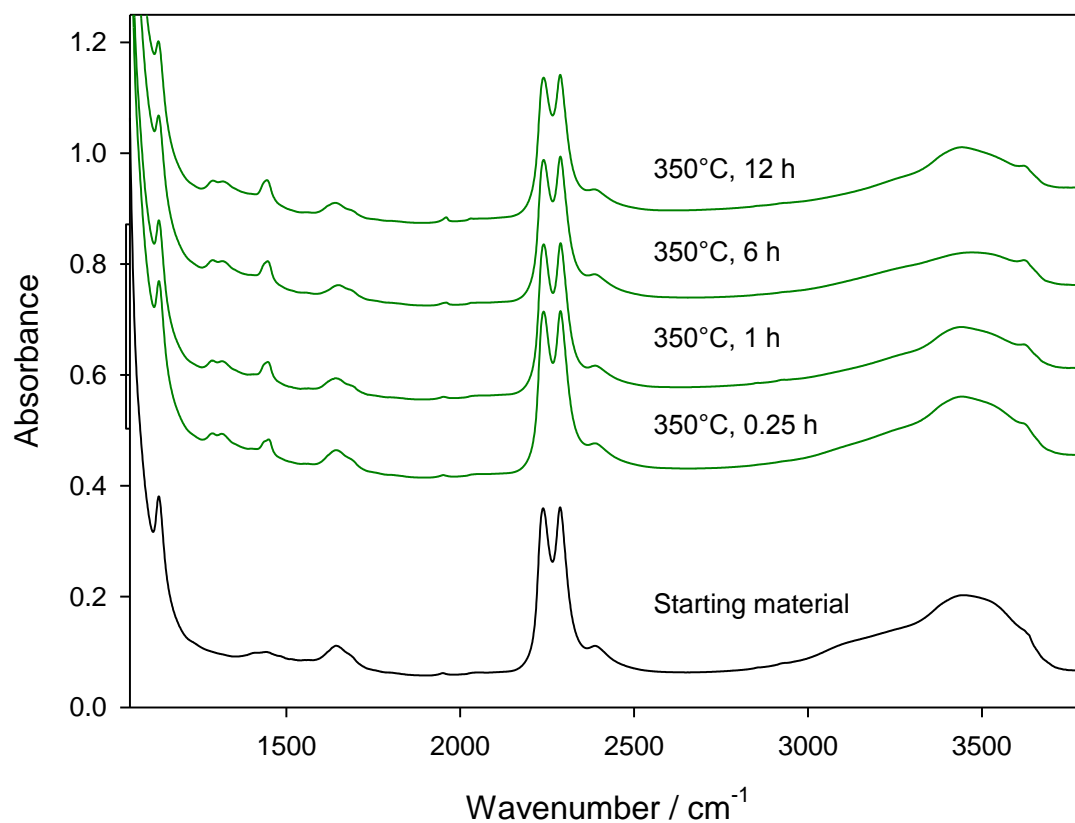
Figure 87: FTIR spectra of the 350 °C series with reaction times from 15 minutes to 12 hours, the spectrum of the starting material is given for comparison (bottom).

The spectra of the 400 °C series exhibit signals of species 'A' at 1290 and 1310 cm^{-1}, which remain constant with increasing reaction time. Carbonate related peak slightly increases with reaction time. The BO_2^- signals show increasing intensities with further extended reaction time.
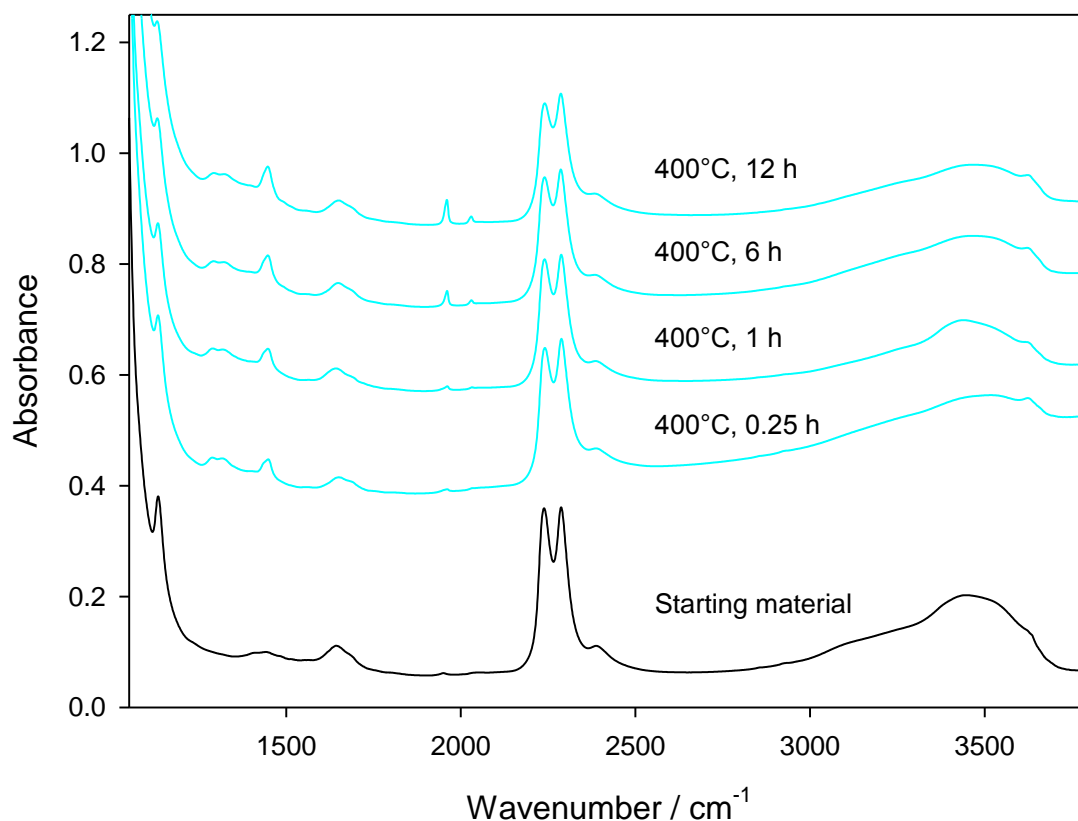
Figure 88: FTIR spectra of the 400 °C series with reaction times from 15 minutes to 12 hours, the spectrum of the starting material is given for comparison (bottom).

6.3.3. TG Series - Atmosphere

In this section, the influence of the atmosphere on the reaction of BH_4^- sodalite was analyzed. Sample material *E* was used as starting material again. The samples were heated for 6 hours at temperatures from 200 to 500 °C under a helium flow and afterwards under synthetic air (both 20 ml/min). The heating and cooling rate was kept constant at 5 °C/min.

Figure 89 shows the mass normalized integrated intensities of BH_4^- and BO_2^- for different temperatures and the two atmospheres chosen in comparison to the starting material. The BH_4^- intensities remained constant up to 200 °C under flowing synthetic air and helium. Above 350 °C the samples showed first dependence of the gas atmosphere used; under flowing synthetic air the intensity of BH_4^- decreased further than under flowing helium at identical temperatures. With further elevation of the reaction temperatures this effect became more pronounced. At 500 °C the BH_4^- intensity of the sample heated under flowing

synthetic air was decreased by 83.7 % compared to the starting material, while the same material heated under flowing helium showed a decrease of 34.4 % only.

Similar effects were observed for the integrated intensities of formed BO_2^-; up to 350 °C the samples showed no significant differences in dependency of the gas atmosphere. At 400 °C the sample heated under flowing synthetic air showed higher intensities of BO_2^- than the sample heated under flowing helium. This effect was even more pronounced at 500 °C; the integrated intensity of BO_2^- was 4 times higher when heated under flowing synthetic air, compared to the sample heated under flowing helium.
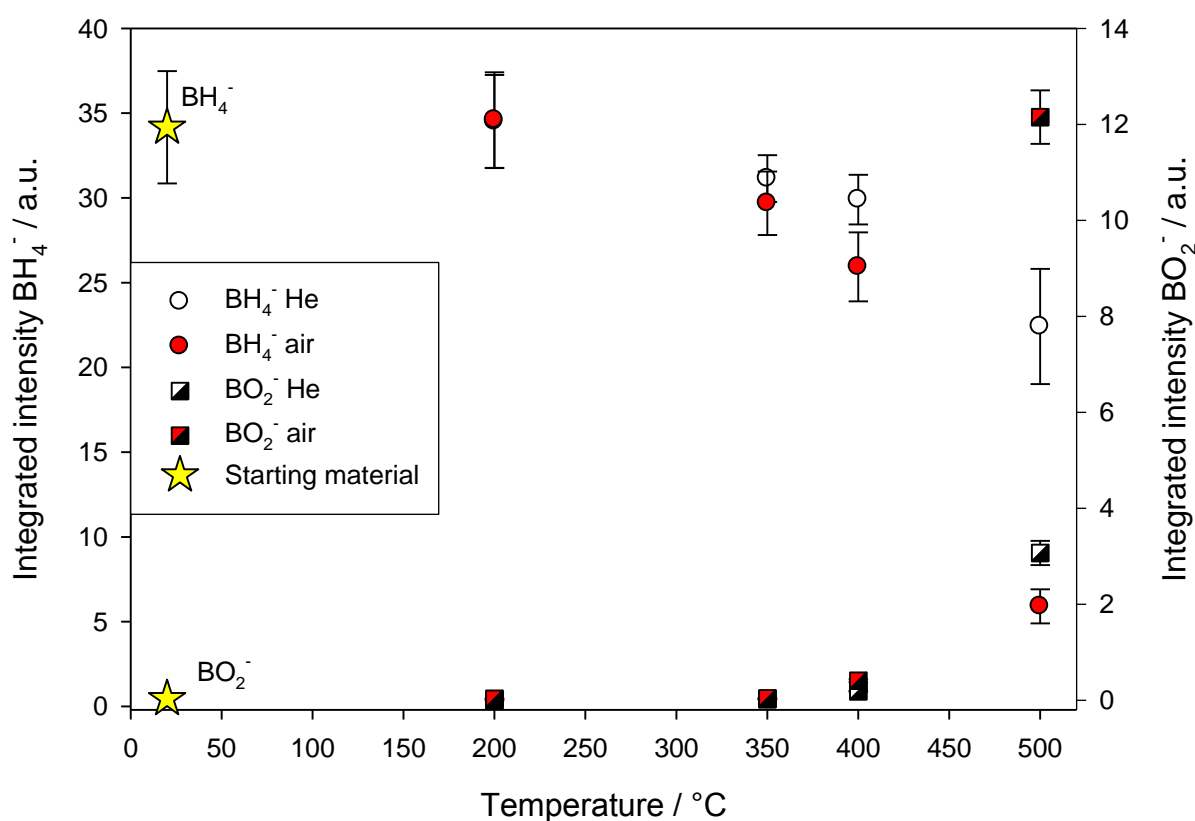
Figure 89: Integrated intensities of BH_4^- and BO_2^- after TG/DTA measurements. Temperature ranges from 200 to 500 °C under flowing synthetic air and helium. Error bars represent 2·σ. Integrated intensity before the thermal treatment is given as reference (yellow stars).

The integrated intensities of species 'A' are displayed in Figure 90. First formed species 'A' can be observed at 250 °C. With further increased temperature the intensities increase, too, until 350 °C. At this temperature the intensities reach a maximum. Up to

500 °C the intensities decrease in a linear way. There is no difference visible if heated in a

flow of air or helium.
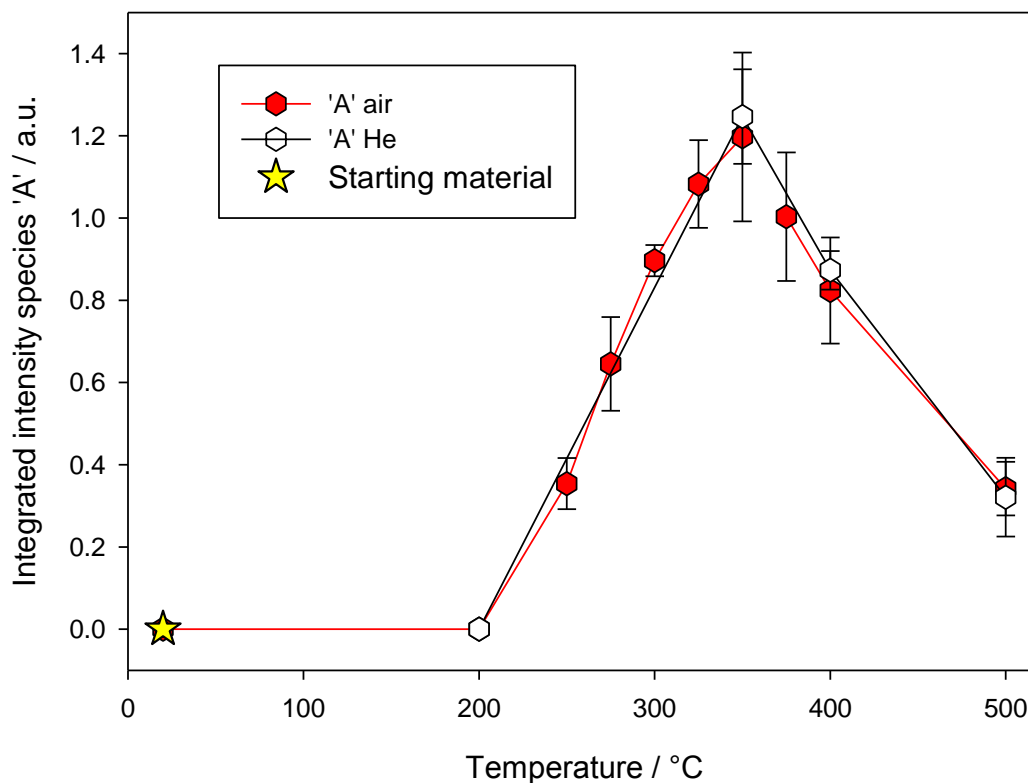
Figure 90: Integrated intensities of species 'A' after TG/DTA measurements. Temperature ranges from 200 to 500 °C under flowing synthetic air and helium. Error bars represent 2·σ. Integrated intensity before the thermal treatment is given as reference (yellow stars).

6.4. Particle Size and Internal Water

All samples of the three synthesis series were heated in TG/DTA under flowing He up to

500 °C (see Chapter 5.1.3., 5.2.3. and 5.3.3.), the products were afterwards analyzed and

compared to the starting material by FTIR.

6.4.1. 120 °C series

The FTIR spectra of the 120 °C synthesis series show the sodalite bands, still after the

thermal treatment. There are several changes visible, concerning the cage fillings and the

water amount. In Figure 91, the spectra are shown from $NaBH_4$/matrix wt-ratio 0.0 to 1.5 from

bottom to top. The two least $NaBH_4$/matrix samples show high amounts of water, visible at

the peaks at 1630 and the broad area around 3500 cm^{-1}. Additionally, both spectra exhibit a sharp signal at 1446 cm^{-1} related to carbonate. The 0.03 sample shows small amounts of residual NaBH$_4$ at the triplet-peak position around 2266 cm^{-1}.

The amount of water and the carbonate peak decrease after the thermal treatment, with increasing NaBH$_4$/matrix ratio. Above a NaBH$_4$/matrix ratio of 0.4, there is no remaining water visible. Samples above NaBH$_4$/matrix of 0.05 also show a new peak pair at 1959 and 2029 cm^{-1}. These peaks are related to the newly formed BO$_2^-$ inside a sodalite cage [27]. This double peak and the remaining amounts of NaBH$_4$ increase with increasing NaBH$_4$/matrix ratios. Furthermore above a NaBH$_4$/matrix ratio of 0.4 there are increasing amounts of new formed peaks at 1290 and 1315 cm^{-1} and around 1360 cm^{-1}.
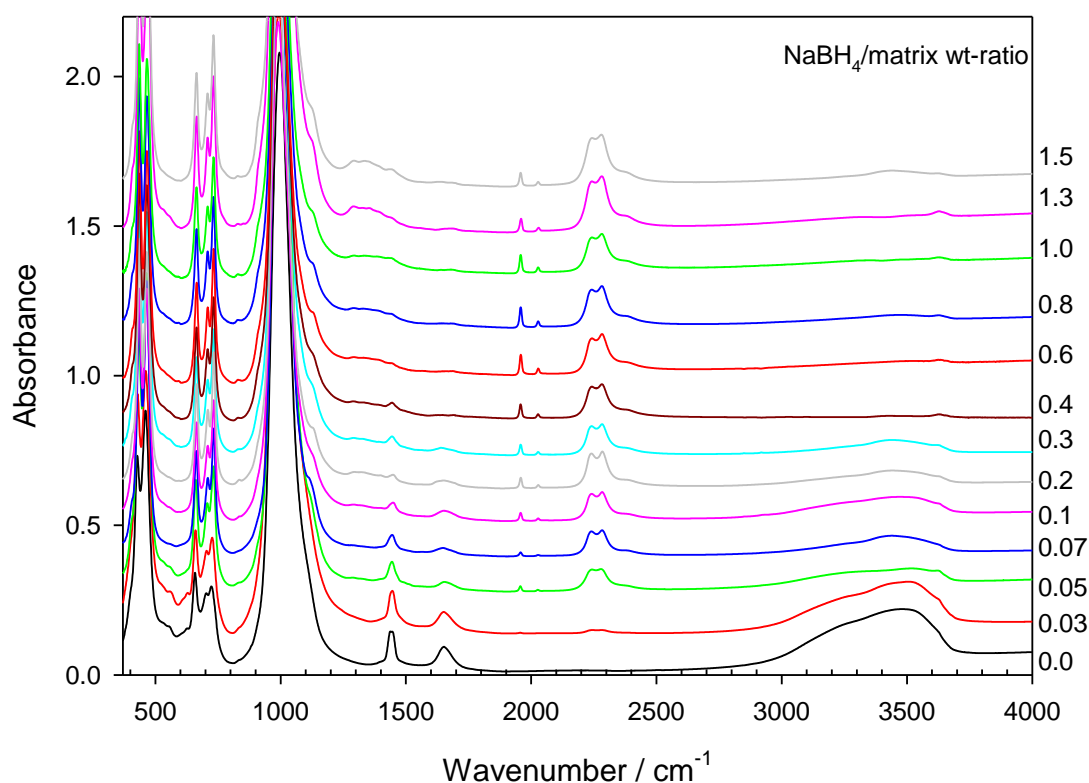
Figure 91: FTIR spectra of the 120 °C series after TG up to 500 °C for varied NaBH$_4$/matrix wt-ratios

Figure 92 summarizes the results of the reaction by comparing the BH$_4^-$ intensities before (red dots) and after (blue dots) the TG/DTA measurements up to 500 °C in flowing

Helium and the resulting percentage decrease of BH_4^- (black squares). The decrease is equivalent to the reaction degree of the BH_4^- in the sodalite cage. After the thermal treatment, the BH_4^- intensities show the same exponential behavior with increasing $NaBH_4$/matrix ratio as the samples before the measurements, this results in a more or less constant, percentage reaction degree of 17 %. Only the $NaBH_4$/matrix ratio of 0.03 shows a higher reaction degree of up to 80 %.
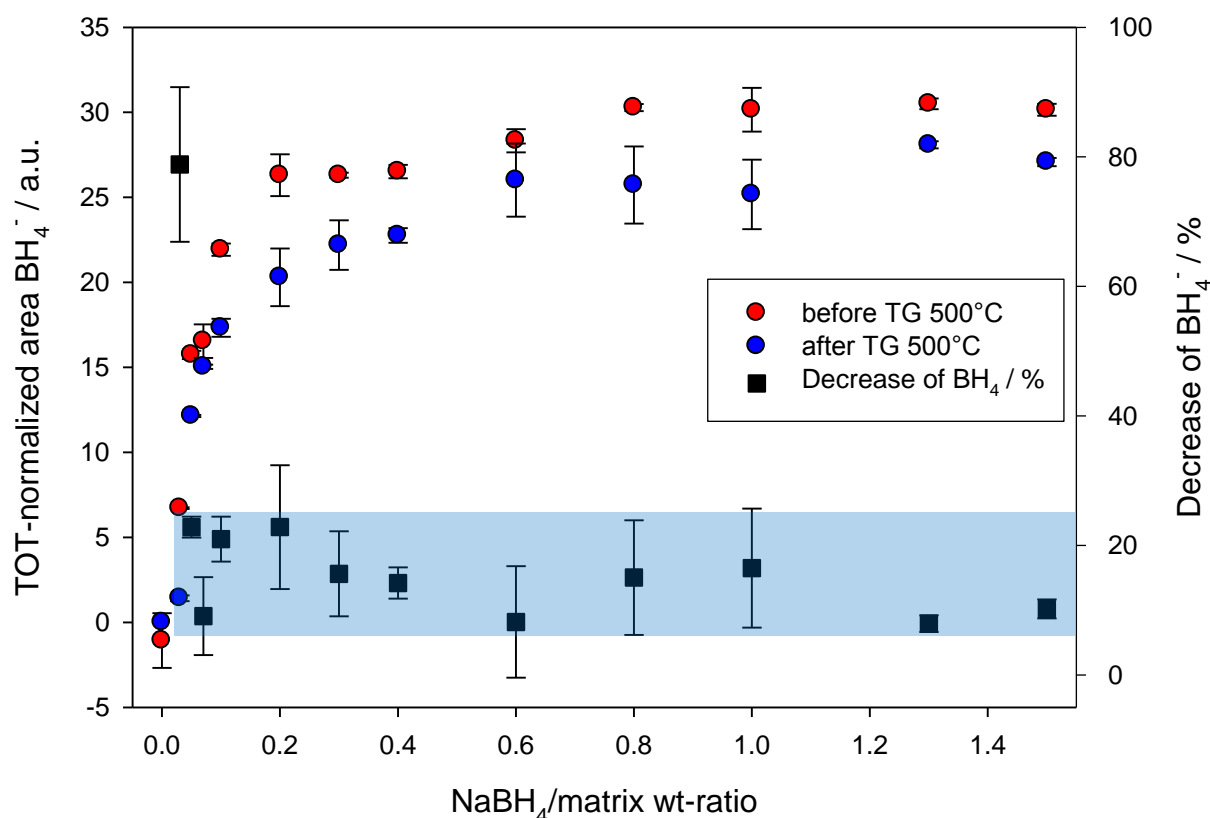
Figure 92: Integrated intensities of BH_4^- of the 120 °C series before and after the thermal treatment up to 500 °C. Additionally shown is the reaction degree.

6.4.2. 80 °C series

The reaction of the 80 °C series via the thermal treatment of the TG/DTA measurements up to 500 °C in helium proceeded similar to the 120 °C series. IR spectra of the samples after the measurements (see Fig. 93) show no changes in the matrix related areas from 370 to 1100 cm^{-1}. Only the samples with a $NaBH_4$/matrix from 0 to 0.2 show molecular water around

1650 cm^{-1} and therefore significant OH signals around 3500 cm^{-1}. The signal at 1450 cm^{-1} is visible in almost all spectra, especially with low NaBH$_4$/matrix ratios, but there is no further trend observable. With increasing NaBH$_4$/matrix ratio the species around 1300 cm^{-1} as well as the BO$_2^-$ double peak at 1950 and 2025 cm^{-1} increase in their intensities.
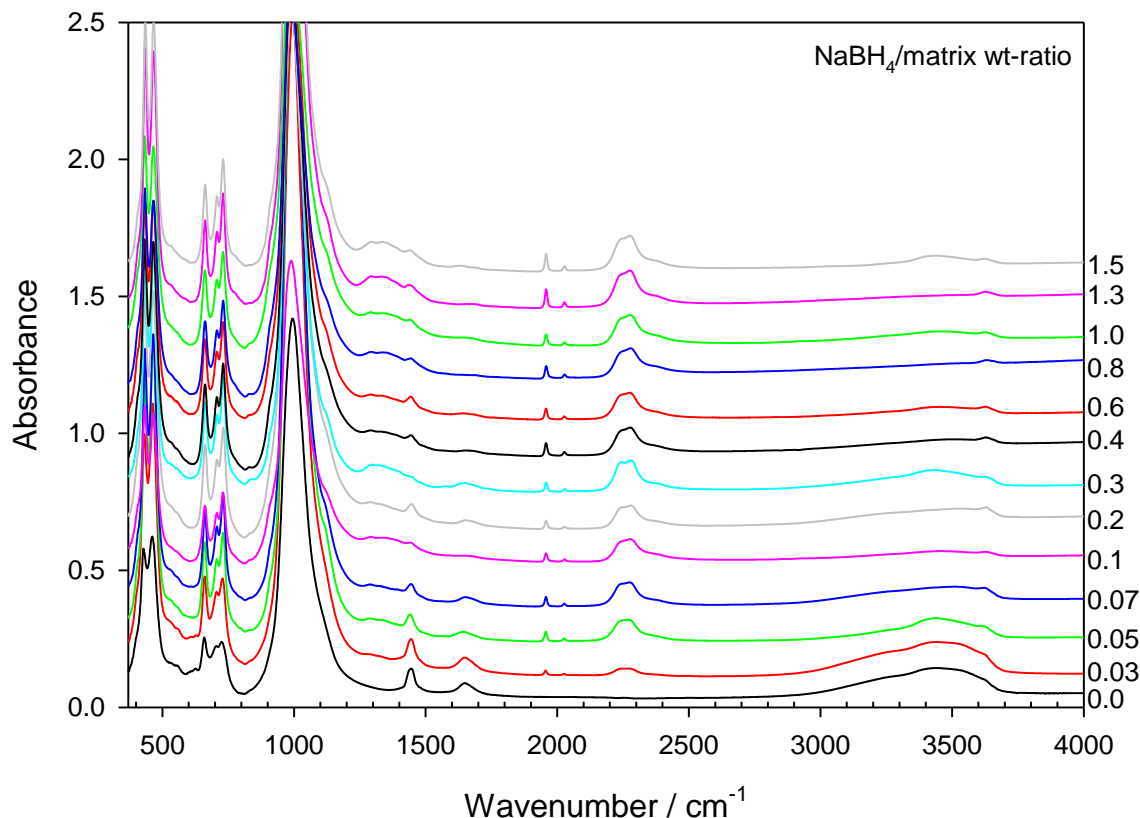
Figure 93: FTIR spectra of the 80 °C series after TG up to 500 °C for varied NaBH$_4$/matrix wt-ratios

Figure 94 shows the comparison of the BH$_4^-$ intensities before (red dots) and after (blue dots) the TG/DTA measurements up to 500 °C in a helium flow and the resulting percentage of BH$_4^-$ decrease (black squares). The decrease is equivalent to the reaction degree of the BH$_4^-$ in the sodalite cage. The integrated intensities before and after the TG show the same proportion. The only difference is the more or less constant reduction of intensity afterwards. This results in a percentage reaction degree of about 23 %. Only the NaBH$_4$/matrix ratio of 0.03 shows a higher reaction degree of about 60 %.
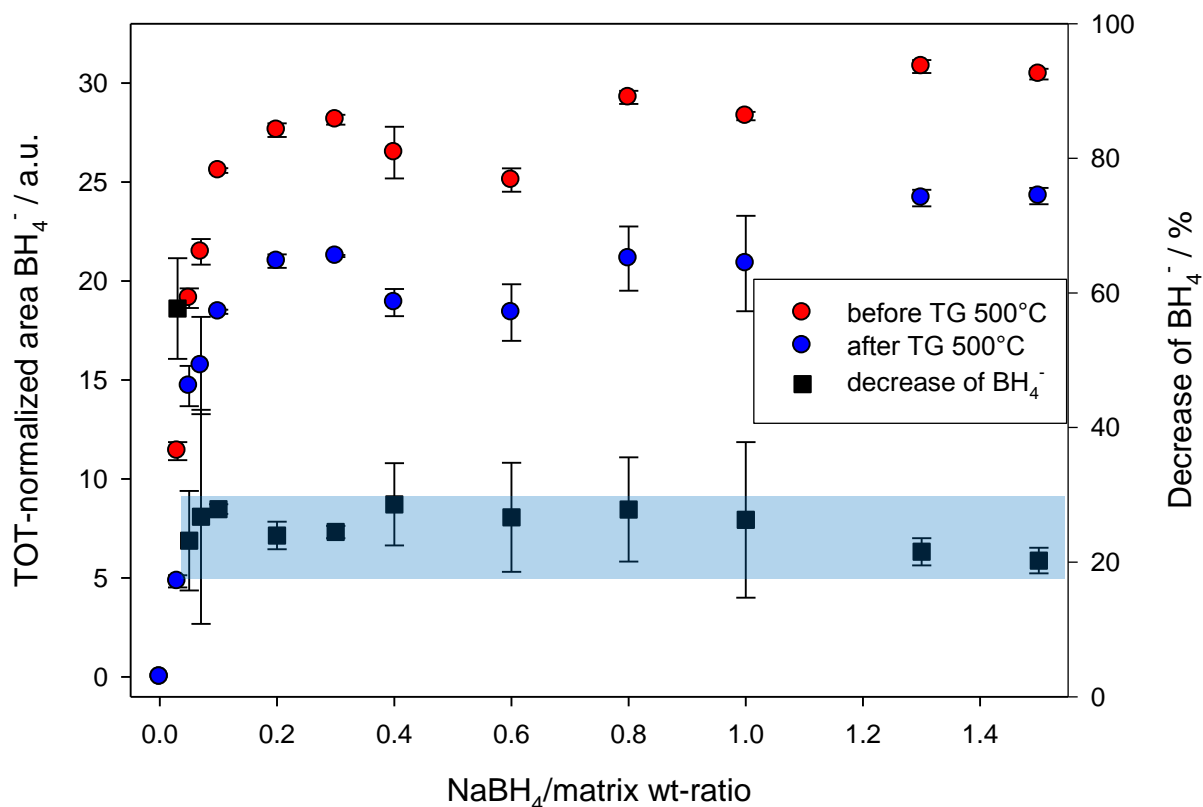
Figure 94: Integrated intensities of BH$_4^-$ of the 80 °C series before and after the thermal treatment up to 500 °C. Additionally shown is the reaction degree.

6.4.3. 60 °C series

The reaction shows significant differences to the 80 °C and 120 °C synthesis series. The samples with NaBH$_4$/matrix ratios from 0 to 0.2 show no BH$_4^-$ signals after the thermal treatment. There are also almost no intermediate species or the final product BO$_2^-$ visible. Furthermore, all spectra show high amounts of water and therefore OH$^-$ vibrations. The matrix related signals show no differences before and after the measurements. Samples with NaBH$_4$/matrix of 0.3 and above, exhibit small amounts of residual BH$_4^-$ and signals of BO$_2^-$. Additionally these samples show signals of further species in the range from 1250 to 1500 cm^{-1}. Those signals need to be evaluated critically, the peak form of the potential species 'A' at 1290 and 1310 cm^{-1} in the microcrystalline sodalites exhibits a double peak, here the signals are broader, which might be a hint for the identification of decomposition products. Those species occur in the microcrystalline sodalites at higher temperatures and

are interpreted as borate-species, outside of the sodalite cages. This explains the leak of visible BO_2^- signals.
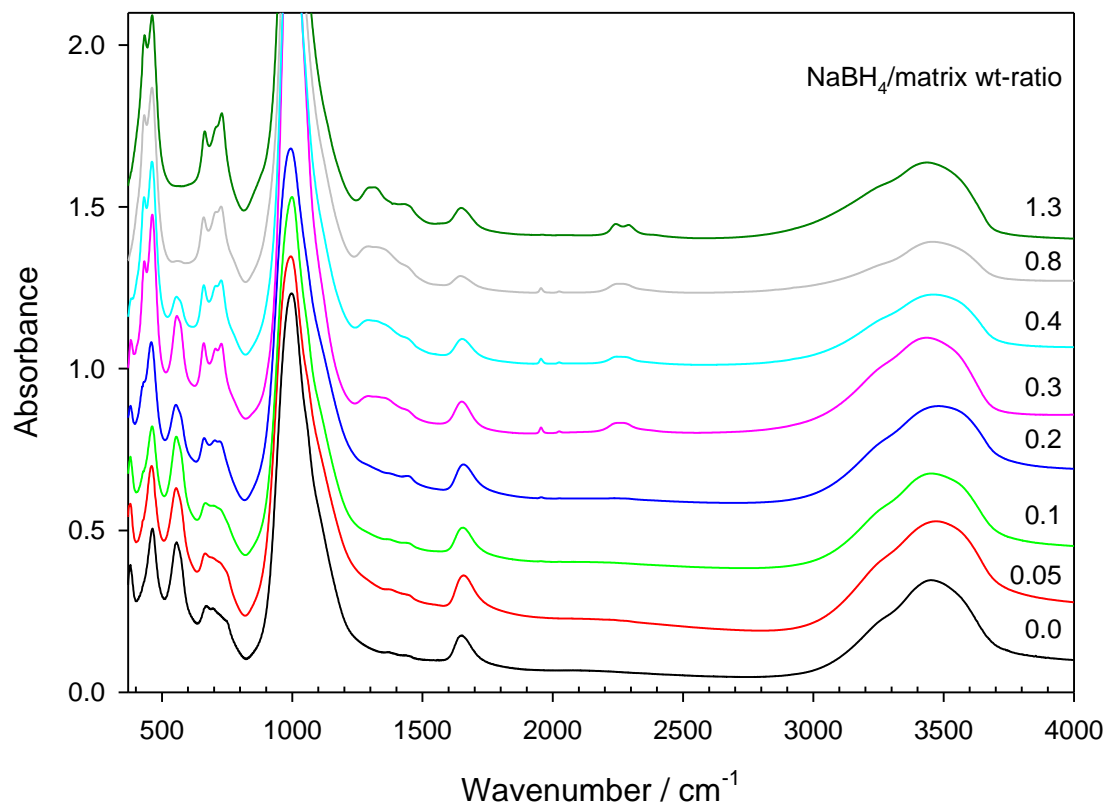
Figure 95: FTIR spectra of the 60 °C series after TG up to 500 °C for varied NaBH₄/matrix wt-ratios

In Figure 96, the mass-normalized integrated intensities of the BH_4^- triplet peak before (red dots) and after (blue dots) the TG/DTA measurements are plotted together with the percentage decrease as a function of the NaBH₄/matrix ratio. The reaction degree of this sample series is throughout the NaBH₄/matrix ratio higher than 70 %.
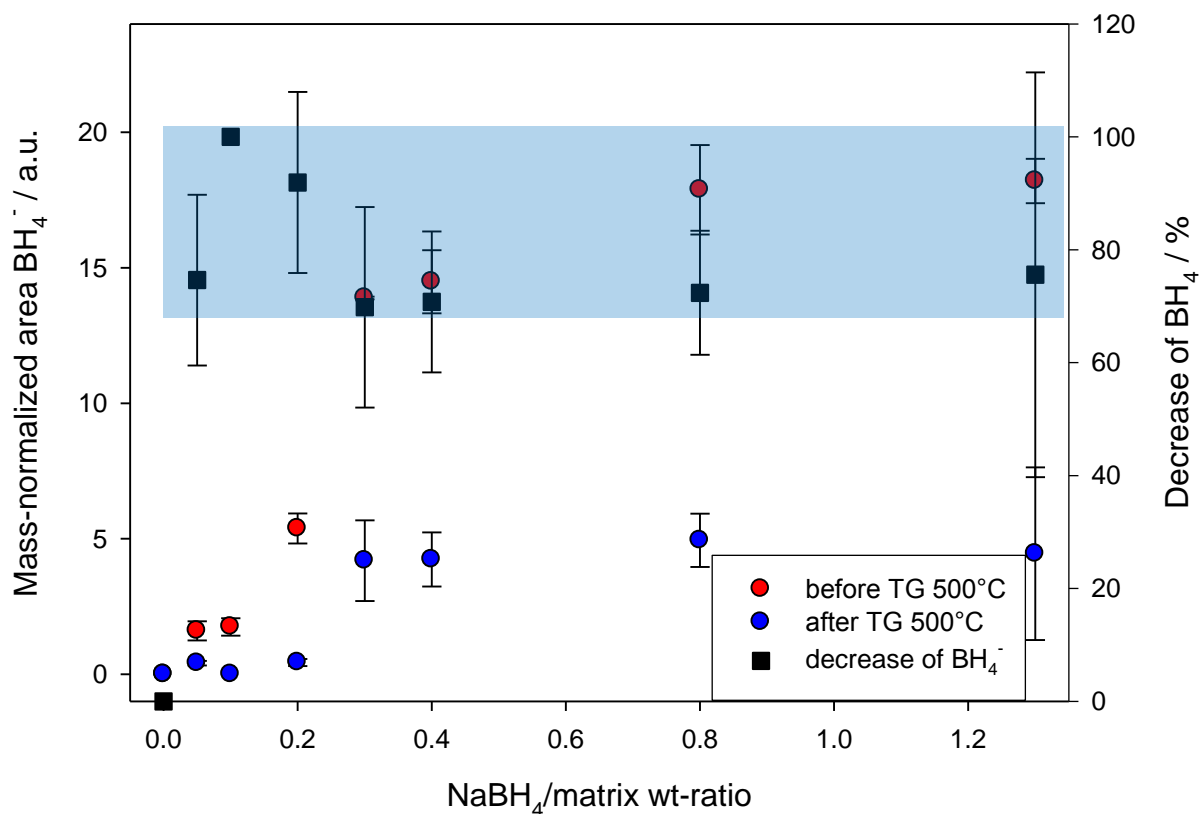
Figure 96: Integrated intensities of BH$_4^-$ of the 60 °C series before and after the thermal treatment up to 500 °C. Additionally shown is the reaction degree.

6.5. External Water

The aim of these analyses is to show, whether externally provided water influences the reaction degree of NaBH$_4$ containing sodalite or if the reaction uses internal water, only.

To analyze the influence of external water, the experiments are carried out in a tube furnace, as shown as a scheme in Figure 97. The experimental setup consists of the furnace with a quartz glass tube (A), two washing flasks filled with water (B and B') and a heating plate (C). The water in washing flask B on the left hand side is heated slightly below its boiling temperature to increase the vapor pressure. Using a nitrogen stream, the water vapor is transported through the furnace and over the sample, positioned in the glass tube in a ceramic combustion boat (D). To prevent the vapor from condensation in the inlet pipe to the furnace and the upper part of the washing flask are isolated with aluminum foil. The

downstream connected washing flask (B') works as bubble counter to control the nitrogen stream.
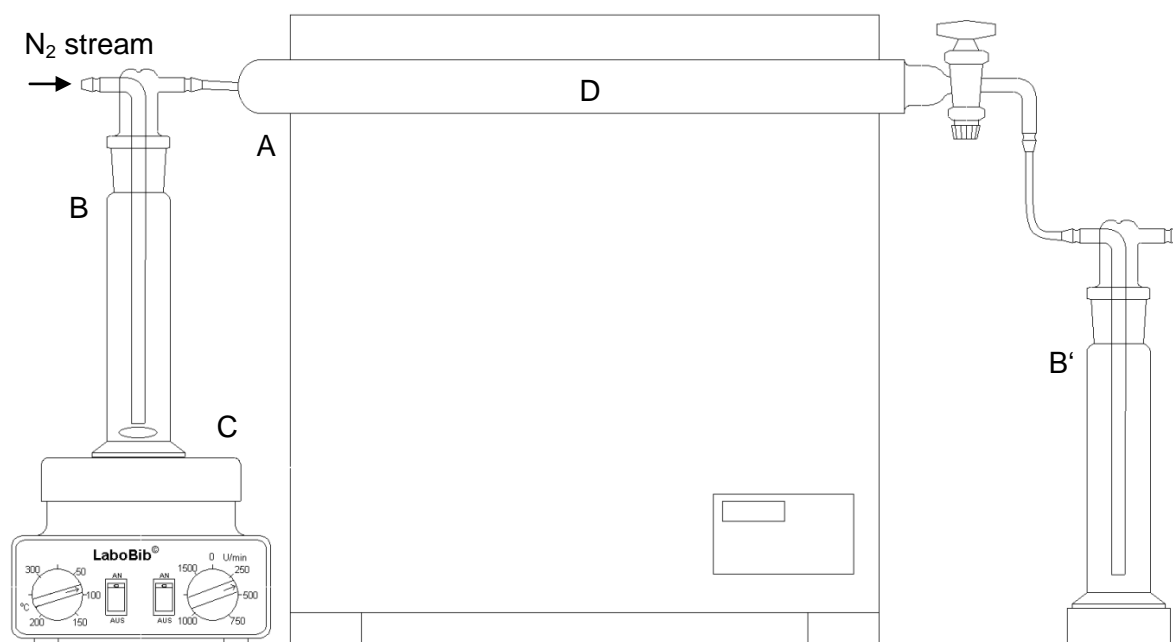
Figure 97: Scheme of the experimental setup heating experiments in a water loaded nitrogen stream. A: Quartz glass tube in a tube furnace; B+B': washing flasks, filled with water; C: heating plate; D: sample in a combustion boat

To ensure, that the nitrogen stream is loaded with water vapor during the whole reaction of two hours, the heating plate and the furnace are pre heated prior to the positioning of the sample inside the tube. During the reaction water condenses at the right hand end of the glass tube, confirming the vapor transport through the reaction chamber. After the reaction time the sample is rapidly cooled down by pulling it to the right hand end of the glass tube outside the furnace. This procedure ensures that the material remains in the nitrogen stream and is therefore unaffected by a possible reaction with air at raised temperatures. The cooling from 400 °C to about 50 °C takes a few minutes only. As reference a series (*E III*) is treated in the same way but without the water filling in washing flask *B*, to compare the results afterwards.

Different synthesis batches of the same composition are used as sample material of the 120 °C microcrystalline sodalite series. Table 42 summarizes the temperatures used and the experimental parameters for the different batches.

Table 42: Sample and experiment parameters for analyzes of influence of external water

Synthesis batch	NaBH$_4$/matrix / wt-ratio	External water used	Experiment duration / h	Temperatures / °C
E III	0.6	no	2	100, 150, 200, 250, 275, 300, 325, 350, 375, 400
E	0.6	yes	2	200, 300, 400
E_repetition	0.6	yes	2	300, 400
E II	0.6	yes	2	250

The samples were analyzed by FTIR before and after the thermal treatment and their integrated intensities of BH$_4^-$ and BO$_2^-$ were determined. In Figure 98, the relative decrease of BH$_4^-$ is shown with respect to the temperature. To improve the comparability, data are given as relative values to the related value of the starting material. The integrated intensities were normalized using the TOT normalization method. Series *E_repetition* was performed to show that the results are reproducible, these analyzes were carried out six months later than series *E*. The error bars represent *2·σ* obtained from three FTIR pellets prepared and measured per sample and temperature.

The starting materials are marked with a cross. For the reference material without external water (black dots) the relative intensities of BH$_4^-$ remain almost constant up to 200 °C. At further increased temperatures the intensities decrease slightly to 0.91 at 350 °C, which equals a reaction degree of about 9 %. With higher temperatures the intensities show no further decrease within the given errors.

The samples, heated in the vapor stream, exhibit a similar decrease of the BH$_4^-$ intensities up to 250 °C. At further elevated temperatures, the BH$_4^-$ intensities show a significant decrease compared to the reference series. At 400 °C the BH$_4^-$ intensities are

reduced by 36 % for both samples, compared to 9 % for the reference. Already at 300 °C the external water leads to a difference: the integrated intensities of BH_4^- are reduced by 12 % while the dry reaction only leads to a reaction degree of 8 %.
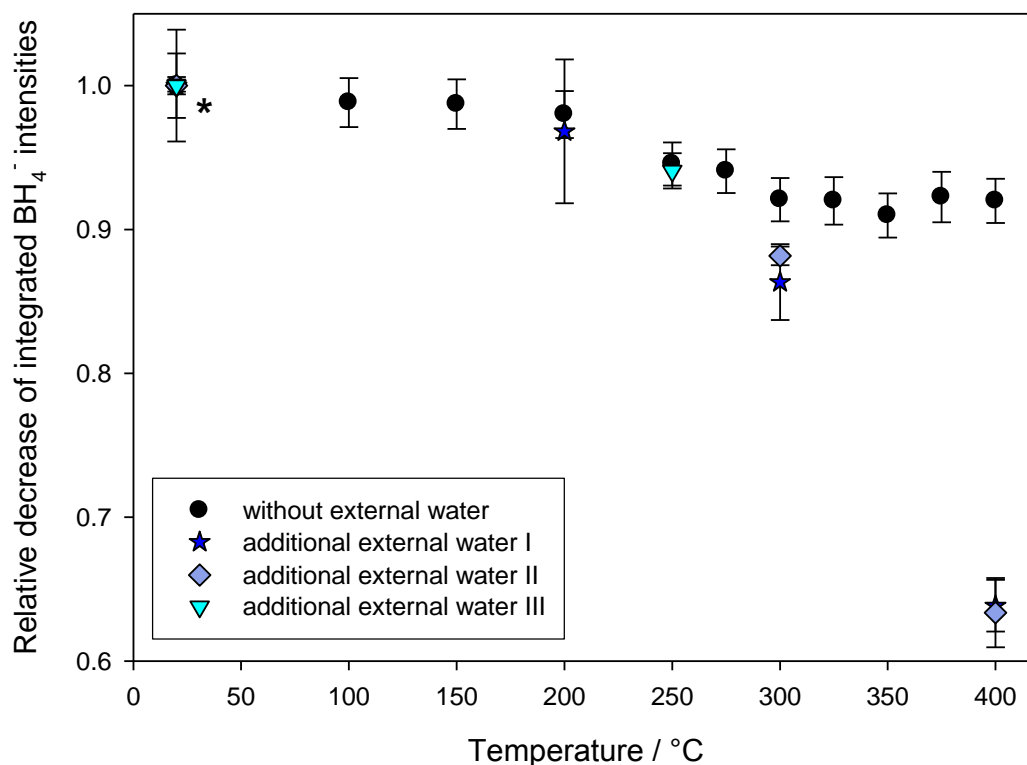
Figure 98: Relative integrated intensities of BH_4^-, obtained by FTIR for different temperatures without external water (black) and with external water, divided in three batches (blue symbols). Error bars represent 2•σ.

The BO_2^- intensities show a first increase above 300 °C for all sample series irrespective if a vapor stream was used or not (Fig. 99). Above 300 °C the intensities increase for the reference series to a maximum of 0.23 area units at 400 °C. At this temperature the two samples which react with externally added water, show a BO_2^- intensity of 0.44 and 0.49 area units, respectively.
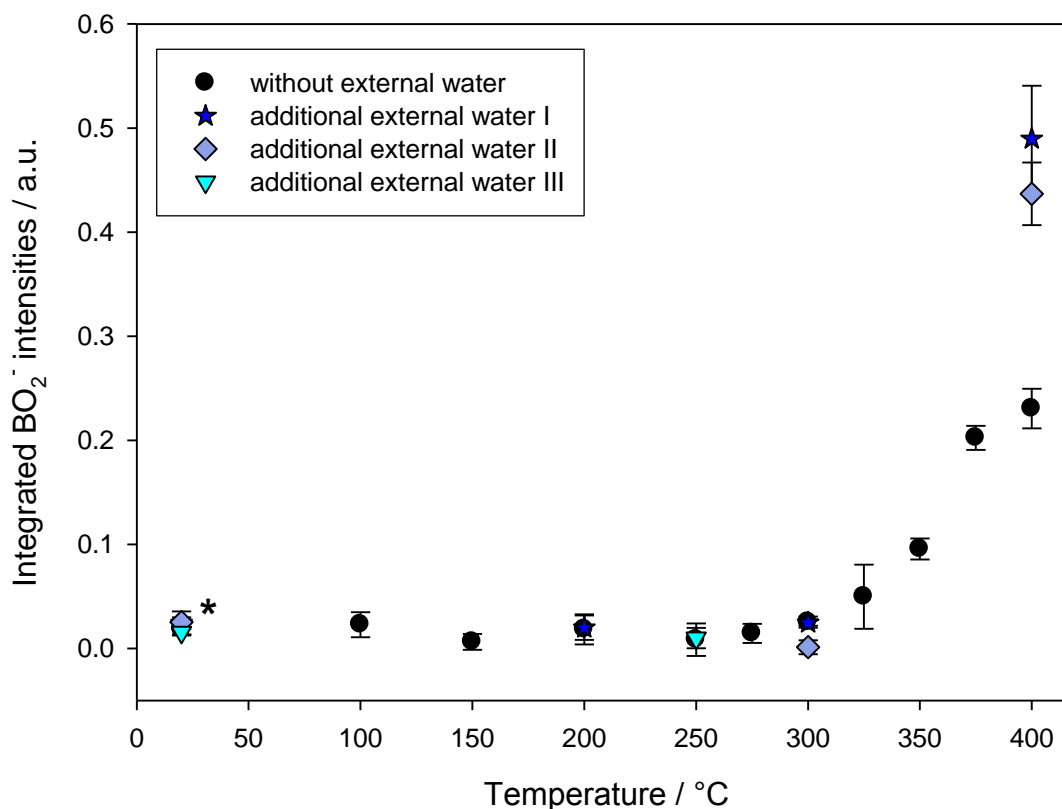
Figure 99: Integrated intensities of BO$_2^-$, obtained by FTIR for different temperatures without external water (black) and with external water, divided in three batches (blue symbols). Error bars represent 2•σ.

Figure 100 displays the integrated intensities of species 'A'. Samples without external water show first intensities of species 'A' at 200 °C, as described in Chapter 6.3.1.. With further increased temperatures the intensities run through a maximum at 350 °C and show a linear decrease above 350 °C. The series with external water shows higher intensities and does not decrease in intensity at temperatures above 350 °C, but the increase slows down.
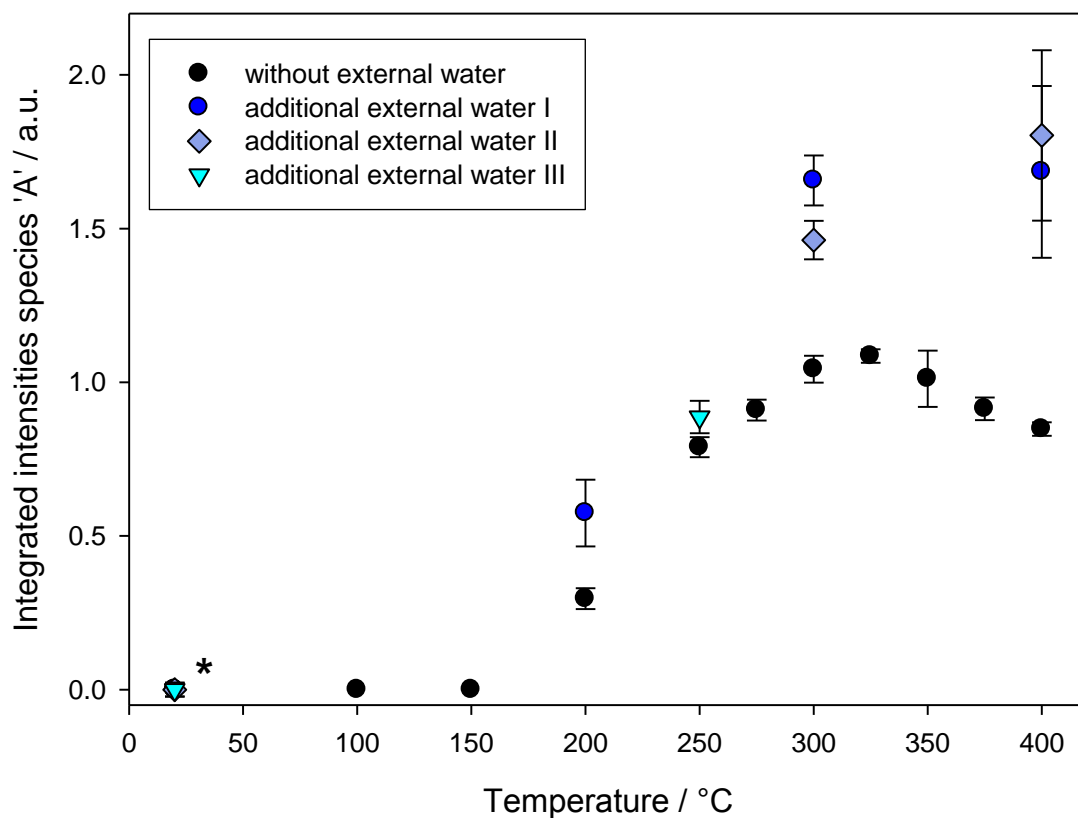
Figure 100: Integrated intensities of species 'A', obtained by FTIR for different temperatures without external water (black) and with external water, divided in three batches (blue symbols). Error bars represent 2•σ.

Figure 101 shows the FTIR spectra of the starting materials and the tempered samples. The spectra are presented as pairs to compare the samples with and without external water for the different temperatures, directly. Spectra of the series *E_repetition* are not presented in Figure 101, due to the fact that they show no significant differences to the analogous series *E*.
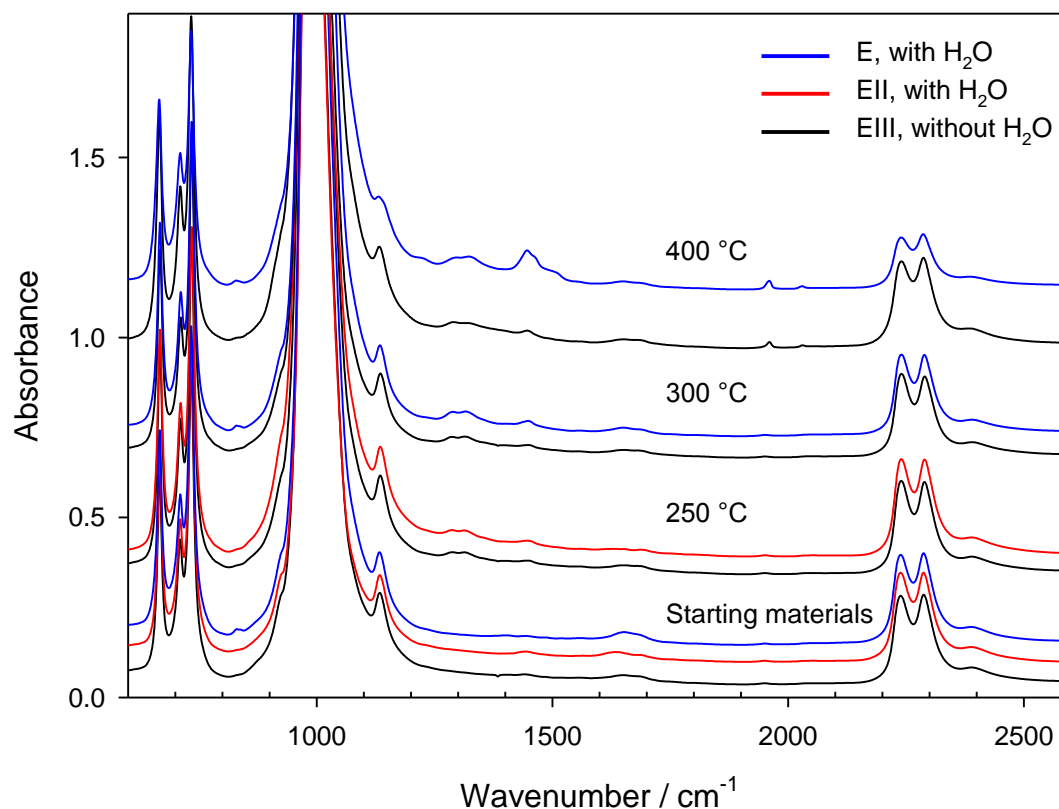
Figure 101: FTIR spectra of the samples E (blue) and EII (red), which were heated in water loaded nitrogen stream and samples EIII (black) as reference in a dry nitrogen stream. Spectra are shown in direct comparison for the different temperatures as pairs with the reference.

The starting materials differ slightly from each other regarding the water and carbonate peak intensities. These small differences occur just by the pellet preparation and are therefore negligible. At 250 °C, both spectra show a small decrease in their BH_4^- intensities and the formation of a double peak at 1290 and 1310 cm^{-1} (species 'A'). Additionally the water related peak around 1630 cm^{-1} decreases. At 300 °C both spectra show the double peak at 1290 and 1310 cm^{-1}, respectively. The intensity of this peak is higher for the sample heated in the vapor stream. Additionally the BH_4^- intensity of this sample is significant lower compared to the dry sample. This effect is even more pronounced at 400 °C. The peak structure around 1450 cm^{-1} (related to $BO(OH)_2^-$) shows a very high intensity for the vapor related sample, while the intensity of the dry sample shows no further increase. The peaks at 1290 and 1310 cm^{-1} remain constant for both samples. At 1959 and

2030 cm^{-1} two new peaks are formed in both spectra. The intensities are significantly increased in the vapor related spectrum, while the intensity of the BH_4^- peaks is decreased.

This shows that the addition of external water leads to an higher reaction degree, all products show higher intensities.

6.6. Dehydration of B(OH)$_4$-Sodalite

The dehydration of B(OH)$_4$-sod was analyzed by FTIR, TG/DTA and ^{11}B NMR. The samples were tempered in the TG/DTA at various temperatures up to 500 °C. The temperature range was analyzed from 80 °C to 500 °C with varied temperature steps to identify the reaction steps clearly. Representative IR spectra are displayed the Figure 102.

The characteristic IR bands of the sodalite structure are located in the wavenumber range from 400 to 1100 cm^{-1}. The δ TOT bands range from 400 to 460 cm^{-1}, the v_{sym} TOT from 650 to 750 cm^{-1} and the v_{as} TOT range from 900 to 1100 cm^{-1}. Additionally the bands of the guest ions can be observed; the starting species $B(OH)_4^-$ has characteristic bands at 3640 cm^{-1} (v_{as} OH of $B(OH)_4^-$). Following Pietsch et al. [27] the species occuring during thermal treatment can be identified as $BO(OH)_2^-$ and BO_2^-. $BO(OH)_2^-$ shows signals around 1475 cm^{-1} (v_{as} B-O), 1230 cm^{-1} (δ B-OH) and 3592 cm^{-1} (v_{as} OH). BO_2^- shows signals at 1955, 2030 cm^{-1} (v_{as} BO_2^-) and 566, 597 cm^{-1} (δ BO_2^-). In Figure 102 the bands of these species are marked by *I* for $B(OH)_4^-$, *II* for $BO(OH)_2^-$ and *III* for BO_2^-, as given in Table 43.

Table 43: Summary of the bands observed, the assigned of the signals and their temperature range of stability.

Species	Signal	Label	Visible in temperature range
B(OH)$_4^-$	v_{as} OH of B(OH)$_4^-$	I	Start - 350 °C
BO(OH)$_2^-$	v_{as} B-O of BO(OH)$_2^-$	II	140 - 350 °C
	δ B-OH of BO(OH)$_2^-$	II'	
	v_{as} OH of BO(OH)$_2^-$	II''	
BO$_2^-$	v_{as} BO$_2^-$	III	from 275 °C
	δ BO$_2^-$	III'	

Between 120 and 140 °C the first signals of formed $BO(OH)_2^-$ become visible in the FTIR spectra. The signals increase with further increased temperatures while the intensity of the $B(OH)_4^-$ peak decreases. There are only minor changes visible in the sodalite structure related peaks. With increasing temperature the peak positions of the ν_{sym} TOT bands shift towards higher wavenumbers. Above 250 °C first signals of BO_2^- become visible and the signals of $BO(OH)_2^-$ start to decrease. Above 400 °C there are no residuals of $B(OH)_4^-$ left concerning FTIR. $BO(OH)_2^-$ is not detectable anymore above 450 °C, while the intensities of BO_2^- increase.
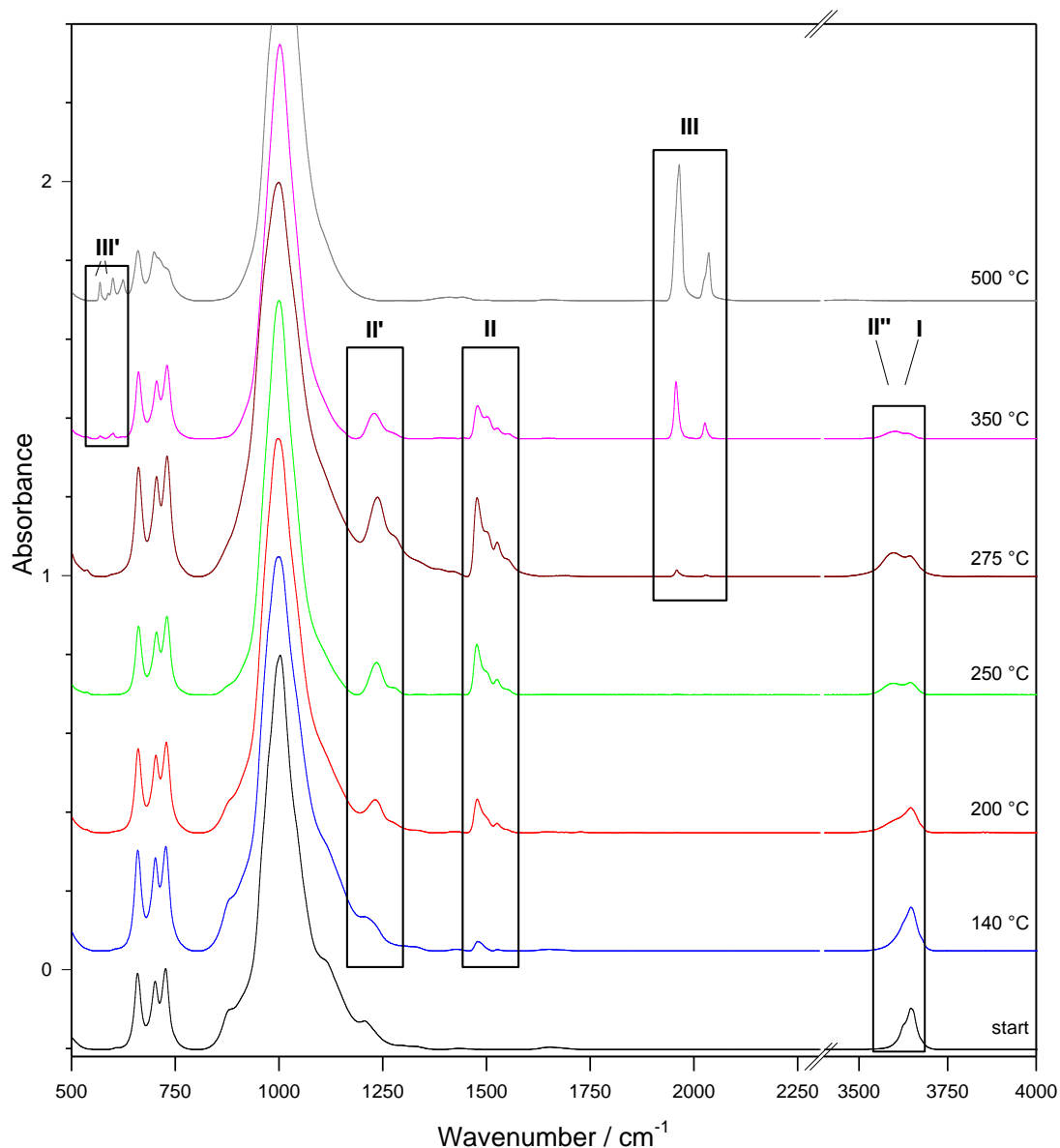
Figure 102: Baseline corrected FTIR spectra of B(OH)₄-Sod after different heating steps. Roman numerals mark the species formed at different temperatures.

FTIR shows a two-step dehydration mechanism. Figure 103 displays the results of TG and DTA measurements (10 K/min heating and cooling rate, flowing He atmosphere 20 ml/min).

The heatflow shows three endothermic effects with peaks at 110, 225 and 410 °C. Since these peaks are also observed in dTG curves at the same temperatures it can be concluded that the endothermic effects correspond to the mass loss, due to dehydration.
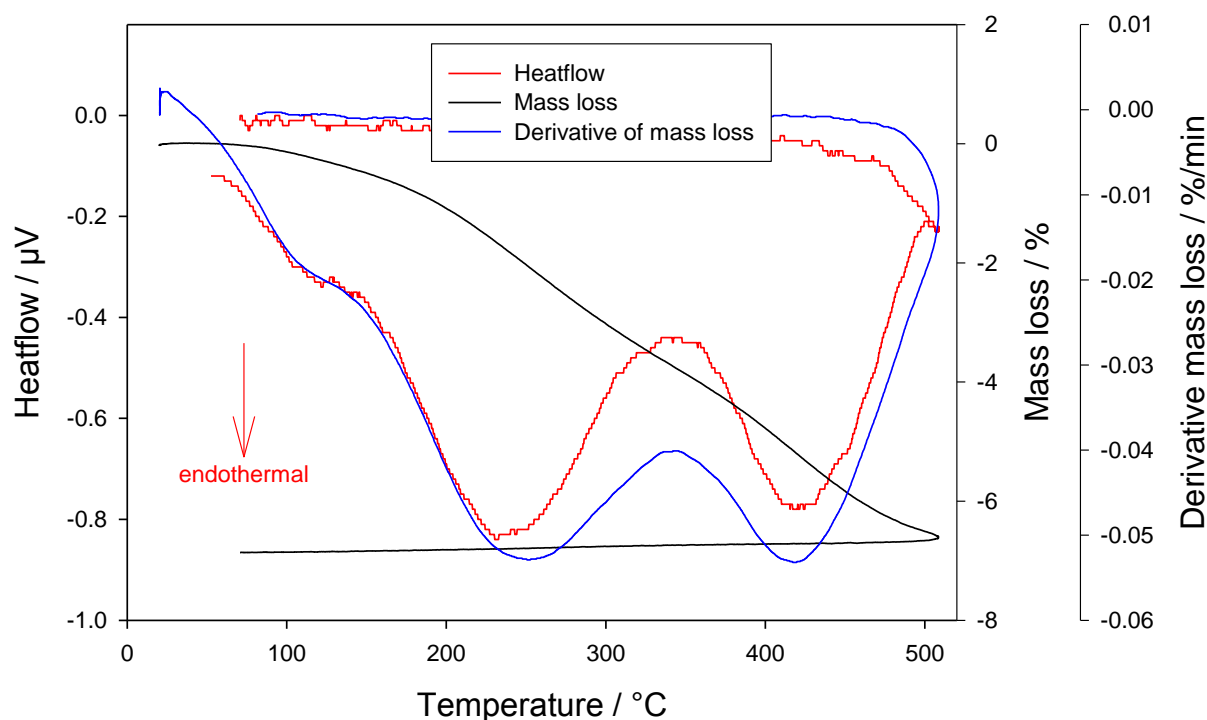
Figure 103: Combined curves of heatflow, mass loss and derivative of mass loss of a TG/DTA analysis up to 500 °C of B(OH)$_4$-Sod.

The two major steps fit to the observations made by FTIR;. above 140 °C mainly BO(OH)$_2^-$ is formed. the effect at 410 °C shows the formation of BO$_2^-$ from the BO(OH)$_2^-$. This observations confirms the two-step mechanism of the dehydration.

The additional signal at 110 °C can be connected to small amounts of water in the FTIR spectrum around 1630 cm^{-1}. From the results obtained for the BH$_4$-sodalite series it can be concluded that the DTA-signal is related to hydro-sod, as shown in Figure 35 in Chapter

5.1.3., for example. The endothermic effects of hydro-sod occur at 110 and 210 °C, too. An ideal $B(OH)_4$-sod of the composition $Na_8[AlSiO_4]_6(B(OH)_4)_2$ loses via dehydration 4 mole of water, which equals 6.82 wt%. The measured mass loss of the sample is 6.9 wt% up to 500 °C. The sample was not heated until its complete decomposition, therefore is the mass loss of 6.9 wt% a bit underestimated. But the amount of hydro-sod is very small, approximately below 1 %.

As third method ^{11}B MQMAS NMR was used to investigate the dehydration of $B(OH)_4$-sod. Three different reaction degrees and the starting material were measured and are shown in the following Figures, the species are marked with roman number analogous to the FTIR spectra. The measuring parameters are given in Table 1 in Chapter 3.2.3.

Figure 104 shows the spectrum of the starting material $B(OH)_4$-sod. The signal of $B(OH)_4^-$ is located at 1.5 ppm at the F2 axis (x axis) and is in good agreement with [86]. It is splitted into two signals at the F1 axis (y axis). The two signals are centered at 5 (I_a) and 16 ppm (I_b), respectively. Both signals are elongated along F1. The signal at 16 ppm (F1) shows a broadening effect along F2 up to 6 ppm additionally.
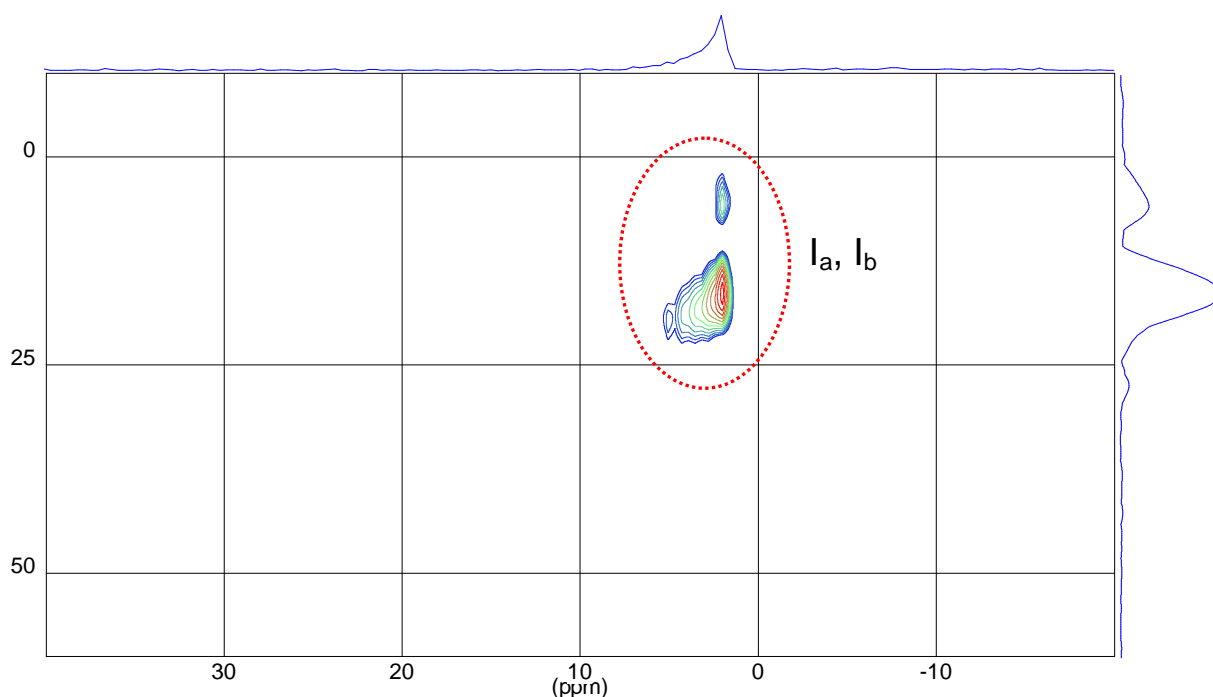
Figure 104: ^{11}B MQMAS NMR spectrum of B(OH)$_4$-sod

Figure 105 shows the spectrum of the B(OH)$_4$-sod tempered for 30 min at 230 °C. The positions of B(OH)$_4^-$ again is at 1.5 ppm at F2 but could show now three signals at 4, 7 and 21 ppm along F1. A new signal is centered at 46 ppm (F1) and 16 ppm (F2) depicting an ecliptic extension. The signal is related to the newly formed BO(OH)$_2^-$, according to infrared spectroscopy marked as II and II' in Fig 102.
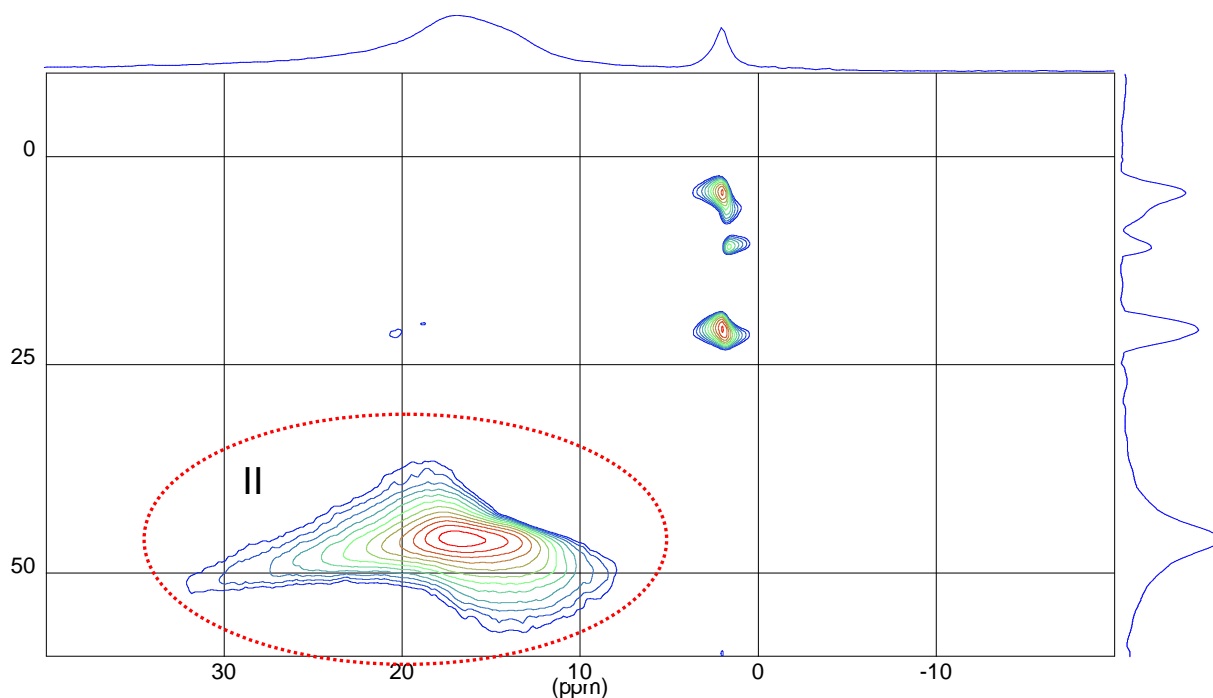
Figure 105: ^{11}B MQMAS NMR spectrum of B(OH)$_4$-sod after 30 minutes heating at 230 °C

The sample that was tempered further up to 325 °C (1h), shows a more complicated spectrum (Fig. 106). Additionally to the already mentioned signals, two new signals can be clearly identified as related to BO$_2^-$. Both signals are elongated along F2; at 49 ppm (F1) from -5 to -14 ppm (III$_a$) and at 52 ppm (F1) from 16 to -1 ppm (III$_b$). The second signal overlaps with the signal of BO(OH)$_2^-$. Around 2 ppm (F1) and 2 ppm (F2) there are two signals visible; one of them is related to residual B(OH)$_4^-$ while the second signal is probably connected to firstly formed BO$_2^-$ (III$_c$). The signal of the BO(OH)$_2^-$ (II) becomes more intense and at around 21 to 30 ppm (F1) and 22 ppm to 14 ppm (F2), respectively two signals with low intensities are visible, these signals could not be identified (uk).
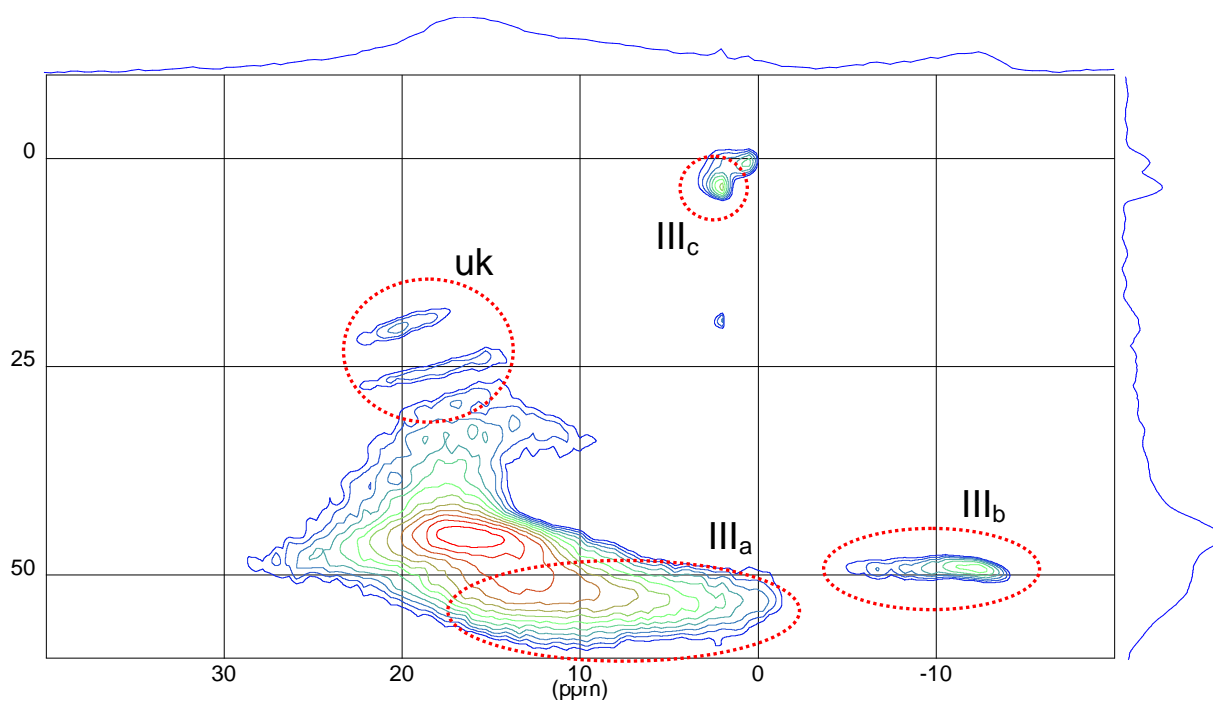
Figure 106: ^{11}**B MQMAS NMR spectrum of B(OH)$_4$-sod after 60 minutes heating at 325 °C**

After tempering for 2 h at 480 °C, the sample shows increased intensities of the signals III$_a$ and III$_c$. The unidentified signals (uk) and the the signal of BO(OH)$_2^-$ (II) are not detectable anymore. A new signal occurs, which is probably a decomposition product (dp). It is located at 56 to 60 ppm (F1), 2 to -2 ppm (F2).
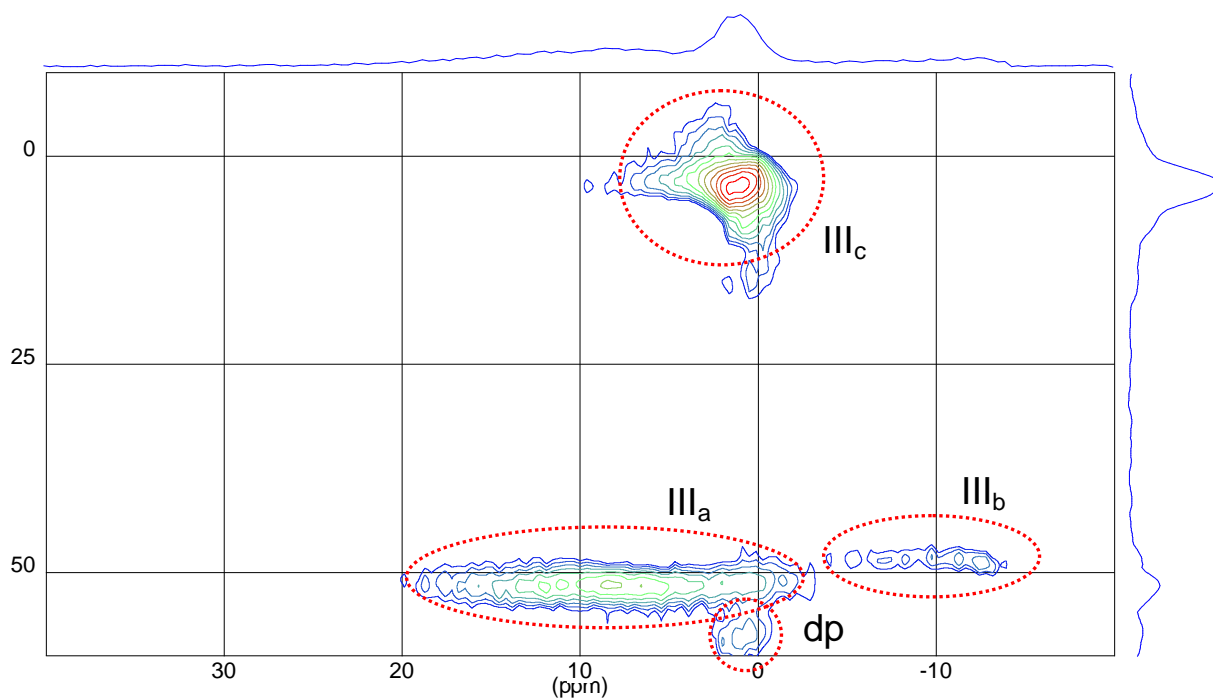
Figure 107: ^{11}**B MQMAS NMR spectrum of B(OH)$_4$-sod after 2 hours heating at 480 °C**

Figure 108 and 109 show the corresponding 2d MAS NMR spectra including the fitted peaks of the $B(OH)_4$-sod and the temper steps up to 480 °C. The peak fit was performed according to the information obtained by the MQMAS spectra. The fitted peak positions are given in Table 44 below.

Table 44: Fitted peak positions of 2d ^{11}B MAS NMR, $B(OH)_4$-sod and the tempered samples up to 480 °C

		20 °C	230 °C	325 °C	480 °C
GL1	Position / ppm	1.90	1.87	1.95	1.89
	Amplitude	55267.23	39072.53	1854.03	3152.90
	Width / ppm	0.55	0.56	0.68	0.53
	Area / %	45.17	29.74	3.01	2.51
GL2	Position / ppm	1.84	1.92		
	Amplitude	9595.50	7464.88		
	Width / ppm	3.94	3.53		
	Area / %	54.83	33.99		
GL3	Position / ppm		13.12	11.85	12.10
	Amplitude		2549.69	1387.43	1534.95
	Width / ppm		7.46	6.26	5.50
	Area / %		23.34	20.05	12.43
GL4	Position / ppm		16.51	16.01	15.81
	Amplitude		2172.73	946.33	589.83
	Width / ppm		4.68	4.96	4.37
	Area / %		12.93	10.91	3.82
GL5	Position / ppm			-12.66	-12.70
	Amplitude			410.20	1006.30
	Width / ppm			2.17	2.52
	Area / %			2.09	3.82
GL6	Position / ppm			-9.16	-9.62
	Amplitude			643.46	786.15
	Width / ppm			9.88	5.52
	Area / %			14.36	6.39
GL7	Position / ppm			-3.96	-4.01
	Amplitude			276.21	768.43
	Width / ppm			2.82	7.03
	Area / %			1.80	7.89
GL8	Position / ppm			0.95	1.03
	Amplitude			1994.46	4723.64
	Width / ppm			5.92	4.65
	Area / %			27.32	32.52
GL9	Position / ppm			6.64	6.52
	Amplitude			1470.25	3320.69
	Width / ppm			6.01	6.29
	Area / %			20.43	30.65

Without the three dimensional MQMAS NMR data a peak fit of the 2-dimensional spectra would not be possible. The fitted spectra show that two peaks are necessary to fit the signal of $B(OH)_4^-$ at 1.80 ppm. From the MQMAS spectrum it could be concluded that $BO(OH)_2^-$ consists of signals with only minor elongation and was therefore fitted with two GL peaks positioned around 13 and 16 ppm, respectively, confirmed by literature for threefold - coordinated non-framework boron [87], [88].
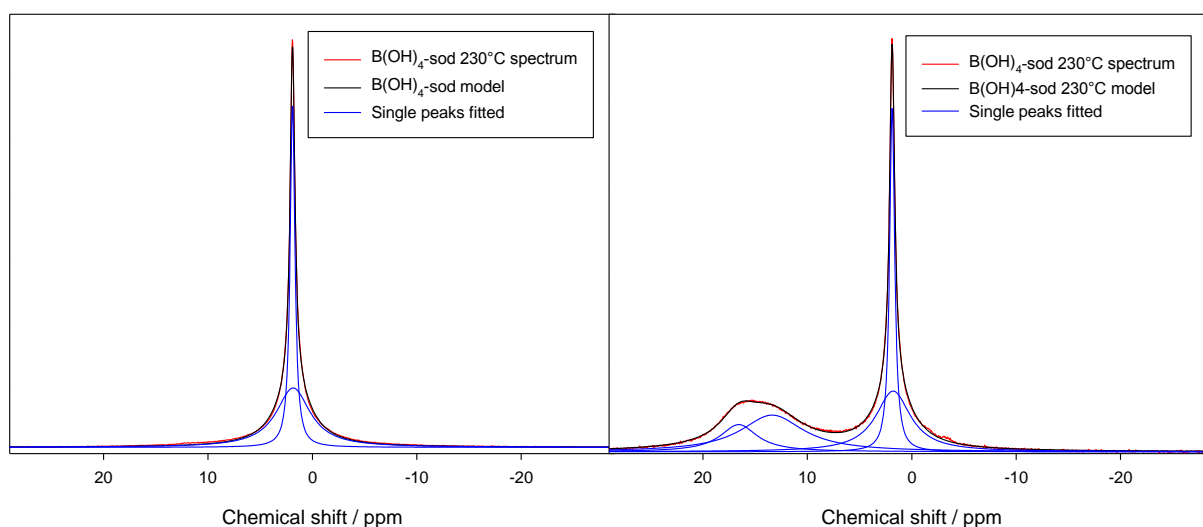
Figure 108: ^{11}B MAS NMR spectra of $B(OH)_4$-sod (left) and $B(OH)_4$-sod after 30 minutes at 230 °C (right). Both spectra are shown with the peak fit model.

Even with the information obtained by MQMAS NMR the spectra of the 325 °C and 480 °C spectra were complicated to fit: At least two new areas occur, the peak around 6 ppm and the range from 0 to -13 ppm. The second range could also be fitted, using a quadrupole signal without significant decrease in precision.
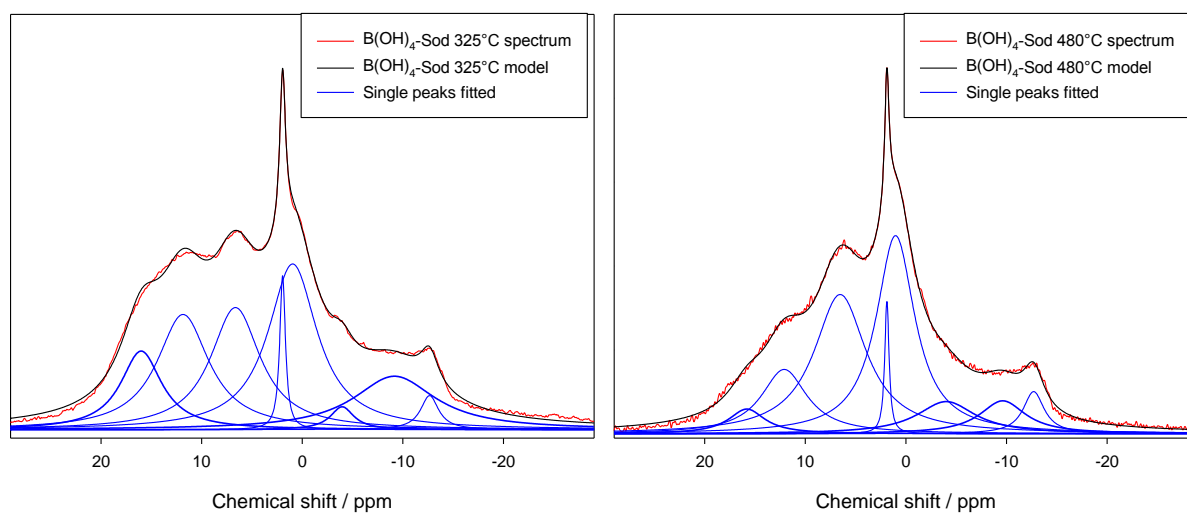
Figure 109: ^{11}**B MAS NMR spectra of B(OH)$_4$-sod after 1 hour at 325 °C (left) and B(OH)$_4$-sod after 2 hours 480 °C (right). Both spectra are shown with the peak fit model.**

6.7. Discussion: Sodalite Mechanism

The most commonly published reaction equation describes the overall reaction but without information about possible intermediate species (for example in [14], [89]):

$$NaBH_4 + (2+x)\ H_2O \rightarrow NaBO_2 \cdot xH_2O + 4\ H_2 \tag{17}$$
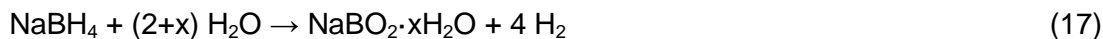
But further approaches need to be taken into account for example Andrieux et al. [90]:

$$BH_4^- + H_3O^+ \rightarrow BH_3 + H_2O + H_2 \tag{18a}$$

$$BH_3 + OH^- \rightarrow BH_3OH^- \tag{18b}$$

This mechanism would go on until $B(OH)_4^-$ which afterwards dehydrates to BO_2^- in two steps.

Following Aiello et al. or Davis and Swain [83], [91] the reaction forms boric acid, which could form $B(OH)_4^-$ afterwards [92]:

$$NaBH_4 + 4\ H_2O \rightarrow 4\ H_2 + NaOH + H_3BO_3 \tag{19a}$$

$$H_3BO_3 + H_2O \rightarrow B(OH)_4^- + H^+ \tag{19b}$$
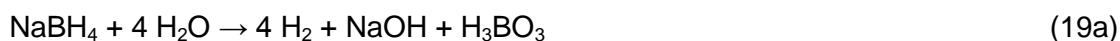
But none of these publications can be used without questioning for this thesis because the enclathration of the BH_4^- in the sodalite structure can affect its energetical environment and forms a steric obstacle. Therefore the reaction could follow a different route.

6.7.1. Reaction Steps

Intermediate Species

The analysis of the reaction time and its influence on the reaction show that the reactant BH_4^- remained constant while the product BO_2^- increased in intensity for example at 400 °C (see. Fig. 83 and 84 in Chapter 6.3.2.). This is only possible, if there are intermediate species existing along the reaction path. The results obtained in this thesis come to the conclusion that at least one more intermediate exists, beside $B(OH)_4^-$ and $BO(OH)_2^-$.

Using the scheme shown below, the signals of intermediate species starting from BH_4^- were tried to separate from the signals of the dehydration steps of $B(OH)_4^-$.
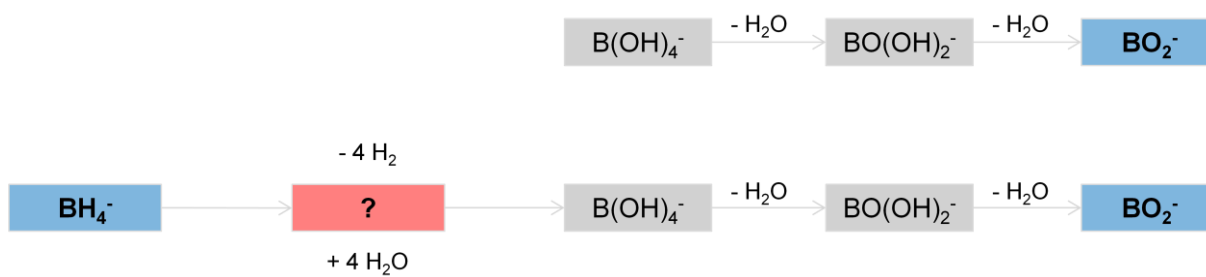
Figure 110: Scheme for separation of sub-reaction

Firstly the signals obtained need to be assigned to the dehydration steps starting from $B(OH)_4^-$ to BO_2^-. Afterwards these signals can be excluded from the signals observed in the thermal reaction of BH_4-sod. The remaining signals should then be related to the intermediate species in the hydrogen release reaction, like species 'A'.

The reaction from $B(OH)_4^-$ is supposed to be a two step dehydration mechanism [45], [93]. Obtained results confirm this theory using methods like TG/DTA, FTIR and NMR as presented in Chapter 6.6. All the methods used give similar information on the temperatures in which the different steps take place; at temperatures above 125 °C $BO(OH)_2^-$ is formed mainly. Above 275 °C BO_2^- is additionally formed from $BO(OH)_2^-$. With further increased temperatures BO_2^- is stable and only small amounts of possible decomposition products are visible in ^{11}B MQMAS spectra (cf. Figure 107).

Figure 111 shows the plotted areas of the peak fit for the different temperatures starting from $B(OH)_4$-sod (data in Table 44). The peaks which show a similar behavior are marked by same colors. GL 1 + 2 can be clearly identified as $B(OH)_4^-$, according to the reference sample synthesized in pure form (Fig. 73 and 102, FTIR; Fig. 104, NMR and [27], [71]). GL 3 + 4 are very likely signals of $BO(OH)_2^-$, due to the first appearance at 230 °C, the decrease afterwards, the FTIR spectra from Figure 102 in Chapter 6.6. and [87]. The only species which increases its intensity at temperatures above 325 °C is BO_2^-, which is therefore related to GL 5 - 7. Peaks 8 and 9 are not clearly identified.
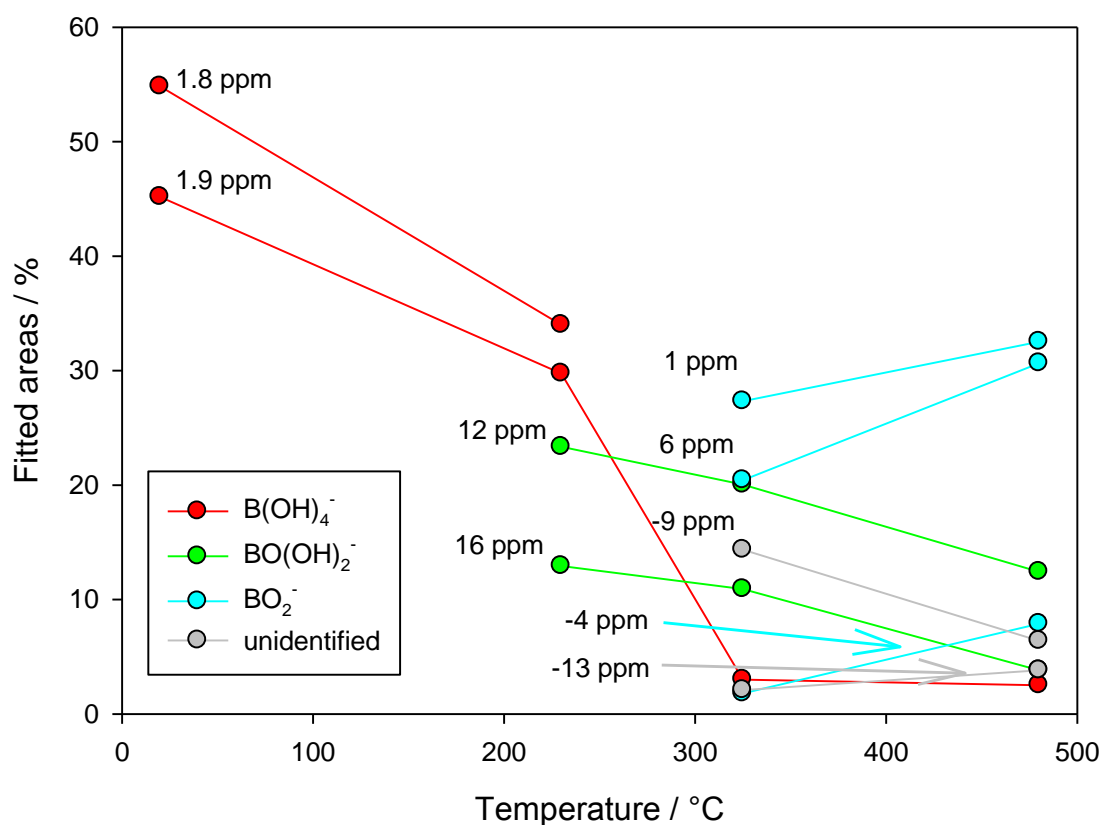
Figure 111: Plotted areas of the fitted peaks of ^{11}B MAS NMR of $B(OH)_4$-sod temper series, data from Table 44. Fitted peak positions are given close to the data points.

This assignment can now be transferred on the ^{11}B MAS NMR data obtained for the thermal reaction starting from BH_4^-.

In Figure 112 the areas of the single fitted peaks are shown as function of the temperature. The first signal with high intensity beside BH_4^- is the quadrupole signal at 16.51 ppm at 250 °C and is therefore assigned to species 'A' (also first occurring signal in IR, too, see Fig. 80). Further signals are fitted at 1.78 ppm, which can be assigned to $B(OH)_4^-$ and at 16.98 ppm, which can be assigned to $BO(OH)_2^-$, both signals are *Gauß-Lorentz* peaks. The signal at -0.51 ppm cannot be identified or assigned. With further increased temperature all peaks show the same behavior; they increase in their areas with increasing temperature, apart from the GL peak at 10.99 ppm, which occurs firstly at 400 °C. This peak is therefore assigned to BO_2^-, its position does not exactly fit to the positions for BO_2^- as described above but FTIR spectra exhibit no indications on further species formed.
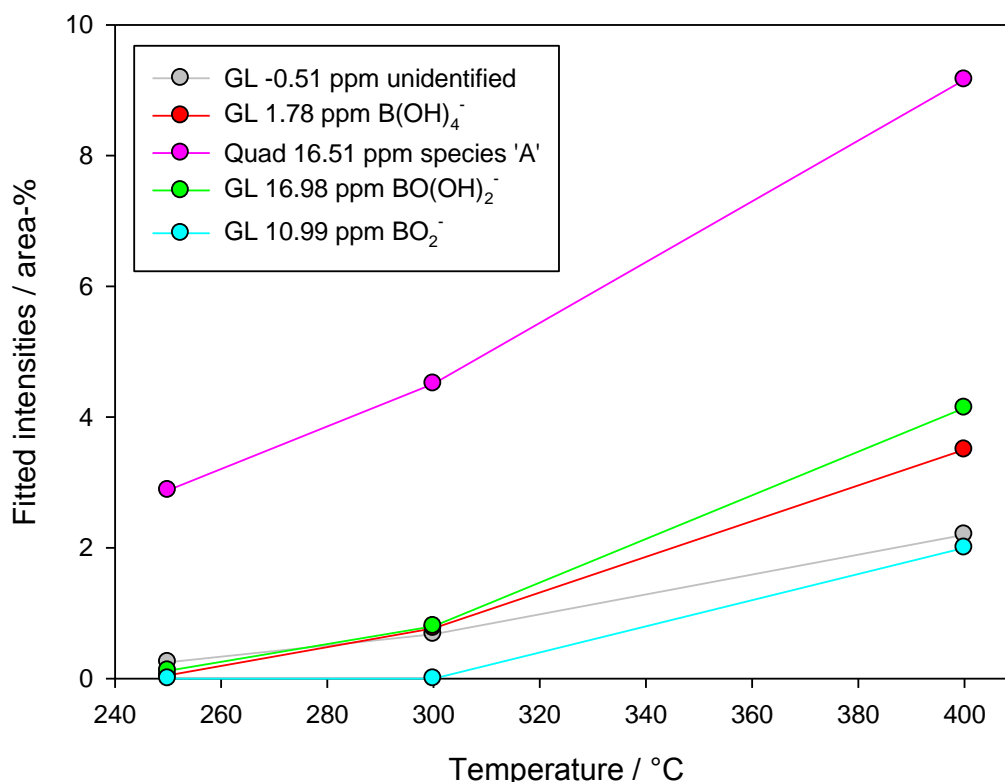
Figure 112: Plot of the fitted intensities of species in the range from -15 to 29 ppm, obtained by ^{11}B MAS NMR.

Figure 113 shows the analogous integrated intensities obtained by FTIR for signals of BH_4^-, BO_2^- and species 'A'. The intensities of BH_4^- decrease with temperature, while the signals of species 'A' increase. At 250 °C this species already shows significant intensity. No further signals are observable at this temperature beside water, some carbonate and BH_4^- (see. Fig. 79). At 300 °C signals of species 'A' increase in intensity, while there are still no further species visible. At 400 °C BO_2^- can be observed, species 'A' remains about constant. Around 1450 cm^{-1} the spectrum shows intensities, assigned to $BO(OH)_2^-$.
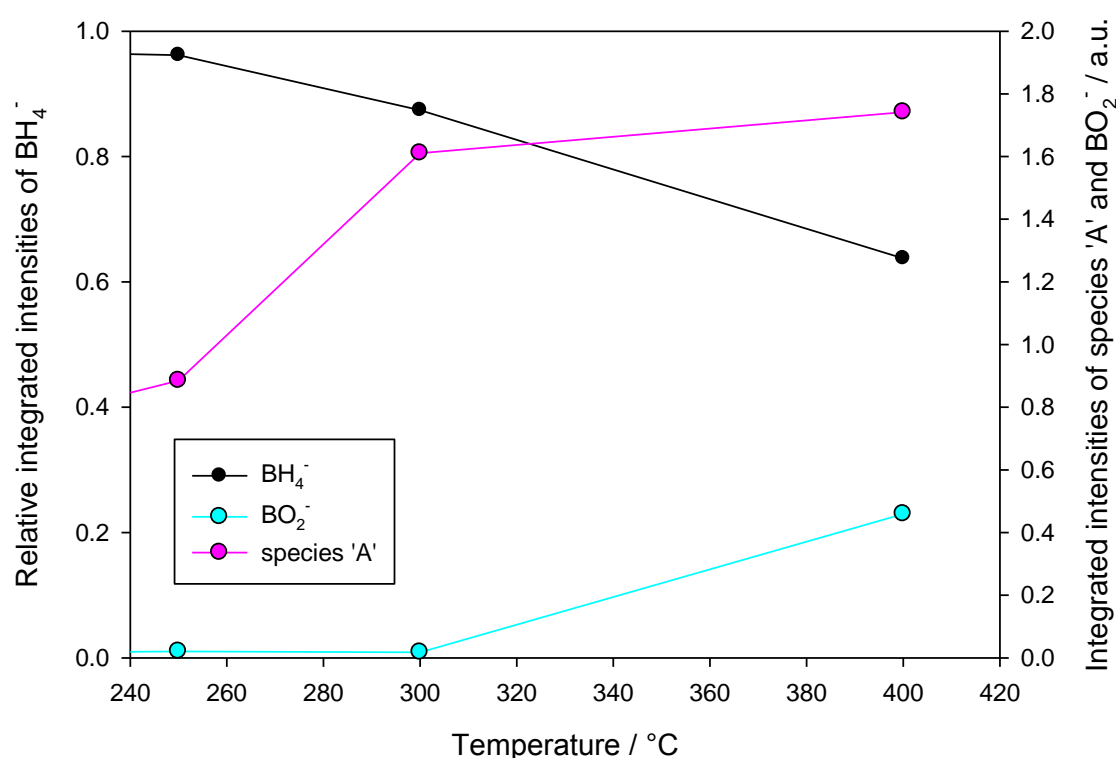
Figure 113: Integrated intensities of assigned signals obtained by FTIR for comparison.

The fitting results of the ^{11}B MAS NMR data show the same tendency as the evaluation of FTIR spectra; signals of BH_4^- decrease in their intensities with increasing temperatures and the sum of the newly formed species increases. Species 'A' behaves identically, the comparison confirms the assignment of the observed signals.

But what molecule or ion is species 'A'?

Species 'A'

Species 'A' as first signal detectable by FTIR via thermal treatment of BH_4-sod was supposed to be one of the possible intermediates H_3BOH^-, $H_2B(OH)_2^-$ or $HB(OH)_3^-$. The analyses done in this thesis strongly indicate that this theory fails:

As first argument works the amount of hydrogen released from pre-reacted BH_4-Sod (144.0 ± 7.71 ml H_2/g sample). The amount can only be correlated to a species without any B-H bond or within the error with maximal one B-H bond per mole (cf. Table 38 in chapter 6.1.).

Secondly the comparison of peak fits of reacted and unreacted BH_4-sod; if species 'A' contains any B-H bonds they should be visible in the FTIR spectrum in the same wavenumber range as the B-H signals of the BH_4^-. But there are no strong indications on newly formed signals. Here it has to be mentioned that the evaluation is not very easy due to the isotopic ratio of ^{11}B and ^{10}B and the *Fermi resonance* affected peak structure. It might be possible that such a new signal exists but it cannot be detected by FTIR without a further enrichment of the species.

As third argument that species 'A' is not one of the mentioned intermediates the NMR results can be used. If species 'A' from FTIR would contain a B-H bond of the given type, it should show a signal between the BH_4^- (-49.09 ppm) and the $B(OH)_4^-$ (1.78 ppm) positions in ^{11}B MAS NMR [90], [94] but there are no signals detectable (cf. Figure 77 in Chapter 6.2.).

The results of the thermal reaction of BH_4-sod in air compared to helium show for species 'A' the identical behavior (Fig. 90). This can only mean that this species is not influenced by direct oxidation and therefore contains no B=O bonds. The signals of species 'A' indeed increase if external water is around (Fig. 100), which means that it contains B-O-H bonds. From the sum of these conclusions it is very likely that species 'A' is H_3BO_3.

Species 'B'

Species 'B' was also under discussion for a long period of time [76], [95]. The new results obtained during this thesis strongly indicate that this signal in the FTIR belongs to carbonate and is not an intermediate step within the reaction mechanism of the hydrogen release from BH_4-sod.

As first argument works that the CS analyses show that carbon is contained in detectable amounts in the BH_4-sod. The amount of carbon decreases with increasing $NaBH_4$/matrix wt-ratios or it increases with increasing water contents, respectively (see Table 34 in chapter 5.4.3.).

Secondly a synthesis was carried out for each of the three series without $NaBH_4$ used. These samples do also show the remarkable peak at 1440 cm^{-1} in FTIR after thermal treatment (see Figures 91 and 93 in chapter 6.4.).

6.7.2. Internal Parameters - Sample

Which water can be used for the reaction and in what temperature range is it available?

As shown in Figure 92 in chapter 6.4. the reaction degree does not change within this series. It can be concluded that the hydro-sodalite amount does not significantly influence the reaction of the BH_4^-. The amount of water used for the reaction seems to be constant: the hydro-sodalite cannot be the source of this water therefore.

The alternative as water source is then most likely the amorphous areas of not entirely crystallized matrix material. This theory is additionally supported by the increased reaction degrees of the less crystalline series synthesized at 80 °C and 60 °C, respectively (cf. Figures 94 and 96 in Chapter 6.4.). The amorphous amount increases with decreasing morphological particle size.
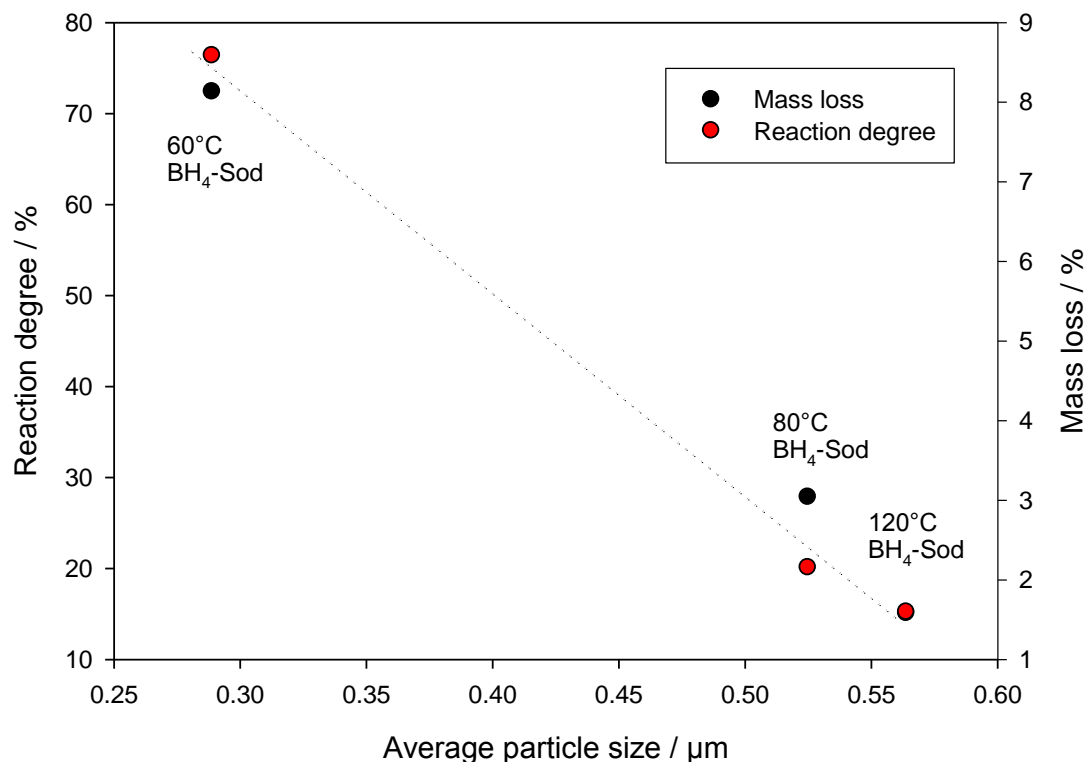
Figure 114: Combination of reaction degree and mass loss as function of the average morphological particle size.

Figure 114 summarizes the close relation between reaction degree and overall water amount, which is closely related to the morphological particle size. Reaction degree and mass loss show a linear trend as function of the average morphologic particle size.

Particle Size

It was possible to demonstrate that the particle size of the BH_4-sod has major effects on the reaction behavior of the hydrogen release reaction. The measured particle size causes side effects which of course do also effect the reaction; bigger particles contain more $NaBH_4$ and less water, they have an higher purity level. In principle bigger particles can store more hydrogen but due to the reduced amounts of water and the smaller surface, the reaction degree by thermal hydrogen release is significantly lower compared to samples with smaller particle sizes. In Figure 92, 94 and 96 in Chapter 6.4. the reaction degrees are shown for

different $NaBH_4$/matrix wt-ratios. For example for a $NaBH_4$/matrix wt-ratio of 0.8 the sample with an average particle size of 525 nm showed a reaction degree of 18 % while the analogous sample with an average particle size of only 289 nm showed a reaction degree of 72 %. The particle size on its own should influence the reaction by the elongated diffusion paths of the internal water. Additionally the smaller surface area of the bigger particles leads to reduced amounts of external water to reach the enclosed $NaBH_4$. The increased surface of smaller particles does also represent crystallographic defects. These defects offer jump possibilities for the Na^+ ions. More Na^+ jumps lead to statistically more often opened pathways for water through the sodalite 6-rings, which are otherwise occupied by the sodium ions. These pathways lead to an increased reaction degree with water.

To compensate the disadvantages of the low reaction degree via thermal hydrogen release for samples with high particle sizes the reaction time needs to be increased and external water needs to be offered. With this approach the enclosed $NaBH_4$ in bigger particles should release hydrogen in higher degrees via thermolysis.

The use of smaller particles allows higher reaction degrees but lower hydrogen amounts. As shown in Figure 59 in Chapter 5.4.2., the amount of hydrogen is reduced by 53 % when the 120 °C series is compared with the 60 °C series.

The evaluation of particle size is based on the morphologic as determined by SEM images. The crystal size was analyzed by XRD data, calculations using the *Scherrer equation* [31]:

$$L = K \cdot \lambda / \Delta(2\theta) \cdot \cos\theta_0 \tag{20}$$

with L=crystal size in Å, K=0.9 (constant for cubic crystals), λ=1.540598 Å, $\Delta(2\theta)$ as FWHM and θ_0 as reflex position.

Figure 115 shows the plotted FWHM values (full width at half maximum) as a function of the reflex positions of the same samples, which were used for the optical particle size determination. Additionally the ideal *Scherrer* values are plotted for average crystal sizes

from 400 to 2000 Å and the values for LaB_6, measured via XRD as standard to determine the apparatus maximum regarding the crystal size determination. The plotted sample values show that it is possible to analyze their average sizes by XRD and the *Scherrer equation* in principle, because the crystal sizes are significantly smaller than the measured standard. But the samples show a deviation of the ideal behavior; this effect can be explained by additional strain effects which are not calculated by the *Scherrer equation*. The most realistic average crystal size should be calculated by reflexes with small angles [96]. Therefore the average crystal size can be estimated for these three samples, only. The average crystal sizes for the 120 °C and 80 °C series with a $NaBH_4$/matrix ratio of 1.3 are about 870 Å and for the 60 °C series about 500 Å.
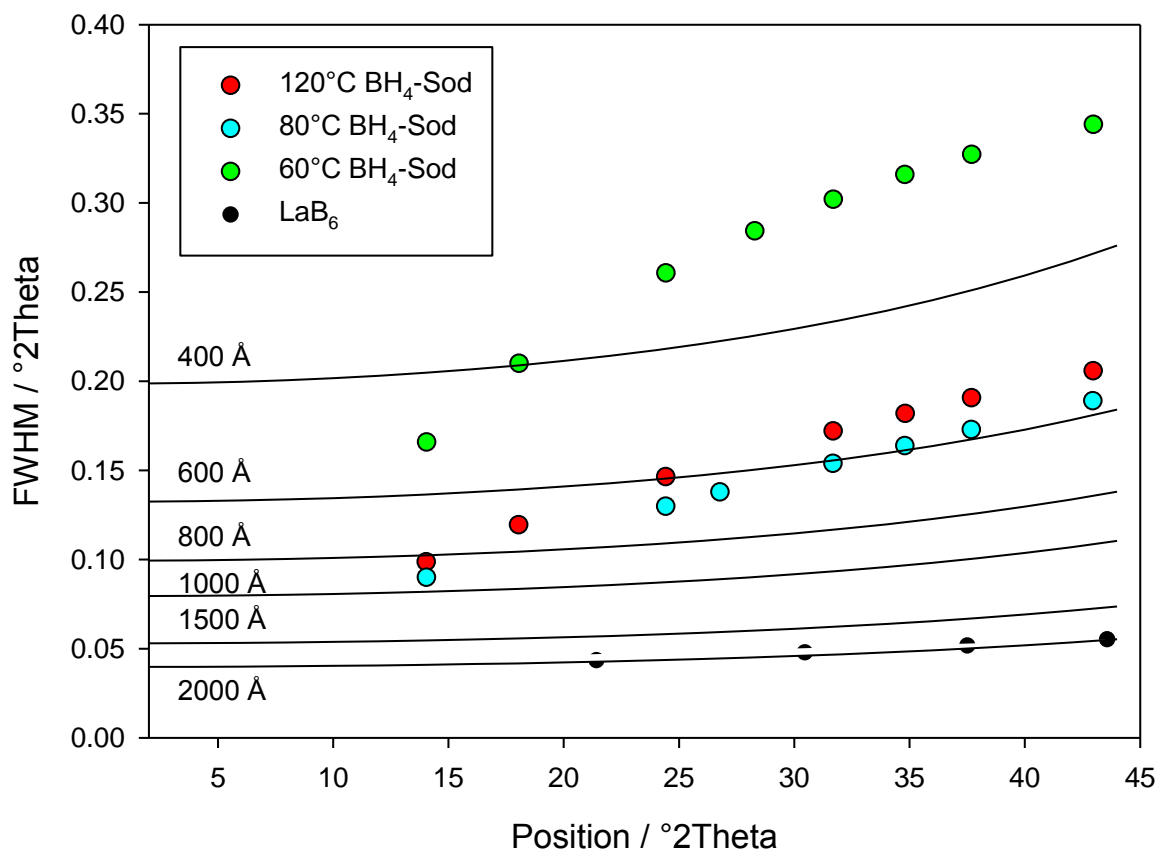
Figure 115: Scherrer plot of the three synthesis series ($NaBH_4$/matrix ratio of 0.8), LaB_6 standard and ideal Scherrer values.

The combination of morphological particle size and the crystal size, together with the water amounts lead to a complete picture regarding the internal structure of the sample materials. The average morphological particle size is for the three series constantly about 6 times higher than the calculated average crystal size, obtained by XRD. It is very likely that the particles contain of about 216 crystals in average with amorphous areas along their crystal boundaries. In these amorphous paths the water for the reaction is bound. Small amounts of co-crystallization of hydro-sod have only minor effects.

6.7.3. External Parameters - Reaction Conditions

<u>External Water</u>

The use of external water in the reaction of BH_4^- shows significantly increased reaction degrees compared to a dry atmosphere at 400 °C. The decrease of BH_4^- related signals using FTIR is 36 % while the dry procedure leads to a decrease of 9 % only (see Figure 98 in Chapter 6.5.). The BO_2^- signals are two times higher when heated under water vapor. This effect can be explained by two effects: The samples used have a $NaBH_4$/matrix wt-ratio of 0.6 and have therefore only minor amounts of internal water. Higher amounts of available water due to the steam increase the reaction degree. Secondly the reaction is avoiding the chemical restraint following the *Le Chatelier* principle [97] and shifts the chemical equilibrium towards the product side because of the excess of water on the reactant side:

$$BH_4^- + 2\,H_2O \rightleftarrows BO_2^- + 4\,H_2 \tag{21}$$

<u>Atmosphere</u>

In Chapter 6.3.3. the difference due to the utilization of different atmospheres such as helium and synthetic air during thermal treatment are investigated. The results strongly indicate an additional reaction step with oxygen at temperatures above 300 °C. At lower temperatures there is no influence of the atmosphere visible. The high amounts of BO_2^- formed at 500 °C strongly indicate a direct oxidation of the bound hydrogen. Here two redox reactions are possible concerning the electron transitions and the stoichiometry:

$$\overset{+III\ -I}{BH_4^-} \quad + \quad \overset{\pm 0}{2\ O_2} \quad \rightleftarrows \quad \overset{+III\ -II}{BO_2^-} \quad + \quad \overset{+I\ -II}{2\ H_2O} \tag{22a}$$

$$\overset{+III\ -I}{BH_4^-} \quad + \quad \overset{\pm 0}{O_2} \quad \rightleftarrows \quad \overset{+III\ -II}{BO_2^-} \quad + \quad \overset{\pm 0}{2\ H_2} \tag{22b}$$
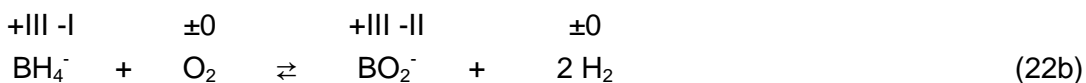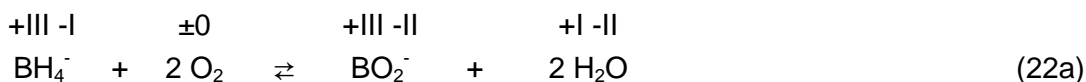
A direct comparison between analyses in flowing He and synthetic air shows differences in the mass loss via TG/DTA. Samples heated under He showed an higher mass loss compared to samples heated under air of about 0.4 wt%. From these small differences in the mass loss, it cannot clearly be distinguished which of the two reactions takes place. The reaction is only an additional path and the ratio which path takes place cannot be evaluated. If the mass would increase significantly the second equation would be more likely because of the higher mass of the absorbed oxygen, compared to the small mass loss due to release of hydrogen only.

Reaction Temperature and Time

The thermal reaction of BH_4^- starts at temperatures above 200 °C. First signals are the formation of species 'A' visible by FTIR at 1290 and 1310 cm^{-1} in combination with a decrease of the BH_4^- signal. The release of hydrogen could also be confirmed by a tracer reaction using the reduction reaction of the formed hydrogen with potassium nitrate [17]. With increased temperature the reaction degree also increases (decrease of BH_4^-). ^{11}B MAS NMR shows new signals in the same temperature range, as described before. The signal at 1.78 ppm confirms that $B(OH)_4^-$ is an intermediate species along the reaction path from BH_4^- to BO_2^-.

The reaction degree as a function of the reaction time cannot be distinguished clearly: In Figure 83 in Chapter 6.3.2. the integrated intensities of the BH_4^- related FTIR signals are shown for different temperatures and reaction times. The temperatures need to be evaluated in three steps; At 250 °C and 400 °C is no linear trend visible (within the given errors), already after short reaction times of 15 minutes to 1 hour the reaction slows down. This effect can be explained by the sample material used. The samples have a NaBH$_4$/matrix wt-ratio of

0.6 and were synthesized at 120 °C, therefore they have only minor water amounts. At 250 °C only small amounts can be mobilized at all. While at 400 °C it is very likely that the reaction degree is more dependent on the overall low water amounts in this case. After longer reaction times there would simply be no more water available for the reaction.

The intermediate temperatures from 300 °C to 375 °C show a more or less linear behavior from 15 minutes to 12 hours reaction time. In this temperature range the water amounts seem to be mobilized slowly and constantly to allow a continuous reaction. The reaction runs slow enough to not expend the whole amount of water in short time scales as it probably happens at 400 °C.

6.7.4. Comparison

The different possibilities need to be compared to answer the question, which way is the most effective one to release hydrogen from BH_4-sodalite and what needs to be taken into account?

One possible reaction path is the acid catalyzed hydrogen release; the reaction processes completely with only a slight excess of a diluted acid and there is no further catalyst necessary. The reaction takes place at room temperature and is therefore energetically very effective. Additionally the amount of water of the sample is negligible, even the almost water-free samples can be used. As disadvantages counts the fact that the reaction kinetics can be controlled only slightly by the acidity. Neither can the reaction be stopped nor could the reaction products be identified. This leads to the problem that a back reaction or a recycling process is not possible, here. The sodalite structure decomposes by the addition of acid, too.

As second way the thermal reaction under inert gas needs to be mentioned. This reaction delivers the weakest reaction degrees, the use of a catalyst might improve the efficiency here. Using small particles with high amorphous amounts or adding external water

can be used to control the reaction. Here the highest amounts of intermediates could be reached, which might become important to realize a back reaction or recycling process. This reaction is the mildest way to preserve the sodalite structure.

The third way is the direct oxidation of BH_4^- in the sodalite cage with the reaction in air or oxygen. This path is only mentioned as a parallel occurring side reaction. The reaction offers increased reaction degrees compared to reaction in inert gas and there is not necessarily external water needed. The sodalite cage remains almost intact. But the direct oxidation takes place at temperatures above 400 °C and the product is BO_2^-, mainly.

7. Conclusion and Outlook

BH$_4$-Gel

It is possible to store high amounts of sodium borohydride with increased stability in a solid state form for several months without any loss. Synthesis and handling of this new material is very simple. Matrix can be characterized as high alkaline geopolymer. The stability is increased due to the high alkalinity of the sample material. The NaBH$_4$ is stabilized even at the presence of water and against thermal reaction. Amounts of stored NaBH$_4$ are with 80 wt% higher than in alkaline solutions with 30 wt% [98], for example.

The enclathration of sodium borohydride in a geopolymer can pose a new impulse in the research field of geopolymers. But the presented results in this thesis can be a start, only. There are several further parameters that need to be taken into account; ammonia borane (NH$_3$BH$_3$), for example, has interesting properties and could be enclosed in an analogous geopolymer matrix, already [99]. The composition of the matrix itself exhibits large potential, too. So far NaBH$_4$ was enclosed in sodium containing geopolymers, only. The use of potassium or lithium bearing geopolymers might allow a further optimization of the enclathration degree. The reaction behavior might be optimized, too, due to a suppression of the amount of sodalite formed. The combination of the hydrogen release abilities of NaBH$_4$ together with the mechanical properties of geopolymers allow interesting further applications.

BH$_4$-sodalite

Using a kaolin based synthesis route it is possible to vary the BH$_4$-sod to hydro-sod ratio. The highest amount of BH$_4$-sod can be reached using NaBH$_4$/matrix wt-ratios of 0.6 at a synthesis temperature of 120 °C, a further increased ratio does not lead to a higher purity of BH$_4$-sod. The amount of amorphous matrix areas can be varied by lowering the synthesis temperature. At the same time, the morphologic particle size decreases, too. It could be shown that the morphologic particle size is closely related to the amount of amorphous areas

in the matrix. Water bound in these areas has a significant influence on the thermal reaction of BH_4^-. Smaller particles lead to increased reaction degrees but also to lowered amounts of BH_4-sod. The results imply that further analyses and syntheses need to be carried out in the near future: It is highly recommended to characterize more synthesis series with intermediate particle sizes, based on kaolin as matrix reactant and the combination of sodium aluminate and sodium metasilicate.

New results on species observed during the thermal reaction of BH_4^- imply a review on previously published theories. Species 'A', so far interpreted as H_3BOH^-, is very likely related to $B(OH)_3$. It is shown that this species is not affected by oxygen meaning a pure boron oxide species is unlikely. Furthermore external water leads to increased signal intensities of this species, implying that B-OH bonds are present. Because no hydrogen can be released from this species it cannot include any B-H bonds. The sum of these results suggests the interpretation of species 'A' as $B(OH)_3$. This means certainly not that the reaction mechanism of BH_4^- does not follow the route over $H_{4-x}B(OH)_x^-$ as intermediates but they could not be detected in the present analyses.

The conclusions on the reaction mechanism obtained in this thesis are summarized in the scheme of the reaction mechanism below:

Starting from BH_4^- three reaction path are possible. *Path 1* is concluded from the analyses on the influence of the atmosphere on the thermal reaction. It shows the direct oxidation of the bound hydrogen to BO_2^-. This path takes place parallel at the presence of oxygen. *Path 2* represents the substitution of hydrogen with OH^- till $B(OH)_4^-$ is formed, which afterwards dehydrates to BO_2^- in two steps. This reaction represents the previously published interpretation of species 'A'. *Path 3* shows the newly concluded intermediate species 'A' as $B(OH)_3$ and the therefore most likely reaction path (marked in red). It shows the same amount of released hydrogen as *Path 2*. The dehydration follows the literature [92] and is confirmed by the presence of $B(OH)_4^-$ and $BO(OH)_2^-$.
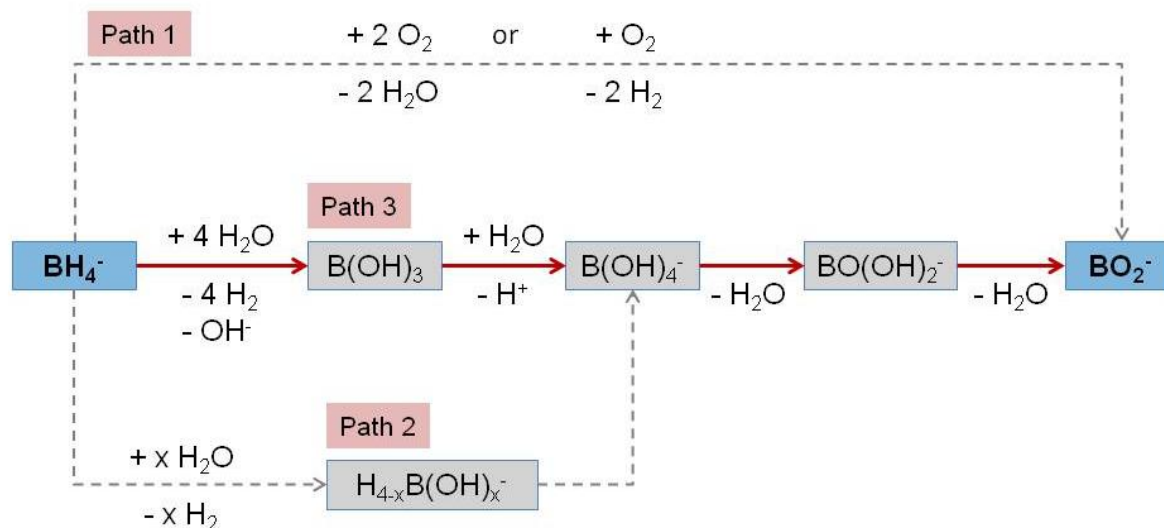
Figure 116: Reaction scheme of the thermal reaction of BH_4^-

These new conclusions need to be considered in the previously done analyses on direct reloading experiments of reacted BH_4-sod with hydrogen [17], too. Here, a hydrogen reinsertion was published, based on increased intensities of species 'A' and has to be reviewed now. Results concerning a partial recycling by addition of MgH_2 under hydrogen pressure are still relevant. These results additionally show an increase of BH_4^- and represent therefore a successful recycling process of reacted BH_4^- in the sodalite, following the ideas of Kojima and Haga [22].

The new results show where to draw on further analyses and methods. Here, first results from the cooperation with the group of Prof. Dr. T. Bredow from the university of Bonn need to be mentioned: Modeling of FTIR and NMR spectra look very promising [100], [101] and from the combination of the modeling and experimental results, further insights on the reaction mechanism of BH_4^- in the sodalite and on $NaBH_4$ itself can be expected.

V. Literature

[1]   R. Scholz, M. Beckmann, C. Pieper, M. Muster, and R. Weber, "Considerations on providing the energy needs using exclusively renewable sources: Energiewende in Germany," *Renew. Sustain. Energy Rev.*, vol. 35, pp. 109–125, Jul. 2014.

[2]   O. Ehret and K. Bonhoff, "Hydrogen as a fuel and energy storage: Success factors for the German Energiewende," *Int. J. Hydrogen Energy*, Mar. 2015.

[3]   B. Bogdanović and M. Schwickardi, "Ti-doped alkali metal aluminium hydrides as potential novel reversible hydrogen storage materials," *Journal of Alloys and Compounds*, vol. 253–254. pp. 1–9, 1997.

[4]   L. Schlapbach and A. Züttel, "Hydrogen-storage materials for mobile applications.," *Nature*, vol. 414, no. 6861, pp. 353–358, 2001.

[5]   B. B. Pradhan, A. A. Harutyunyan, D. Stojkovic, J. J. Grossman, P. Zhang, M. M. Cole, V. Crespi, H. Goto, J. Fujiwara, and P. P. Eklund, "Large cryogenic storage of hydrogen in carbon nanotubes at low pressures," *Journal of Materials Research*, vol. 17, no. 09. pp. 2209–2216, 2002.

[6]   Y. H. Hu and E. Ruckenstein, "Clathrate Hydrogen Hydrate — A Promising Material for Hydrogen Storage," *ChemInform*, vol. 37, no. 21, May 2006.

[7]   F. Schüth, "Mobile Wasserstoffspeicher mit Hydriden der leichten Elemente," *Nachrichten aus der Chemie*, vol. 54, no. 1, pp. 24–28, Jan. 2006.

[8]   D. J. Tranchemontagne, K. S. Park, H. Furukawa, J. Eckert, C. B. Knobler, and O. M. Yaghi, "Hydrogen Storage in New Metal–Organic Frameworks," *J. Phys. Chem. C*, vol. 116, no. 24, pp. 13143–13151, Jun. 2012.

[9]   A. Züttel, A. Borgschulte, and S.-I. Orimo, "Tetrahydroborates as new hydrogen storage materials," *Scr. Mater.*, vol. 56, no. 10, pp. 823–828, May 2007.

[10]   H. I. Schlesinger, H. C. Brown, A. E. Finholt, J. R. Gilbreath, H. R. Hoekstra, and E. K. Hyde, "Sodium Borohydride, Its Hydrolysis and its Use as a Reducing Agent and in the Generation of Hydrogen," *J. Am. Chem. Soc.*, vol. 75, no. 3, pp. 215–219, 1953.

[11]   P. Martelli, R. Caputo, A. Remhof, P. Mauron, A. Borgschulte, and A. Züttel, "Stability and Decomposition of $NaBH_4$," *J. Phys. Chem. C*, vol. 114, no. 15, pp. 7173–7177, 2010.

[12]   P. P. Prosini and P. Gislon, "Water consumption during solid state sodium borohydride hydrolysis," *Int. J. Hydrogen Energy*, vol. 35, no. 22, pp. 12234–12238, Nov. 2010.

[13]   D. M. F. Santos and C. a. C. Sequeira, "Sodium borohydride as a fuel for the future," *Renew. Sustain. Energy Rev.*, vol. 15, no. 8, pp. 3980–4001, Oct. 2011.

[14]   U. B. Demirci, O. Akdim, and P. Miele, "Ten-year efforts and a no-go recommendation for sodium borohydride for on-board automotive hydrogen storage," *Int. J. Hydrogen Energy*, vol. 34, no. 6, pp. 2638–2645, Mar. 2009.

[15]   U. B. Demirci and P. Miele, "Sodium tetrahydroborate as energy/hydrogen carrier, its history," *Comptes Rendus Chim.*, vol. 12, no. 9, pp. 943–950, Sep. 2009.

[16]   M. T. Kelly and J. V Ortega, "Review of Chemical Processes for the Synthesis of Sodium Borohydride," 2004.

[17] J. Buhl, L. Schomborg, and C. H. Rüscher, "Enclosure of Sodium Tetrahydroborate (NaBH$_4$) in Solidified Aluminosilicate Gels and Microporous Crystalline Solids for Fuel Processing," in *Hydrogen Storage*, J. Liu, Ed. InTech, 2012, pp. 49–90.

[18] J. K. Lee, H. Ann, Y. Yi, K. W. Lee, S. Uhm, and J. Lee, "A stable Ni–B catalyst in hydrogen generation via NaBH4 hydrolysis," *Catal. Commun.*, vol. 16, no. 1, pp. 120–123, Nov. 2011.

[19] J.-H. Kim, K.-T. Kim, Y.-M. Kang, H.-S. Kim, M.-S. Song, Y.-J. Lee, P. S. Lee, and J.-Y. Lee, "Study on degradation of filamentary Ni catalyst on hydrolysis of sodium borohydride," *J. Alloys Compd.*, vol. 379, no. 1–2, pp. 222–227, Oct. 2004.

[20] Ç. Çakanyıldırım and M. Gürü, "Production of NaBH$_4$ and hydrogen release with catalyst," *Renew. Energy*, vol. 34, no. 11, pp. 2362–2365, Nov. 2009.

[21] S. Bennici, A. Garron, and A. Auroux, "Maximizing the hydrogen yield in the catalyzed hydrolysis of pure borohydride powders," *Int. J. Hydrogen Energy*, vol. 35, no. 16, pp. 8621–8625, Aug. 2010.

[22] Y. Kojima and T. Haga, "Recycling process of sodium metaborate to sodium borohydride," *Int. J. Hydrogen Energy*, vol. 28, no. 9, pp. 989–993, Sep. 2003.

[23] A. E. Sanli, İ. Kayacan, B. Z. Uysal, and M. L. Aksu, "Recovery of borohydride from metaborate solution using a silver catalyst for application of direct rechargable borohydride/peroxide fuel cells," *J. Power Sources*, vol. 195, no. 9, pp. 2604–2607, May 2010.

[24] J. Buhl, L. Schomborg, and C. H. Rüscher, "NaBH$_4$ in solidified aluminosilicate gel: a new hydrogen storage with interesting properties," in *Cleantech 2012*, 2012, p. 440.

[25] C. H. Rüscher, L. Schomborg, A. Schulz, and J.-C. Buhl, "Basic Research on Geopolymer Gels for Production of Green Binders and Hydrogen Storage," in *Developments in Strategic Materials and Computational Design IV*, W. M. Kriven, J. Wang, Y. Zhou, A. L. Gyekenyesi, S. Kirihara, and S. Widjaja, Eds. Hoboken, NJ, USA: John Wiley & Sons, Inc., 2013, pp. 97–114.

[26] J.-C. Buhl, T. M. Gesing, and C. H. Rüscher, "Synthesis, crystal structure and thermal stability of tetrahydroborate sodalite Na$_8$[AlSiO$_4$]$_6$(BH$_4$)$_2$," *Microporous Mesoporous Mater.*, vol. 80, no. 1–3, pp. 57–63, May 2005.

[27] H. H. E. Pietsch, M. Fechtelkord, and J. Buhl, "The formation of unusually twofold coordinated boron in a sodalite matrix," *J. Alloys Compd.*, vol. 257, no. 1–2, pp. 168–174, 1997.

[28] D. Hakan, and P. Yozgatli, "Unsicherheitsbilanzen in der quantitativen FT-IR-Spektroskopie," Dissertation, Humboldt-Universität zu Berlin, Mathematisch-Naturwissenschaftliche Fakultät I, publiziert am 22.05.2002

[29] C. H. Rüscher, "Chemical reactions and structural phase transitions of sodalites and cancrinites in temperature dependent infrared (TIR) experiments," *Microporous Mesoporous Mater.*, vol. 86, no. 1–3, pp. 58–68, Nov. 2005.

[30] D. Massiot, F. Fayon, M. Capron, I. King, S. Le Calvé, B. Alonso, J.-O. Durand, B. Bujoli, Z. Gan, and G. Hoatson, "Modelling one- and two-dimensional solid-state NMR spectra," *Magn. Reson. Chem.*, vol. 40, no. 1, pp. 70–76, Jan. 2002.

[31] A. Guinier, *X-ray Diffraction in Crystals, Imperfect Crystals and Amorphous Bodies*. 1994.

[32] L. Schomborg, C. H. Rüscher, and J. Buhl, "Thermal Stability and quantification of hydrogen release of $NaBH_4$ enclosed in aluminosilicate gels," *Krist. Suppl.*, no. 32, p. 62, 2012.

[33] P. W. Atkins and J. De Paula, *Physikalische Chemie*. John Wiley & Sons, 2013.

[34] M. Binnewies, M. Jäckel, H. Willner, and G. Rayner-Canham, *Allgemeine und Anorganische Chemie*. Spektrum Akademischer Verlag, 2010.

[35] C. A. Schneider, W. S. Rasband, and K. W. Eliceiri, "NIH Image to ImageJ: 25 years of image analysis," *Nat. Methods*, vol. 9, no. 7, pp. 671–675, Jun. 2012.

[36] Y. Filinchuk and H. Hagemann, "Structure and Properties of $NaBH_4 \cdot 2H_2O$ and $NaBH_4$," *Eur. J. Inorg. Chem.*, vol. 2008, no. 20, pp. 3127–3133, Jul. 2008.

[37] J. Goubeau and H. Kallfass, "Die Reaktion Natriumborhydrid und Wasser," *Zeitschrift für Anorg. und Allg. Chemie*, vol. 299, p. 12, 1959.

[38] C. Schutte, "The infrared spectrum of thin Films of sodium borohydride," *Spectrochim. Acta*, 1960.

[39] J. A. A. Ketelaar and C. J. H. Schutte, "The borohydride ion (BH_4^-) in a face-centred cubic alkali-halide lattice," *Spectrochim. Acta*, vol. 17, no. 12, pp. 1240–1243, Jan. 1961.

[40] M. Hesse, H. Meier, and B. Zeeh, *Spektroskopische Methoden in der organischen Chemie*, vol. 2, no. 5. 2005.

[41] G. Renaudin, S. Gomes, H. Hagemann, L. Keller, and K. Yvon, "Structural and spectroscopic studies on the alkali borohydrides MBH4 (M = Na, K, Rb, Cs)," *J. Alloys Compd.*, vol. 375, no. 1–2, pp. 98–106, Jul. 2004.

[42] D. R. Lide, "CRC Handbook of Chemistry and Physics, 84th Edition, 2003-2004," *Handb. Chem. Phys.*, vol. 53, p. 2616, 2003.

[43] H. Meekes, T. Rasing, P. Wyder, A. Janner, and T. Janssen, "Raman and infrared spectra of the incommensurate crystal Na_2CO_3," *Phys. Rev. B*, vol. 34, no. 6, pp. 4240–4254, 1986.

[44] Z. Assi and C. H. Rüscher, "Thermogravimetric, temperature dependent infrared and XRD investigations on $NaBO_2.xH_2O$ system," in *Kristallogr. Suppl.*, 2014, pp. 75–76.

[45] B. H. Liu and Z. P. Li, "A review: Hydrogen generation from borohydride hydrolysis reaction," *J. Power Sources*, vol. 187, no. 2, pp. 527–534, Feb. 2009.

[46] J. Davidovits, "Geopolymers and Geopolymeric Materials," *J. Therm. Anal.*, vol. 35, pp. 429–441, 1989.

[47] R. A. Fletcher, K. J. D. Mackenzie, C. L. Nicholson, and S. Shimada, "The composition range of aluminosilicate geopolymers," *J. Eur. Ceram. Soc.*, vol. 25, no. 9, pp. 1471–1477, Jun. 2005.

[48] S. J. O'Connor and K. J. D. Mackenzie, "A new hydroxide-based synthesis method for inorganic polymers," *J. Mater. Sci.*, vol. 45, no. 12, pp. 3284–3288, Mar. 2010.

[49] Y. Zhang, W. Sun, and Z. Li, "Infrared spectroscopy study of structural nature of geopolymeric products," *J. Wuhan Univ. Technol. Sci. Ed.*, vol. 23, no. 4, pp. 522–527, Sep. 2008.

[50] C. H. Rüscher, E. Mielcarek, W. Lutz, A. Ritzmann, and W. M. Kriven, "Weakening of Alkali-Activated Metakaolin During Aging Investigated by the Molybdate Method and Infrared Absorption Spectroscopy," *J. Am. Ceram. Soc.*, vol. 93, no. 9, pp. 2585–2590, Apr. 2010.

[51] C. H. Rüscher, E. Mielcarek, W. Lutz, A. Ritzmann, and W. M. Kriven, "Aging process of alkali activated metakaolin." Ceramic Transactions 215 , pp. 315-324, 2010.

[52] P. J. De Bièvre and G. H. Debus, "Absolute isotope ratio determination of a natural boron standard," *Int. J. Mass Spectrom. Ion Phys.*, vol. 2, no. 1, pp. 15–23, Jan. 1969.

[53] A. Pozio, M. Defrancesco, G. Monteleone, R. Oronzio, S. Galli, C. Dangelo, and M. Marrucci, "Apparatus for the production of hydrogen from sodium borohydride in alkaline solution," *Int. J. Hydrogen Energy*, vol. 33, no. 1, pp. 51–56, Jan. 2008.

[54] *Encyclopedia of Reagents for Organic Synthesis*. Chichester: John Wiley & Sons, Ltd, 2001.

[55] L. M. Abts, J. T. Langland, and M. M. Kreevoy, "Role of water in the hydrolysis of tetrahydroborate ion," *J. Am. Chem. Soc.*, vol. 97, no. 11, pp. 3181–3185, May 1975.

[56] A. Belkly, M. Helderman, V. L. Karen, and P. Ulkch, "New developments in the Inorganic Crystal Structure Database (ICSD): Accessibility in support of materials research and design," *Acta Crystallogr. Sect. B Struct. Sci.*, vol. 58, no. 3 PART 1, pp. 364–369, 2002.

[57] J. Löns and H. Schulz, "Strukturverfeinerung von Sodalith, $Na_8Si_6Al_6O_{24}Cl_2$," *Acta Crystallogr.*, vol. 23, no. 3, pp. 434–436, Sep. 1967.

[58] E. M.Flanigen, H. Khatami, and H. A. Szymanski, "*Molecular Sieve Zeolites-I*", vol. 101. Washington DC.: American Chemical Society, 1974.

[59] A. Aronne, S. Esposito, C. Ferone, P. Pernice, N. Federico, I. I. P. Tecchio, L. Materiali, A. Territorio, V. G. Di Biasio, and C. Fr, "FTIR study of the thermal transformation of barium-exchanged zeolite A to celsian," *J. Mater. Chem.*, no. 12, pp. 3039–3045, 2002.

[60] D. Akolekar, A. Chaffee, and R. F. Howe, "The transformation of kaolin to low-silica X zeolite," *Zeolites*, vol. 19, no. 5–6, pp. 359–365, Nov. 1997.

[61] J.-C. Buhl, "The properties of salt-filled sodalites. Part 3. Synthesis and thermal behaviour of basic and non-basic carbonate enclathrated sodalites," vol. 219, pp. 205–214, 1993.

[62] J. Weidlein, U. Müller, and K. Dehnicke, *Schwingungsfrequenzen: Hauptgruppenelemente*. 1981.

[63] F. M. Jaeger, "On the constitution and the structure of ultramarine," *Trans. Faraday Soc.*, vol. 25, p. 320, Jan. 1929.

[64] W. H. Baur and R. X. Fischer, "A historical note on the sodalite framework: The contribution of Frans Maurits Jaeger," *Microporous Mesoporous Mater.*, vol. 116, no. 1–3, pp. 1–3, Dec. 2008.

[65]   S. Bachmann and J.-C. Buhl, "Crystallization, characterization and structure of nitrite aluminogermanate sodalite $Na_8[AlGeO_4]_6(NO_2)_2$," *Microporous Mesoporous Mater.*, vol. 28, no. 1, pp. 35–47, Mar. 1999.

[66]   G. M. Johnson, P. J. Mead, and M. T. Weller, "Synthesis of a range of anion-containing gallium and germanium sodalites," *Microporous Mesoporous Mater.*, vol. 38, no. 2–3, pp. 445–460, Aug. 2000.

[67]   I. Poltz, L. Robben, J.-C. Buhl, and T. M. Gesing, "Synthesis, crystal structure and temperature-dependent behavior of gallogermanate tetrahydroborate sodalite $|Na_8(BH_4)_2|[GaGeO_4]_6$," *Microporous Mesoporous Mater.*, vol. 174, pp. 54–61, Jul. 2013.

[68]   J. Felsche and S. Luger, "Phases and Thermal Decomposition Characteristics of Hydro-Sodalites $Na_{6+x}[AlSiO_4]_6(OH)_x$ nH_2O," *Thermochim. Acta*, no. 118, pp. 35–55, 1987.

[69]   F. Hund, "Nitrit-, Cyanid- und Rhodanid-Sodalith," *Zeitschrift für Anorg. und Allg. Chemie*, vol. 511, no. 4, pp. 225–230, Apr. 1984.

[70]   T. M. Gesing and J.-C. Buhl, "Crystal structure of sodium alumosilicate cyanide, $Na_8[AlSiO_4]_6(CN)_2$," *Synthesis (Stuttg).*, vol. 218, 2003.

[71]   J.-C. Buhl, C. Mundus, J. Löns, and W. Hoffmann, "On the Enclathration of $NaB(OH)_4$ in the β-Cages of Sodalite: Crystallization Kinetics and Crystal Structure," *Zeitschrift Naturforsch.*, no. 49a, pp. 1171–1178, 1994.

[72]   E. C. Moloy, R. T. Cygan, F. Bonhomme, D. M. Teter, and A. Navrotsky, "Molecular Simulations of Anhydrous $Na_6[Al_6Si_6O_{24}]$ Sodalite," *Chem. Mater.*, vol. 16, no. 11, pp. 2121–2133, 2004.

[73]   N. Khosrovani, "Flexibility of Network Structures," *J. Solid State Chem.*, vol. 11, no. 121, pp. 2–11, 1996.

[74]   H. W. Langmi, A. Walton, M. M. Al-Mamouri, S. R. Johnson, D. Book, J. D. Speight, P. P. Edwards, I. Gameson, P. A. Anderson, and I. R. Harris, "Hydrogen adsorption in zeolites A, X, Y and RHO," in *Journal of Alloys and Compounds*, 2003, vol. 356–357, pp. 710–715.

[75]   J.-C. Buhl, "Zeolith mit Bortetrahydrid-gefüllten ß-Käfigen und Verfahren zu dessen Herstellung" *Patent DE 10229910 B4*, 2005.

[76]   J.-C. Buhl, L. Schomborg, and C. H. Rüscher, "Tetrahydroborate sodalite nanocrystals: Low temperature synthesis and thermally controlled intra-cage reactions for hydrogen release of nano- and micro crystals," *Microporous Mesoporous Mater.*, vol. 132, no. 1–2, pp. 210–218, Jul. 2010.

[77]   J.-C. Buhl, C. H. Rüscher, L. Schomborg, and F. Stemme, "Nanocrystalline $NaBH_4^-$ enclathrated zeolite SOD: a model for the improvement of safeness and reactivity of boron hydride based hydrogen storage systems," in *Clean Technology 2010*, 2010, pp. 236–239.

[78]   C. S. Cundy and P. a Cox, "The Hydrothermal Synthesis of Zeolites: History and Development from the Earliest Days to the Present Time The Hydrothermal Synthesis of Zeolites : History and Development from the Earliest Days to the Present Time," vol. 103, no. February, pp. 663–702, 2003.

[79]   R. M. Barrer, *Hydrothermal Chemistry of Zeolites*, vol. 31, no. 4. Academic Press, 1983.

[80]   C. M. B. Henderson and D. Taylor, "Infrared spectra of anhydrous members of the sodalite family," *Spectrochim. Acta Part A Mol. Spectrosc.*, vol. 33, no. 3–4, pp. 283–290, 1977.

[81]   M. Wiebcke, P. Sieger, J. Felsche, G. Engelhardt, P. Behrens, and J. Schefer, "Sodium aluminogermanate hydroxosodalite hydrate $Na_{6+x}[Al_6Ge_6O_{24}](OH)_x$ nH_2O ($x \approx$ 1.6, $n \approx$ 3.0): Synthesis, phase transitions and dynamical disorder of the hydrogen dihydroxide anion, $H_3O_2^-$, in the Cubic high-temperature form," *Zeitschrift für Anorg. und Allg. Chemie*, vol. 619, no. 7, pp. 1321–1329, Jul. 1993.

[82]   J. Gardiner and J. Collat, "The Hydrolysis of Sodium Tetrahydroborate. Identification of an Intermediate," A*m. Chem. Soc.*, vol. 1933, no. 1, pp. 8–9, 1964.

[83]   R. E. Davis and C. G. Swain, "General Acid Catalysis of the Hydrolysis of Sodium Borohydride," *J. Am. Chem. Soc.*, vol. 82, no. 22, pp. 5949–5950, Nov. 1960.

[84]   K. Nakamoto, *Infrared and Raman Spectra of Inorganic and Coordination Compounds*, vol. 85, no. May. 1986.

[85]   B. M. Concha, M. Chatenet, F. Maillard, E. A. Ticianelli, F. H. B. Lima, and R. B. de Lima, "In situ infrared (FTIR) study of the mechanism of the borohydride oxidation reaction.," *Phys. Chem. Chem. Phys.*, vol. 12, no. 37, pp. 11507–16, Oct. 2010.

[86]   J.-C. Buhl, G. Engelhardt, and J. Felsche, "Synthesis, X-ray diffraction and MAS n.m.r. characteristics of tetrahydroxoborate sodalite, $Na_8[AlSiO_4]_6[B(OH)_4]_2$," *Zeolites*, vol. 9, pp. 40–44, 1989.

[87]   B. Wrackmeyer, "Nuclear magnetic resonance spectroscopy of boron compounds containing two-, three- and four-coordinate boron," 1988.

[88]   P. J. Bray, "NMR and NQR studies of boron in vitreous and crystalline borates," *Inorganica Chim. Acta*, vol. 289, no. 1–2, pp. 158–173, Jun. 1999.

[89]   Ç. Çakanyıldırım and M. Gürü, "Hydrogen cycle with sodium borohydride," *Int. J. Hydrogen Energy*, vol. 33, no. 17, pp. 4634–4639, Sep. 2008.

[90]   J. Andrieux, U. B. Demirci, J. Hannauer, C. Gervais, C. Goutaudier, and P. Miele, "Spontaneous hydrolysis of sodium borohydride in harsh conditions," *Int. J. Hydrogen Energy*, vol. 36, no. 1, pp. 224–233, Jan. 2011.

[91]   R. Aiello, J. H. Sharp, and M. A. Matthews, "Production of hydrogen from chemical hydrides via hydrolysis with steam," *Int. J. Hydrogen Energy*, vol. 24, no. 12, pp. 1123–1130, 1999.

[92]   S. S. Gujral, "UV-Visible Spectra Analysis of Boric Acid in Different Solvents: A Case Study," *Int. J. Pharm. Sci. Res.*, vol. 6, no. 2, pp. 830–834, 2015.

[93]   T. K. Hoefs and J.-C. Buhl, "Thermal behaviour of $NaBH_4$-sodalites with alumosilicate framework: Influence of cage water content and the surrounding conditions," *Mater. Res. Bull.*, vol. 46, no. 11, pp. 2173–2178, Nov. 2011.

[94]   G. Guella, C. Zanchetta, B. Patton, and a Miotello, "New insights on the mechanism of palladium-catalyzed hydrolysis of sodium borohydride from ^{11}B NMR measurements.," *J. Phys. Chem. B*, vol. 110, no. 34, pp. 17024–17033, 2006.

[95]   C. H. Rüscher, F. Stemme, L. Schomborg, and J. Buhl, "Low temperature hydrogen release," *Ceram. Trans.*, 2009.

[96]   R. E. Dinnebier and S. J. L. Billinge, *Powder diffraction: Theory and practice*. 2008.

[97]   A. F. Holleman and E. Wiberg, *Lehrbuch der anorganischen Chemie*. 1995.

[98]   C. Cento, P. Gislon, and P. P. Prosini, "Hydrogen generation by hydrolysis of $NaBH_4$," *Int. J. Hydrogen Energy*, vol. 34, no. 10, pp. 4551–4554, May 2009.

[99]   L. Schomborg, Z. Assi, J.-C. Buhl, C. H. Rüscher, and M. Wark, "Ammonia-Borane Geopolymer (AB-G) Composite," in *39th Int'l Conf & Expo on Advanced Ceramics & Composites*, 2015 accepted paper.

[100]   M. Marcus, T. Bredow, L. Schomborg, C. H. Rüscher, and J.-C. Buhl, "Structure and IR spectra of $Na_8[AlSiO_4]_6(BH_4)_2$ sodalite: Comparison between theoretical predictions and experimental data.," *Zeitschrift für Krist.*, no. 32, pp. 89–90, 2012.

[101]   A. G. Schneider, T. Bredow, L. Schomborg, and C. H. Rüscher, "Structure and IR vibrational spectra of $Na_8[AlSiO_4]_6(BH_4)_2$: comparison of theory and experiment.," *J. Phys. Chem. A*, vol. 118, no. 34, pp. 7066–73, Aug. 2014.

VI. Acknowledgements

During the experimental work in the lab and the writing of this thesis I have been supported with ideas, suggestions and practical assistance by various people. I would like to thank all involved very much. Furthermore, I would especially like to thank:

Prof. Dr. C. H. Rüscher for the interesting and demanding selection of topics, his very good supervision and support and for all the lively discussions

Prof. Dr. J.-Ch. Buhl for the interesting and demanding selection of topics, as well as for his support and numerous suggestions

Prof. Dr. T. Bredow and A. G. Schneider for the good cooperation and the lively discussions

Dr. M. Fechtelkord for the NMR measurements and support during evaluation

Dr. S. Schuth for the CS analyses

Dr. S. Fanara for supporting me during the KFT measurements

Prof. Dr. H. Behrens and Dr. A.-M. Welsch for their support and suggestions at all times

The student research assistants and students who did analyses under my supervision: F. Kiesel (Dehydration of $B(OH)_4$-Sod, $NaBH_4$-Gel), M. Vadodi (BH_4-Sod syntheses) and R. Balzer ($NaBH_4$-Gel)

Workgroup Crystallography and office 325

All my friends, especially for the everyday moral support and the suitable distraction when most necessary and helpful

I would especially like to thank my parents and my brother for their support and confidence during my entire studies.

VII. Curriculum Vitae

■ Personal Details

name: Lars Schomborg
date of birth: 02.01.1984 in Osnabrück

■ Research Interests

- ➢ Hydrogen storage systems
- ➢ Material science, R&D of function materials
- ➢ Analytics
- ➢ Zeolites, customized properties

■ Work Experience and Internships:

since Sep. 2011   Research assistant at the Institute of Mineralogy, Leibniz Universität Hannover (LUH)
2009 – 2011   Student research assistant at the Institute of Mineralogy, LUH, Crystallography group
2008   Internship Federal Institute for Geosciences and Natural Resources (BGR), Hannover
2007 – 2009   Student research assistant at the Institute of Mineralogy, LUH, Tutor of 'Chemistry for natural scientists'

■ Education

since Sep. 2011   PhD student at the Institute of Mineralogy, LUH
2009 – 2011   Master of Science Geoscience, LUH
2006 – 2009   Bachelor of Science Geoscience, LUH
2004 – 2006   Diploma student Chemistry, LUH
2003 – 2004   Diploma student Material Science, CAU Kiel
1996 – 2003   German secondary school leaving examination (Abitur)

■ Additional Skills

- ➢ *Languages:* German (native), English (fluent), France (basic)
- ➢ *Software* (selection): MS Office, SigmaPlot, Opus, ArcGIS, Topas, dmfit
- ➢ *Analytical methods* (selection): x-ray diffraction, infrared spectroscopy, differential thermo analytics, thermogravimetry, scanning electron microscope, nuclear magnetic resonance spectroscopy

VIII. Publications

[1]   C. H. Rüscher, F. Stemme, <u>L. Schomborg</u>, and J. Buhl, "Low temperature hydrogen release," *Ceram. Trans.*, vol. 217, pp. 65–70, 2009.

[2]   C. H. Rüscher, <u>L. Schomborg</u>, and J.-C. Buhl, "Thermally Controlled Water Injection into BH_4-Sodalite for Hydrogen Formation Investigated by IR Absorption," *Diffus. Fundam.*, vol. 12, pp. 37–39, 2010.

[3]   J.-C. Buhl, <u>L. Schomborg</u>, and C. H. Rüscher, "Tetrahydroborate sodalite nanocrystals: Low temperature synthesis and thermally controlled intra-cage reactions for hydrogen release of nano- and micro crystals," *Microporous Mesoporous Mater.*, vol. 132, no. 1–2, pp. 210–218, Jul. 2010.

[4]   J.-C. Buhl, C. H. Rüscher, <u>L. Schomborg</u>, and F. Stemme, "Nanocrystalline $NaBH_4$-enclathrated zeolite SOD: a model for the improvement of safeness and reactivity of boron hydride based hydrogen storage systems," in *Clean Technology 2010*, 2010, pp. 236–239.

[5]   <u>Schomborg L.</u>, Rüscher C. H., Buhl J-Ch. "Hydrogen release and reinsertion reactions in $(BH_x\text{-}(OH)_y\text{-}O_z)$-SOD zoned crystal systems", *Z. Kristallogr. Suppl.* no. 31: 24, 2011.

[6]   J. Buhl, <u>L. Schomborg</u>, and C. H. Rüscher, "Enclosure of Sodium Tetrahydroborate (NaBH4) in Solidified Aluminosilicate Gels and Microporous Crystalline Solids for Fuel Processing," in *Hydrogen Storage*, J. Liu, Ed. InTech, 2012, pp. 49–90.

[7]   J. Buhl, <u>L. Schomborg</u>, and C. H. Rüscher, "$NaBH_4$ in solidified aluminosilicate gel: a new hydrogen storage with interesting properties," in *Clean Tech 2012*, 2012, p. 440.

[8]   <u>L. Schomborg</u>, C. H. Rüscher, and J. Buhl, "Thermal Stability and quantification of hydrogen release of NaBH4 enclosed in aluminosilicate gels," *Krist. Suppl.*, no. 32, p. 62, 2012.

[9]   Depnath, T., Hussain, A., <u>Schomborg, L.</u>, Rüscher, C.: "Synthesis and characterization of new compositions with mullite type structure: $Bi_2Cr_xM_{4-x}O_9$ (M=Al, Ga) and $Bi_{2-x}Sb_xAl_4O_9$", *Krist. Suppl.*, no. 32: 119, 2012

[10]   M. Marcus, T. Bredow, <u>L. Schomborg</u>, C. H. Rüscher, and J.-C. Buhl, "Structure and IR spectra of $Na_8[AlSiO_4]_6(BH_4)_2$ sodalite: Comparison between theoretical predictions and experimental data.," *Krist. Suppl.*, no. 32, pp. 89–90, 2012.

[11]   Rüscher, C.H., <u>Schomborg, L.</u>, Schulz, A., Buhl, J. C.: "Basic research on geopolymer gels for production of green binders and hydrogen storage", *Developments in Strategic Materials and Computational Design IV: Ceramic Engineering and Science Proceedings*, Vol. 34, Issue 10, 97 – 114, 2013

[12]   A. G. Schneider, T. Bredow, <u>L. Schomborg</u>, and C. H. Rüscher, "Structure and IR vibrational spectra of $Na_8[AlSiO_4]_6(BH_4)_2$: comparison of theory and experiment.," *J. Phys. Chem. A*, vol. 118, no. 34, pp. 7066–73, Aug. 2014.

[13]   <u>L. Schomborg</u>, Z. Assi, J.-C. Buhl, C. H. Rüscher, and M. Wark, "Ammonia-Borane Geopolymer (AB-G) Composite," in *39th Int'l Conf & Expo on Advanced Ceramics & Composites*, 2015 accepted paper.